Hydrothermal alterations, Cu-Ag mineralizations and structural geology of the volcanic rocks from Seival Mine, Camaquã Neoproterozoic Basin, Southern Brazil

Rodrigo Winck Lopes

UNIVERSITÉ CÔTE D'AZUR

ÉCOLE DOCTORALE
SCIENCES FONDAMENTALES ET APPLIQUÉES

UFRGS
UNIVERSIDADE FEDERAL DO RIO GRANDE DO SUL

THÈSE DE DOCTORAT

ALTERATIONS HYDROTHERMALES, MINERALISATION CU-AG ET GEOLOGIE STRUCTURALE DES ROCHES VOLCANIQUES DE LA MINE DE SEIVAL, BASSIN NEOPROTEROZOIQUE DE CAMAQUÃ, SUD DU BRESIL

Rodrigo Winck LOPES

Laboratoire Géoazur

Présentée en vue de l'obtention
du grade de docteur en Sciences de la Terre
d'Université Côte d'Azur
et de l'Universidade Federal do Rio Grande do Sul
Dirigée par : Dr. Christophe Renac / Dr. André Sampaio Mexias
Soutenue le : le 23 octobre 2018

Devant le jury, composé de :
Ana Maria Pimentel Mizusaki, Professeure, UFRGS
André Sampaio Mexias, Professeur, UFRGS
Christophe Renac, Professeur, UCA
Everton Marques Bongiolo, Professeur associé, UFRJ
Maria José Maluf de Mesquita, Professeure associée, UNICAMP

CNPq Conselho Nacional de Desenvolvimento Científico e Tecnológico
CIÊNCIA SEM FRONTEIRAS
CAPES

UNIVERSITÉ CÔTE D´AZUR
ECOLE DOCTORALE DES SCIENCES
FONDAMENTALES ET APPLIQUEES

UNIVERSIDADE FEDERAL DO RIO GRANDE DO SUL
INSTITUTO DE GEOCIÊNCIAS
PROGRAMA DE PÓS-GRADUAÇÃO EM
GEOCIÊNCIAS

Thèse de doctorat

En cotutelle internationale
Présentée en vue de l'obtention du grade
de docteur de l'Universite Côte d'Azur
et
de l'Universidade Federal do Rio Grande do Sul
Discipline
Sciences de la Terre
Ecole Doctorale Sciences Fondamentales et Appliquées
Laboratoire Géoazur

Présentée et soutenue
par
Rodrigo Winck LOPES

ALTERATIONS HYDROTHERMALES, MINERALISATION CU-AG ET GEOLOGIE STRUCTURALE DES ROCHES VOLCANIQUES DE LA MINE DE SEIVAL, BASSIN NEOPROTEROZOIQUE DE CAMAQUÃ, SUD DU BRESIL

HYDROTHERMAL ALTERATIONS, CU—AG MINERALIZATIONS AND STRUCTURAL GEOLOGY OF THE VOLCANIC ROCKS FROM SEIVAL MINE, CAMAQUÃ NEOPROTEROZOIC BASIN, SOUTHERN BRAZIL

Dirigée par **Dr. Christophe Renac** / **Dr. André Sampaio Mexias**

Soutenue le **23 octobre 2018**
Devant le jury composé de:

Ana Maria Pimentel Mizusaki	Professeure, UFRGS	Examinatrice
André Sampaio Mexias	Professeur, UFRGS	Directeur de thèse
Christophe Renac	Professeur, UCA	Co–Directeur de thèse
Everton Marques Bongiolo	Professeur associé, UFRJ	Rapporteur
Maria José Maluf de Mesquita	Professeure associée, UNICAMP	Rapporteur

RÉSUMÉ

Les roches volcanogéniques de la Mine de Seival appartiennent à la Formation Hilário du Bassin de Camaquã, d'âge Néoprotérozoique. Cette zone contient six mines inactives avec diverses zones de prospection du cuivre et de l'argent. Les minéralisations semblent associées à un contrôle structural en régime cassant. La compréhension des transformations chimiques liées à l'hydrothermalisme et associées aux paléo-contraintes est assez méconnue dans la région. L'étude présentée fut basée sur l'obtention de mesures structurales pour comprendre les contraintes et leur cinématique dans la région, associée aux transformations chimiques des minéraux des phases magmatiques et hydrothermales de haute et basse températures. Fractures et les minéralisations montrent une direction principale N40-60°E/70-88°NW souvent associées à des veines de calcite. Les structures profondes de direction NW-SE et NE-SW étaient liées aux filons volcaniques, aux circulations de fluides hydrothermaux et aux minéralisations associées. Une modélisation thermodynamique utilisant les différentes phases minérales (magmatiques et hydrothermales) a permis d'estimer les températures de haute (tardi-magmatique) et basse (altération hydrothermale). L'albitisation (650 à 250°C) s'est produite en association avec une chloritisation (312 à 120°C). La déstabilisation des sulfures primaires (pyrite et chalcopyrite) dans les sulfures riches en cuivre (bornite-chalcocite) était associée à des interstratifiés de chlorite/smectite à des températures d'environ 250 à 50°C. Ces mêmes interstratifiés chlorite/smectite indiquent des zones riches en cuivre. Les événements plus tardifs (<150°C) souvent associés à la précipitation de barytine ont été étudiés par la chimie et les concentrations en Éléments Terres Rares de cette dernière. Cette étude montre que la source du baryum est liée au processus d'albitisation puis à l'oxydation des sulfures lors de circulation l'eau météoriques.

Mots clés: Altération hydrothermale; Minéralisations de Cu-Ag; Géologie structurale; Bassin de Camaquã.

ABSTRACT

The volcanogenic rocks of the Seival Mine belong to Hilário Formation from Camaquã Basin, with ages Neoproterozoic. This area contain six inactive mines with and several zones with copper and silver prospects. Mineralization were associated to structural control in brittle regime. The understanding of chemical transformation of hydrothermal alteration related to paleostress is not very well understood in the region. The present study was based on obtaining structural measures to understand the stresses and kinematics in the region, associated with chemical transformations of the minerals of the magmatic and high– to low–temperatures hydrothermal phases. Fractures and mineralizations have a main direction N40–60°E /70–88°NW often associated with calcite veins. The deep NW-SE and NE-SW direction structures were related to volcanic lodes, fluid circulation and associated mineralizations. A thermodynamic modeling using different mineral phases (magmatic and hydrothermal) allowed to estimate the high (late–magmatic) and low (hydrothermal alteration) temperatures. The destabilization of primary sulphides (pyrite and chalcopyrite) in copper-rich sulphides (bornite–chalcocite) was associated with chlorite/smectite mixed–layers with temperatures around ~ 250 to 50 °C. These chlorite/smectite mixed–layers indicate areas rich in copper. Later events (<150 °C) often associated with barite precipitation were studied through mineral chemistry and concentrations of Rare Earth Elements. This study showed that the source of barium is related to the process of albitization and subsequent destabilization of sulfides during the circulation of meteoric water.

Keywords: Hydrothermal alteration; Cu–Ag mineralizations; Structural geology; Camaquã Basin.

RESUMO

As rochas vulcanogênicas da Mina do Seival pertencem à Formação Hilário da Bacia do Camaquã, de idade Neoproterozoica. Esta área possui seis minas inativas e diversas zonas com prospectos de cobre e prata. As mineralizações foram associadas ao controle estrutural em regime rúptil. O entendimento das transformações químicas relacionadas ao hidrotermalismo e associadas ao paleostresse é pouco conhecida na região. O estudo apresentado foi baseado na obtenção de medidas estruturais para entender os esforços e sua cinemática na região, associadas às transformações químicas dos minerais das fases magmática e hidrotermal de alta e baixa temperaturas. Fraturas e mineralizações tem uma direção principal N40–60°E/70–88°NW associadas a veios de calcita. As estruturas profundas de direção NW-SE e NE-SW foram relacionadas aos filões vulcânicos, a circulação de fluidos e as mineralizações associadas. Uma modelagem termodinâmica utilizando diferentes fases minerais (magmática e hidrotermal) permitiu estimar as altas (tardi–magmática) e baixas (alteração hidrotermal) temperaturas. A albitização (650 a 250°C) ocorreu associada à cloritização (312 a 120°C). A desestabilização dos sulfetos primários (pirita e calcopirita) em sulfetos ricos em cobre (bornita–calcocita) foi associada aos interestratificados de clorita/esmectita com temperaturas em torno de ~250 a 50°C. Esses interestratificados de clorita/esmectita indicam zonas ricas em cobre. Os eventos posteriores (<150°C) frequentemente associados à precipitação de barita foram estudados através da química mineral e concentrações de Elementos Terras Raras. Este estudo mostrou que a fonte de bário está relacionada ao processo de albitização e posterior desestabilização de sulfetos durante a circulação de água meteórica.

Palavras-Chaves: Alteração hidrotermal; Mineralizações de Cu-Ag; Geologia estrutural; Bacia do Camaquã.

Esta tese foi elaborada no Instituto de Geociências da Universidade Federal do Rio Grande do Sul e no laboratório Géoazur da Université Cotê D´Azur de Nice Sophia-Antipolis.

Universidade Federal do Rio Grande do Sul
Instituto de Geociências
PPGGEO – Programa de Pós-Graduação em Geociências
Avenida Bento Gonçalves
9500, 91509-900
Porto Alegre, RS
Brasil

Université Cotê D´Azur
ED.SFA – École Doctorale
Sciences Fondamentales et Appliquées
Nice Sophia-Antipolis, Parc Valrose
28 avenue Valrose
06108 Nice Cedex 2
França

Laboratoire Géoazur
Campus CNRS, les Lucioles 1
250, rue Albert Einstein
06560 Valbonne
França

Esta tese foi financiada pelo Conselho Nacional do Desenvolvimento e Pesquisa (CNPq), Programa Ciências Sem Fronteiras (número do processo: 200081/2014-4) e Coordenação de Aperfeiçoamento de Pessoal de Nível Superior (CAPES).

“SE VOCÊ PERSEGUE DOIS COELHOS AO MESMO TEMPO...
NÃO VAI PEGAR NENHUM DOS DOIS”

AGRADECIMENTOS

Ao Conselho Nacional de Desenvolvimento Científico e Tecnológico (CNPq) pela concessão de bolsa de estudos no exterior e à Coordenação de Aperfeiçoamento de Pessoal de Nível Superior (CAPES) pela bolsa de estudos no Brasil.

Ao Programa de Pós-Graduação em Geociências (PPGGEO) e ao Instituto de Geociências pela Excelência Acadêmica e qualidade do curso. À Universidade Federal do Rio Grande do Sul (UFRGS) pelo ensino de qualidade e gratuito. À Université de Côte d´Azur (Nice-Sophia Antipolis) e ao laboratório Géoazur pela infraestrutura.

Aos meus orientadores, Prof. Dr. André Mexias e Prof. Dr. Christophe Renac, pelas orientações e ensinamentos.

À Profª. Drª. Márcia Gomes e aos Profs. Dr. Lauro Nardi, Dr. Ruy Phillip e Dr. Everton Bongiolo pelo auxílio na escrita dos manuscritos científicos. Aos colegas Prof. Dr. Eduardo Fontana, Dr. Marcos Bicca, geólogo Marcelo Lindenberg e graduando Bruno Petracco pelos ensinamentos, colaborações nos trabalhos de campo e preparação de amostras.

A todos os meus familiares e aos meus amigos pelo apoio.

LISTA DE TABELAS

LISTA DE FIGURAS

SUMÁRIO

ESTRUTURA E ORGANIZAÇÃO DA TESE

Esta tese de doutorado está estruturada em torno de um artigo científico publicado e dois artigos submetidos em revistas científicas. Consequentemente, sua organização compreende as seguintes partes principais:

a) Introdução sobre o tema e descrição do objeto da pesquisa de doutorado, onde estão sumarizados os objetivos, a filosofia de pesquisa desenvolvidas e o estado da arte sobre o tema de pesquisa;

b) Artigos publicados e/ou submetidos a periódicos com corpo editorial permanente e revisores independentes, escritos pelo autor durante o desenvolvimento deste Doutorado;

c) Anexos, compreendendo: artigos nos quais o doutorando é co-autor, resumos publicados em eventos relacionados ao tema central da tese e materiais de apoio.

A presente tese é intitulada “Alterações hidrotermais, mineralizações de Cu-Ag e geologia estrutural das rochas vulcanogênicas da Mina do Seival, Bacia Neoproterozoica do Camaquã, sul do Brasil”. A tese foi realizada na forma de doutorado sanduíche em acordo de cotutela entre a Universidade Federal do Rio Grande do Sul (Brasil) e a Université Côte D´Azur (França).

No capítulo 1 é apresentada uma introdução aos principais assuntos e objetivos presentes na síntese integradora desta tese. Essa parte contém também a localização da área de estudo, a amostragem e a descrição dos métodos utilizados durante o desenvolvimento da tese.

No capítulo 2 é apresentada a contextualização relacionada à Bacia do Camaquã. Para isso, são apresentadas a estratigrafia, a geologia e os dados geocronológicos existentes, bem como a Associação Shoshonítica de Lavras do Sul e suas principais características. Por último, é descrito um breve histórico sobre as mineralizações na área de estudo. O capítulo 3 trata sobre o estado atual da arte relacionado à Mina do Seival. Desse modo, apresenta-se o mapa geológico, descreve-se brevemente a geologia estrutural, a petrografia e a alteração hidrotermal da área.

No capítulo 4 são apresentados o manuscrito publicado e os submetidos, atendendo as normas estabelecidas pelo Programa de Pós-Graduação em Geociências da Universidade Federal do Rio Grande do Sul. Cada manuscrito pode ser lido de forma independente dos demais sem prejuízo à sua compreensão. O primeiro manuscrito é intitulado "Au–Cu–Ag mineralization controlled by brittle structures in Lavras do Sul Mining District and Seival Mine deposits, Camaquã Basin, southern Brazil", publicado no *Journal of South America Earth Science*. O segundo manuscrito é intitulado "Mineral assemblages and temperature associated with Cu–enrichment in the Seival area (Camaquã Basin, Neoproterozoic of Southern Brazil)", submetido ao *Journal of Geochemical Exploration*. O terceiro manuscrito é intitulado "Composition and REE analysis of barite from Seival Mine Cu–Ag deposits (Camaquã Basin, Neoproterozoic of Southern Brazil)", submetido ao *Brazilian Journal of Geology*.

O capítulo 5 contém as considerações finais da tese na forma de uma síntese integradora das principais conclusões obtidas. No capitulo 6 são listadas as referências bibliográficas citadas nos capítulos que antecedem os manuscritos, permanecendo as referências dos artigos listados nos mesmos. Nos anexos consta a capa do artigo publicado em co-autoria (ANEXO A) e os resumos de trabalhos apresentados durante o período de doutoramento (ANEXO B), com o objetivo de mostrar o avanço no conhecimento sobre o tema. Também são apresentados o mapa de pontos (ANEXO C), a tabela de pontos (ANEXO D), as medidas estruturais (ANEXO E), os dados de microssonda eletrônica (ANEXO F) e os difratogramas de raios X (ANEXO G).

A Mina do Seival tem sido investigada pelo presente autor desde a Graduação em Geologia com o projeto temático intitulado "Alteração Hidrotermal e Mineralizações de Cobre na Mina do Seival, Bacia do Camaquã, RS", que caracterizou a alteração hidrotermal na área, bem como forneceu um mapa geológico de detalhe para a continuidade dos estudos. Em continuidade, o projeto de mestrado intitulado "Caracterização petrográfica e geoquímica da Mina do Seival, Bacia do Camaquã, RS" teve como objetivo fornecer informações sobre a

petrografia e geoquímica das rochas da região da Mina do Seival, bem como caracterizar as minas e as ocorrências de cobre.

A PROPOS DE LA STRUCTURE DE CETTE THÈSE

Cette thèse est structurée autour de trois manuscrits soumis dans des revues internationales, et le candidat et le premier auteur du manuscrit, dont l'un a déjà été publié. Par conséquent, l'organisation comprend les étapes suivantes:

a) Introduction à la question et la description de l'objet de recherche de le candidat, où sont résumés les objectifs et mis au point la méthodologie de recherche et d'un résumé substantiel écrit en langue Française ;

b) Les manuscrits soumis dans des revues avec examinateurs indépendants, écrit par l'auteur lors de l'élaboration de son doctorat ;

c) Annexes: articles dans lesquels est co-auteur, résumés publiés dans des événements, liés au thème central de la thèse et le matériel supplémenter.

RESUME ETENDU

Les manuscrits

Manuscrit 1:

Au–Cu–Ag mineralization controlled by brittle structures in Lavras do Sul Mining District and Seival Mine deposits, Camaquã Basin, southern Brazil (Journal of South America Earth Science);

Manuscrit 2:

Mineral assemblages and temperature associated with Cu–enrichment in the Seival area (Camaquã Basin, Neoproterozoic of Southern Brazil) (Journal of Geochemical Exploration);

Manuscrit 3:

Composition and REE analysis of barite from Seival Mine Cu–Ag deposits (Camaquã Basin, Neoproterozoic of Southern Brazil) (Brazilian Journal of Geology).

- Le présent résumé vise à présenter un compte-rendu des résultats et conclusions contenus dans les manuscrits publié et soumis comme une exigence partielle pour obtenir le titre de Docteur en Sciences de l'Université Fédérale du Rio Grande do Sul – Brésil et de l'Université Cotê D´Azur – France;
- Le premier chapitre est l'introduction, le deuxième chapitre présente une synthèse de la géologie et le troisième est la méthodologie qui comprend les trois manuscrits publié et soumis;
- Le quatrième chapitre comprend les principales discussions et les considérations finales de chaque manuscrit;
- Les références de ce résumé se trouvent dans le Chapitre 6 de cette thèse.

1. INTRODUCTION

Le Bassin Camaquã contient d'importants dépôts d'or, de cuivre et d'argent (Remus et al., 2000; Bongiolo et al., 2011; Renac et al., 2014). Dans la section du centre-ouest de ce bassin, les roches volcanogeniques (Lopes et al., 2014; Fontana et al., 2017) et plutoniques (Mexias et al., 2005) montrent une altération décrite comme altération hydrothermale tardi-magmatique (Mexias et al., 1990c et 2005; Bongiolo et al., 2011; Fontana et al., 2017).

La zone d'étude est située à 308 km de Porto Alegre, RS - Brésil. La localité se situe entre les limites municipales de Caçapava do Sul et de Lavras do Sul, insérée dans les cartes géologiques et topographiques, Folha Arroio América (SH.22–Y–A–IV–1, 1975), échelle 1/50.000 entre coordonnées géographiques 30°41' à 30°45' S et 53°45' à 53°48' W.

La séquence volcanogénique de la 'Mina do Seival' contient six mines d'argent cuivre inactives (Reischl, 1978; Lopes et al., 2014). Des différentes mines ont ~ 0,20 Mt, avec un contenu de ~ 1,40 % de cuivre (Reischl, 1978). Les sulfures de cuivre disséminés dans des tufs à lapilli, des andésites et agglomérés volcaniques, ainsi que sur des plans de failles ou fractures. La chlorite, les interstratifiés chlorite/smectite, la malachite, l'azurite, l'hématite, la calcite, la barytine et le quartz sont associés aux sulfures de cuivre.

La chimie des minéraux magmatiques, des altérations hydrothermales et des minéralisations ainsi que le contrôle structural des dépôts minéraux ne sont pas bien caractérisées dans cette région. Cette thèse se propose de mieux les caractériser dans le but de mieux comprendre ces minéralisations.

2. GÉOLOGIE RÈGIONAL

La région de Lavras do Sul est constituée d'un socle composé de roches ultramafiques, de métagranitoïdes et de schistes (Cambaí Complexes). Ce socle est partiellement recouvert des roches sédimentaires de la Formation Maricá (Borba et al., 2006). Ces roches plutoniques et volcano-sédimentaires furent intrudées par les roches du complexe de Lavras do Sul (Mexias et al., 2005; Bongiolo et al., 2011),

granitoïdes, vulcanites acides et basiques d'affinité shoshonitique. La zone de la 'Mina do Seival' se situe à proximité de ces corps plutoniques et volcaniques dans des dépôts volcano-sédimentaires de la Formation Hilário antérieure à l'activité magmatique de Lavras do Sul.

Les roches volcano-sédimentaires de la 'Mina do Seival' sont des tufs à lapilli, andésites, agglomérés volcaniques et filons andésitiques et trachyandésitiques. Une plus grande proportion de conglomérats polymictique et des andésites vésiculaires forment la partie Est où ce sont déposés la plus récente Formation Santa Fé du groupe Santa Bárbara.

Dans la zone fut l'objet d'une extraction minière (i: Barite; ii: João Dahne, iii: Morcego; iv: Meio; v: Cruzeta; vi: Alcides) sur six sites miniers, désormais inactifs (Reischl, 1978) ont été exploités dans la Formation Hilário. Ces carrières à ciel ouvert et galeries semblent associés à une structuration régionale d'orientation NE-SW et parfois NW-SE.

3. METHODES

Les observations pétrographiques, la diffraction de rayons X, les mesures structurales, la géochimie et la chimie minérale collaborent à cette compréhension de l'hydrotermalisme dans la région. Le travail sur le terrain et la pétrographie ont rendu possible la classification de la roche, la description de la minéralogie et des aspects texturaux, mettant l'accent sur les phases secondaires dites d'altération. Grâce à la diffraction de rayons X, à la chimie minérale et à la géochimie des Éléments Terres Rares, il a été possible d'établir une corrélation entre les éléments liés à la minéralisation de cuivre. Sont présentées ci-dessous les principales méthodes utilisées et leurs applications dans cette thèse :

- Description pétrographique d'échantillons de surface et de 7 forages (ayant jusqu'à 130 m de profondeur) pour la compréhension de la lithologie;
- Analyse structurale avec mesures cinématiques et direction des failles/fractures pour la détermination des paléo-contraintes de la région;

- Minéralogie et cristallographie des phases d'altération, dont les minéraux argileux, ont été obtenues par la diffraction des rayons X.
- Chimie minérale des phases magmatiques (andésine - labradorite, augite et biotite) et hydrothermales (albite, titanite, chlorite, smectite et minéraux interstratifiés chlorite/smectite) mesurés par microsonde électronique.
- Géochimie des éléments traces, mesurés par ICPMS, extraits de concentrés de plagioclase, de barytine et de calcite.

4. DISCUSSION ET CONSIDERATIONS FINALES

Les minerais, et les assemblages minéraux, les caractéristiques structurales varient entre chacunes des zones minières de 'Mina do Seival' et le district Minier de Lavras do Sul. La principale différence est liée à l'influence de roches magmatiques granitiques de Lavras do Sul et les roches volcanogeniques de 'Mina do Seival'. La presence d'un métamorphisme de contact entre les deux zones et la présence de nombreuses intrusions et filons andésitiques ainsi que les structures faillée et filonienne différent semblent être responsables d'une partie des minéralisations (Cu -Au : Lavras ; Cu-Ag : Seival) entre les deux zones. Dans la Mina do Seival, les minéralisations suivent l'alignement des filons andesitiques d'orientation NE-SW, tandis que dans le District Minier de Lavras do Sul, les minéralisations suivent une direction principale NW-SE.

Les études minéralogies des roches volcano-sédimentaires de Seival et la prédominance des argiles traduisent une altération hydrothermale intense. Ces minéraux majoritairement argileux remplacent les minéraux magmatiques primaires (phénocristaux de plagioclase et de pyroxène), la matrice microcristalline feldspathique, ou remplissent le bord d'amygdales et de cavités. Ces argiles sont généralement associées à du quartz, de la calcite, de l'hématite et des minéraux opaques. Ces argiles sont des smectites, interstratifiés de chlorite/ smectite, corrensite et des chlorites. Les filons de trachyandésite à biotite sont d'ailleur plus altérés que ceux d'andésite et les minéraux ferromagnésiens remplacés par des chlorites et oxydes de fer.

Les mesures des structures cassantes (linéaments et failles) à la Mina do Seival et Lavras do Sul font l'objet d'un travail de reconstitution des contraintes présentées dans le **manuscrit I**. Les principales contraintes obtenues présentent les orientations compression NW-SE, compression NE-SW et distension ENE-WSW. Des arguments de chronologie relative permettent d'identifier que les failles NE-SW sont antérieures à NW-SE. Cette chronologie relative suggéré une compression NW-SE antérieure à la compression NE-SW. Cette paléo-contrainte (NW-SW) a également été associée au contrôle des structures minéralisées. Les failles et les fractures de direction NE-SW sont associées à la faille majeure Cabritos-Perau et celles de direction NW-SE sont associées à la faille de Palma-Jacques. Grâce à cela, nous avons relié le NW-SE compression à l'évolution tectonique au cours de la phase de transtension (600-580 Ma) associée à l'agglutination des blocs dans le Bouclier Sul-rio-grandense. Cette paléo-contrainte fut responsable du magmatisme des dykes et des structures minéralisées.

La chimie minérale de stades magmatiques et hydrothermaux tardi-magmatiques est présentée dans le **manuscrit II**. Cette étude caractérise la signature chimique des minéraux magmatiques préservés, les effets de l'albitisation et les produits d'altération hydrothermale comme le chlorite, la smectite et les minéraux interstratifiés associés à la précipitation de sulfures de cuivre. Cet manuscrit présente la chimie minérale de l'augite, de la biotite, titanite et de l'andésine-labradorite transformée en albite formées par des processus magmatiques et tardi-magmatiques (600-250 °C). Cette altération de haute température correspond aux fluides magmatiques tardifs, comme en témoigne la géochimie des Éléments Terres Rares de plagioclases primaires et secondaires. La chimie de minéraux d'altération comme les Mg-smectites, interstratifiés chlorite/smectite et Mg-chamosite reflète la métastabilité des minéraux tardi-magmatiques avec un apport d'eau non-magmatique, la diminution de température et une mobilité des éléments métalliques.

Enfin, les données de composition et géochimiques d'Éléments Terres Rares des barytes sont présentée dans le **manuscrit III.** Ces barytes précipitent dans les

failles associées au oxyde de fer et la calcite. Cette minéralogie indique la circulation de fluide oxydant. Les conditions thermiques des fluides sont contraintes la minéralogie des argiles (<150 °C) et barite. Les analyses des concentrés de baryte et de calcite montrent des concentrations en Éléments Terres Rares différentes. Ces différences des origines météoriques différentes pour ces 2 minéraux. Il pourrait s'agir de précipitation diachrones avec des sources distinctes de Ba, S et Ca, C. Pour les barytes, la source de baryum est probablement magmatique. L'analyse sur roche totale a montré qu'albitisation du plagioclase est liée à l'enrichissement d'ETR en barytes et a indiqué un fluide oxydant météorique riche en SO_4^{-2} comme source de sulfate, étant donné que la source de chaleur et les fluides chauds peuvent être reliés aux intrusions andésitiques. Ainsi, nous interprétons l'altération hydrothermale était responsable de l'enrichissement des valeurs en Éeléments Terres Rares des barytes.

1. INTRODUÇÃO

A Bacia do Camaquã e as rochas graníticas associadas de idade Neoproterozoica contêm significativos depósitos de ouro, cobre, prata, chumbo e zinco (Remus et al., 2000; Bongiolo et al., 2011; Renac et al., 2014). Dentre estes, o maior depósito de cobre-ouro e chumbo-zinco desta bacia é a Mina do Camaquã, hospedada em uma sequência de rochas sedimentares (Ronchi et al., 2000; Remus et al., 2000; Laux et al., 2005; Renac et al., 2014). Este depósito possui uma reserva de minério de ~30,8 Mt, com teor médio de ~1,06 % de cobre, ocorrendo como calcopirita, pirita, bornita, calcocita, ouro, prata e hematita na forma de veios maciços, stockwork ou disseminados na rocha.

Na seção centro-oeste desta bacia, as rochas vulcanogênicas (Lopes et al., 2014; Fontana, 2017; Fontana et al., 2017) e plutônicas (Mexias et al., 2005) são caracterizadas por uma alteração pervasiva descrita como alteração hidrotermal tardi-magmática (Mexias et al., 1990c e 2005; Bongiolo et al., 2011; Fontana et al., 2017). Neste contexto, as áreas estudadas de Lavras do Sul e Seival hospedam ouro-cobre nas rochas graníticas e cobre-prata nas unidades vulcanogênicas.

As rochas do Distrito Mineiro de Lavras do Sul compreendem dezenove depósitos ou ocorrências (Mexias et al., 2007; Bongiolo et al., 2011). Dentro desses depósitos as zonas de minério consistem em veios de quartzo ricos em sulfetos (Mexias et al., 2005) associados à alteração hidrotermal de "sericita", clorita, pirita, calcopirita e minério de ouro e cobre (Bongiolo et al., 2011).

A sequência vulcanogênica da Mina do Seival possui seis minas inativas de cobre-prata (Reischl, 1978; Lopes et al., 2014). A reserva foi cubada em ~0,20 Mt de rocha mineralizada com um teor de ~1,40 % de cobre (Reischl, 1978). Os sulfetos ricos em cobre ocorrem associados com interestratificado clorita/esmectita. Esses sulfetos estão disseminados na porosidade de rochas como o lapili tufo e do aglomerado vulcânico, assim como formam uma rede de stockwork e veios ao longo de planos de falha ou fratura.

A relação da química do hidrotermalismo e das mineralizações com o paleostresse e controle estrutural não é bem caracterizada na região. Além disso,

apenas algumas análises de geoquímica em baritas foram realizadas na Bacia do Camaquã. Minha proposta nesta tese é a caracterização da química mineral das fases hidrotermais tardi-magmáticas de alta a baixa temperatura, assim como a determinação dos esforços estruturais responsáveis pela circulação do fluido hidrotermal e pelas mineralizações.

1.1 Objetivos

O objetivo principal desta tese é caracterizar os esforços envolvidos, as estruturas que controlam a migração de fluidos mineralizantes e as assembleias minerais da Mina do Seival, para com isso determinar uma relação mineralógica entre as fases magmática e de alteração hidrotermal e as mineralizações de cobre-prata. A contribuição desse estudo, para a área de trabalho, é a caracterização da alteração hidrotermal e, para a grande área de conhecimento, uma contribuição na exploração de depósitos similares da Bacia do Camaquã ou ambientes similares. Com a obtenção de testemunhos de sondagens e coleta de amostras nos trabalhos de campo, foi possível levantar algumas questões importantes ainda não conhecidas, como:

- Quais são os esforços e as estruturas que controlam o fluxo hidrotermal e as mineralizações?

- Quais são as modificações químio-mineralógicas associadas à alteração hidrotermal e as mineralizações?

- Quais são as temperaturas dos processos hidrotermais envolvidos?

Portanto, o objetivo geral desta tese é responder a estas e outras questões asociadas, tentando detalhar o máximo possível através das técnicas que foram disponibilizadas. O que chama a atenção no estudo é a relação da alteração hidrotermal com as estruturas que controlam a percolação do fluido hidrotermal e a deposição do minério. A principal novidade apresentada nesta tese é uma caracterização das assembleias minerais na área estudada, assim como um levantamento estrutural na região.

1.2 Localização e vias de acesso

A área de estudo está situada a cerca de 308 km de Porto Alegre, percorre-se 240 km pela rodovia BR-290, 17 km pela BR-392 e 51 km pela RS-357, sentido SW, até o limite entre os municípios de Caçapava do Sul e Lavras do Sul (Fig. 1). O acesso a área da Mina do Seival se dá por estrada não pavimentada. A localidade está inserida na carta topográfica do Serviço Geológico do Exército, Folha Arroio América (SH.22–Y–A–IV–1, 1975), em escala de 1:50.000, entre as coordenadas geográficas 30°41' a 30°45' S e 53°45' a 53°48' W.

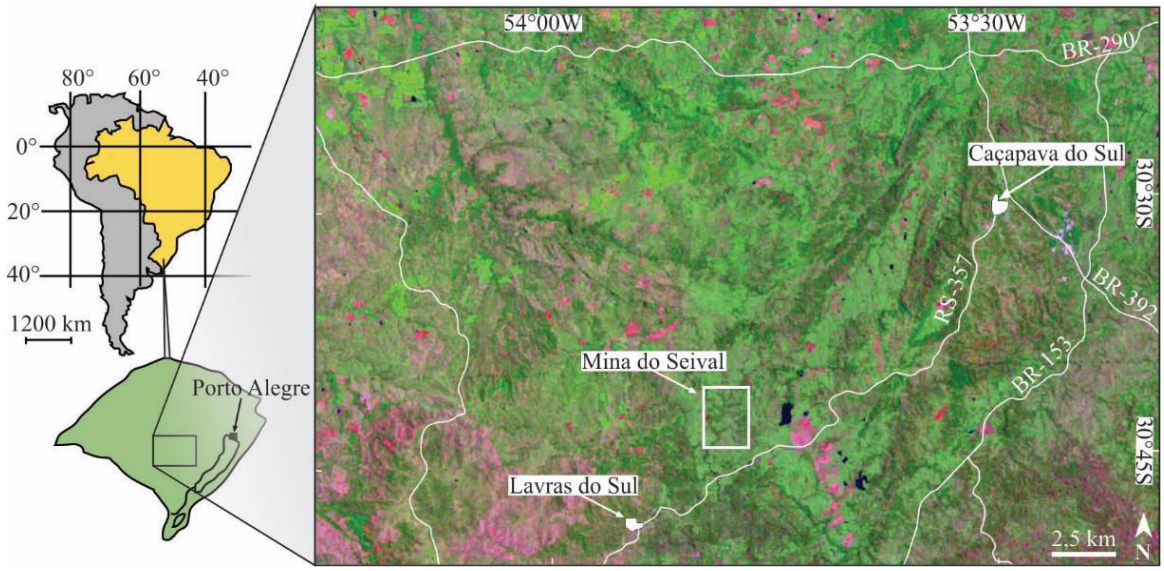

Figura 1. Localização da área de estudo e vias de acesso sobre uma imagem Landsat TM 147 (adaptado de Toniolo et al., 2007).

1.3 Amostragem

A amostragem realizada em trabalhos de campo teve como objetivo comparar e caracterizar as diferentes litologias e texturas. A amostragem também foi realizada em testemunhos de sondagem, com a vantagem de poder observar variações destas em profundidade e em sequência e também compará-las com as feições encontradas nos afloramentos. Foram amostrados sete testemunhos de sondagem na área da Mina do Seival.

1.4 Métodos utilizados

O trabalho teve como metodologia revisão bibliográfica, trabalhos de campo, análises petrográficas, análises estruturais, difratometria de raios X e química mineral. A partir dos trabalhos de campo e petrografia, as rochas da Mina do Seival foram classificadas, e foram descritas sua mineralogia e seus aspectos texturais com ênfase nas fases secundárias que ocorrem como minerais de alteração. Com a difratometria de raios X e química mineral em diversas fases, foi possível estabelecer uma correlação dos elementos ligados às mineralizações e a sua relação com o controle estrutural.

A partir do objetivo traçado, a utilização das técnicas foi uma etapa importante para obter os resultados esperados. Para facilitar, a descrição das técnicas utilizadas foi dividida em oito partes.

Para isso, foram realizadas análises químicas em amostras de campo e em testemunhos de sondagens de diversas fases minerais, assim como medidas estruturais em falhas e fraturas. Dessa maneira, com o auxílio da petrografia, química mineral, difratometria de raios X e geologia estrutural foi possível avançar no conhecimento da alteração hidrotermal, das temperaturas envolvidas nos processos de cristalização e dos esforços responsáveis pela circulação de fluidos e mineralizações.

1.4.1 Revisão bibliográfica

A revisão bibliográfica reuniu um conjunto de publicações referentes às áreas de estudo e a assuntos relacionados ao tema, como química mineral, alteração hidrotermal, mineralizações de cobre, e sobre a Bacia do Camaquã, sistematizando assim um coleção de referências dos métodos e de comparação geológica a serem utilizados neste trabalho.

1.4.2 Campo e descrição de testemunhos de sondagem

Essa etapa consistiu na realização de trabalhos de campo para a coleta de amostras, descrições das ocorrências e mineralizações. O mapeamento geológico contribuiu para a representação da distribuição das rochas na área. A descrição de

testemunhos de sondagens possibilitou analisar a rocha em profundidade de uma maneira menos alterada por processos de intemperismo e superficiais. Para isso, foram utilizados equipamentos tradicionais como GPS (Datum Córrego Alegre), marretas, martelos, bússolas, lupa de mão, máquina fotográfica, caderneta de campo e equipamentos de proteção individual.

Os trabalhos de campo foram realizados em cinco dias de maio de 2013, onde foram coletadas amostras para química mineral, e quatro dias em agosto de 2016, para realização de medidas estruturais. Em 2017 foi realizado um campo de dois dias para coleta de amostras específicas na Mina da Barita. Também foram incorporados dados e amostras de trabalhos de campo anteriores (2011 e 2012), relativos à monografia de conclusão de curso e dissertação de mestrado. Com isso, foram amostrados 120 pontos, subdivididos quando necessário.

Os testemunhos de sondagem foram descritos, além de coletadas amostras de mão de sete testemunhos de sondagem na área da Mina do Seival. Seis desses furos de sondagem foram realizados pela Companhia Brasileira de Cobre (CBC), em ~1978, hoje pertencentes à Votorantim Metais, que realizou o sétimo furo de sondagem em 2010 e gentilmente possibilitou a coleta das amostras. Os testemunhos de sondagem descritos e coletados foram: 31 amostras do SV 78-11 – Ocorrência Vila do Torrão, Linha 800 – (30°43’21” S e 53°46’56” W) e 28 amostras do SV 78-01 (30°43’22” S e 53°47’0” W); 13 amostras do SV 78-15 – Ocorrência Lagoa do Jacaré, Linha 700 – (30°43’14” S e 53°47’18” W) e 10 amostras do SV 78-16 (30°43’12” S e 53°47’20” W); 8 amostras do SV 78-18 – Mina do Meio, Linha 900 – (30°42’26” S e 53°46’41” W) e 11 amostras do SV 78-09 (30°42’27” S e 53°46’44” W); 10 amostras do SV 001 – Mina Alcides – (30°43’45” S e 53°47’08” W). Nessa amostragem foram coletadas um total de 111 amostras.

1.4.3 Imagens utilizadas no mapeamento geológico

Os materiais utilizados no mapeamento geológico foram a Folha do Exército - Arroio América (SH.22–Y–A–IV–1, 1975) na escala 1:50.000 e um mapa geológico da região desenvolvido por Reischl (1978) com poucos detalhes litoestatigráficos. Também se utilizou imagem TM Landsat banda 4 e imagens de satélite obtidas pelo

software Google Earth, além de fotointerpretação através de fotografias aéreas, que foram utilizadas para traçar os contatos dos litotipos, as estruturas e as falhas, auxiliando a compreensão da estruturação das minas, assim como sua relação com falhas e estruturas locais/regionais.

1.4.4 Pós campo

A reformulação do mapa geológico anterior (Reischl, 1978; Lopes, 2011; Lopes et al., 2014) foi realizada com a ferramenta GIS com a geração de um novo mapa geológico apresentado na parte 3 desta tese. O ANEXO C contém o número do ponto, localização com a UTM em Datum Córrego Alegre, unidade litológica e tipo de rocha, bem como profundidade nas amostras de testemunho de sondagem.

1.4.5 Geologia estrutural

A análise de imagens de satélite consistiu na visualização e no traçado dos lineamentos que ocorrem na região e na escala regional. Foram utilizados dois modelos de imagens *Aster*: *ASTER*, banda do visível (*VINIR* 15 m, infravermelho muito próximo) e ASTER de relevo sombreado (*Hillshade*). A imagem *QuickBird* é multiespectral (quatro bandas) e tem 60 cm de resolução, utilizada para visualização do terreno em escalas variadas. Estes lineamentos foram traçados utilizando o *Software ArcGis* para a geração de um mapa de lineamentos no formato de *shape file*.

Para o levantamento dos dados estruturais foram realizadas análises nas 6 minas aflorantes na área. As medidas estruturais foram obtidas com bússola, e o método utilizado para as medidas foi a trama ou *dip-dip*, que consiste em medir a direção para a qual o plano mergulha e o seu mergulho.

As estruturas observadas nos trabalhos de campo foram classificadas como fraturas e falhas. As fraturas foram consideradas aquelas estruturas que não apresentavam indícios de movimentação marcados pelas estrias de falha, enquanto que para a classificação das falhas levou-se em conta a relação entre o mergulho do plano da falha e o mergulho da estria contida neste plano (Angelier, 1994). As falhas foram classificadas como normais e transcorrentes (sinistrais e dextrais). As

falhas normais e a cinemática transcorrente foram identificadas a partir das relações de movimento entre teto e muro.

A análise cinemática consiste na reconstrução do movimento atuante na rocha e sua deformação (Davis e Reynolds, 1996). No caso do sentido do movimento das falhas, foi possível observar estrias e degraus presentes sobre o plano. Estas estrias são causadas pela imperfeição do plano de falha, gerando atrito no movimento dos blocos. Após a medição de estruturas, os dados foram processados utilizando o *software Win-Tensor* (Delvaux e Sperner, 2003) para a confecção dos estereogramas. Os conceitos utilizados foram baseados nos trabalhos de Riedel (1929) e nos experimentos de Tchalenko (1970) apresentados por Twiss e Moores (1992), Davis e Reynolds (1996) e Hatcher (1995). Estes modelos apresentam as relações angulares entre as estruturas geradas a partir de um campo de tensões, bem como as direções previstas para cada uma. Com estes dados foi possível determinar o estilo de deformação atuante na área de estudo e definir o eixo principal de tensão. No ANEXO E são apresentados os dados de geologia estrutural do manuscrito I.

1.4.6 Caracterização petrográfica

A mineralogia, as texturas e as relações entre os minerais foram identificadas com o uso de diversos microscópios em diferentes instituições de ensino e foram fotografadas sempre que possível ou necessário. A análise petrográfica foi realizada em amostras coletadas nos trabalhos de campo e de testemunhos de sondagem. Um total de 91 lâminas petrográficas foram confeccionadas no Instituto de Geociências – UFRGS amostradas nos trabalhos de campo (37 lâminas) e testemunhos de sondagem SV 78-11 (19 lâminas), SV 78-01 (9 lâminas), SV 78-15 (11 lâminas), SV 78-16 (6 lâminas), SV 78-18 (4 lâminas) e SV 78-09 (5 lâminas), relativos também à monografia de conclusão de curso e à dissertação de mestrado.

1.4.7 Caracterização mineralógica

A caracterização mineralógica primária e secundária foi realizada através das técnicas de difratometria de raios X (DRX), microscopia eletrônica de varredura

(MEV) e microssonda eletrônica (MSE). A seguir, é apresentada cada uma dessas técnicas.

1.4.7.1 Difratometria de raios X

As análises de DRX tiveram como objetivo a caracterização dos minerais de alteração e do controle de pureza em minerais separados, como no caso da barita. Foram confeccionados cerca de 50 difratogramas pelo método do pó e 41 difratogramas pelo método das amostras orientadas, estando presentes esses últimos no ANEXO G.

Os fragmentos de amostras foram moídos em grau de ágata até a porção pó. Foram separados cerca de 8 ml (medida do frasco) de pó de cada amostra. Após moagem e ultrassom, as amostras passaram pelo agitador por no mínimo 24 horas, tempo determinado para obter a fração desejada de < 0,4 μm. Essas amostras foram analisadas em lâmina orientada na forma natural, saturada com etileno-glicol e serem aquecidas a 550ºC durante duas horas (calcinadas). O equipamento utilizado foi o difratômetro SIEMENS BRUKER AXS Modelo D5000 com goniômetro θ-θ do Laboratório de Difratometria de Raios X (CPGq-IG-UFRGS). A radiação é Kα em tubo de Cu nas condições analíticas de 40 kV e 25 mA.

Assembleias minerais de alteração hidrotermal foram identificadas nos difratogramas confeccionados, tais como: clorita, esmectita, interestratificado de clorita/esmectita e carbonatos presentes nas rochas. Os argilominerais foram identificados por comparação com padrões do banco de dados do computador (JCPDS), sendo indicado e referenciado o pico mais importante do mineral. Para interpretação das análises utilizou-se o *software DiffractPlus* e *Match 3*.

O método de DRX dificilmente identifica estruturas cristalinas que ocorram em quantidades inferiores a 3 a 5% na amostra analisada. Um cálculo estimativo classificou os difratogramas de raios X que indicaram interestratificados de clorita/esmectita, segundo os critérios adotados por Beaufort e Meunier (1994), calculados através do programa *NEWMOD* (Reynolds, 1985) em colaboração com a tese publicada por Fontana (2017).

1.4.7.2 Microscopia eletrônica de varredura

Para um estudo preliminar de química mineral e identificação mineralógica, foi utilizado um microscópio eletrônico de varredura (MEV). Com isso, foi possível realizar um mapeamento da distribuição de elementos químicos nos minerais, principalmente de plagioclásio e alguns argilominerais. Para este estudo utilizou-se o microscópio eletrônico Jeol JSM-5800 com detectores de elétrons secundários (SEM), elétrons primários retroespalhados (BSE) e detector de energia dispersada (EDS), Noran pertencente ao Centro de Microscopia Eletrônica da UFRGS. Também se utilizou o microscópio eletrônico Zeiss EVO LS15, 20 kV, 2.5 nA com o detector X-Max Oxford EDS, pertencente ao IAEA (UNESCO), do Principado de Mônaco, durante o período de doutorado sanduíche.

1.4.7.3 Microssonda eletrônica

Os minerais ígneos e hidrotermais foram analisados para química mineral. Os minerais ígneos analisados foram piroxênio, plagioclásio e biotita, enquanto os minerais hidrotermais analisados foram albita, titanita, clorita, esmectita e interestratificado clorita/esmectita. Todas as análises foram realizadas no Laboratório de Microssonda Eletrônica do IG-UFRGS, nos anos de 2013, 2015 e 2017. As análises de química mineral quantitativas foram obtidas por microssonda eletrônica marca CAMECA, modelo SXFive (15 kV, 15 nA 10s *counting time* equipado com coletores TAP, PET e LIF). Os padrões utilizados foram: albita para Na; jadeita para Si; diopsídeo para Mg, Ca; sanidina para Al, K; rutilo para Ti; rodonita para Mn; hematita para Fe. O teor de bário no plagioclásio foi determinado com padrão de bário-feldspato (ortoclásio) e com feixe de 5 µm com 10 seg para cada elemento e 5 seg para o ruído de fundo (*background*). As análises de barita foram determinadas com feixe de 5 µm (15 kV, 100 nA) com 30 seg para o pico e 10 para o ruído de fundo.

Os elementos maiores utilizados (SiO_2, TiO_2, Al_2O_3, FeO_{total}, MnO, MgO, CaO, Na_2O e K_2O) foram recalculados para sua fórmula estrutural (*atom per formula unit: a.p.f.u.*) assumindo o oxigênio estrutural para cada fase mineral: feldspatos (32), piroxênio (12), titanita (5), biotita (22), esmectita (22), clorita (28) e

interestratificado clorita/esmectita (28). As proporções de Fe^{2+} e Fe^{3+} foram ajustadas para obter um melhor balanço de cargas em cada análise. No ANEXO F são apresentados os dados de microssonda eletrônica do manuscrito II.

1.4.8 Geoquímica de concentrados de plagioclásio, barita e calcita

As microanálises para elementos traços em concentrados de plagioclásio, barita e calcita foram realizadas com um Perkin Elmer modelo 320 Laser ASC em um espectrômetro de massa PE Sciex. O laser é um Nd YAG operado em 1064 nm, com repetição de 1-10 Hz, com tamanho de pulso de 8 ns e um pulso de energia de 120 mJ. Essa etapa foi realizada no Laboratoire de Chimie da Université Côte D´Azur, França. Os Elementos Terras Raras foram escolhidos a partir dos padrões, tendo em vista a similaridade e a possibilidade satisfatória de bons resultados para as rochas da Mina do Seival. O *software* utilizado pelo equipamento para exposição e interpretação de análises foi ELAN Instrumental Control Session.

2. CONTEXTUALIZAÇÃO - BACIA DO CAMAQUÃ

Nesta parte do trabalho é descrito o estado da arte da geologia regional com descrição da Bacia do Camaquã, Associação Shoshonítica de Lavras do Sul e mineralizações associadas.

2.1 Bacia do Camaquã

A orogenia que promoveu a colagem de terrenos Neoproterozoicos deu origem ao Paleocontinente Gondwana Ocidental (Fig. 2). A Província Mantiqueira (Almeida e Hasui, 1984) se alonga do sul da Bahia até o Uruguai. No estado do Rio Grande do Sul o cinturão de cisalhamento Dom Feliciano é denominado Escudo Sul-rio-grandense. Essa faixa móvel é associada com a colisão dos Crátons de La Plata e Kalahari.

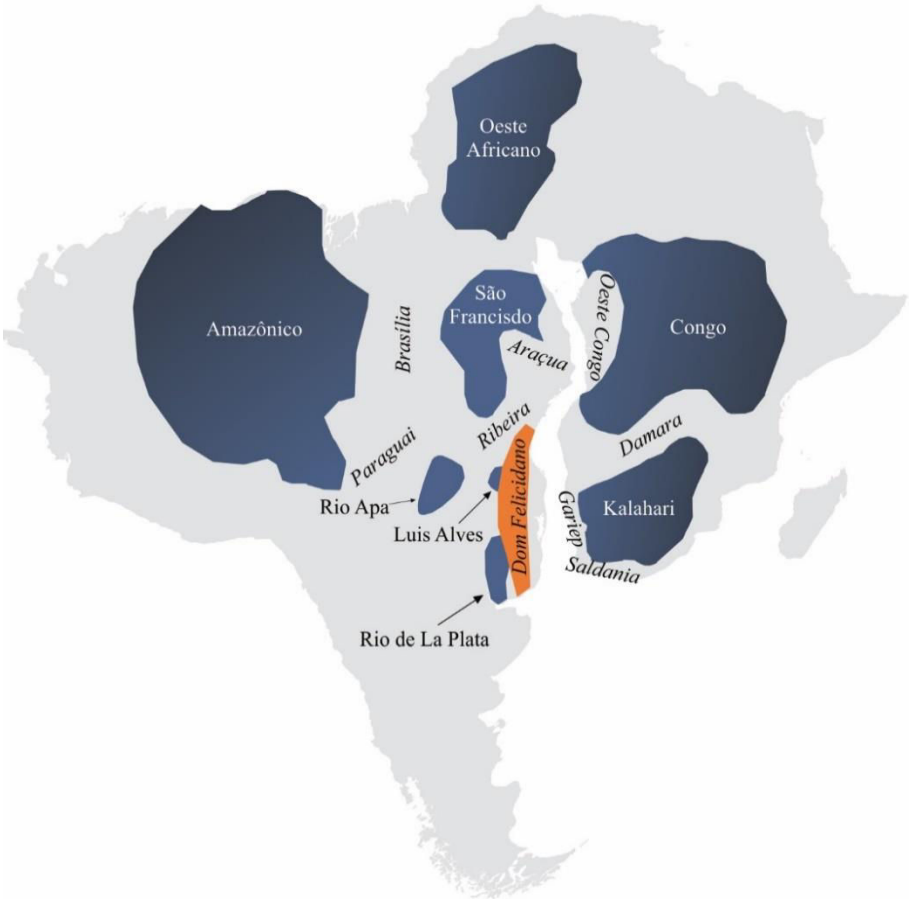

Figura 2. Mapa da área do Gondwana Ocidental com a indicação dos crátons (área em azul) e das faixas móveis (em itálico na figura) (adaptado de Almeida e Hasui, 1984).

Associado ao Escudo Sul-rio-grandense, ocorre a Bacia do Camaquã, uma bacia plutono-vulcano-sedimentar com idades Neoproterozoica-Cambriana (Fig. 3), de elongação NE-SW, onde situa-se a área de estudo. Essa bacia pode ser correlacionada com a Bacia do Itajaí no estado de Santa Catarina (Guadagnin et al., 2010; Basei et al., 2011; Font et al.; 2011), com a Bacia de Castro no estado do Paraná, e com as bacias de Barriga Negra, Piriápolis, San Carlos e Cerros de Aguirre no Uruguai (Sánchez-Bettucci et al., 2009) e com a Bacia do Nama na Namíbia (Meert et al., 1997) (Fig. 4).

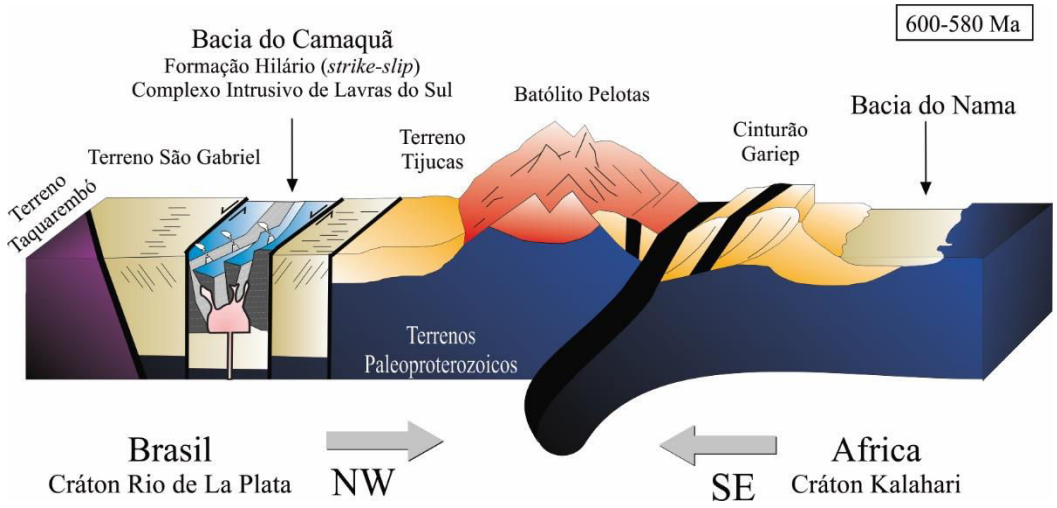

Figura 3. Modelo evolutivo do Escudo Sul-rio-grandense (600-580 Ma) com representação da colisão entre os crátons Rio de la Plata e Kalahari (sem escala; mod. de Chemale Jr., 2000; Bongiolo et al., 2011; Gastal et al., 2015).

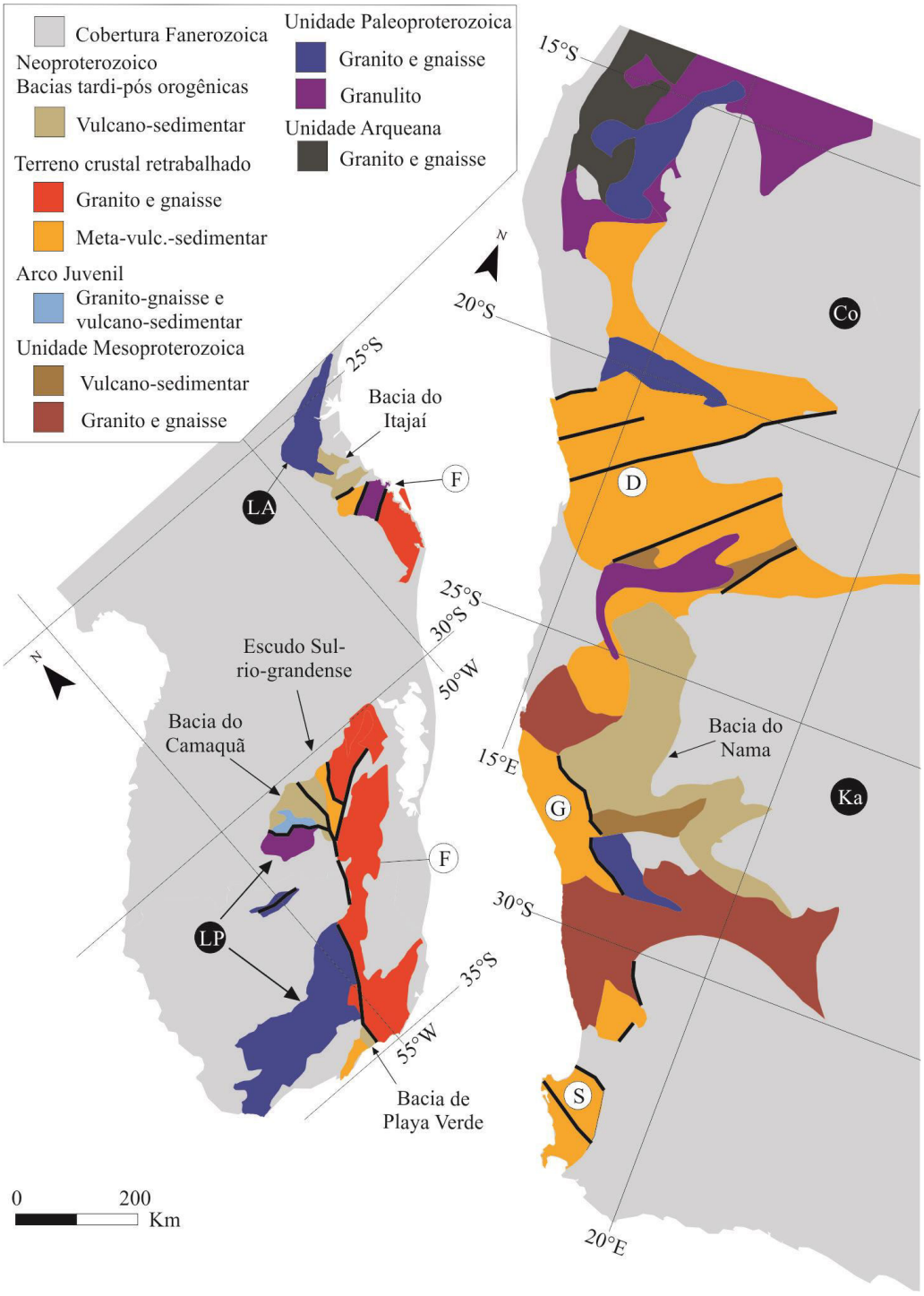

Figura 4. Mapa das rochas Neoproterozoicas do Sul do Brasil e Uruguai (à esquerda) e oeste da Namíbia e África do Sul (à direita), com indicação dos crátons, cinturões e bacias associadas (adaptado de Guadagnin et al., 2010 e referências contidas). Chaves: Co = Cráton do Congo; Ka = Cráton Kalahari; LP = Cráton Rio de la Plata; LA = Cráton Luis Alves; F = Cinturão Dom Feliciano; G = Cinturão Gariep; S = Cinturão Saldania; D = Cinturão Damara.

O Escudo Sul-rio-grandense consiste em Terreno Taquarembó, Terreno São Gabriel, Terreno Tijucas e Batólito Pelotas (Chemale Jr., 2000; Hartmann et al., 2007). Esses terrenos tectônicos possuem três zonas de cisalhamento principais: Ibaré; Caçapava do Sul; Dorsal do Canguçu. O Terreno São Gabriel está separado do Terreno Taquarembó pela Zona de Cisalhamento Ibaré (NW-SE), localizado a sudoeste e separado do Terreno Tijucas pela Zona de Cisalhamento Caçapava do Sul (NE-SW), localizada a leste (Saalmann et al., 2005; Hartmann et al., 2007). O Terreno São Gabriel possui estruturas principais de direção NE-SW representada pelas falhas Cabritos-Perau e Segredo (Fig. 5).

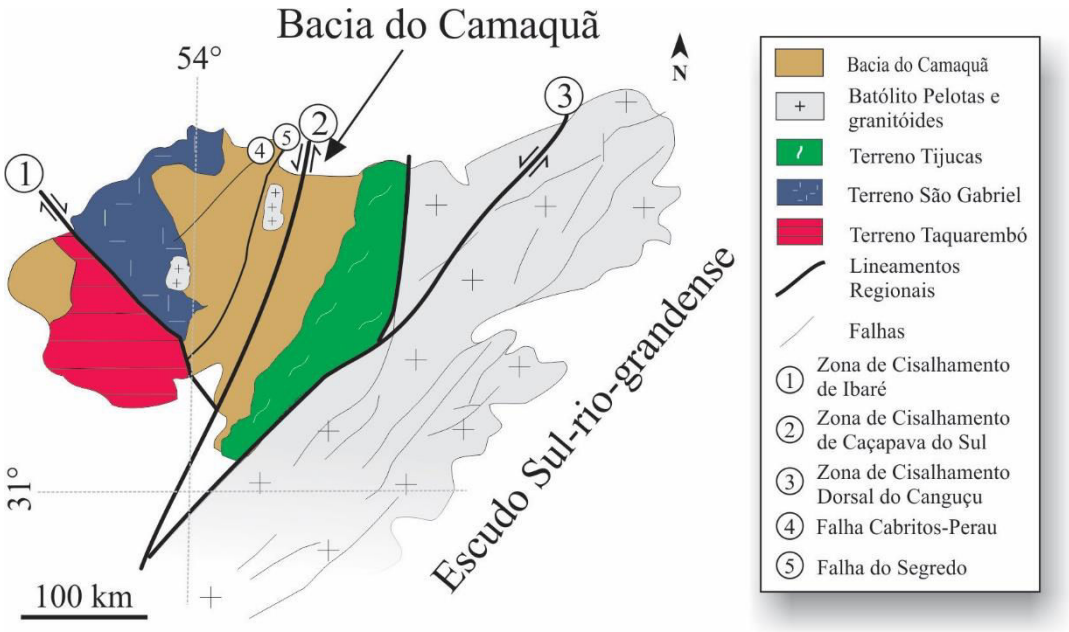

Figura 5. Mapa esquemático da geologia do Escudo Sul-rio-grandense com os 4 blocos tectônicos e localização da Bacia do Camaquã (mod. de Hartmann et al., 2007).

O embasamento da Bacia do Camaquã compreende gnaisse, paragnaisse e rochas meta-vulcano-sedimentar, com movimento NW-SE, deformadas entre 750-680 Ma (Chemale Jr., 2000; Saalmann et al., 2011). A Bacia de Camaquã é dividida em quatro grupos e várias formações depositadas em quatro eventos diferentes: i) o Grupo Maricá é depositado como parte de uma bacia de retro-arco ou *foreland* (Chemale Jr., 2000; Borba et al., 2008); ii) as unidades do Grupo Bom Jardim são depositadas em uma bacia do tipo *transpresional strike-slip* (Lima et al., 2007; Janikian et al., 2008); iii) as unidades dos grupos Santa Bárbara são formadas em

um evento *transtensional strike-slip* (Paim et al., 2000; Bicca et al., 2013); iv) O Grupo Guaritas é formado durante um evento de subsidência transtensional (Bicca et al., 2013; Oliveira et al., 2014) (Fig. 6).

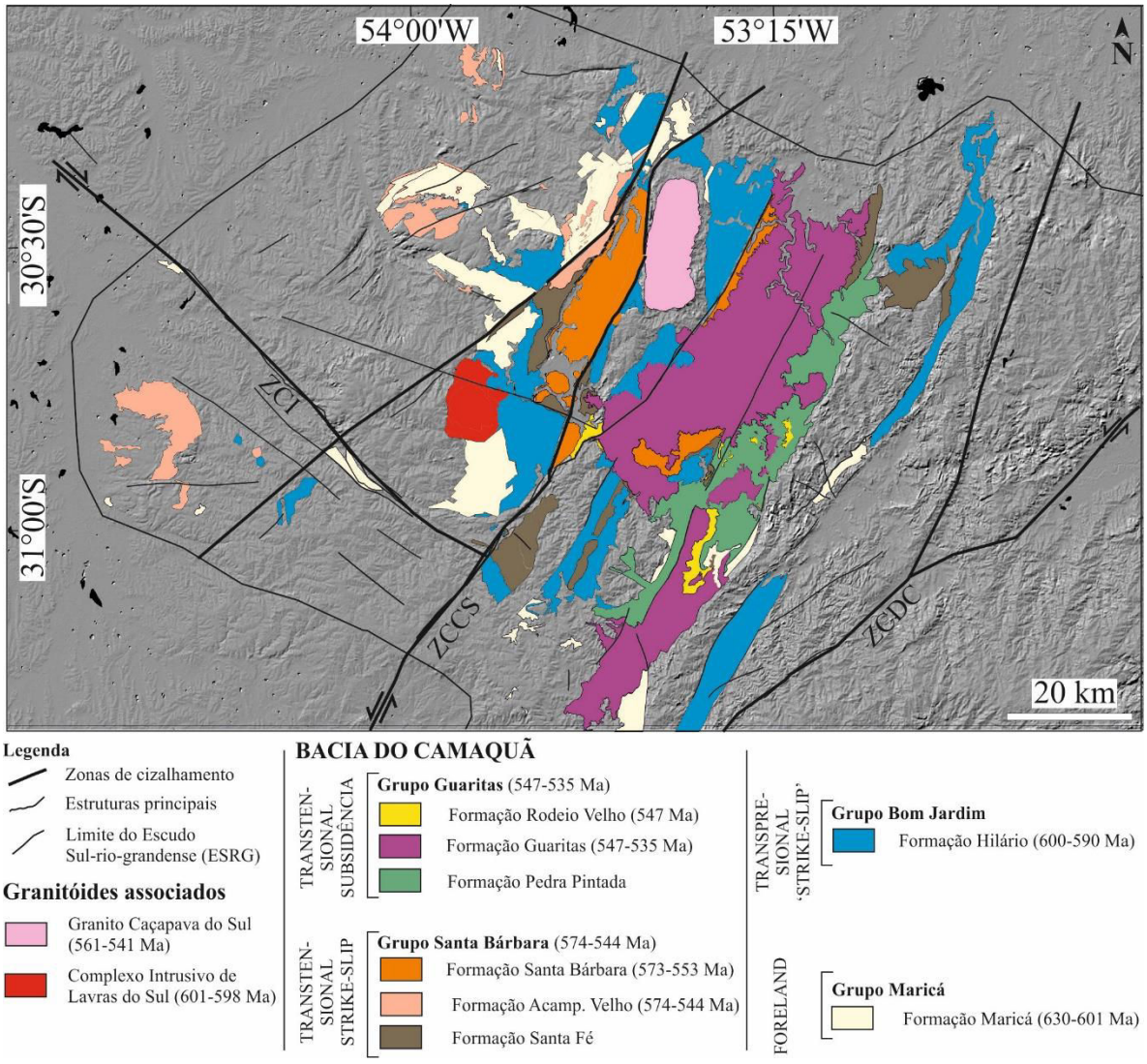

Figura 6. Mapa Geológico da Bacia de Camaquã com transparência de 50%. As principais estruturas e falhas estão marcadas sobre uma imagem *Hillshade ASTER* (mod. de Wildner et al., 2002; Toniolo et al., 2007). Zonas de Cisalhamento: ZCI = Ibaré; ZCCS = Caçapava do Sul; ZCDC = Dorsal do Canguçu.

Na Bacia de Camaquã, as jazidas mais significativas são as Minas do Camaquã, que possuem o maior volume de minério (Remus et al., 2000; Laux et al., 2005; Renac et al., 2014), compreendendo as minas Uruguai, São Luiz Cu-(Au, Ag) e o depósito Santa Maria Pb/Zn-(Cu, Ag). Outro importante depósito de cobre é

o Cerro dos Martins, hospedado em rochas vulcanogênicas e sedimentares do Grupo Bom Jardim (Remus et al., 2000; Toniolo et al., 2004), localizado na região de Caçapava do Sul. As minas Crespos e Silveira ocorrem associadas ao magmatismo Acampamento Velho, ao norte da Mina do Seival. A localização das principais minas associadas à Bacia do Camaquã é apresentada na Figura 7.

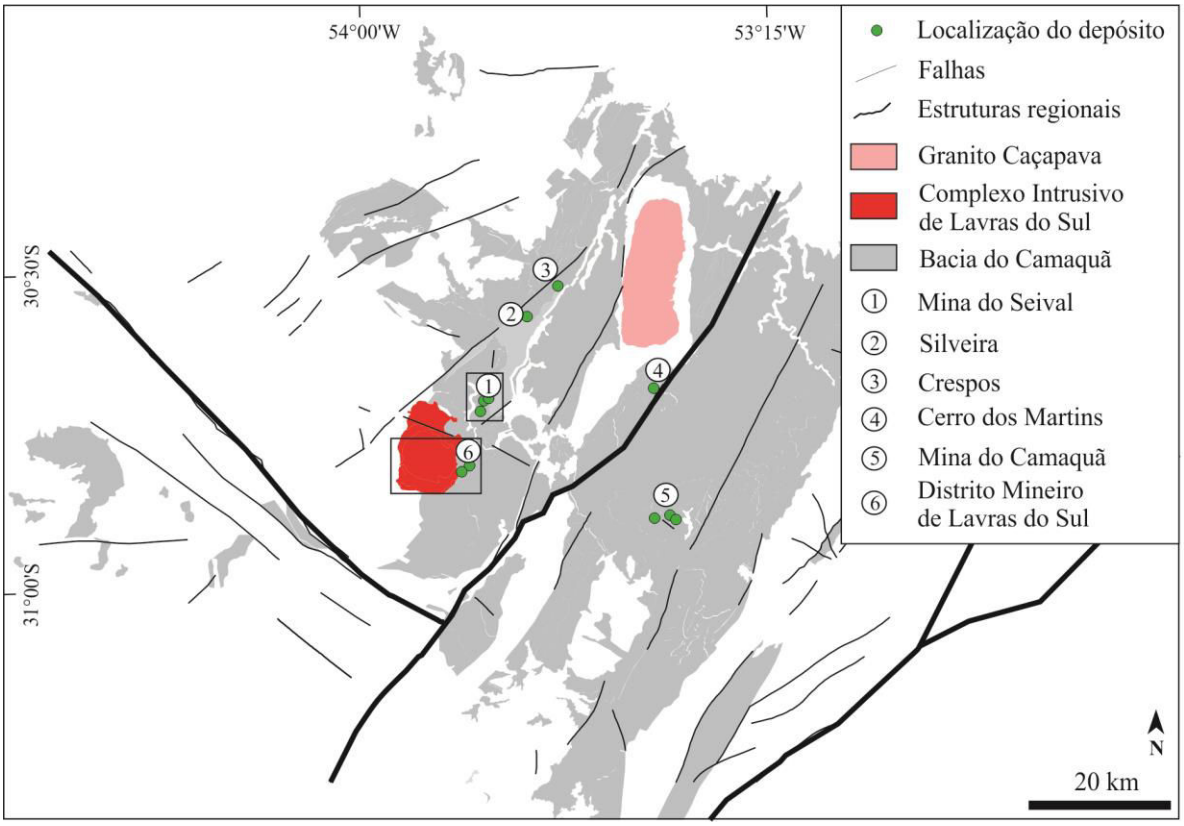

Figura 7. Localização das principais minas de Cu, Au-Cu e Pb-Zn na Bacia do Camaquã (mod. de Toniolo et al., 2007).

2.2 Estratigrafia da Bacia do Camaquã

O Grupo Maricá é representado pela Formação Maricá, interpretada como uma sequência sedimentar de rochas com clastos vulcânico (Borba et al., 2008) com aproximadamente 4.000 metros de espessura (Paim et al., 2000) dividida em três pacotes sedimentares (Borba et al., 2006).

Neste trabalho, consideramos o Complexo Intrusivo de Lavras do Sul correlato ao Grupo Bom Jardim, e ambos pertencem à Associação Shoshonítica de Lavras do Sul (Lima e Nardi, 1998). O Grupo Bom Jardim é uma sequência de 2.000

metros de espessura (Janikian et al., 2003) de rochas vulcano-sedimentares da Formação Hilário, representadas por lava andesítica de fluxo (Nardi e Lima, 1985) e rochas piroclásticas (Lopes et al., 2014) associadas a rochas lamprofíricas (Lima e Nardi, 1998) e sedimentares na porção oeste e central da bacia. O Complexo Intrusivo de Lavras do Sul corta a Formação Hilário e é composto de um núcleo de fase plutônica (Nardi, 1984; Raposo e Gastal, 2009; Gastal et al., 2015) e intrusões superficiais de rochas monzoníticas concentradas principalmente na margem nordeste (Nardi, 1984; Gastal et al., 2006).

O Grupo Santa Bárbara é composto por rochas vulcano-sedimentares da Formação Santa Fé, rochas sedimentares da Formação Santa Bárbara (Bicca et al., 2013; Oliveira et al., 2014) e rochas vulcânicas bimodais da Formação Acampamento Velho (Sommer et al., 2011; Almeida et al., 2012).

O Grupo Guaritas hospeda rochas vulcânicas da Formação Rodeio Velho e pacotes sedimentares da Formação Pedra Pintada e Guaritas (Almeida et al., 2012; Oliveira et al., 2014). A Figura 8 representa um perfil estratigráfico simplificado da Bacia do Camaquã com uma breve descrição dos grupos associados.

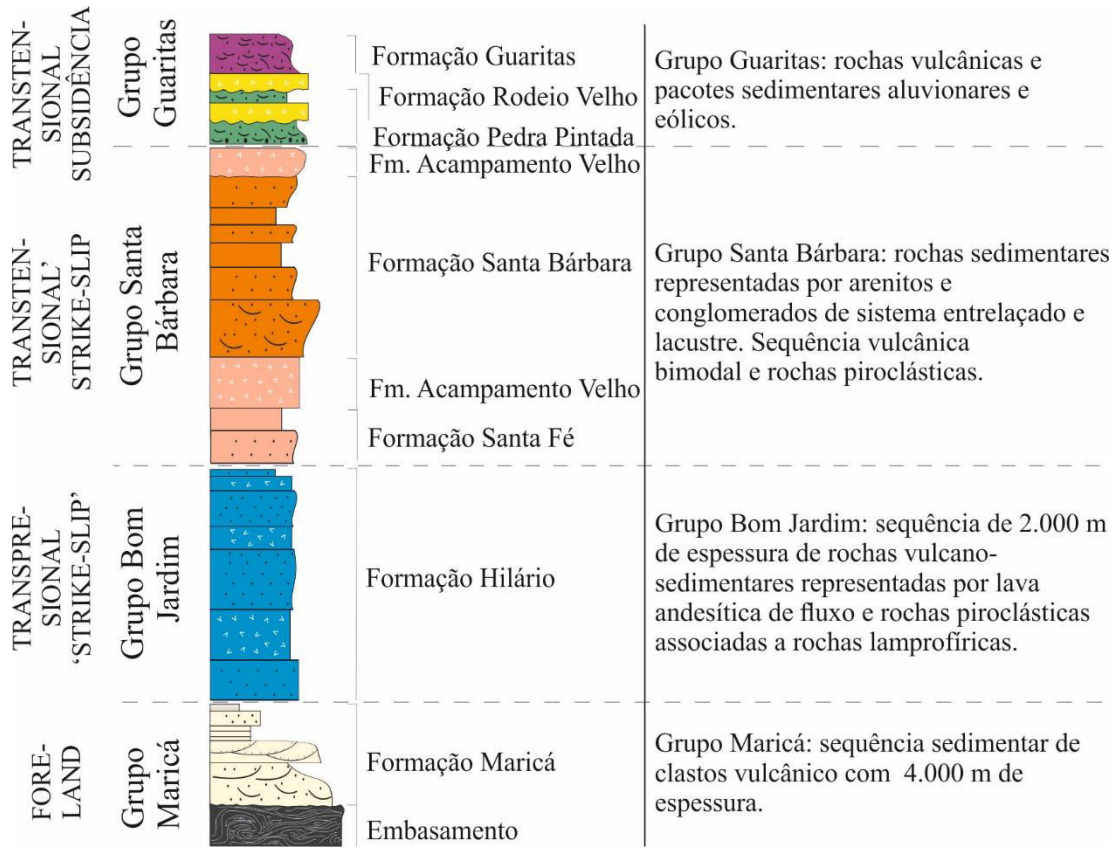

Figura 8. Perfil estratigráfico simplificado das sequências vulcano-sedimentar da Bacia do Camaquã (mod. de Wildner et al., 2002; Almeida et al., 2012).

2.3 Dados geocronológicos

Os dados geocronológicos disponíveis são ainda restritos. Existe um questionamento em relação às rochas da Formação Hilário com idades referentes às lavas andesíticas de fluxo que ocorrem próximo à área.

A Formação Maricá foi datada pelo método $^{238}Pb/^{206}U$ com 630 ± 3,4 Ma, (Borba et al., 2008) em zircão de um clasto riolítico do conglomerado localizado no planalto Ramada, sul da cidade de Vila Nova do Sul, interpretado como uma idade de proveniência ou idade máxima. O zircão detrítico de arenito localizado a oeste e próximo a Lavras do Sul tem a base deposicional máxima no topo desta unidade, com idade de 601 ± 13 Ma (Almeida et al., 2012), datada pelo mesmo método.

As primeiras idades determinadas em plagioclásios de rochas andesíticas na Formação Hilário pelo método K-Ar estão entre 510-535 Ma (Ribeiro e Teixeira, 1970). As idades preliminares obtidas pelo método Rb/Sr têm idades de 510 e 535

Ma (Cordani et al., 1974) e 580 Ma em zircão $^{238}Pb/^{206}U$ (Remus et al., 1999) para as rochas intermediárias. Chemale Jr. (2000) mencionou idade de 592 Ma para a Formação Hilário. A sequência vulcânica tem idades, pelo método $^{40}Ar/^{39}Ar$ em plagioclásio, de 590 ± 6 Ma para a base do ciclo vulcânico e idades de 586 ± 8 Ma para o ciclo efusivo superior (Janikian et al., 2008; Janikian et al., 2012), onde o platô de idades das amostras de lava andesítica de fluxo mostrou porcentagem cumulativa de ^{39}Ar liberado. O método $^{238}Pb/^{206}U$ analisado em zircão obteve idades de 590,5 ± 5,7 Ma a partir do depósito de tufo. As rochas lamprofíricas da Associação Shoshonítica de Lavras do Sul, localizadas a 2 km em sentido sul da Mina do Seival, foram datadas pelo método $^{238}Pb/^{206}U$ em zircão com idades de 591,8 ± 3,0 Ma (Almeida et al., 2012), sendo interpretadas como pertencentes à Formação Hilário. O Cerro da Angélica, localizado cerca de 30 km a leste da área de estudo, foi datado em grãos de zircão pelo método de $^{238}Pb/^{206}U$ com idades de 600,5 ± 2,4 Ma para dique granítico, interpretada como a idade de cristalização do granito (Janikian et al., 2012).

A Formação Santa Bárbara foi datada pelo método $^{238}Pb/^{206}U$ em zircão com idades de 573 ± 18 Ma (Chemale Jr., 2000), 574 ± 7 e 572 ± 6,5 Ma (Janikian et al., 2012) na região central da bacia. Na região das Minas de Camaquã, no leste da bacia, as análises de proveniência de zircão pelo método $^{238}Pb/^{206}U$ obtiveram idades de 566 ± 6,9 Ma, interpretadas como idade de deposição máxima (Bicca et al., 2013). As idades deposicionais máximas das três sequências deposicionais primárias da Formação Santa Bárbara, em sucessão ascendente, são 567,9 ± 5,9 Ma, 562,5 ± 5,5 e 553 ± 22 Ma (Oliveira et al., 2014).

A Formação Acampamento Velho foi datada pelo método $^{238}Pb/^{206}U$ apresentando idades de 549,3 ± 5 Ma em grãos de zircão das rochas hipo-abissais riolíticas do Planalto Ramada (Sommer et al., 2005). As rochas vulcânicas ácidas da região de Caçapava do Sul foram datadas com 574 ± 7 Ma (Janikian et al., 2008) e 553 ± 5,4 Ma (Almeida et al., 2012) e consideradas como base da sequência. A Formação Acampamento Velho foi datada pelo método $^{238}Pb/^{206}U$ em zircão de riolitos subalcalinos, na região Passo do Salsinho com idades de 573 ± 18 Ma

(Chemale Jr., 2000; Almeida et al., 2002), e na associação intrusiva da região do planalto Taquarembó (Gastal e Lafon, 2001) com idades de 572 ± 3 Ma. A nova datação na Formação Acampamento Velho em zircão pelo método $^{238}Pb/^{206}U$ indicou uma idade de cristalização de 560 ± 2 Ma para o ignibrito densamente soldado, 560 ± 14 Ma para o traquito máfico e 562 ± 2 Ma para o riolito subvulcânico (Matté et al., 2016).

As idades centrais de granodiorito em zircão pelo método $^{238}Pb/^{206}U$ (Remus et al., 2000) foram revistas por Gastal et al. (2006) e apresentam idades de 601 ± 2 Ma. Novas análises pelo método $^{207}Pb/^{206}Pb$ em zircão do sienogranito da borda apresentam idades de 598 ± 3 Ma, rochas monzonítica-dioríticas (Monzonito Tapera) de 601 ± 5 Ma, e monzonito (Arroio dos Jaques) de 599 ± 7 Ma. Gastal et al. (2006) descreveu algumas idades mais jovens com 580 ± 1,8 Ma em granito com alteração hidrotermal associada à mineralização aurífera. O Granito Jaguari foi datado pelo método $^{207}Pb/^{206}Pb$ com idades de 567 ± 4 Ma, representando um evento distinto do magmatismo Lavras do Sul (Gastal et al., 2006).

As análises de isótopos de Pb em calcopirita, pirita e bornita da região das Minas do Camaquã, em arenitos e rochas de minérios, apresentam idades de 592 ± 5 Ma (Remus et al., 1997), podendo ser temporalmente correlacionadas ao granito de Lavras e à lava andesítica de fluxo da Formação Hilário. A borda alcalina ácida do Complexo Intrusivo de Lavras do Sul foi datada em zircão apresentando idades de 580 ± 11 Ma pelo método $^{238}Pb/^{206}U$ (Leite, 1995). O Complexo de Granito de Caçapava do Sul tem idades de ~550 Ma pelo método $^{238}Pb/^{206}U$ (Nardi e Bitencourt 1989; Remus et al., 1997). A Tabela 1 e a Figura 9 ilustram os dados geocronológicos da Bacia do Camaquã e granitos associados.

Tabela 1. Dados geocronológicos da Bacia do Camaquã e granitos associados. Chaves: (1) Borba et al., 2008; (2) Almeida et al., 2012; (3) Janikian et al., 2008; (4) Janikian et al., 2012; (5) Liz et al., 2009b; (6) Sommer et al., 2005; (7) Matté et al 2016; (8) Bicca et al., 2013; (9) Oliveira et al., 2014; (10) Remus et al., 1999; (11) Gastal et al., 2006; (12) Chemale Jr., 2000.

Groupo	Unidade	Idade e autor	Mineral	Método
Guaritas	Guaritas	535 ± 10 Ma (9)	zircão	SHRIMP
Guaritas	Guaritas	547 ± 6 Ma (9)	zircão	SHRIMP
Guaritas	Rodeio Velho	547 ± 6.3 Ma (2)	zircão	LA-ICP-MS
Santa Bárbara	Acamp.Velho	560 ± 2; 560 ± 14 Ma; 562 ± 2 Ma (7)	zircão	SHRIMP
Santa Bárbara	Acamp.Velho	579,9 ± 13; 569,8 ± 4,6 Ma (4)	zircão	SHRIMP
Santa Bárbara	Acamp.Velho	544,2 ± 5,5 Ma (4)	zircão	TIMS
Santa Bárbara	Acamp.Velho	553 ± 5,4 Ma (2)	zircão	LA-ICP-MS
Santa Bárbara	Acamp.Velho	574 ± 7 Ma (3)	zircão	SHRIMP
Santa Bárbara	Acamp.Velho	549,3 ± 5 Ma (6)	zircão	SHRIMP
Santa Bárbara	Santa Bárbara	567,9 ± 5,9 Ma; 562,5 ± 5,5 Ma (9)	zircão	SHRIMP
Santa Bárbara	Santa Bárbara	566 ± 6,9 Ma (8)	zircão	SHRIMP
Santa Bárbara	Santa Bárbara	553 ± 22 Ma (9)	zircão	SHRIMP
Santa Bárbara	Santa Bárbara	573 ± 18 Ma(12)	zircão	SHRIMP
Bom Jardim	Lavras do Sul	587 ± 4 Ma (5)	zircão	SHRIMP
Bom Jardim	Lavras do Sul	599 ± 2; 586 ± 3 Ma (11)	zircão	SHRIMP
Bom Jardim	Lavras do Sul	580 ± 1,8 Ma (10)	zircão	SHRIMP
Bom Jardim	Arroio dos Jaques	599 ± 7 Ma (11)	zircão	evaporação
Bom Jardim	Arroio dos Jaques	601 ± 5 Ma (11)	zircão	evaporação
Bom Jardim	Lavras do Sul	598 ± 3 Ma (11)	zircão	evaporação
Bom Jardim	Tapera	601 ± 2 Ma (11)	zircão	evaporação
Bom Jardim	Hilário	600,5 ± 2,4 Ma (3)	zircão	SHRIMP
Bom Jardim	Hilário	591,8 ± 3,0 Ma (2)	zircão	LA-ICP-MS
Bom Jardim	Hilário	590,5 ± 5,7 Ma (3)	zircão	SHRIMP
Bom Jardim	Hilário	587 ± 8 Ma (3)	plagioclásio	Ar-Ar
Bom Jardim	Hilário	590 ± 6 Ma (3)	plagioclásio	Ar-Ar
Maricá	Maricá	601 ± 13 Ma (2)	zircão	LA-ICP-MS
Maricá	Maricá	630 ± 3,4 Ma (1)	zircão	SHRIMP

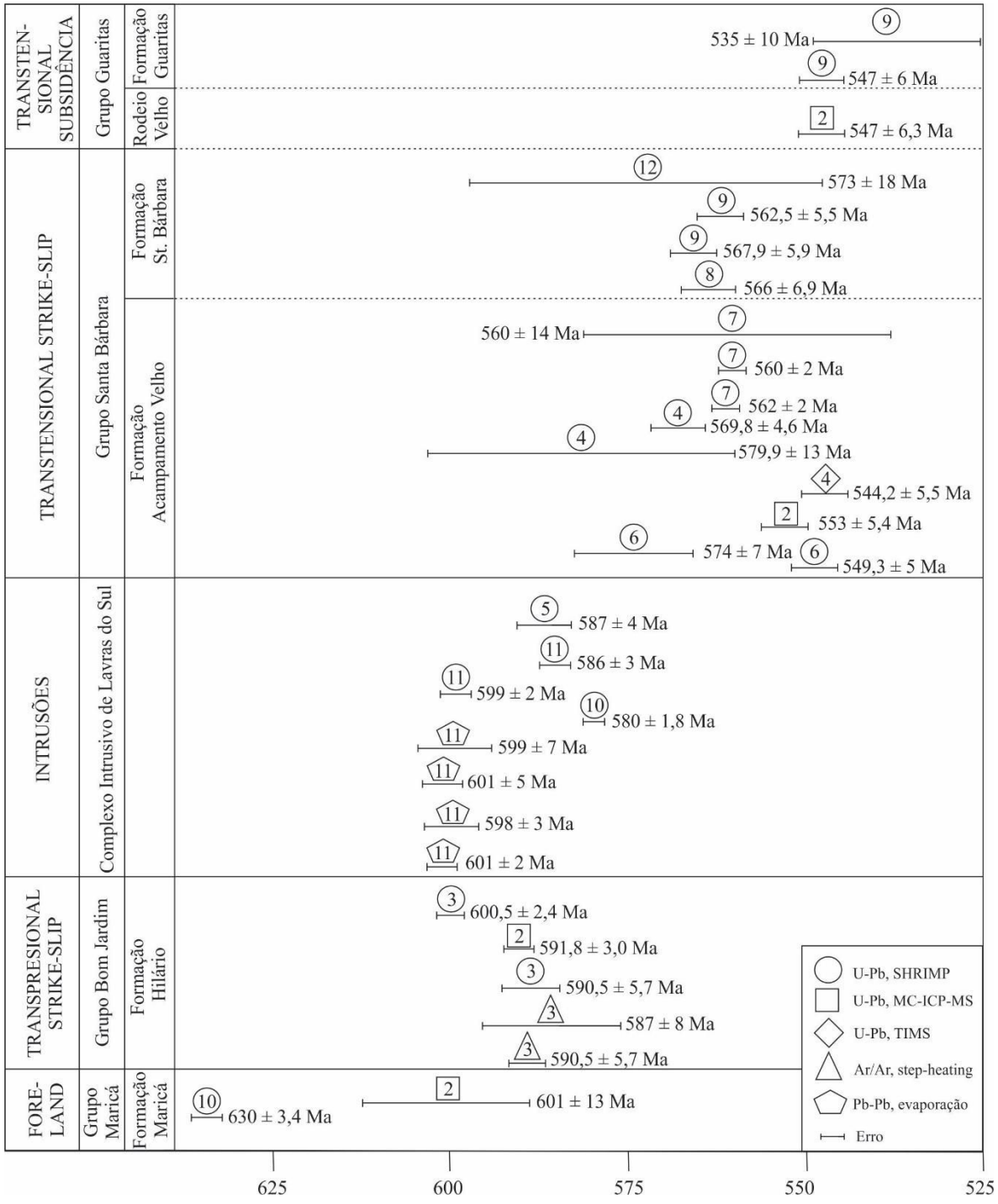

Figura 9. Ilustração sintética dos dados geocronológicos da Bacia do Camaquã e Granitos associados. Chaves: (1) Borba et al., 2008; (2) Almeida et al., 2012; (3) Janikian et al., 2008; (4) Janikian et al., 2012; (5) Liz et al., 2009b; (6) Sommer et al., 2005; (7) Matté et al 2016; (8) Bicca et al., 2013; (9) Oliveira et al., 2014; (10) Remus et al., 1999; (11) Gastal et al., 2006; (12) Chemale Jr., 2000.

2.4 Associação Shoshonítica de Lavras do Sul

A Associação Shoshonítica de Lavras do Sul apresenta características de um magmatismo pós-colisional relacionado aos estágios finais da orogenia Brasiliana, conforme discutido em Lima e Nardi (1998), Sommer et al. (2006) e Liz et al. (2009). Localizada no Terreno São Gabriel, possui estratigraficamente na base traqui-basaltos potássicos, sucedidos por quatro ciclos efusivos shoshoníticos, além de depósitos piroclástico de queda e fluxo (Lima, 1995). Ocorrem intrusões monzonítica rasa, dique traquiandesítico a riolítico e lamprófiro espessartítico (Müller et al., 2012). A fração plutônica da Associação Shoshonítica de Lavras do Sul é representada pelo Complexo Intrusivo de Lavras do Sul (Gastal et al., 2015) e a porção vulcanogênica é representada pela Formação Hilário. A Figura 10 representa a parte centro-oeste da Bacia do Camaquã e delimita a área da Associação Shoshonítica de Lavras do Sul.

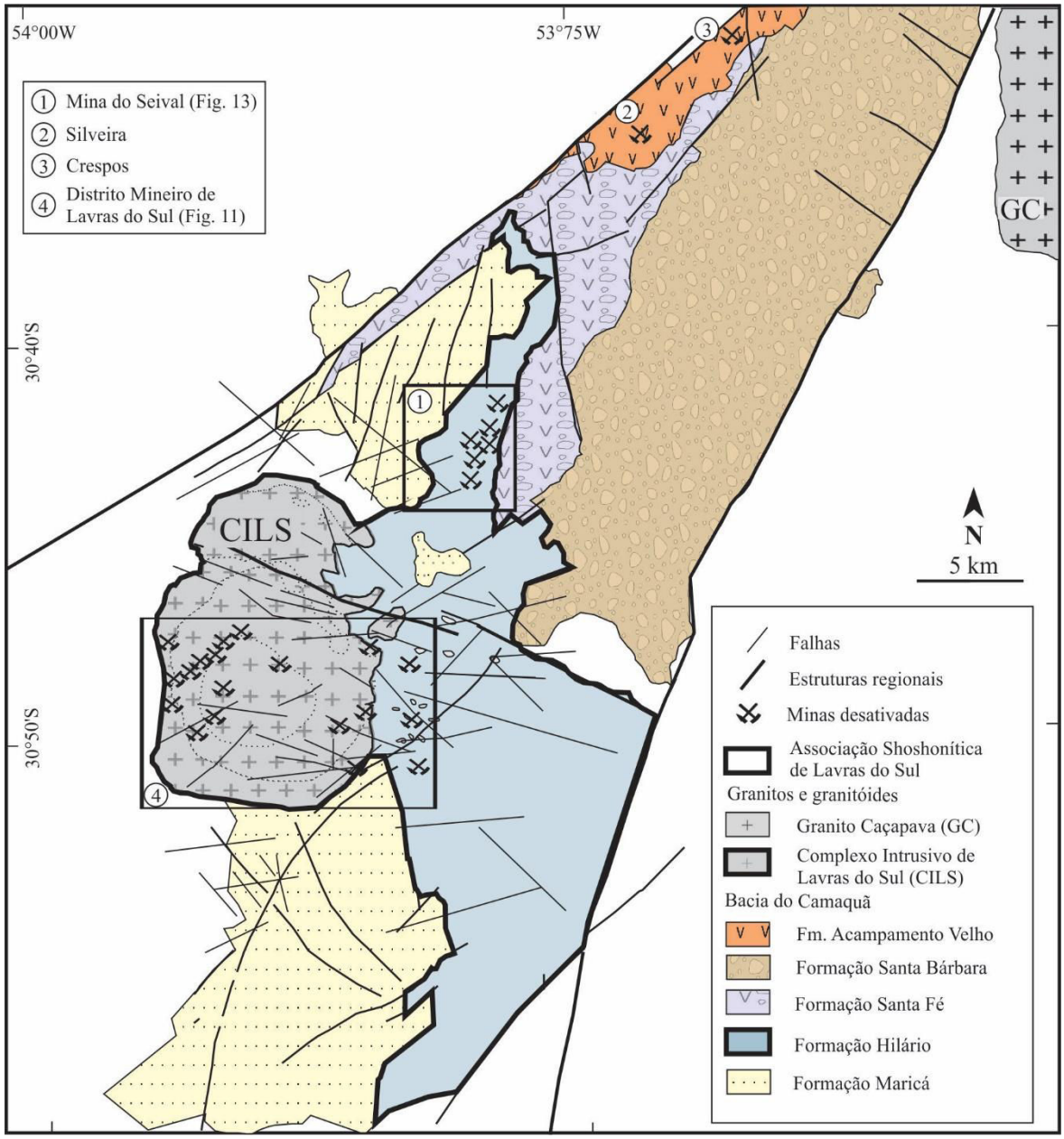

Figura 10. Mapa geológico do centro-oeste da Bacia do Camaquã com indicação da área da Associação Shoshonítica de Lavras do Sul (mod. de Toniolo et al., 2007; Gastal et al., 2015).

As rochas vulcanogênicas básicas da Associação Shoshonítica de Lavras do Sul possuem composições traquibasáltica a traquiandesítica pelo diagrama TAS e mostram que o potássio é superior ao valor de sódio, sendo classificadas como traquibasaltos potássicos e shoshonitos (Lima e Nardi, 1998). Ocorrem expressivos

depósitos efusivos aliados a uma fração piroclástica de fluxo de natureza traquiandesítica a riolítica (Lima, 1995), especialmente na porção sudeste do Complexo Intrusivo de Lavras do Sul, o que permite sugerir uma extração gradativa do magma responsável pela geração de um sistema de caldeira (Gastal et al., 2015).

As intrusões monzoníticas rasas concentram-se principalmente na borda nordeste do Complexo Intrusivo de Lavras do Sul, definindo um padrão geométrico semicircular, semelhante ao encontrado em terrenos vulcânicos associados a caldeiras, como sugerido por Lima (1995) e Gastal et al. (2015). Estes foram posicionados em condições epizonais, tendo incorporado grande quantidade de xenólitos do pacote de vulcanoclástica basculada durante o evento de subsidência de caldeira. Temporalmente vinculados aos monzonitos hipabissais ocorrem os diques riolíticos e as últimas manifestações efusivas intermediárias. Rochas latíticas estão representadas por diques com direção NW-SE na porção nordeste de Lavras do Sul. As rochas graníticas são caracterizadas pela zonação inversa de fácies.

2.5 Histórico das mineralizações da Mina do Seival

Devido à descoberta de mineralizações de ouro no sul do Brasil, também foram descobertas as ocorrências de cobre. Na primeira metade do século XX, em torno do ano de 1930, a maior exploração de cobre no sul do Brasil ocorreu na região conhecida como Mina do Seival.

Em 1901, as ocorrências foram descritas e pesquisadas por companhias particulares e estatais, até o ano de 1931. Após, a Cia E.F. e Minas de São Jerônimo realizaram uma série de escavações rasas. Em 1937, a mina foi explorada por uma companhia de Porto Alegre e teve seu teor avaliado em 4,7% de Cu. A Cia Indústria Eletro-Químicas S/A explorou entre os anos de 1939-42. No período de 1935-62, a mina foi lavrada intermitentemente com produção de cobre eletrolítico e sulfato de cobre. Nos anos de 1955-62, a mina chegou a produzir cerca de 1.000 toneladas de minério por mês, com teor médio de 1,6% de Cu total (1,0% Cu sulfetado). Entre os anos de 1942-64, a Mina da Barita foi cubada em torno de 64.000 toneladas, com 1,71% de cobre e 70 ppm de prata. Em 1957, a Mina João Dahne foi explorada

através de uma trincheira de dezena de metros, lavrando minério de baixo teor. Após isso, a Mina Alcides teve sua produção ligada à extração de sulfatos para correção de solos agrícolas.

A Companhia Brasileira do Cobre (CBC), nos anos de 1977 e 1978, realizou uma série de pesquisas na região, incluindo campanhas de sondagem que foram incorporadas nesse trabalho. Reischl (1978) classificou e nomeou as mineralizações na área, sendo elas: (i) Mina da Barita: corpo de minério lenticular de direção NE-SW, mergulhando 50º para NW, na forma de calcocita em bolsões irregulares junto às falhas, com uma reserva em torno de 64.000 toneladas e teor de 1,7% de Cu (sulfetado e oxidado), com alta Ag associada (70 ppm) e barita como o principal mineral de ganga; (ii) Mina João Dahne: explorada em 1957 por uma trincheira de dezenas de metros, com baixo teor, e direção NE-SW com mergulho acentuado; (iii) Mina do Morcego: lavrada e considerada antieconômica devido à elevada presença de oxidados (70% do minério) com calcocita e malaquita finamente disseminada em superfície, próximo a zonas de fraturas da lava andesítica de fluxo, com direção N-S a NE-SW; (iv) Mina do Meio: malaquita na forma de concentrações irregulares controladas pelo fraturamento do tufo andesítico com direção N-S a NE-SW; (v) Mina da Cruzeta: calcocita na forma de veios ao longo de fraturas e raramente disseminada com direção NE-SW e NW-SE subvertical em lava andesítica de fluxo porfirítica; (vi) Mina Alcides: bolsões de calcocita finamente disseminados em lapili tufo com ganga a base de barita e preenchendo falhas de direção N-S; (vii) Ocorrências Lagoa do Jacaré e Vila do Torrão são caracterizadas por malaquita em superfície e calcocita disseminada, controladas pelo fraturamento da rocha em concentrações irregulares, numa ganga de barita e calcita. Portanto, é notável um forte controle estrutural, associado ao fraturamento e falhas da rocha estando ligadas as mineralizações. A partir de 2000, a Mina do Seival despertou interesse de várias empresas multinacionais. Entretanto, o investimento foi baixo e não ocorreram muitas pesquisas. Ainda é gerada uma grande expectativa para a exploração desses depósitos.

2.6 Histórico das mineralizações do Distrito Mineiro de Lavras do Sul

O Distrito Mineiro de Lavras do Sul contém diversas minas e prospectos com ouro e cobre associado, sendo elas as minas Aurora, Bloco do Butiá, Caneleira, Cerritos (Pires e Resende), Dourada, Galvão, Mato Feio, Olaria, Paredão, Pitangueira, Taruman, Valdo Teixeira, Virgínia, São José, Santo Expedito e Zeca Souza, associadas ao Complexo Intrusivo de Lavras do Sul, e as minas de Volta Grande, Cerro Rico, Saraiva e Merita, associadas à Formação Hilário (Bongiolo et al., 2011).

Goñi (1961) apresentou um trabalho com base nos aspectos metalográficos, a partir da primeira análise detalhada ao microscópio óptico das rochas mineralizadas de Lavras do Sul. Ele destacou que o cobre não ocorre apenas nas rochas vulcanogênicas da Formação Hilário, mas também é encontrado nas rochas do Complexo Intrusivo de Lavras do Sul. Barbosa e Constantino (1961), estudando o minério de cobre na área de Volta Grande, determinaram a "influência positiva" do granito na lava andesítica de fluxo mineralizada, discutindo a influência do magmatismo granítico *versus* andesítico na formação das jazidas do Seival e Camaquã. Ribeiro et al. (1966), ao estudarem as mineralizações na quadrícula de Caçapava do Sul, salientaram que as mineralizações cupríferas nas áreas de Volta Grande e Vista Alegre estariam relacionadas às rochas andesíticas, alojadas em filões e em falhas secundárias. Na década de 70, a Companhia de Pesquisa e Recursos Minerais (CPRM) fez um grande levantamento e amostragem de todas as ocorrências. Kaul e Zir Filho (1974) apresentaram a tipologia, o controle tectônico e aspectos genéticos para as mineralizações auríferas de Lavras do Sul. Os autores descreveram as principais ocorrências e as classificaram quanto ao tipo (filoneano ou disseminado) tanto nas rochas graníticas (disseminado do Bloco do Butiá) como na sequência vulcânica encaixante. Apresentaram um detalhado estudo estrutural/tectônico para o Distrito Mineiro de Lavras do Sul, assim denominado pela primeira vez, demonstrando que os esforços compressivos de direção próxima a E-W atuaram sobre os granitos e as rochas vulcanogênicas, gerando falhas de tensão onde preferencialmente estariam encaixadas as estruturas e filões mineralizados.

Mostraram que as quantidades de cobre nos granitos são insignificantes, ao contrário das rochas vulcanogênicas, onde as concentrações atingiram valores economicamente interessantes para a época. Neste caso, a ligação genética do cobre com a lava andesítica de fluxo foi defendida pelos autores. Nas décadas de 1980-90, a Companhia Rio-grandense de Mineração (CRM) explorou ouro na região de Lavras do Sul. Nardi (1984) atribuiu a geração das soluções hidrotermais à intrusão dos pertita granitos e outras intrusões alcalinas, tendo estas sido responsáveis pelas mineralizações no Granito Lavras do Sul, bem como nas sequências vulcanogênicas e sedimentares. Por fim, Mexias et al. (1990b) propôs que a intrusão granítica teria atuado como fonte de calor na geração e manutenção de um sistema hidrotermal cujas características, bem como os padrões de zonação dos produtos de alteração muito se assemelham ao que se observa nos depósitos do tipo pórfiro (Mexias et al., 1990a).

A Figura 11 ilustra as mineralizações do Distrito Mineiro de Lavras do Sul. As mineralizações na Mina do Seival são apresentadas em detalhe no Capítulo 3.

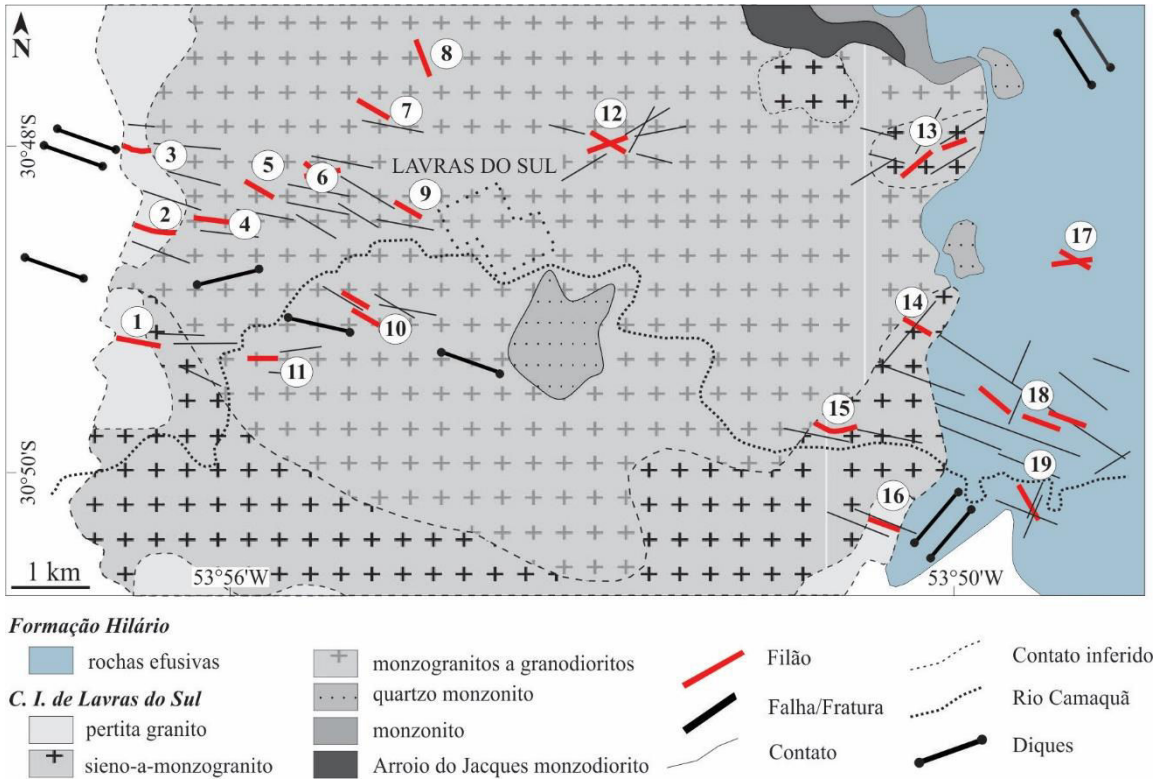

Figura 11. Mapa geológico do Distrito Mineiro de Lavras do Sul e localização das mineralizações (mod. de Bongiolo, 2002). Depósitos e ocorrências: 1 = Bloco do Butiá; 2 = Galvão; 3 = Zeca Souza; 4 = Caneleira; 5 = Taruman; 6 = Olaria; 7 = Pitangueira; 8 = Santo Expedito; 9 = Paredão; 10 = São José; 11 = Virgínia; 12 = Cerritos (Pires e Resende); 13 = Dourada; 14 = Aurora; 15 = Mato Feio; 16 = Valdo Teixeira; 17 = Cerro Rico; 18 = Volta Grande; 19 = Saraiva.

3. ESTADO DA ARTE - MINA DO SEIVAL

Nessa parte do trabalho é apresentado o mapeamento geológico, geologia estrutural, petrografia e descrição das mineralizações, como base para a compreensão dos manuscritos científicos apresentados no Capítulo 4.

3.1 Mapeamento geológico

A região da Mina do Seival é constituída por um embasamento (parte 2.1) composto por metaultramafito, metagranitoide e xisto (Complexo Cambaí), parcialmente coberto por rochas sedimentar da Formação Maricá e vulcanogênica da Formação Hilário (Chemale Jr., 2000; Paim et al., 2000; Hartmann et al., 2007). Este conjunto foi posteriormente sobreposto e intrudido por rochas do Complexo Intrusivo de Lavras do Sul (Nardi, 1984; Bongiolo et al., 2011; Gastal et al., 2015). Vulcanitos ácidos e básicos, de afinidade alcalina sódica saturada em sílica, e rochas sedimentares do Grupo Santa Bárbara sucedem esta associação (Paim et al., 2000; Toniolo et al., 2007).

Na Mina do Seival, a Formação Hilário é representada por lava andesítica de fluxo, lapili tufo, aglomerado vulcânico e corpos hipo-abissais de composição andesítica a traquiandesítica, principalmente diques de orientação NE-SW. As rochas piroclásticas são lapili tufo com mineralogia a base de plagioclásio e piroxênio, variando conforme a profundidade. As lavas andesíticas de fluxo podem ser amigdalóides com matriz fina ou porfiríticas. Em algumas porções, essas rochas vulcanogênicas encontram-se intensamente fraturadas. O aglomerado vulcânico é composto de piroclastos arredondados em uma matriz afanítica de coloração escura. Todo este conjunto é coberto pelas rochas conglomerática e vulcânica vesiculada da Formação Santa Fé (Toniolo et al., 2007). Esse conglomerado polimítico de clasto-suportado varia de centimétrico a decamétrico, enquanto que a vulcânica vesiculada possui matriz a base de plagioclásio e vesículas de 0,2 a 0,5 cm, o que difere da lava andesítica de fluxo da Formação Hilário. Os depósitos aluvionares são sedimentos fluviais dominantemente arenosos e localizam-se na porção oeste da área de estudo ao longo do Arroio Teixeira. As projeções

estereográficas mostram diferentes padrões para o acamamento entre as formações Hilário e Santa Fé.

Na área da Mina Seival, a Formação Hilário tem caimento para NW e ângulo de inclinação de ~30°, enquanto que próximo ao granito Lavras do Sul e na Formação Santa Fé ela possui caimento para ~E-W e ângulos de ~10 a 20°. Um mapa de pontos é apresentado no ANEXO C. Na Figura 12 são apresentados a localização dos testemunhos de sondagem e perfis da parte 3.3. A Figura 13 ilustra o mapa geológico de detalhe da área. Uma tabela de pontos com nome das amostras coletadas, unidade a que pertencem, localização e litologia associada é apresentada no ANEXO D.

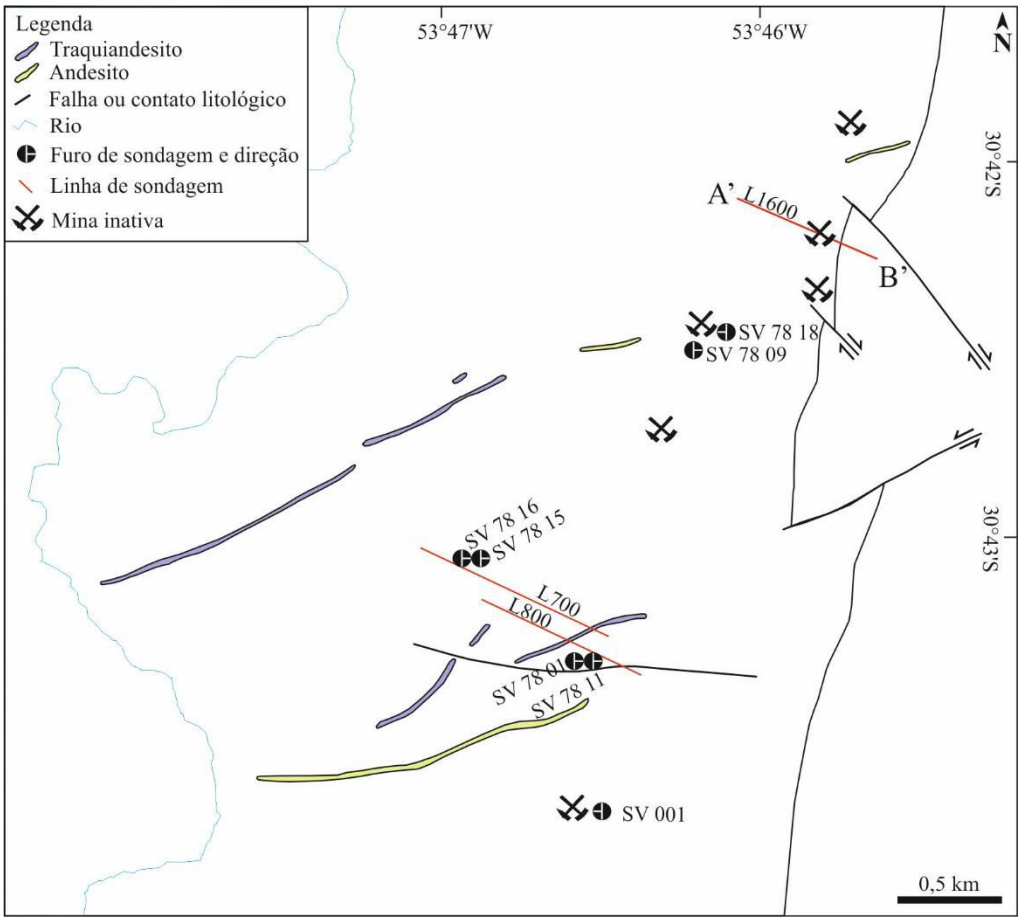

Figura 12. Mapa com localização das linhas e dos furos de sondagem, bem como indicação do nome e direção de cada furo de sondagem. Também são ilustrados os diques de andesito a traquiandesito e o contato litológico entre as formações Hilário e Santa Fé.

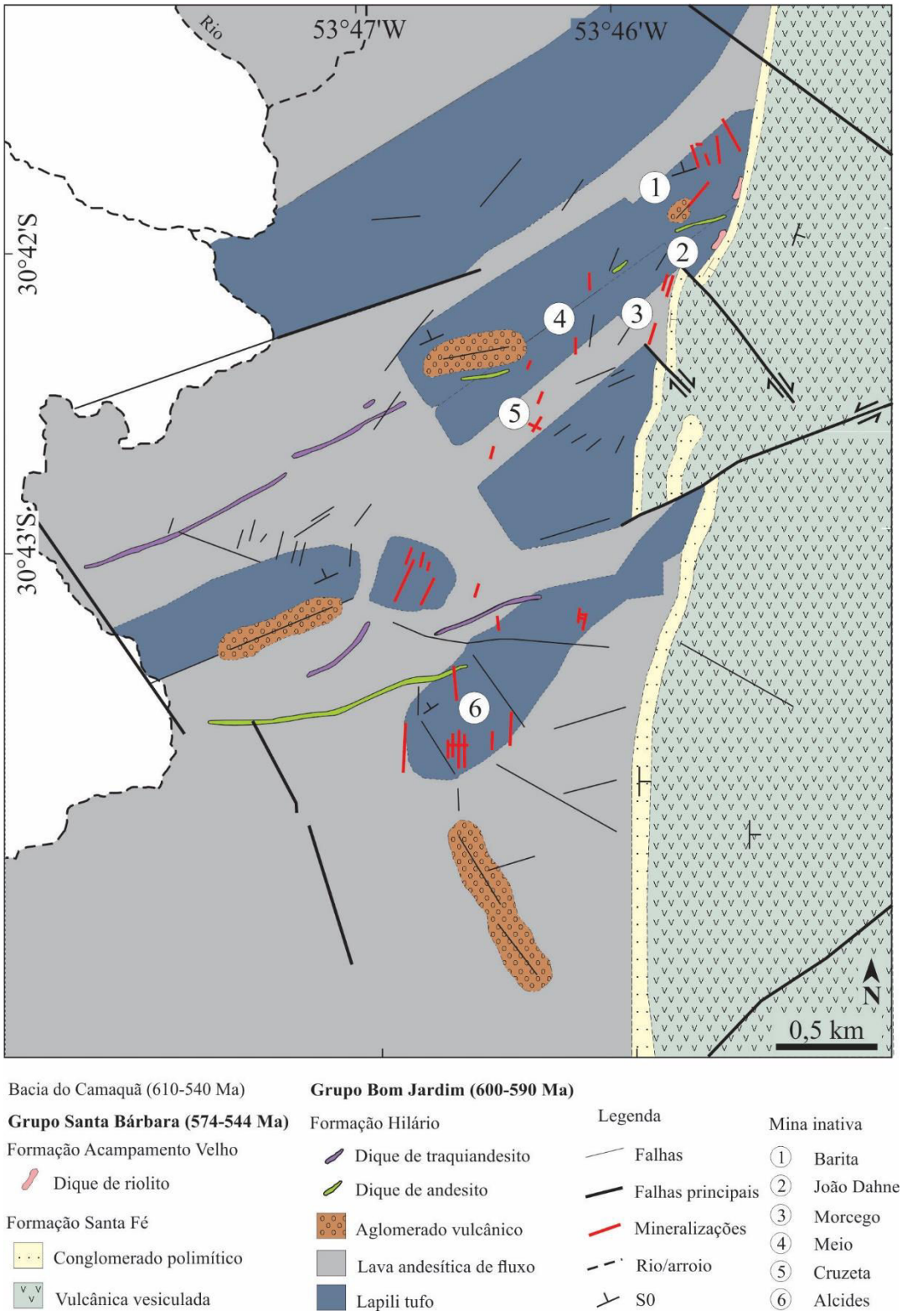

Figura 13. Mapa Geológico da Mina Seival (mod. de Reischl, 1978; Lopes et al., 2014) contendo localização das antigas minas, falhas, mineralizações, caimento das rochas, rio e estradas.

3.2 Geologia estrutural

A geologia estrutural descrita no manuscrito I foi realizada em duas áreas. Iniciou-se com o levantamento estrutural das mineralizações da Mina do Seival, tendo em vista que nesses locais ocorrem estrias de falhas, possibilitando medições de cinemática. Também foram adicionados dados do perfil na estrada RS-357, cedidos pelo prof. Everton Marques Bongiolo, da Universidade Federal do Rio de Janeiro, em algumas mineralizações do Distrito Mineiro de Lavras do Sul e Formação Hilário. Esses dados foram levantados durante seu estudo de mestrado e doutorado com o acompanhamento do prof. Ruy Paulo Philipp, da Universidade Federal do Rio Grande do Sul, entre os anos de 2002 e 2006. Os pontos marcados da geologia estrutural estão simplificados na Figura 14, e os dados medidos e calculados estão compilados na tabela do ANEXO E.

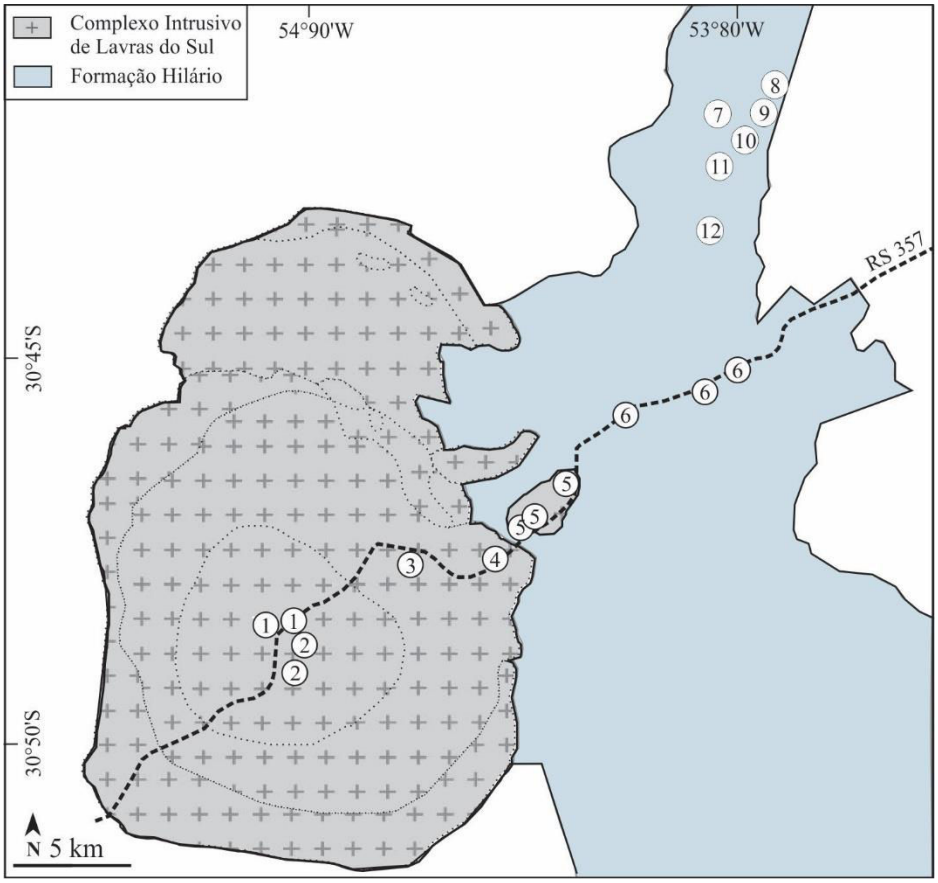

Figura 14. Mapa de pontos da área do Distrito Mineiro de Lavras do Sul (exceto PT 18) e mapa dos pontos/minas da área da Mina do Seival. Chaves: 1 = Mina da Barita, 2 = Mina João Dahne, 3 = Mina do Morcego, 4 = Mina do Meio, 5 = Mina Cruzeta, 6 = Mina Alcides.

Como mencionado anteriormente, a Mina do Seival e o Distrito Mineiro de Lavras do Sul estão localizados no Terreno São Gabriel do Escudo Sul-rio-grandense. As duas falhas principais com mergulho vertical a subvertical dentro deste terreno são Cabritos-Perau e Segredo, ambas com direção NE-SW sinistral (ver Figuras 5 e 6). Neste trabalho, a Falha de Cerro Alegre é considerada como a continuação ao sul da Falha do Segredo. No norte do Complexo Intrusivo de Lavras do Sul, a Falha Palma-Jacques é um lineamento que controla a posição dos granitóides e das rochas vulcanogênicas separando a Formação Hilário em andesitos de fluxo na porção central e sequência piroclástica-andesito na porção norte (Lopes et al., 2014). A Falha Palma-Jacques tem direção NW-SE com uma última cinemática sinistral (Gastal et al. 2015). No sul do complexo granítico de Lavras do Sul, a Falha Volta Grande é o lineamento que controla a porção sul das rochas vulcanogênicas e granitoides.

As rochas vulcanogênicas da Mina do Seival estão muito fraturadas, evidenciando uma tectônica rúptil em que predominam fraturas subverticais de direção NE-SW e NW-SE. As estruturas rúpteis são em grande parte resultantes de reativações das zonas de cisalhamento de direção NE-SW. A reativação das falhas é função direta da orientação dos campos tensionais principais durante os eventos tectônicos que afetaram o Escudo Sul-rio-grandense. O sistema de falhas com direção NW-SE é correlacionável ao Lineamento de Ibaré, localizada a oeste da área de estudo. Portanto, a unidade não apresenta feições deformacionais dúcteis, sendo afetada somente por falhas e fraturas subverticais de direção dominantemente NE-SW e subordinadamente NW-SE.

As medidas de falhas obtidas para a Mina do Seival e para o Distrito Mineiro de Lavras do Sul tiveram a correção através do *software Win-Tensor* (Delvaux and Sperner, 2003). No manuscrito I, também são interpretadas as medidas de fraturas e veios de ambas as áreas estudadas.

3.3 Petrografia

Como mencionado anteriormente, as rochas vulcanogênicas da Mina do Seival são lava andesítica de fluxo, lapili tufos, aglomerados vulcânicos e corpos hipoabissais de composições andesíticas a traquiandesíticas (Tab. 2). Nessa parte do trabalho são descritas as rochas vulcanogênicas que ocorrem na área.

Tabela 2. Tabela mineralógica das rochas vulcanogênicas da Mina do Seival com descrição da textura, mineralogia e localização.

Rocha	Textura	Mineralogia	Localização
Lava andesítica amigdalóide de fluxo	Traquítica com micrólitos de plagioclásios orientados.	Micrólitos de plagioclásio, piroxênio e quartzo. Amigdalas preenchidas principalmente por clorita-calcita, clorita-esmectita-calcita ou clorita-quartzo.	Principalmente no sul da área.
Lava andesítica porfirítica de fluxo	Traquítica com matriz grossa a fina rica em micrólitos de piroxênio e plagioclásio.	Fenocristais de plagioclásio e piroxênio em uma matriz a base de micrólitos de plagioclásio.	Principalmente no nordeste da área proximo ao contato com a Formação Santa Fé.
Lapili tufo	Matriz é um tufo grosso (0,05 a 0,12 mm) composto por cristaloclastos de plagioclásio, quartzo, matriz vítrea microcristalina e material opaco. Piroclastos possuem formas diversas, desde arredondadas a angulosas, geralmente com bordas curvilíneas.	Matriz rica em plagioclásio ou plagioclásio e piroxênio; Piroclastos com diversas composições (lava andesítica porfirítica e amigdaloidal de fluxo, lava andesítica de fluxo avermelhado e rochas piroclásticas).	Toda a área.
Aglomerado vulcânico	Matriz afanítica com piroclastos arredondados.	Matriz porosa; piroclastos de composição vulcânica, principalmente andesitíca.	Em zonas de falha.
Dique de andesito	Traquítica marcada pelos fenocristais de plagioclásio.	Plagioclásio, ± K-feldspato, quartzo e piroxênio.	Orientação NE-SW
Dique de traquiandesito	Traquítica marcada pelos fenocristais de plagioclásio.	Plagioclásio, quartzo, biotita e piroxênio.	Orientação NE-SW

As lavas andesíticas de fluxo podem ser separadas em amigdalóides e porfiríticos. As lavas andesíticas amigdalóides de fluxo possuem matriz fina a base de micrólitos de plagioclásios orientados com textura traquítica e os pseudomorfos de minerais máficos, como piroxênio e possivelmente anfibólio. As amígdalas têm cerca de 0,5 a 1,0 mm e aparentam orientação por fluxo, e por vezes coalescência, com formas achatadas ou arredondadas. São preenchidas por diversos minerais, principalmente calcita, clorita e/ou quartzo. As lavas andesíticas porfiríticas de fluxo possuem matriz grossa a fina rica em micrólitos de piroxênio e plagioclásio. O

fenocristal de piroxênio geralmente é zonado, e o de plagioclásio é alterado para albita. A textura traquítica é marcada pela orientação dos micrólitos de plagioclásio. A Figura 15 apresenta as principais características das amostras de lavas andesíticas de fluxo.

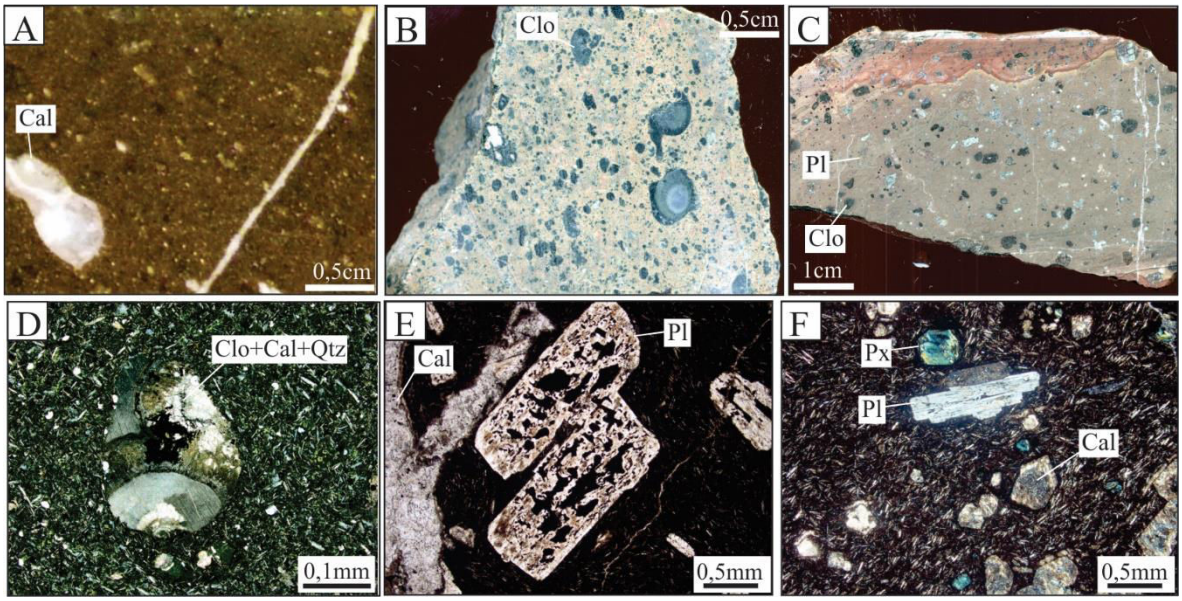

Figura 15. A) FM07 – Amostra de testemunho de sondagem de lava andesítica amigdalóide de fluxo preenchida por calcita; B) WL13 - Amostra de mão de lava andesítica porfirítica de fluxo com minerais máficos alterados para clorita; C) WL19 - Amostra de mão de lava andesítica porfirítica de fluxo a base de plagioclásio e piroxênio alterados para clorita; D) RFM32 - Fotomicrografia em luz polarizada de lava andesítica amigdalóide de fluxo preenchida por clorita, calcita, quartzo e minerais opacos; E) WL19 - Fotomicrografia em luz natural de lava andesítica porfirítica de fluxo com fenocristal de plagioclásio alterado para calcita; F) WL19 - Fotomicrografia em luz polarizada de lava andesítica porfirítica de fluxo com fenocristal de plagioclásio e piroxênio alterados para calcita. Chaves: Cal = calcita, Clo = clorita, Pl = plagioclásio, Qtz = quartzo, Px = piroxênio.

As rochas piroclásticas foram classificadas com base na granulometria em lapili tufo e aglomerados vulcânicos. São compostas por piroclastos de diferentes composições (lava andesítica porfirítica, lava andesítica amigdalóide, lava andesítica avermelhada e rochas piroclásticas) e possuem diversas formas, desde arredondadas a angulosas, geralmente com bordas curvilíneas. A matriz da rocha piroclástica é um tufo grosso (0,05 a 0,12 mm) a fino (<0,05 mm) composto por cristaloclastos de plagioclásio, ± piroxênio, quartzo, matriz vítrea microcristalina e material opaco. As rochas piroclásticas foram separadas, de acordo com a composição da matriz, em ricas em plagioclásio e ricas em plagioclásio e piroxênio.

Na rocha piroclástica rica em plagioclásio, a matriz é composta por material fino, amorfo, descrito como cinza ou pó vulcânico, ou até mesmo porção vítrea com muitos cristaloclastos e partes de cristaloclastos de plagioclásio e quartzo. As rochas piroclásticas são predominantemente de lava andesítica de fluxo ricas em plagioclásio. Na rocha piroclástica rica em plagioclásio e piroxênio, a matriz é composta por material grosso a muito fino com muitos cristaloclastos e partes de cristaloclastos de plagioclásio, piroxênio e quartzo. Nessas últimas, os piroclastos são predominantemente de lava andesítica de fluxo ricas em plagioclásio e piroxênio. Em geral, o lapili tufo possui uma grande variação na composição dos piroclastos, sendo distinguíveis pela mineralogia e cor de alteração. A Figura 16 apresenta as principais características das amostras de lapili tufo.

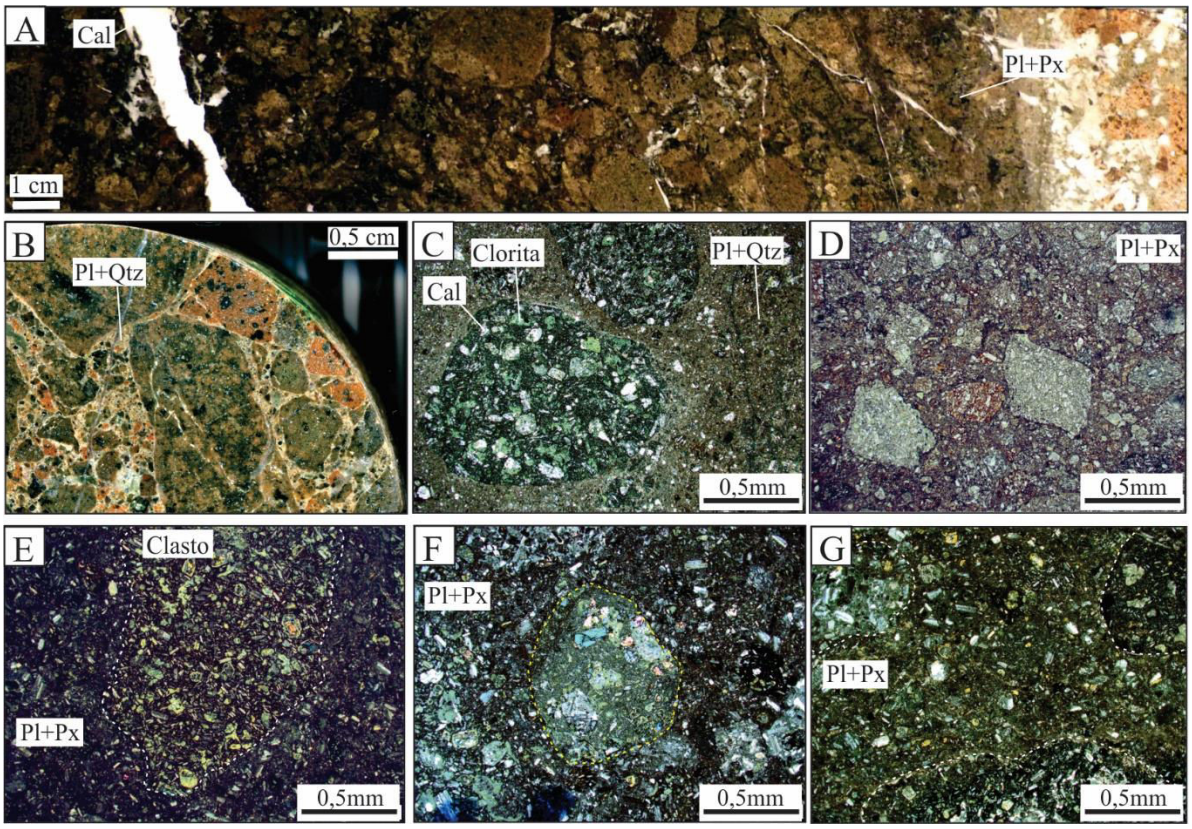

Figura 16. A) FM 52 - Fotografia macroscópica de testemunho de sondagem de lapili tufo com matriz grossa a base de plagioclásio, piroxênio e quartzo; B) FM65 – Amostra de testemunho de sondagem de lapili tufo com matriz fina a base de plagioclásio e quartzo; C) RFM48 - Fotomicrografia em luz polarizada de lapili tufo com matriz fina a base de plagioclásio e quartzo; D) FM44 - Fotomicrografia em luz polarizada de lapili tufo com matriz grossa a base de plagioclásio, piroxênio e quartzo com variação de piroclastos e diferentes

cores; E, F e G) FM60, FM60 e FM62 - Fotomicrografia em luz polarizada de lapili tufo com matriz média a base de plagioclásio, piroxênio e quartzo. Chaves: Cal = calcita, Pl = plagioclásio, Px = piroxênio, Qtz = quartzo.

O aglomerado vulcânico ocorre preferencialmente em zonas de falhas com matriz afanítica porosa. Os piroclastos arredondados são de composição vulcânica, principalmente lavas andesíticas de fluxo amigdalóide e porfirítica. A Figura 17 ilustra o aglomerado vulcânico na área da Mina Barita.

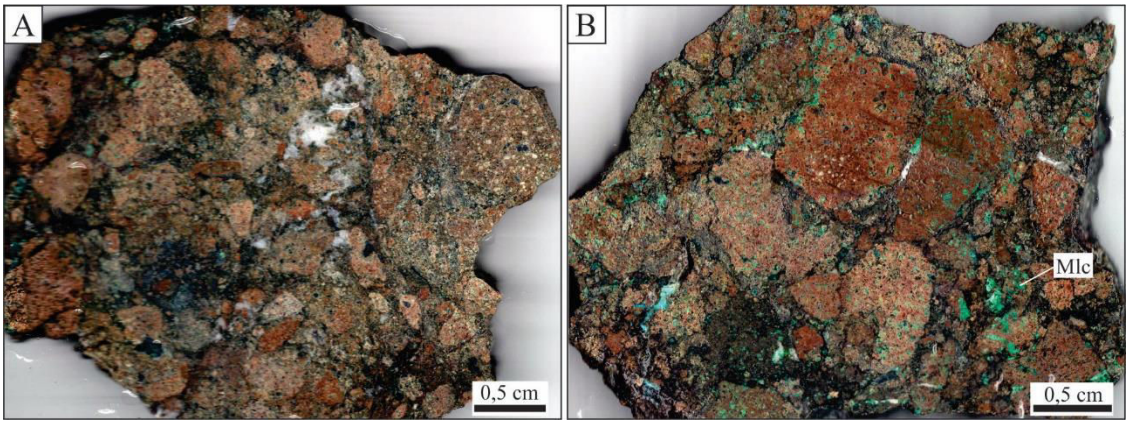

Figura 17. Fotografia macroscópica de amostras de mão. RFM48 - Aglomerado vulcânico alterado (A) e preenchido por malaquita (B). Chave: Mlc = malaquita.

As rochas subvulcânicas são representadas pelos diques de andesito e traquiandesito. Os diques de andesito possuem textura traquítica com fenocristais abundantes de plagioclásio e ±K-feldspato com intensa sericitização e substituição para ilita. Os plagioclásios possuem bordas e planos de maclas corroídas e preenchidas por clorita, calcita e titanita. Pseudomorfos de piroxênio são geralmente substituídos por clorita, calcita, titanita e opacos dispersos em matriz composta por micrólitos de plagioclásios e piroxênios. Algumas amostras dos diques de traquiandesito possuem cor avermelhada devido à oxidação de minerais contendo ferro. A alteração da matriz é predominantemente hematita e por vezes clorita, quartzo, titanita, calcita e esmectita. Os diques de traquiandesito possuem cor amarronzada com fenocristais de plagioclásio e biotita lamelar numa matriz oxidada, composta por plagioclásio, quartzo, ±K-feldspato e hematita. Associados à biotita observam-se cristais euédricos de apatitas e amorfos de óxido de ferro. A Figura 18 apresenta as amostras dos diques de andesito e traquiandesito.

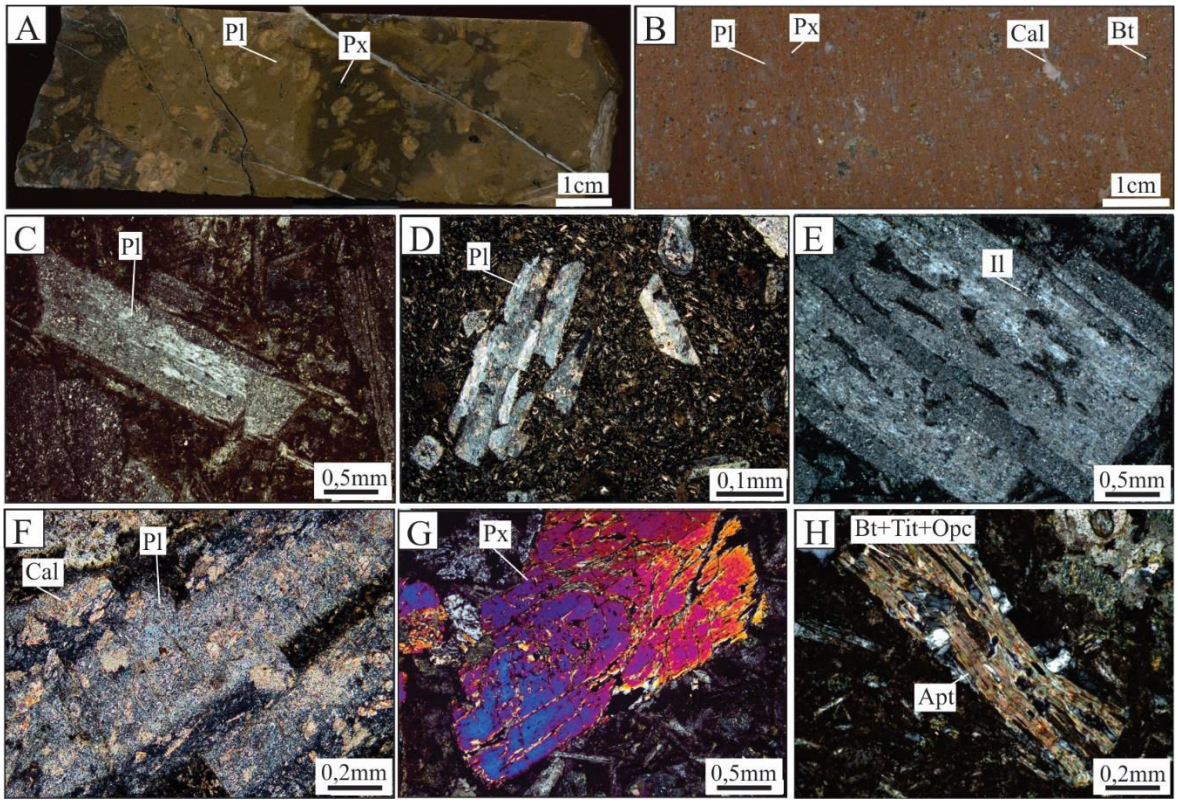

Figura 18. A) FM30 - Fotografia de testemunho de sondagem de dique de andesito com fenocristais de plagioclásio e piroxênio e com oxidação da matriz (cor marrom mais claro); B) RFM51 - Fotografia de amostra de mão de dique de traquiandesito com fenocristais de plagioclásio, piroxênio e biotita com intensa oxidação da matriz (cor avermelhada) e alteração dos máficos para calcita; C) DD62 - Fotomicrografia em luz polarizada de dique de andesito com zonação do plagioclásio; D) RFM66 - Fotomicrografia em luz polarizada de dique de andesito com fenocristais de plagioclásio e textura traquítica da matriz com micrólitos de plagioclásio; E) DD62 - Detalhe de fotomicrografia em luz polarizada de dique de andesito com alteração do plagioclásio para ilita; F) RFM66 - Detalhe de fotomicrografia em luz polarizada de dique de andesito com plagioclásio intensamente alterado para calcita; G) DD62 - Fotomicrografia em luz polarizada de dique de andesito com fenocristal preservado de piroxênio; H) RFM51 - Fotomicrografia em luz polarizada de dique de traquiandesito com fenocristal de biotita associado com titanita, apatita e minerais opacos. Chaves: Pl = plagioclásio, Px = piroxênio, Cal = calcita, Il = ilita, Bt = biotita, Tit = titanita, Opc = minerais opacos, Apt = apatita.

3.4 Argilominerais

Os argilominerais foram classificados com o auxílio da técnica de difratometria de raios X (DRX). Esses argilominerais ocorrem nas rochas com intensa alteração hidrotermal substituindo minerais primários, matriz microcristalina ou preenchendo a borda de amígdalas e cavidades. Geralmente, os argilominerais ocorrem associados a quartzo, calcita, hematita e minerais opacos. Os argilominerais também substituem o piroxênio e/ou minerais máficos. A intensa cloritização e carbonatação na matriz ocasiona a formação de aglomerados de argilominerais ou uma completa substituição dos minerais máficos. Os argilominerais identificados na Mina do Seival são: esmectita; interestratificados de clorita e esmectita; corrensita; clorita. Os diques de traquiandesito com biotita estão alterados principalmente para clorita, calcita e óxido de ferro (hematita). Os diques de traquiandesito possuem uma alteração hidrotermal mais intensa (alto L.O.I.; Lopes et al., 2014) quando comparados aos diques de andesito. A ilita aparece na DRX de rocha total e está alterando fenocristais e micrólitos de plagioclásios, principalmente nas rochas com intensa alteração e próximas às minas e ocorrências. A Figura 19 mostra esses argilominerais em micrografia, a Figura 20 mostra um perfil com a distribuição espacial desses argilominerais e a Figura 21 contém os mais representativos difratogramas de raios X. No ANEXO G estão todos os difratogramas realizados pelo método das argilas orientadas, caracterizando assim os tipos de argilominerais.

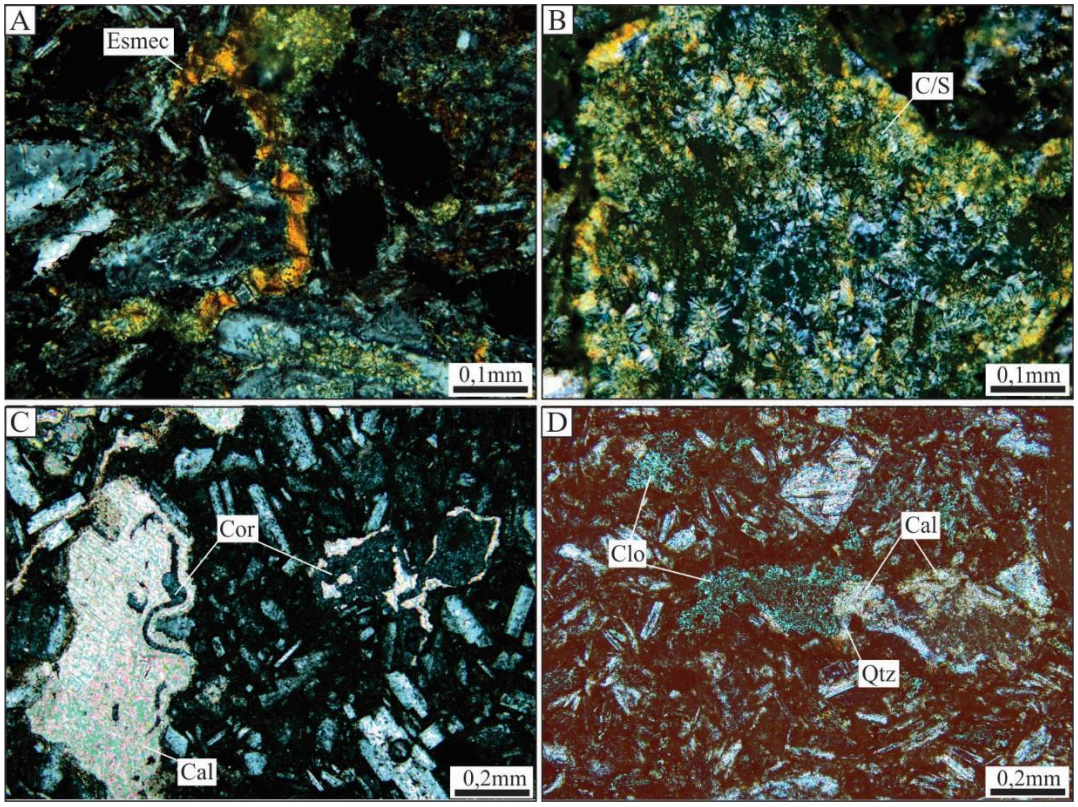

Figura 19. Fotomicrografia em luz polarizada dos argilominerais da Mina do Seival. A) SV77 - Lava andesítica amigdalóide de fluxo com esmectita (mod. de Fontana et al., 2017); B) FM25 - Lava andesítica amigdalóide de fluxo com interestratificado clorita/esmectita; C) FM13 - Dique de andesito com corrensita e calcita; D) RFM48 – Matriz de lapili tufo com clorita, calcita, quartzo, sulfeto, titanita e minerais opacos (mod. de Fontana et al., 2017). Chaves: Esmec = esmectita, C/S = interestratificado clorita/esmectita,Cor = corrensite, Cal = calcita, Clo = clorita, Qtz = quartzo.

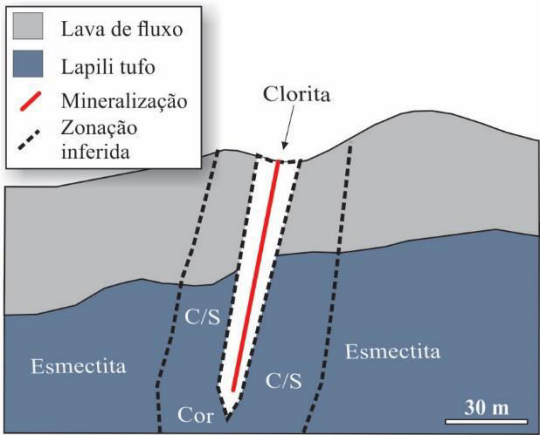

Figura 20. Perfil esquemático com a distribuição espacial dos argilominerais com clorita, interestratificado clorita/esmectita (C/S) e corrensita (Cor) próximo às fraturas/falhas e esmectita mais distante (mod. de Fontana et al., 2017).

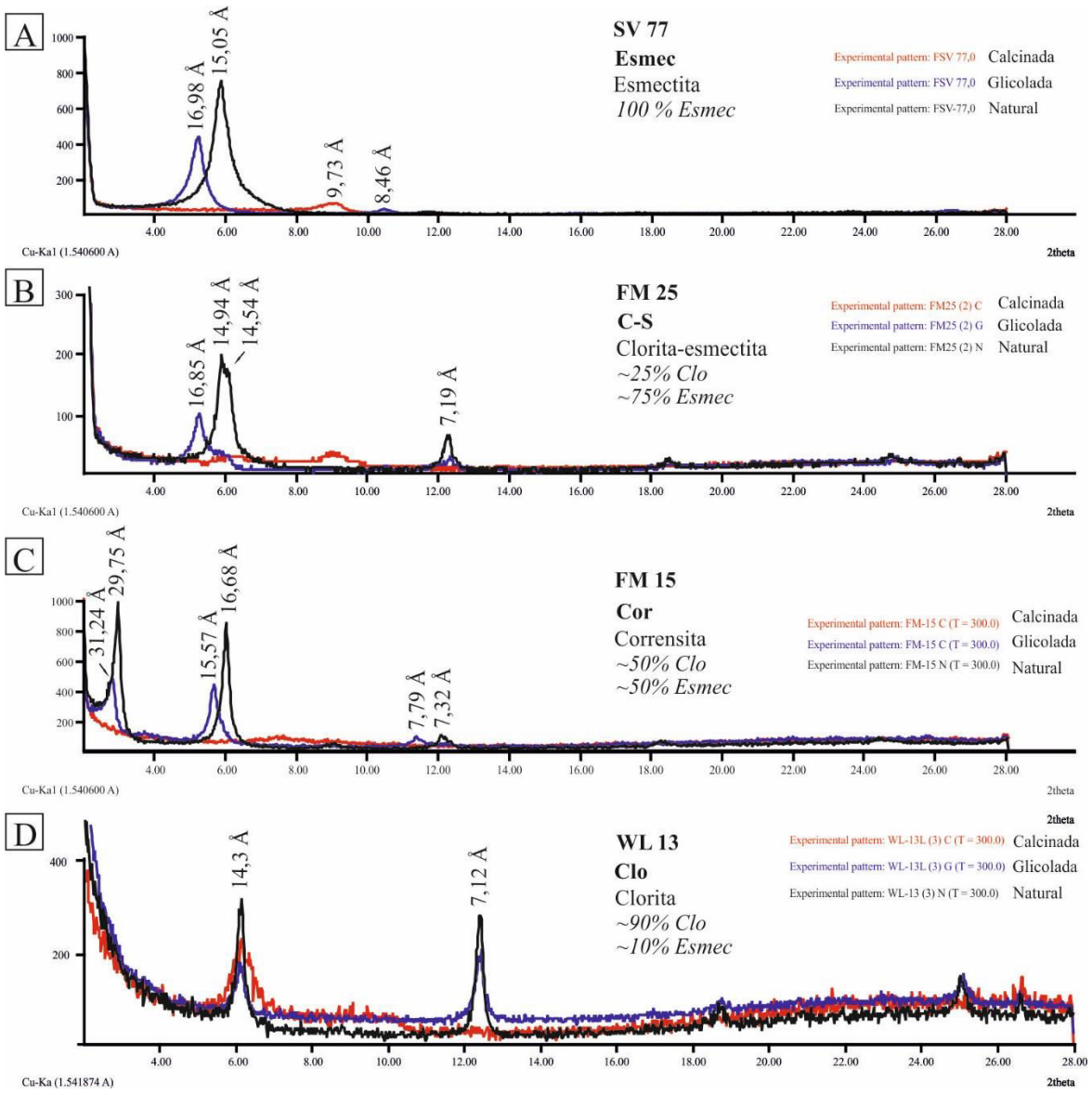

Figura 21. Difratogramas de raios X da Mina do Seival. A) Esmectita em lava andesítica amigdalóide de fluxo; B) Interestratificado clorita/esmectita em lava andesítica amigdalóide de fluxo; C) Corrensita em diques de andesito; D) Clorita em lava andesítica porfirítica de fluxo da Mina do Morcego.

Após a interpretação dos difratogramas de raios X, podemos caracterizar dois episódios de alteração hidrotermal (Tab. 3). A alteração hidrotermal argílica intermediária é caracterizada pela esmectita na forma fibrosa e cristalina. A esmectita também está associada com cristobalita (quartzo), ocorrendo nos interstícios dos grãos e dentro de piroclastos vulcânicos, podendo também ocorrer alterando o material vítreo. A alteração propilítica é caracterizada pela assembleia

mineralógica de clorita, interestratificado clorita/esmectita, corrensita, titanita, carbonato (calcita), sulfeto de cobre (calcocita e bornita), barita, quartzo e hematita. Essa alteração ocorre tanto pervasiva, indicando um evento de maior temperatura, quanto venular de carbonato (calcita), clorita e quartzo. Os veios preenchem fraturas das rochas, às vezes ocorrendo quartzo euédrico associado com carbonato e pequenos cristais de calcocita e bornita (Fig. 22A, B e C), geralmente corroídos.

Tabela 3. Tabela paragenética da Mina do Seival com a indicação dos tipos de alteração hidrotermal e a mineralogia associada.

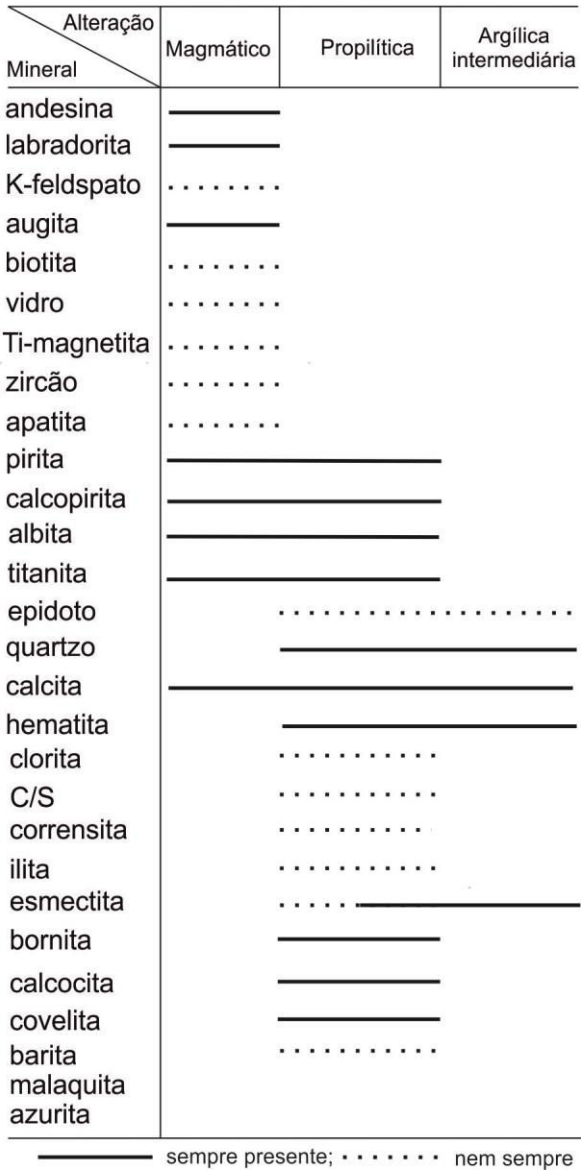

A alteração pervasiva transforma a grande maioria dos minerais máficos e subordinadamente os feldspatos que ocorrem na matriz e piroclastos. O piroxênio aparece totalmente substituído para clorita, carbonato e hematita. A alteração supergênica é representada pela malaquita e azurita e ocorre nas zonas mineralizadas (Fig. 22D). A silicificação ocorre sempre em falhas e fraturas substituindo parcial ou totalmente a rocha, descrita como textura *Vuggy* (Fig. 22E). Os sulfetos ricos em cobre (calcocita e bornita) estão corroídos (Fig. 22F e G). Os sulfetos de ferro e cobre-ferro são pirita e calcopirita (Fig. 22H). A barita ocorre preenchendo fraturas de espessuras centimétricas e sob a forma de cristais tabulares geminados, localmente alterados.

A Figura 22 ilustra os sulfetos da Mina do Seival e a alteração supergênica.

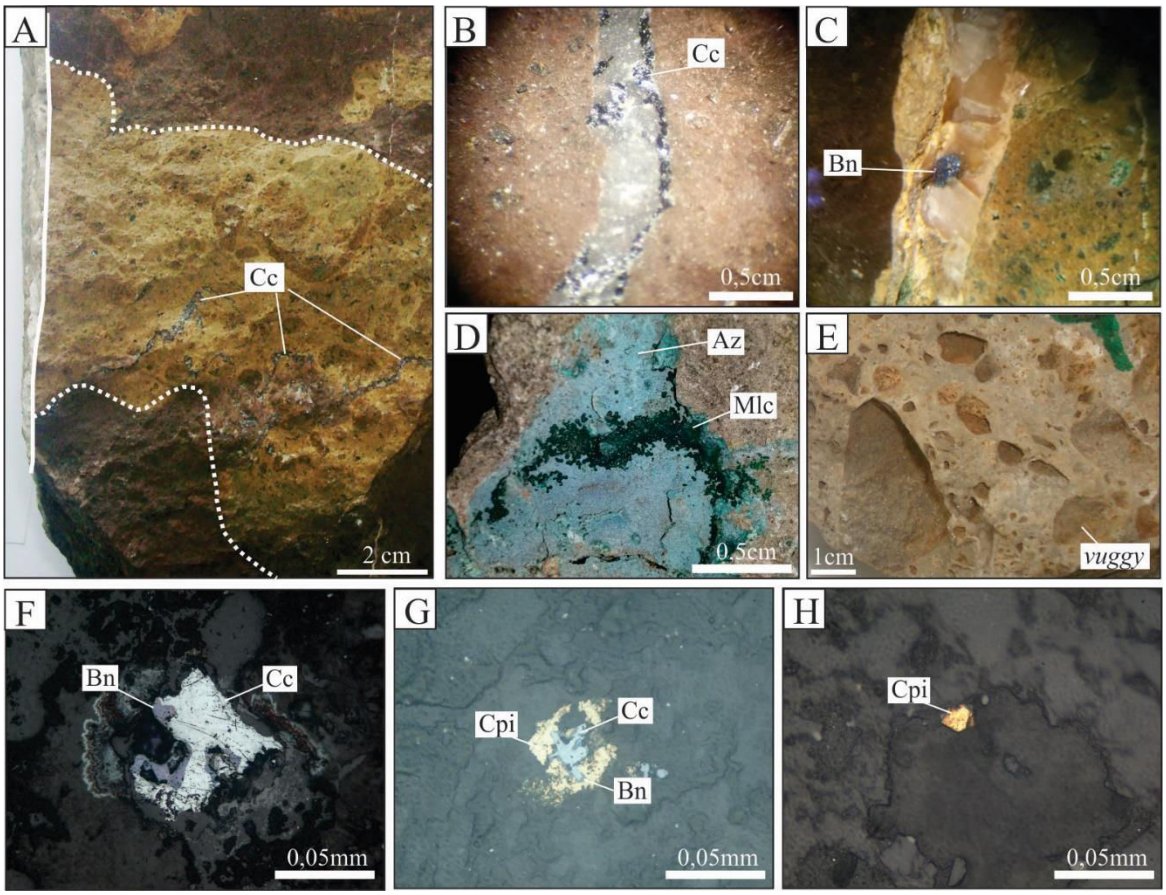

Figura 22. A) WL11 - Amostra de mão de lapili tufo mineralizado da Mina do Meio com bolsões de diferentes cores e associação de veios de calcocita; B) WL11 - Foto de lupa evidenciando calcocita associada a veio de calcita; C) RFM48N - Foto de lupa evidenciando bornita associada a veio de calcita; D) WL07 - Associação de malaquita e azurita como

alteração de sulfetos de cobre; E) WL07 - Silicificação de matriz marcado pela textura vuggy; F) FM83 - Micrografia em luz refletida da reação de calcocita e bornita,; G) FM07 - Micrografia em luz refletida da reação de calcocita e calcopirita coronítica (mod. de Fontana et al., 2017); H) FM81 - Micrografia em luz refletida da calcopirita associada com clorita e quartzo na matriz. Chaves: Cc = calcocita, Bn = bornita, Az = azurita, Mlc = malaquita, Cpi = calcopirita.

3.5 Mineralizações

As mineralizações na Mina do Seival estão descritas em Reischl (1978), sendo elas: (1) Mina Barita; (2) Mina João Dahne; (3) Mina Morcego; (4) Mina do Meio; (5) Mina Cruzeta); (6) Mina Alcides. As mineralizações ocorrem na intersecção dos planos de falhas. Uma descrição detalhada dessas minas e ocorrências é apresentada nos trabalhos de Reischl (1978) e em Lopes (2013). A geoquímica de solo mostra as anomalias de cobre (Reischl, 1978) e evidencia o padrão alinhado das mineralizações (Fig. 23).

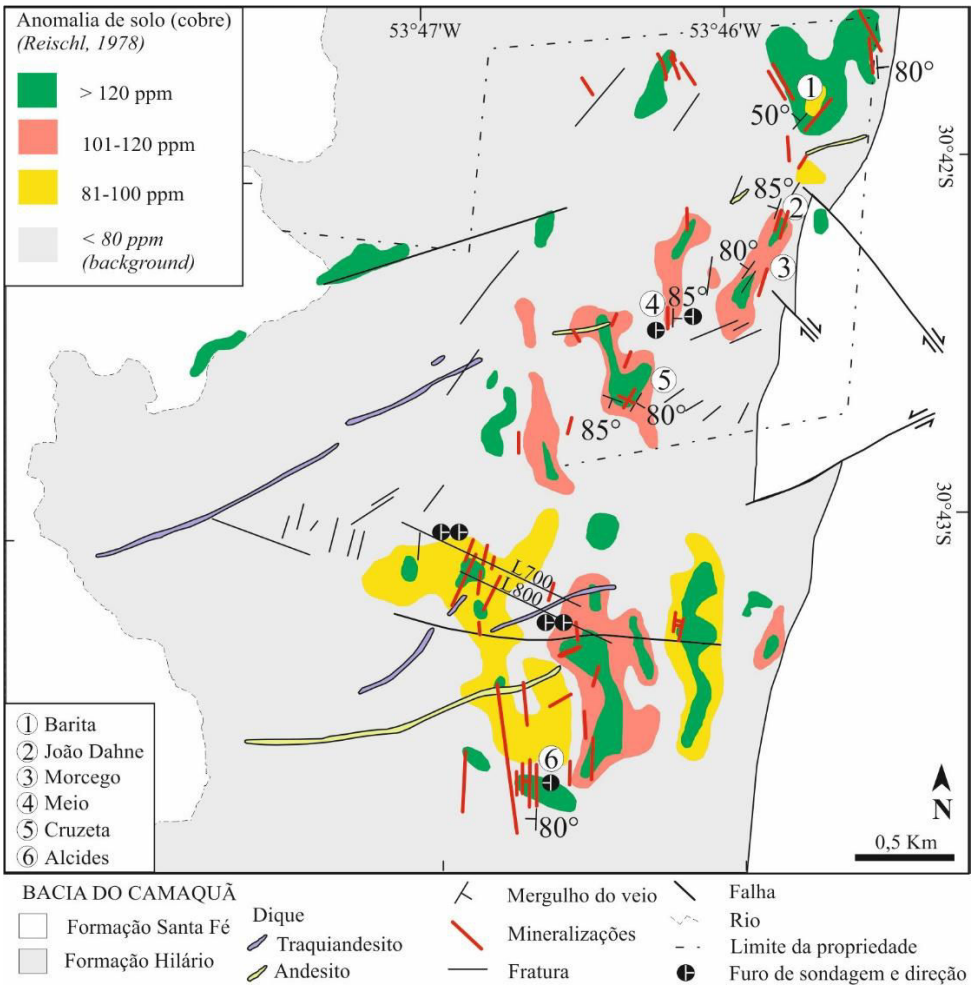

Figura 23. Geoquímica de solo com anomalias de cobre, localização das minas inativas e furos de sondagem (mod. de Reischl, 1978).

A Figura 24 ilustra três perfis litológicos do mapa geológico simplificado da Figura 12.

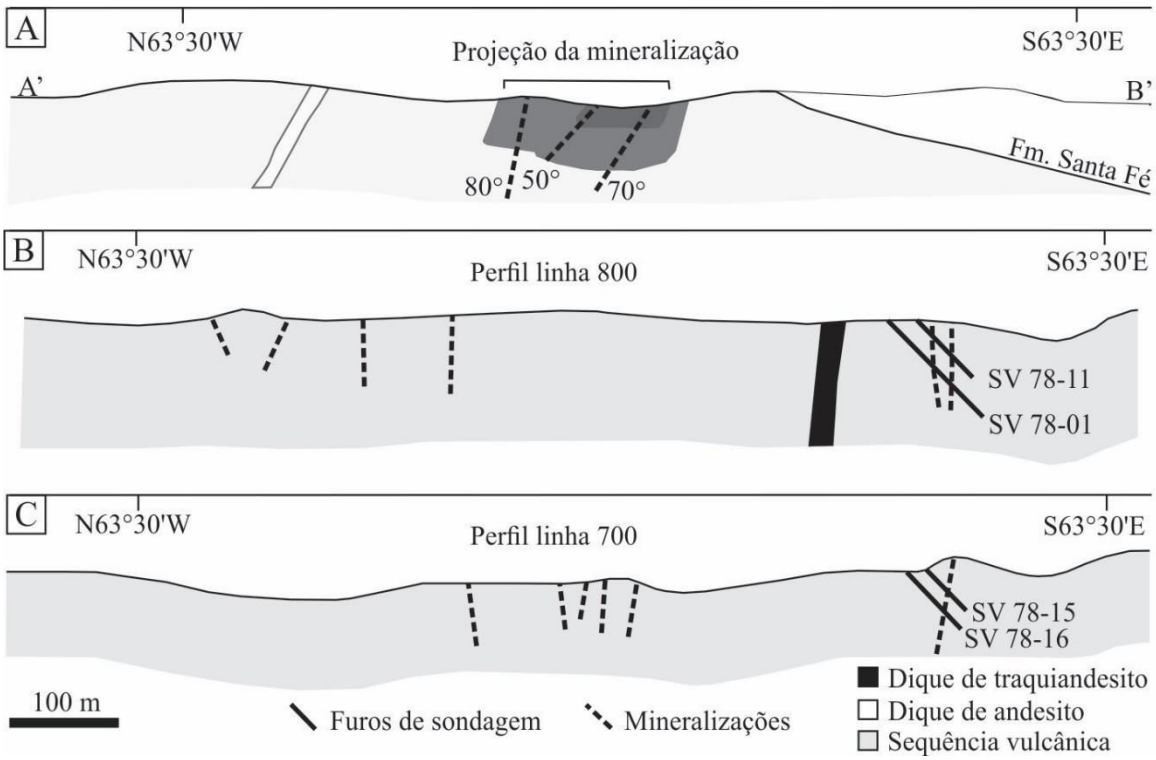

Figura 24. Perfil A-B da figura 20 ilustrando a projeção da mineralização na Mina João Dahne (mod. de Reischl, 1978).

A Tabela 4 apresenta uma compilação descritiva de cada uma das seis minas que compreende o depósito da Mina do Seival com tonelagem e teores de Cu e Ag para as minas desativadas.

Tabela 4. Descrição simplificada das mineralizações na Mina do Seival com principais características, tonelagem (*= inferido) e teores de Cu e Ag (Reischl, 1978). Ton. = tonelagem.

Mina	Rocha	Contexto	Ton.	Teores	Características
Barita	Lapili tufo / aglomerado vulcânico	Mina desativada com trincheira inundadas com fácil acesso a extremidades e topo. Difícil acesso ao filão principal. A 200 m em sentido norte existem várias escavações. Pilhas de rejeito.	64.000	1,71% Cu e 70 ppm Ag	Falha de direção 40° NE (100 m de extensão) e filão imbricado em várias direções a partir desta principal. Filão de 2 m de espessura com "pockets" de cores avermelhado e amarelado. Muitos veios de barita com direção N-S.
João Dahne	Lapili tufo / lava andesítica de fluxo	Mina desativada com 3 trincheiras. A mais ao norte tem difícil acesso e muita vegetação. A mais ao sul está inundada e com acesso muito difícil. A cava ao centro é de fácil acesso e com menor dimensão. Pilhas de rejeito.	20.000*	-	3 trincheiras/cavas principais com minério disseminado. Contato entre piroclástica e lava andesítica porfirítica de fluxo. As dimensões da cava variam de 20 a 40 m.
Morcego	Lava andesítica de fluxo	Filão e pequena galeria de 4x4 m. Acesso pela mata ciliar.	15.000	2,5% Cu	Filão de 2 m com mergulho subvertical e minério disseminado. Cava com 10 m de extensão.
Meio	Lapili tufo	Trincheira não inundada com 60 m de extensão e poço. Fácil acesso.	18.000	0,6% Cu e 15 ppm Ag	Trincheira de 2 m de espessura de direção N-S com "pockets" de cores avermelhado e amarelado e minério disseminado.
Cruzeta	Lava andesítica de fluxo	Acesso difícil pela pilha de rejeito até o interior da cava/trincheira. 2 filões sendo o de direção NW inundado.	15.000*	-	Minério disseminado ao longo dos planos de falha/fratura com 30 m de extensão.
Alcides	Lapili tufo	Fácil acesso as cavas e pilhas de rejeito. 3 cavas principais parcialmente inundadas.	70.000	0,83% Cu e 16 ppm Ag	7 falhas/fraturas com direção 30 m de extensão com minério disseminado.

A Figura 25 ilustra as mineralizações em planta. As localizações das mineralizações podem ser encontradas nas seguintes coordenadas geográficas: 1) Mina da Barita (30°41’52” S e 53°46’25” W); 2) Mina João Dahne (30°42’10” S e 53°46’20” W); 3) Mina do Morcego (30°42’24” S e 53°46’27” W); 4) Mina do Meio (30°42’26” S e 53°46’43” W); 5) Mina Cruzeta (30°42’41” S e 53°46’51” W); 6) Mina Alcides (30°43’45” S e 53°47’08” W).

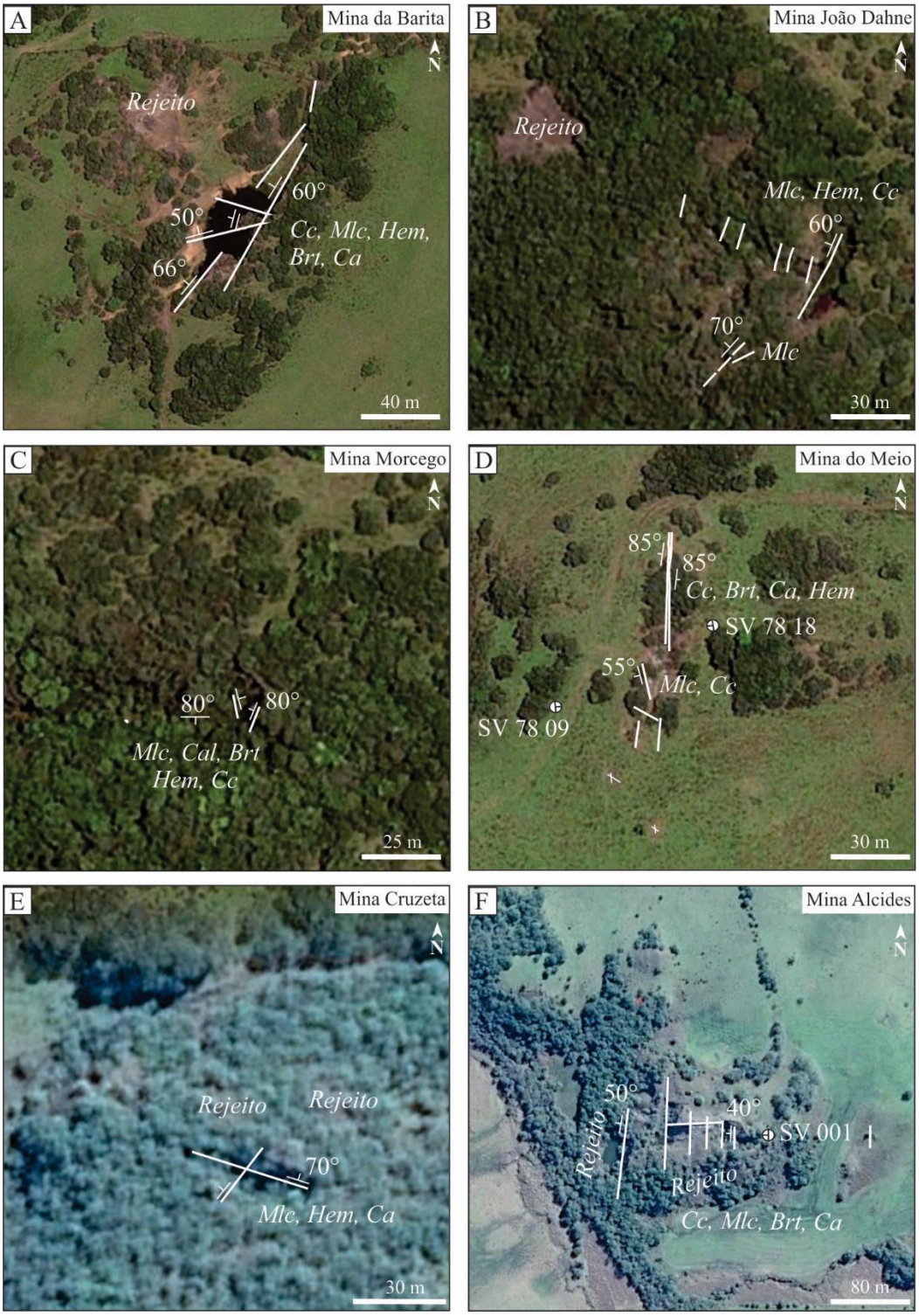

Figura 25. Imagens de satélite com detalhamento em planta das mineralizações (linhas brancas). A) Mina da Barita; B) Mina João Dahne; C) Mina do Morcego; D) Mina do Meio; E) Mina Cruzeta; F) Mina Alcides. Chaves: Cc = calcocita, Mlc = malaquita, Hem = hematita, Brt = barita, Ca = calcita. Figuras B, C e D mod. de Reischl (1978). Fonte: *Google Earth*.

A Figura 26 é modificada de Reischl (1978) e ilustra seis furos de sondagem plotados na Figura 12 com identificação prévia dos contatos litológicos, localização das amostras no ANEXO D e teores de Cu e Ag.

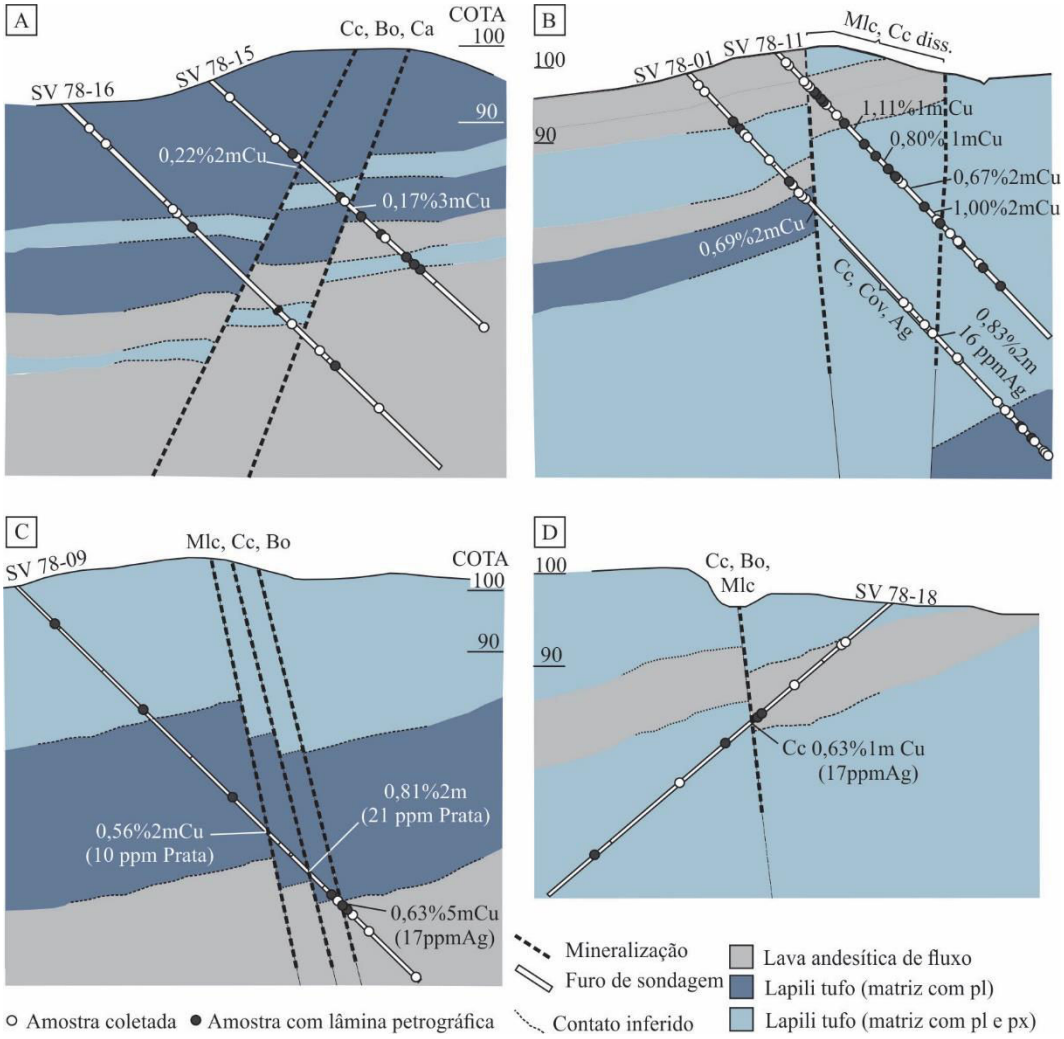

Figura 26. Perfil litológico e de amostragem de 6 furos de sondagem da Mina do Seival (mod. de Reischl, 1978). A) Linha 700: furos SV 78-16 e SV 78-15; B) Linha 800: furos SV 78-01 e SV 78-11; C) Mina do Meio: SV 78-09; D) Mina do Meio: SV 78-18. Chaves: Cc = calcocita; Cov = covelita; Bo = bornita; Ca = calcita; Mlc = malaquita; Pl = plagioclásio; Px = Piroxênio.

4. MANUSCRITOS

4.1 Manuscrito I

O manuscrito I foi submetido ao *Journal of South American Earth Sciences* em 02/01/2018. Após uma primeira revisão o manuscrito foi resubmetido em 07/05/2018. Uma nova revisão foi solicitada e o manuscrito foi resubmetido em 01/08/2018. Uma última revisão foi solicitada e o manuscrito foi aceito para publicação em 21/08/2018, e publicado online em 29/08/2018. A versão publicada online foi inserida na presente tese. A tabela suplementar com os dados estruturais é apresentada no ANEXO E.

Journal of South American Earth Sciences 88 (2018) 197–215

Contents lists available at ScienceDirect

Journal of South American Earth Sciences

journal homepage: www.elsevier.com/locate/jsames

Au–Cu–Ag mineralization controlled by brittle structures in Lavras do Sul Mining District and Seival Mine deposits, Camaquã Basin, southern Brazil

R.W. Lopes[a,b,*], A.S. Mexias[a], R.P. Philipp[a], E.M. Bongiolo[c], C. Renac[b], M.M. Bicca[a], E. Fontana[d]

[a] Universidade Federal do Rio Grande do Sul, Instituto de Geociências, Avenida Bento Gonçalves, 9500, 91501–970, Porto Alegre, RS, Brazil
[b] Université Côte d'Azur, CNRS, OCA, IRD, Géoazur, 250 rue Albert Einstein, Sophia Antipolis, 06560, Valbonne, France
[c] Instituto de Geociências, Universidade Federal do Rio de Janeiro (UFRJ), Av. Athos da Silveira Ramos, 274, Cidade Universitária, Ilha do Fundão, CEP 21941–916, Rio de Janeiro, Brazil
[d] UFVJM – Universidade Federal dos Vales do Jequitinhonha e Mucuri, Centro de Geociências, Instituto de Ciência e Tecnologia, Rodovia MGT 367 – Km 583, no 5000 – Alto da Jacuba, Diamantina, MG, Brazil

Au–Cu–Ag mineralization controlled by brittle structures in Lavras do Sul Mining District and Seival Mine deposits, Camaquã Basin, southern Brazil

R.W. Lopes [a,b,*], A.S. Mexias [a], R.P. Philipp [a], E.M. Bongiolo [c], C. Renac [b], M.M. Bicca [a], E. Fontana [d]

[a] Universidade Federal do Rio Grande do Sul, Instituto de Geociências, Avenida Bento Gonçalves, 9500, 91501–970 Porto Alegre, RS, Brazil
[b] Université Côte d'Azur, CNRS, OCA, IRD, Géoazur, 250 rue Albert Einstein, Sophia Antipolis 06560, Valbonne, France
[c] Instituto de Geociências, Universidade Federal do Rio de Janeiro (UFRJ). Av. Athos da Silveira Ramos, 274, Cidade Universitária, Ilha do Fundão, CEP 21941–916, Rio de Janeiro, Brazil
[d] UFVJM – Universidade Federal dos Vales do Jequitinhonha e Mucuri, Centro de Geociências, Instituto de Ciência e Tecnologia, Rodovia MGT 367 – Km 583, nº 5000 – Alto da Jacuba, Diamantina, MG, Brazil
* Corresponding author.

E–mail address: rodrigo.winck@ufrgs.br (R.W. Lopes), andre.mexias@ufrgs.br (A.S. Mexias), ruy.philipp@ufrgs.br (R.P. Philipp), ebongiolo@geologia.ufrj.br (E.M. Bongiolo), christophe.renac@unice.fr (C. Renac), marcos.mb83@gmail.com (M.M. Bicca), eduardo.fontana@ict.ufvjm.edu.br (E. Fontana)

Abstract

The mineralization of the Lavras do Sul Mining District and Seival Mine are controlled by brittle structures associated with the emplacement of the volcanogenic rocks and granitoids located in Lavras do Sul region, southernmost Brazil. This magmatism is associated with the evolution of the Camaquã Basin, an Ediacaran basin generated during the post–collisional stage of development of the Dom Feliciano Belt. The regional tectonic process has led to the activation of a large–scale high–angle shear zones and intense fracturing in the brittle to brittle–ductile regime. The relative chronology of structures and stress–field variations were recognized through remote sensing and structural data. The ore–deposits are controlled by extensional fractures and normal fault systems with a N70°W/70–85°NE direction in Lavras do Sul and a N40–60°E/70–88°NW direction in Seival and are disseminated or occur associated with quartz and calcite veins, respectively. We made a comparison of structures going from regional scale to smaller mineralized areas. The structural analysis of remote sensing and geophysical images (aeromagnetometry and aerogamma–spectrometry) integrated with structural data allowed us to reconstruct the paleostress tensor that generated the main fault systems and associated fractures of the host rock, which enabled the hydrothermal fluid circulation and the ore deposition. The integration of structural data such as fault slip planes, slickenlines, shear fractures systems, extensional fractures and kinematic indicators with the stratigraphic data allowed us to reconstruct the main directions of the tectonic efforts associated with the emplacement of the mineralizing magmas. The mineralization is

associated with the sinistral N70°W/80–88°NE oriented Palma–Jacques Fault in the Lavras do Sul Mining District as well as the sinistral N50°E/80–88°SE oriented Cabritos–Perau Fault and the sinistral N20°E/80–88°SW oriented Segredo Fault in Seival Mine region. Their maximum compressional stresses are subhorizontal and NW–SE oriented, while a late subhorizontal and NE–SW oriented compressional stress affected only the rocks of the Seival Mine. These two main compressive stresses are associated with the development of a transcurrent (escape) tectonics during the final evolution of the Dom Feliciano Belt, constrained by U–Pb zircon geochronology between 600–580 Ma. Transcurrent and normal NE–SW oriented faults are more expressive in volcanogenic rocks of the Seival Mine area, while extensional vein–type NW–SE oriented fractures are the most important structures in the Lavras do Sul area. We suggested that N70°W/70–88°NE oriented monzonitic dikes in Lavras do Sul and N50°E/70–88°NW oriented andesitic to trachyandesitic dikes in Seival area are probably the source of the mineralization.
Keywords: Dom Feliciano Belt, Camaquã Basin, structural geology, ore deposits, Neoproterozoic.

1. Introduction

Structurally controlled mineralization is well documented in Au–Cu–Ag deposits of orogenic belts. These deposits tend to be formed by reactivation of shear zones, allowing the development of intense fracturing, leading to fluid percolation and ore deposits. This sort of mineralizations is characteristic of porphyry–epithermal models (Seedorff et al., 2005; Sillitoe, 2010), as occurs in Potrerill Cu–Mo porphyry deposits and El Hueso Au epithermal deposits (Sillitoe, 1991), Nevada porphyry (Carten, 1986; Barton and Johnson, 2000), and as well as in iron oxide copper–gold deposits (IOCG, Dilles and Einaudi, 1992; Sillitoe, 2003; Mark et al., 2006).

In the Sul–rio–grandense Shield, the ore deposits are associated with development of NE–SW and NW–SE oriented shear zones that cross cut the Camaquã Basin and associated granitoid rocks of Late Neoproterozoic age. Along these faults, a series of Au, Cu, Ag, Pb and Zn–rich ores occur within volcanogenic and granitoid rocks associated with the Camaquã Basin, a post–collisional basin related to the final evolution of the Neoproterozoic Dom Feliciano Belt (Paim et al., 2000 and 2014; Remus et al., 2000; Laux et al., 2005; Bongiolo et al., 2011; Renac et al., 2014). The Camaquã Basin presents NE–SW elongated structure bounded by steeply dipping brittle faults and filled with immature terrigenous sedimentary successions with volcanic and volcanoclastic intercalations. The basin is aligned

parallel to the major structures of the underlying Dom Feliciano Belt, which was formed during the main collisional event of the Brasiliano–Pan African Orogeny in the region. The Camaquã Basin comprises more than 10.000 meters of sedimentary and volcanogenic successions that record the paleogeographic evolution of the region between ca. 610 Ma and 530 Ma. This basin is ideal for paleostress analysis since they are affected by very low–grade metamorphism and low rates of brittle–ductile deformation. In addition it is possible to recognize the depositional paleoenvironments and stratigraphic elements to obtain the age of the volcanic units through the geochronological analysis and to delimit the distinct subsidence events through the recognition of nonconformities (Almeida et al., 2012b; Philipp et al., 2016a). The integration of this set of information allows to determe an absolute chronology for the tectonic events occurred during the evolution of the basin.

We present structural data on brittle faults as fault slip planes, slickenlines striations and fractures systems of sedimentary and volcanic rocks of Bom Jardim Group of the Camaquã Basin, as well as some younger units, in order to establish the chronology of the deformational events and the relationships with the Cu–Pb–Au mineralization, and to distinguish the directions of paleostress axes related to basin formation from those that were responsible for its later deformation.

This paper analyzes the relationships between the main regional structures and the structural features observed in mineralized areas using remote sensing structural data, including measurements of faults, lineations and fractures from non–mineralized and mineralized areas. When possible, we determined the stress orientation at the time of mineralization by kinematic indicators associated with dextral and sinistral transcurrent or normal faults. The interpretation of tectonic structures allowed the reconstruction of a relative chronology and paleostress field associated with ore deposition.

2. Geological setting

2.1 Regional geology and tectonic structures

The Mantiqueira Province is a NE–SW mobile belt running parallel to the southern and eastern coast of Brazil extending for more than 3,000 km from Bahia State (NE of Brazil) to Uruguay. The Mantiqueira orogenic system is of one of the main Neoproterozoic orogens formed during the assembly of West Gondwana. It comprises the Dom Feliciano (Uruguay and southern Brazil), Ribeira (Paraná, São Paulo, Minas Gerais and Rio de Janeiro states) and Araçuaí belts (Espírito Santo, eastern Minas Gerais and southern Bahia states; e.g., Heilbron and Machado, 2003). Its African counterpart includes the Saldania–Gariep, Damara, Kaoko and West Congo belts. Several models have been presented to explain the tectonic evolution of this orogen and its role in the assembly of West Gondwana (e.g., Cordani et al., 2003; Basei et al., 2008). The southern portion of the Mantiqueira Province represents a zone of collision between the Rio de La Plata (Brazil) and the Kalahari (Africa) cratons (Almeida and Hasui, 1984; Silva et al., 2005). The southern Brazilian and Uruguay shields are subdivided in two geotectonic units: the Rio de La Plata Craton and Dom Feliciano Belt (Fig. 1) (Chemale Jr., 2000; Hartmann et al., 2007; Philipp et al., 2016a). In southern Brazil, the Rio de La Plata Craton is represented by the Taquarembó Terrane, composed by Paleoproterozoic (2.45 to 1.8 Ga) ortho– and paragneisses of amphibolite to granulite facies (Chemale Jr., 2000; Philipp et al., 2016a). The Dom Feliciano Belt is constituted by the São Gabriel Terrane, the Tijucas Terrane and the Pelotas Batholith, units composed by petrotectonic associations generated between Tonian and Ediacaran periods (930–540 Ma). The evolution of the Dom Feliciano Belt units is related to Brasiliano Orogenic Cycle and involves three main orogenic episodes denominated Passinho (890–850 Ma), São Gabriel (770–680 Ma) and Dom Feliciano (650–540 Ma) (Saalmann et al., 2006 and 2010; Philipp et al., 2016a; Hueck et al., 2018).

The São Gabriel Terrane take place in the northwest portion of the Dom Feliciano Belt and is represented by ophiolitic complexes (Leite et al., 1998; Chemale Jr., 2000) and arc–related rocks, including ortho– and paragneisses, low–grade metavolcano–sedimentary associations and late–orogenic granitic to dioritic magmatism, covered by late–orogenic basin (930–680 Ma) (Remus et al., 1999;

Saalmann et al., 2006; Hartmann et al., 2011; Lena et al., 2014; Gubert et al., 2016; Vedana et al., 2017). In this terrane, the development of rocks association was related to the closure of the Charrua Ocean through the formation of two magmatic arcs accretionary systems generated during Passinho (890–850 Ma) and São Gabriel (770–680 Ma) orogenies (Saalmann et al., 2010; Philipp et al., 2016a and 2018).

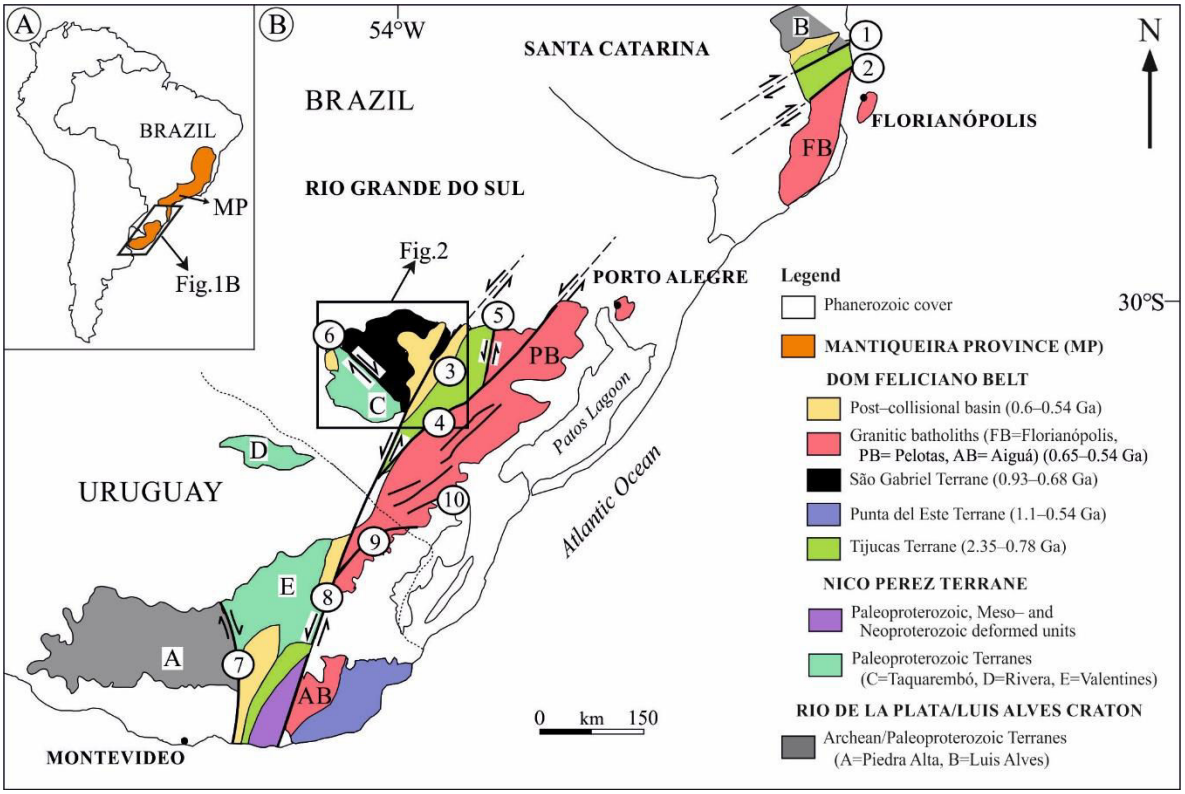

Figure 1. A) Southern part of the Mantiqueira Province localization in South America. B) Geotectonic units of the southern Brazilian and Uruguay shields and localization of the studied area (from Hartmann et al., 2007; Oyhantçabal et al., 2011; Philipp et al., 2016a). Shear zones: 1= Itajaí–Perimbó; 2= Major Gercino; 3= Santana da Boa Vista; 4= Dorsal do Canguçu; 5= Passo do Marinheiro; 6= Ibaré; 7= Sarandi Del Yí; 8= Sierra Ballena; 9= Cerro Amaro; 10= Arroio Grande.

The Sul–rio–grandense Shield shows three major regional–scale lineaments: (i) The Ibaré Shear Zone (Luzardo and Fernandes, 1990; Philipp et al., 2016a) with NW–SE (N40–50°W) direction, defining the contact between Taquarembó and São Gabriel terranes, (ii) the Caçapava do Sul Shear Zone (Costa, 1997) with NE–SW (N20°E) direction, separating São Gabriel and Tijucas terranes, and (iii) the Dorsal

do Canguçu Shear Zone (Mesquita and Fernandes, 1990; Fernandes et al., 1992; Philipp et al., 1993) with NE–SW (N40–50°E) direction, delimiting the Tijucas Terrane and the Pelotas Batholith.

The Ediacaran to Cambrian basins of the southeastern portion of the Mantiqueira Province, like Itajaí (SC), Camaquã (RS), Barriga Negra, Piriápolis, San Carlos and Cerros de Aguirre (Uruguay), were formed over Paleoproterozoic rocks of the Rio de La Plata Craton and over the Neoproterozoic units of the Dom Feliciano Belt (Almeida et al., 2012b). These basement units were affected by Brasiliano orogenic deformation associated with collisional metamorphism, dated by the U–Pb zircon method (SHRIMP and LA–ICPMS) between 650 to 620 Ma, and with the post–collisional metamorphism associated to transcurrent shear zones between 600 to 560 Ma (Leite et al., 1998; Saalmann et al., 2010; Chemale Jr. et al., 2011; Camozatto et al., 2013a,b; Philipp et al., 2016a,b).

The Camaquã Basin is the largest and best known of the post–collisional strike slip basins of the south portion of Mantiqueira Province, with an area of 3.000 km^2 divided into four sub–basins. The geology and stratigraphy of the Camaquã Basin was investigated by many authors, and the evolution of its units was recognized and related to the events of subsidence and deformation during the post–collisional stage of Dom Feliciano orogenesis (ca. 620 to 530 Ma), characterizing the final evolution of the SW Gondwana supercontinent (Chemale Jr., 2000; Hartmann et al., 2007; Saalmann et al., 2010; Philipp et al., 2016a). Detailed stratigraphic descriptions and available geochronological data from volcanogenic units of the basin can be found in Lima and Nardi (1998), Paim et al. (2000), Wildner et al. (2002), Janikian et al. (2003, 2005 and 2012), Fambrini et al. (2005 and 2007), Borba et al. (2006 and 2008), Paim and Scherer (2007) and Almeida et al. (2009, 2010 and 2012b).

The Camaquã Basin is composed of four sedimentary successions accompanied by three volcanic associations deposited between ~600 to 530 Ma ago in different depocenters and resulted from the activation of distinct syn–depositional faults. The lithostratigraphic units of the basin base belong to Maricá Group (630–601 Ma), composed by the intercalation of fluvial and pebbly sandstones, marine fine–grained

sandstones and siltstones. The Bom Jardim Group (600–590 Ma) occurs above and is constituted by deep to shallow lacustrine sandstone, conglomerate, rhythmite and mudstone with expressive occurrence of intermediate to basic volcanic and pyroclastic rocks. These units are covered by the acid volcanic and volcanoclastic rocks of the Acampamento Velho Formation (574–550 Ma) and by the alluvial sandstone, conglomerate and rhythmites of the Santa Bárbara Group. The basin top is composed of the alluvial sandstone and conglomerate, aeolian sandstone and mudstones of the Guaritas Group (540–530 Ma). Basic and intermediate subvolcanic rocks of the Rodeio Velho Suite cut across the other units of the Guaritas Group, frequently occurring as shallow intrusive sills (Almeida et al., 2012a). The studied area is located in the south portion of the São Gabriel Terrane, on the western rim of the Camaquã Basin, in a major structure of NE–SW direction denominated Santa Bárbara Rift (Fig. 2) (Robertson, 1966).

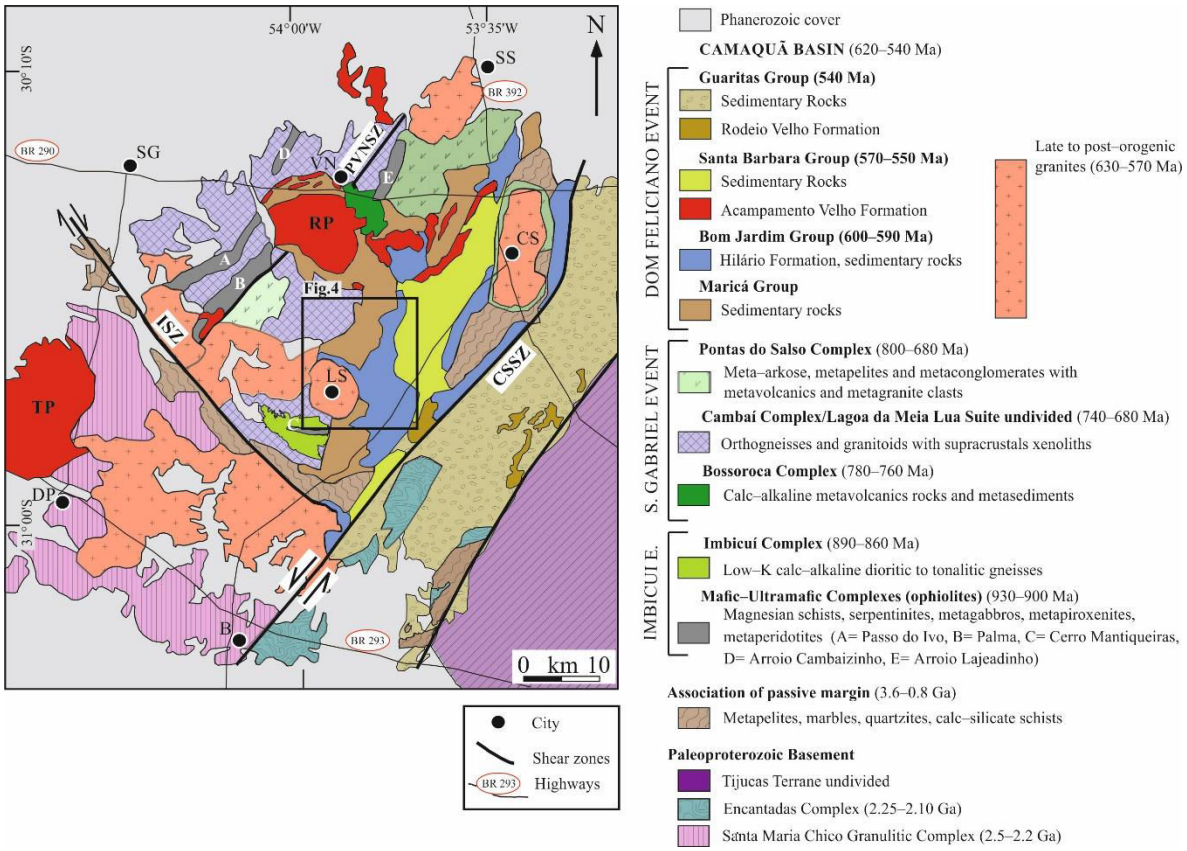

Figure 2. Geological map of the São Gabriel Terrane. Cities: SS= São Sepé; CS= Caçapava do Sul; VN= Vila Nova do Sul; LS= Lavras do Sul; DP= Dom Pedrito; B=

Bagé. Shear zones: PVNSZ= Passinho/Vila Nova; ISZ= Shear Zone Ibaré; CSSZ= Shear Zone Caçapava do Sul (from Philipp et al., 2016a).

Paim et al. (2000) divided the sedimentary succession of the basin into five units separated by unconformities. The Maricá Allogroup was interpreted as a foreland succession, while Bom Jardim Allogroup was described as a transpressional strike–slip basin succession presenting inverse faults and folds. The Cerro do Bugio and Santa Bárbara allogroups were characterized as two successions formed during transtensional events. Finally, the Guaritas Allogroup was featured by a transtensional subsidence event that filled a half–graben generated by the reactivation of NE–SW oriented regional fault systems.

The tectonic setting of the Ediacaran to Cambrian basins is controversial, and a series of different models have been proposed. The currently accepted conceptions can be grouped into three main types: (i) syn–orogenic settings, mainly of peripheral foreland basins (e.g., Fragoso–Cesar, 1991; Gresse et al., 1996; Paim et al., 2000), (ii) post–collisional settings, with strike–slip or pull–apart basins (e.g., Oliveira and Fernandes, 1991 and 1992; Machado and Sayeg, 1992; Paim et al., 2000) and (iii) anorogenic settings, with extensional origin (Fragoso–Cesar et al., 2000 and 2001; Almeida et al., 2012b; Janikian et al., 2012). The existence of different models is the result of the increment of the studies on the structural and tectonic record preserved within the basins and of the recent U–Pb geochronology zircon data. Most of the hypotheses are based on models generated from the tectonic significance of the metamorphic and granitic rocks of the basement of the basin. Indeed, very few papers with paleostress tensor data and kinematic analysis of the Camaquã Basin have been published (Almeida et al., 2012b).

Despite the importance of the Camaquã Basin to elucidate some important issues, such as the mineralization episodes and the origin of the basin, or to evaluate the tectonic conditions of the final stage of the Brasiliano Orogenic Cycle, very few studies have focused on structural analysis. As highlighted by Almeida et al. (2012b), the majority of the published tectonic interpretations are based on hypotheses of the supposed role of the Camaquã Basin in regional tectonic models.

2.2 Camaquã Basin structures

The distribution of the Camaquã Basin fill is delimited by NE–SW oriented elongated depressions, separated by the basement highs, represented by the Santana da Boa Vista and Vigia domes, Capané Antiform, Caçapava do Sul and Lavras do Sul highlands. The alternation between domes and elongated basins (pull–apart type) associated with transcurrent and oblique high–angle shear zones have been interpreted as the result of compressive deformational processes, which dominated the final evolution of the Dom Feliciano Belt (Chemale Jr., 2000; Silva et al., 2005; Saalmann et al., 2010; Philipp et al., 2016a). These processes are associated with the collision between the Rio de La Plata and Kalahari cratons during the construction of the SW portion of the Gondwana paleocontinent (Saalmann et al., 2010; Philipp et al., 2016a; Hueck et al., 2018). The evolution of this collisional system originated the processes of tectonic escape that distributed the deformation through the alternation between bands with transpressional (domes) and transtensional regimes (elongated basins) (Fernandes et al. 1992; Philipp et al., 2016a). These basement highs are limited by steeply dipping NE–SW oriented fault zones, referred as Irapuá Fault System by Ribeiro et al. (1966). The same authors also highlighted the occurrence of steeply dipping NW–SE oriented fault zones, denominated Cerro da Vigia Fault System.

Based on stratigraphic analysis of individual sedimentary and volcanic groups of the Camaquã Basin, recent researchers (Fragoso–Cesar et al., 2000, Paim et al., 2000, Janikian et al., 2003 and 2005; Fambrini et al., 2005 and 2007; Borba et al., 2006; Lima et al., 2007; Almeida et al., 2010 and 2012b) demonstrated the influence of the syn–sedimentary faults at the border of Camaquã Basin and its importance to the facies architecture evolution. Most researchers highlighted the occurrence of large transcurrent faults within the boundaries of each major depositional cycle. The facies architecture of most stratigraphic groups indicated deposition in alluvial–fan and braided fluvial systems running toward the center of the basin. These

characteristics suggested that the kinematics of failure were associated with simultaneous transcurrent and extension movements.

The occurrence of volcanic successions in Bom Jardim, Santa Bárbara and Guaritas groups of the Camaquã Basin and associated granites, indicate a relationship between the high thermal gradient of the crust and the main transcurrent fault systems. The isotope and geochemical composition of the volcanic associations suggests magmatism related to the mantle upwelling, occurred during around of 50 Ma (Lima and Nardi, 1998; Wildner et al., 2002; Sommer et al., 2006; Lima et al., 2007). The importance of extensional and strike–slip kinematic is described during the post–collisional stage of the Dom Feliciano Orogeny associated to the latest escape movements of the main shear zones that affected the Dom Feliciano Belt and generated the Camaquã Basin (Fernandes et al., 1992; Chemale Jr., 2000; Paim et al., 2000 and 2014; Philipp et al., 2016a).

2.3 Geology of the Lavras do Sul Mining District and Seival Mine

The rocks of the Lavras do Sul Mining District and Seival Mine area are limited by the Caçapava do Sul and Ibaré shear zones and Cabritos–Perau, Segredo and Palma–Jacques as subsidiary faults (Fig. 3). The basement rocks occur west and south of the mineralized areas and are represented by tectonic interleave of mafic to ultramafic rocks of the Cerro Mantiqueira Ophiolite, tonalitic to dioritic gneisses of the Imbicuí Complex (890–850 Ma) (Philipp et al., 2016a), tonalitic to dioritic and metagranites of the Cambaí Complex (740–700 Ma) (Leite et al., 1998; Hartmann et al., 2011) and by the low–grade metavolcano–sedimentary rocks of the Marmeleiro Complex. These petrotectonic units constitute E–W oriented belts interpreted as arc–related associations generated during the Passinho and São Gabriel orogenies (890–850 and 760–680 Ma) (Chemale Jr., 2000; Hartmann et al., 2007; Saalmann et al., 2010; Philipp et al., 2018). These units recorded an orogenic metamorphism generated under low– to medium–grade and low–pressure conditions. The contacts between the units of the São Gabriel Terrane are tectonic and are related to the processes of deformation and collisional metamorphism generated during the final

evolution of this terrane. These relationships are associated with a main regional compression with sigma 1 positioned in the NW–SE direction (Chemale Jr., 2000; Saalmann et al., 2010; Philipp et al. 2018).

The Camaquã Basin is represented by the sedimentary and volcanic rocks associated with the Maricá, Bom Jardim, Santa Bárbara and Guaritas groups. The Maricá Group is composed of an approximately 4000 m total thick sedimentary sequence with volcanic clast (Paim et al., 2000; Almeida et al., 2009 and 2010; Borba et al., 2008) and has been subdivided into three sedimentary packages (Borba et al., 2006).

In the Seival Mine, the Bom Jardim Group is represented by the effusive successions of Hilário Formation, including lapilli tuff, volcanic agglomerate, andesite lava flows and andesitic to trachyandesite dikes (Fig. 4) (Reischl, 1978; Lopes et al., 2014). The alteration minerals occur in halos related to fractures and faults with chlorite, chlorite/smectite mixed–layers and smectite associated with titanite and calcite (Fontana et al., 2017). On the east side of granitoids, the Hilário Formation is represented by tuff, lapilli tuff, volcanic agglomerate and andesite lava flows with chloritic alteration represented by chlorite, epidote and calcite in a temperature of ~300 °C and east bedding direction. The NE–SW to NW–SE oriented andesitic and lamprophyric dikes have subvertical disposition. The shoshonitic affinity of the rocks from Hilário Formation and Lavras do Sul Intrusive Complex form the Lavras do Sul Shoshonitic Association, defined by Lima and Nardi (1998).

Lavras do Sul Intrusive Complex is represented by plutonic granitic and shallow intrusions concentrated mainly in the northeastern margin (Nardi, 1984; Gastal et al., 2006; Bongiolo et al., 2011). The granitoids are represented by a ring structure composed by Lavras do Sul Granite, Arroio dos Jaques Monzonite and Tapera Granite (Gastal et al., 2006). Lavras do Sul Granite is represented by porphyritic quartz–monzonite, granodiorite and syenogranite to monzogranite rocks (Gastal et al., 2006; Liz et al., 2009b). The granite intrusion caused contact metamorphism in the older volcanogenic rocks of the Hilário Formation. The shallow intrusions are represented by monzonitic and lamprophyric dikes and small intrusions (Lima and

Nardi, 1998; Liz et al., 2009b) with mixing and mingling textures (Müller et al., 2012). The Au and Cu–Ag mineralizations are hosted in granitoids of Lavras do Sul Mining District and in Bom Jardim Group sedimentation of Seival Mine area (Fig. 4), respectively.

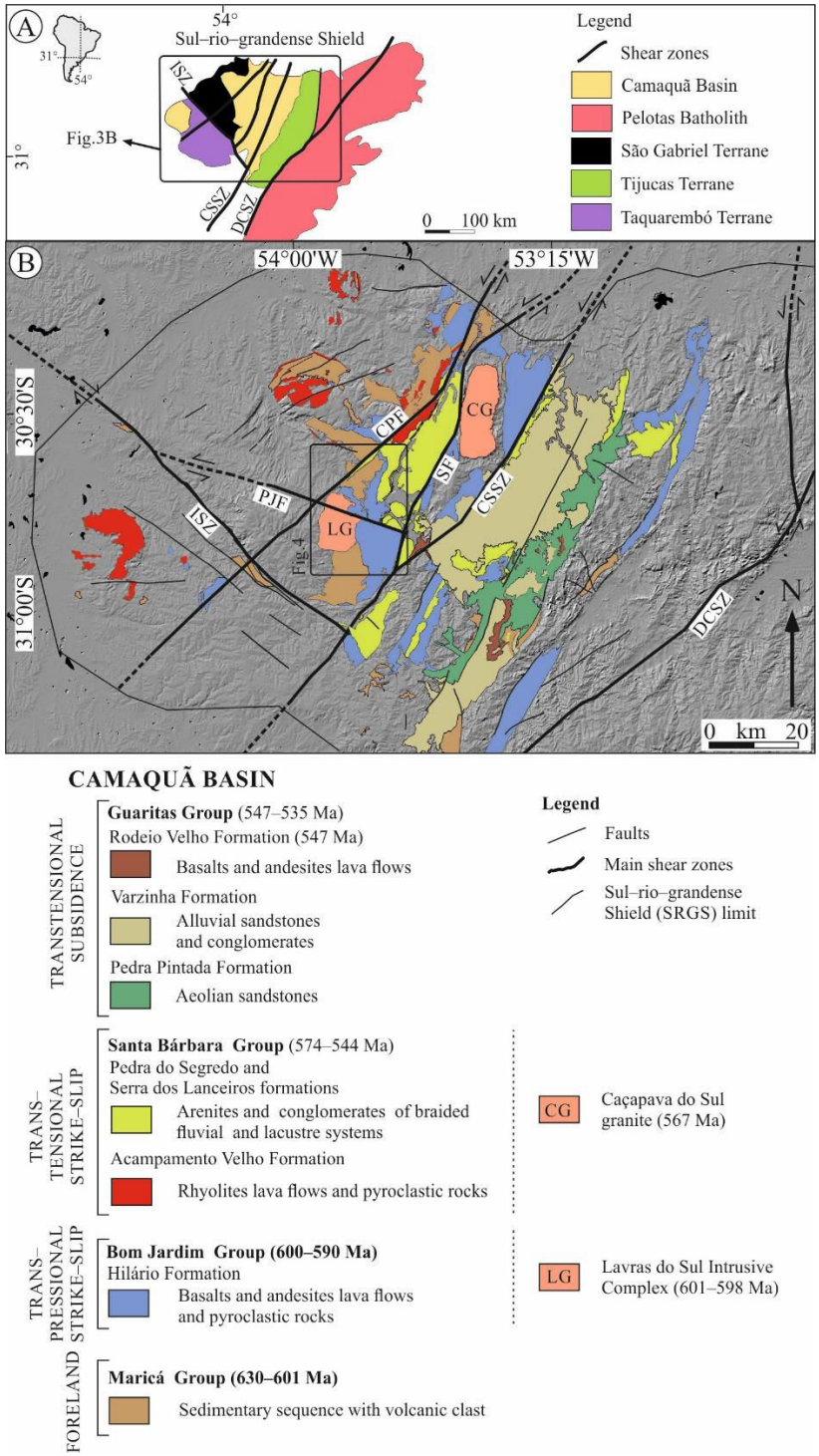

Figure 3. Geological map of the Camaquã Basin with the regional and local structures (modified from Wildner et al., 2003; Toniolo et al., 2007) in an ASTER digital image (elevation models; Toniolo et al., 2007). The black rectangle comprises the area of the geologic map showed in Figure 4. Shear zones: ISZ= Ibaré; CSSZ=

Caçapava do Sul; DCSZ= Dorsal do Canguçu. Faults: CPF= Cabritos–Perau; SF= Segredo; PJF= Palma–Jacques.

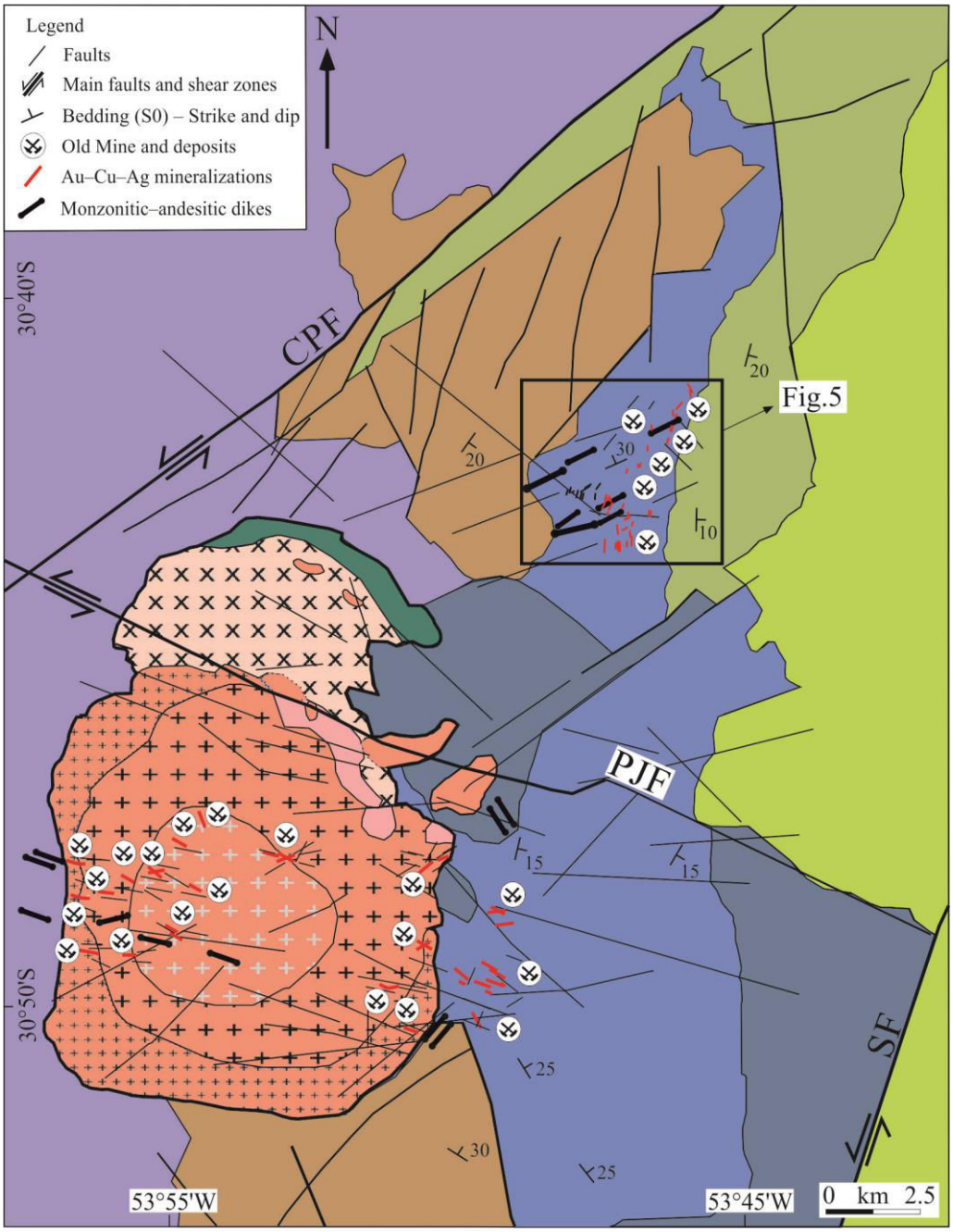

LAVRAS DO SUL INTRUSIVE COMPLEX (601–598 Ma)

Lavras do Sul Granite

- Pertite granite
- Quartz monzonite (587 Ma)
- Syeno–to monzogranite (598 Ma)
- Granodiorite (599 Ma)

Arroio dos Jacques Granite

- Monzodiorite (601–599 Ma)

Tapera Granite

- Monzonite to monzodiorite (601 Ma)
- Diorite

CAMAQUÃ BASIN (630–540 Ma)

Santa Bárbara Group (573–544 Ma)

Santa Fé Formation

- Arenite and conglomerate
- Andesite lava flows and conglomerate

Bom Jardim Group (600–590 Ma)

Hilário Formation

- Andesite lava flows
- Tuff, lapilli tuff and volcanic agglomerate

Maricá Group (630–601 Ma)

- Arenite and conglomerate

- Basement (930–680 Ma)

Figure 4. Geological map of the Lavras do Sul Mining District and Seival Mine (square) (modified from Reischl, 1978; Gastal and Lafon, 1998; Bongiolo, 2002; Toniolo et al., 2007). Shear zones: ISZ= Ibaré; CSSZ= Caçapava do Sul; DCSZ= Dorsal do Canguçu. Faults: CPF= Cabritos–Perau; SF= Segredo; PJF= Palma–Jacques.

2.4 Description of the copper–bearing bodies of the Lavras do Sul Mining District and Seival Mine

The Au–Cu prospects of the Lavras do Sul Mining District host nineteen inactive mines or deposits located in the granitoid rocks of Lavras do Sul Intrusive Complex and volcanogenic rocks of Hilário Formation (Fig. 4) (Mexias et al., 2007; Bongiolo et al., 2011). The multi–intrusive activity generated pervasive and vein–type fractures represented by ore–zones, quartz and sulfide–rich veins (Mexias et al., 1990a,b and 2005; Bongiolo et al., 2011). The alteration assemblages consist of clays, quartz and sulfides (Bongiolo et al., 2011). The estimated temperatures were determined by chlorite geothermometry and mineral characteristics, and the alteration assemblages were classified as: potassic (> 350 °C) with ± alkali feldspar, biotite, tourmaline, chalcopyrite and alunita; propylitic (250 to 350 °C) with ± alkali feldspar, biotite, tourmaline, chalcopyrite and alunita; phyllic (> 300 °C) with quartz, ± chlorite, ± phengite, ± illite, sulfide (pyrite>chalcopyrite) and ore (Au>Cu); intermediate argillic alterations (160 to 230 °C) with illite–smectite, carbonate, ± chlorite, hematite and ± corrensite (Bongiolo et al., 2008). The pyrite, chalcopyrite, arsenopyrite and Au are associated to propylitic–potassic alteration (Bongiolo et al., 2008 and 2011; Liz et al., 2009a) with assemblage of phengite, chlorite and illite/smectite mixed–layers (Mexias et al., 1990c; Bongiolo et al., 2008 and 2011). These mineralized structures formed a NW–SE direction trend parallel to Palma–Jacques Fault.

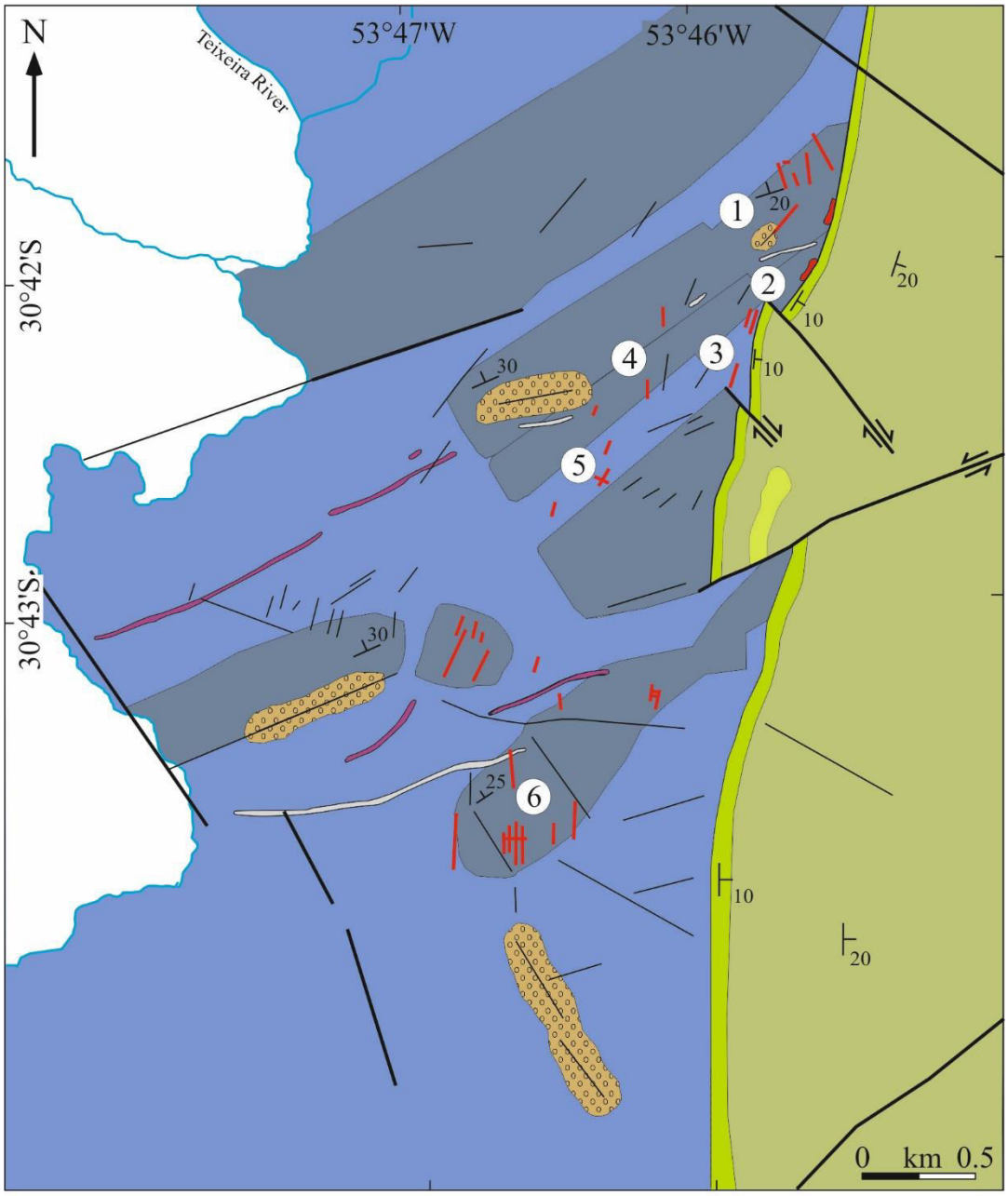

Figure 5. Seival Mine geological map. Sequence of lapilli tuff, volcanic agglomerate and andesite lava flows with andesitic to trachyandesitic dikes (NE direction) of the

Hilário Formation, polymictic conglomerate and vesicular andesite lava flows of the Santa Fé Formation and rhyolite dikes of the Acampamento Velho Formation (modified from Reischl, 1978; Lopes et al., 2014) with inactive open pit mines, faults and mineralization localization. Keys: 1= Barita; 2 = João Dahne; 3= Morcego; 4= Meio; 5= Cruzeta; 6= Alcides.

The Seival Mine area hosted six inactive Cu–bearing mines and several prospects ca. 0.20 Mt of mineralized rocks with an average grade of ~1.40 % Cu (Fig. 5) (Reischl, 1978; Lopes et al., 2014). Fractures and faults contain Cu–rich sulfides as chalcopyrite, bornite, chalcocite and covellite (Fontana et al., 2017). This Cu–enrichment is related to propylitic alteration with formation of albite (600 to 350 °C), Mg–chamosite to Fe–clinochlore (251 to 180 °C) and smectite (< 250 °C). The lower temperature of alteration are associated to an increasing proportion of meteoric water in the host rock with precipitation of barite, calcite and quartz (150 to 80 °C; Fontana et al., 2017). In preserved parts of these inactive mines, a stockwork of veins (Fig. 6A), volcanic agglomerate (Fig. 6B) and porosity of volcaniclastics rocks (Fig. 6C) host Cu–rich sulfides (Fontana et al., 2017). The open pit and prospects (ca. ~N–S to N40–60°E oriented) seem to form a trend of mineralized structures, fracture and dikes (Reischl, 1978). These alteration process can be related to these andesitic intrusions and local hydrothermal cells.

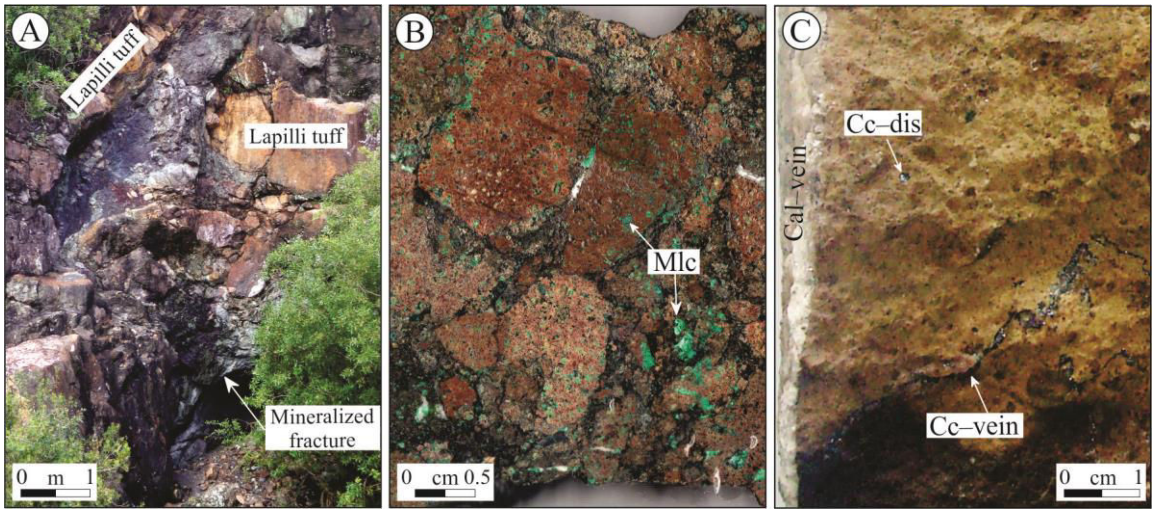

Figure 6. The different mineralogical assemblages associated with the mineralizations in the Seival Mine. A) Mineralized stockwork structure with subvertical and irregular form influenced by high permeability of lapilli tuff in Barita Mine; B) Malachite deposition in cavities and matrix of volcanic agglomerate in Barite

Mine; C) Hydrothermal vein sample in lapilli tuff with millimetric vein and disseminated chalcocite in a pocket of chlorite–chalcocite (light green) and chlorite–hematite (dark–red) cut by calcite vein in Meio Mine. Keys: Mlc= Malachite; Cc–vein= Chalcocite vein; Cc–dis= Disseminated chalcocite; Cal–vein= Calcite–vein.

3. Methods

In order to evaluate the structural framework of the granitic and volcano–sedimentary units of the Lavras do Sul Mining District and the Seival Mine area, data were collected on a regional scale and on an outcrop scale. Regional data were obtained from delineation of the lineaments in the satellite imagery. The lineaments were defined from negative and positive linear features, delimited only in their visible portion. Regional lineaments (n= 2114) were extracted through GIS tool on Hill shade ASTER (VNIR 15 meters; Toniolo et al., 2007) and TM Landsat (band #4) satellite images. Structures were recorded as (i) fractures or (ii) faults based on discontinuity surfaces or slickenlines, respectively, within 1:10.000 scale density, and the whole regional dataset was integrated with published data on the same area (Kaul, 1975 and 1976; Gastal et al., 2015). In this study, the longer lineaments were interpreted as deep and ancient crustal structures. We also used as indicators of relative chronology: (i) the cut–off relationships between the structures; (ii) the orientation of dikes; (iii) extensions and influences of structures on rocks adjacent to the studied region. The length distribution was divided into long (5 to 40 km) and short (0.1 to 4 km) lineaments and was described as main and secondary structures, respectively. The division of the regional structures was based on Picada (1971), with three main directions: NE–SW (0–30°), NNE–SSW (31–90°) and NW–SE (271–359°). These main and secondary structures may be associated with timing or competency of rocks.

For the reconstitution of the paleostress fields, more than 162 measurements were collected on faults with striations distributed in 12 outcrops of the volcanic and sedimentary successions of the Bom Jardim Group in the Camaquã Basin and of the granitoids in the Lavras do Sul Intrusive Complex. The successive tectonic events were classified using relative chronology criteria based on stratigraphic data from the Camaquã Basin and superimposition of slickenlines fibers and striations.

The stratigraphy of this basin was based on the available geochronological data (Almeida et al., 2012a; Janikian et al., 2012).

Structural measurements on faults and fractures were carried out in the field. We have also collected data along slickensides, including groove lineation and kinematic analysis (Supplementary Table). The Win–Tensor software (Delvaux and Sperner, 2003) was used to produce stereograms and to reconstruct paleostress directions of principal stress axes (Twiss and Moores, 1992; Angelier, 1994; Hatcher, 1995). The paleostress was determined by three main stress axes σ1, σ2 and σ3 (σ1 ≥ σ2 ≥ σ3), stress ratio R (R= [σ2-σ3]/[σ1-σ3]) and a stress regime index R' (see Delvaux and Sperner, 2003). In the Win–Tensor software, paleostress values were adjusted to optimize and refine the paleostress inversion results (for more details, see Delvaux and Sperner, 2003). A relative chronology of paleostress was then integrated into the geological maps of the Lavras do Sul Mining District and Seival Mine with available data from the mineralized locations (i.e., Reischl, 1978; Bongiolo et al., 2011). The interpretation of the paleostress tensor analyses of this paper were compared with the analysis of the structural data from other mineralized areas of the Camaquã Basin (e.g., Almeida et al., 2012b; Santos et al., 2012; Bicca et al., 2013). The macroscopic classification of fractures was used according to Twiss and Moores (1992).

4. Results

4.1 Regional structures

In a regional perspective, the topographic lineament directions are potential indicators of geologic structures. The measurements of the main fault systems and shear zones of the Sul–rio–grandense Shield show a strong predominance of NE–SW orientations (Fig. 7A). These patterns comprise valleys and crests. The main lineament patterns are mostly oriented along N31–90°E (~62 %; Fig. 8A), N0–30°E (~18 %; Fig. 8B) and N0–90°W (~18 %; Fig. 7A; Fig. 8C). The rose diagram of the lineament frequency distribution performed on an ASTER image, shows a bimodal distribution with longer (from 5 to 30 km) and moderate (< 5 km) lengths. The long

ones present N50°E and N70°W orientation located on the limit of the São Gabriel Terrane close to Lavras do Sul Mining District and Seival area. The shorter lineaments located within the studied areas show N40–60°E and N70°W directions, as well as subordinated ~N–S. They are dominantly N70°W (1–3 km) and N50°E (< 1 km) in Lavras do Sul Mining District and in Seival Mine, respectively. The ~N–S (~1 %) and ~E–W (5 %) patterns are shorter (< 2 km) and less pronounced in comparison to the NE–SW and NW–SE ones (Fig. 7B, C).

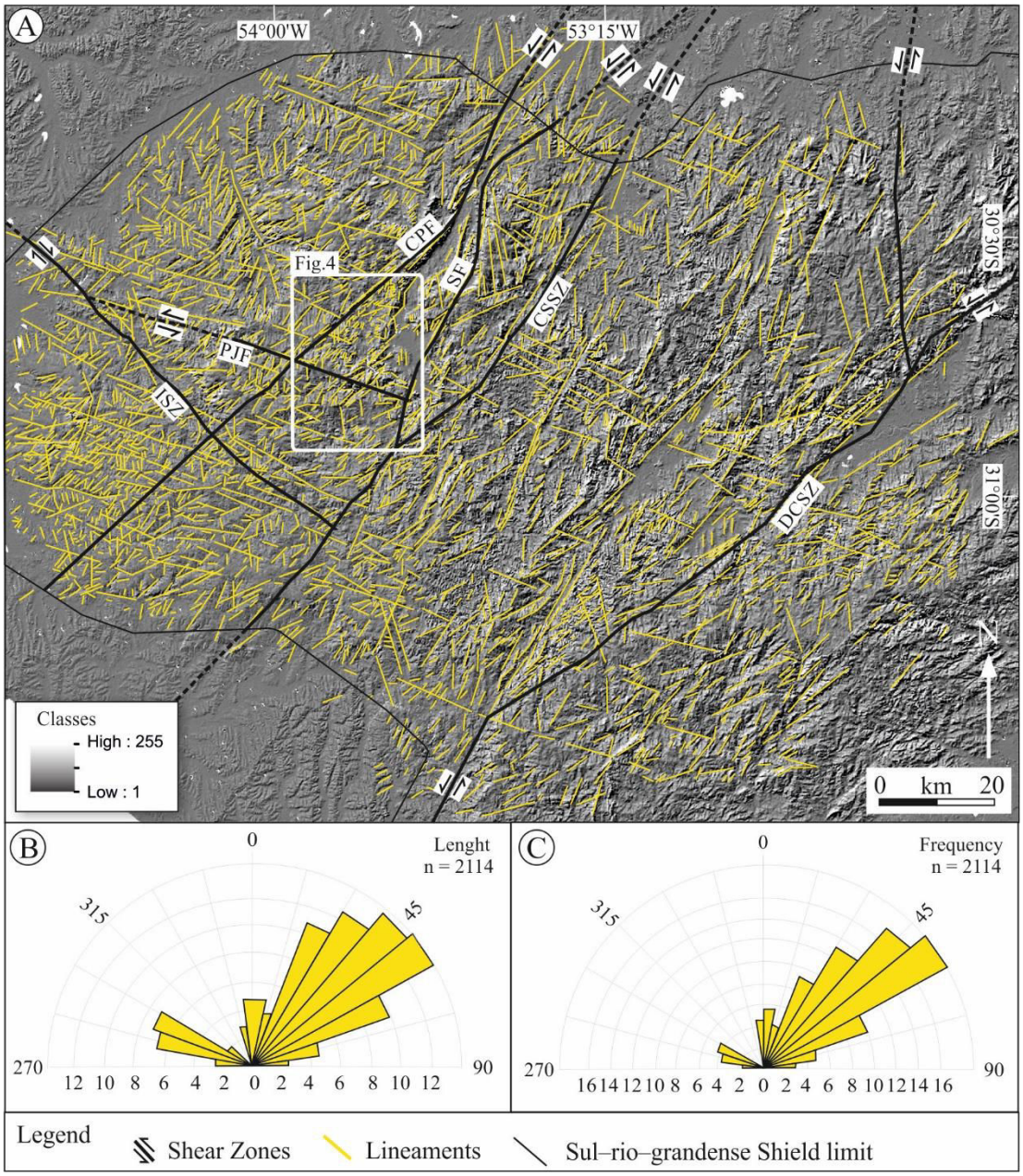

Figure 7. A) Lineaments map marked in 1:10.000 scale on an ASTER digital elevation model (Toniolo et al., 2007) from the Sul–rio–grandense Shield. Rose diagram with the statistical analysis of the lineaments and their length (B) and frequency (C). Shear zones: ISZ= Ibaré; CSSZ= Caçapava do Sul; DCSZ= Dorsal do Canguçu. Faults: CPF= Cabritos–Perau; SF= Segredo; PJF= Palma–Jacques.

Correlated lineaments are found in volcanogenic and granitic rocks of Lavras do Sul Mining District. In granitoids and volcanogenic rocks the main structures are represented by Cabritos–Perau Fault, Segredo Fault and Palma–Jacques Fault with

N50°E/80–88°SE, N20°E/80–88°NW and N70°W/80–88°NE orientations, respectively. Dikes with ~3–5 meters of width and ~0.2–1 km length have a much smaller length than lineaments in the area. These dikes are composed of N70°W/70–88°NE oriented monzonitic rocks and N50°E/70–88°SE oriented andesitic to trachyandesitic rocks in Lavras do Sul Mining District and in Seival Mine area, respectively. In Lavras do Sul the N70°W/70–88°NE oriented faults are parallel to the Palma–Jacques Fault. In Seival Mine the N50°E/70–88°NW oriented dikes and faults are parallel to the Cabritos–Perau Fault, located 5 km north of Seival area.

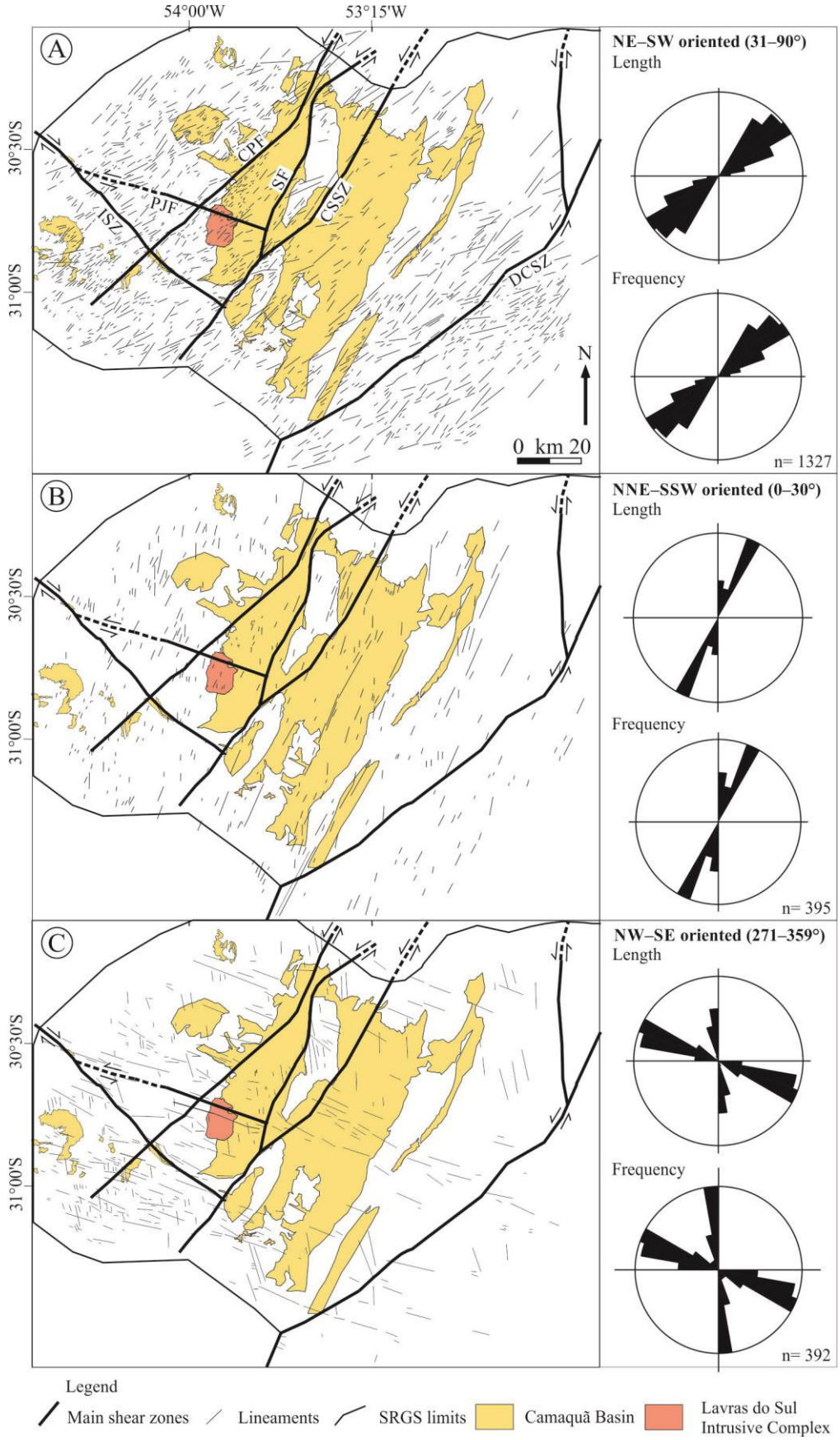
54°00'W
53°15'W
30°30'S
31°00'S
A
CPF
SF
CSSZ
PJF
ISZ
DCSZ
N
0 km 20
NE–SW oriented (31–90°)
Length
Frequency
n= 1327
B
NNE–SSW oriented (0–30°)
Length
Frequency
n= 395
C
NW–SE oriented (271–359°)
Length
Frequency
n= 392
Legend
Main shear zones
Lineaments
SRGS limits
Camaquã Basin
Lavras do Sul
Intrusive Complex

Figure 8. Structural maps of the Sul–rio–grandense Shield area with respective length and frequency lineaments rose diagram. Delimitation of Camaquã Basin and Lavras do Sul Intrusive Complex are marked in shades of gray. A) 31–90° (NE–SW oriented) lineaments patterns; B) 0–30° (NNE–SSW oriented) lineaments patterns; C) 271–359° (NW–SE oriented) lineaments patterns. Shear zones: ISZ= Ibaré; CSSZ= Caçapava do Sul; DCSZ= Dorsal do Canguçu. Faults: CPF= Cabritos–Perau; SF= Segredo; PJF= Palma–Jacques.

4.2 Structural geology

The N60°W/80–88°NE oriented Ibaré and N40°E/80–88°NW oriented Caçapava do Sul shear zones are the main structures in the São Gabriel Terrane. The Hilário Formation close to Lavras do Sul has volcano–sedimentary beds of N20°E/15°SE direction. On the other hand, in Seival area the dominant lapilli tuff has a bedding of N70°E/30°NW direction. The fault kinematic indicators of Lavras do Sul Mining District and Seival Mine are represented by slickensides or fault plane (Fig. 9A) and slickenlines or lineation with dextral (Fig. 9B), sinistral (Fig. 9C) and normal (Fig. 9D) sense of movement.

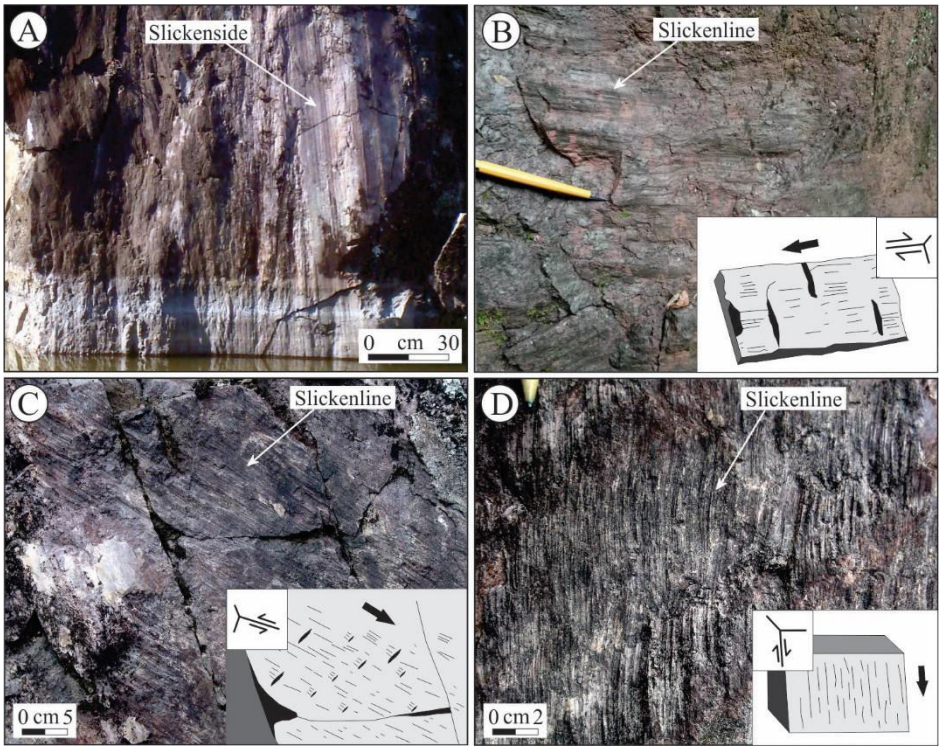

Figure 9: Photography of the measured kinematic indicators. A) Slickenside of footwall block in normal fault; B) Subhorizontal dextral sense of movement in

transcurrent fault; C) Slickenside with sinistral sense of movement in transcurrent fault; D) Slickenside with vertical sense of movement in normal fault.

In the Lavras do Sul Mining District, transcurrent faults parallel to fracturing are predominant. The fault orientation of Lavras do Sul area are mainly N40°E/70–88°SE (~70%) and N40°W/70–88°NE (~30%) oriented. However, faults in the Hilário Formation close to granites are mainly vertical– to subvertical NE–SW (40%) and NW–SE (60%) oriented. In the Lavras do Sul granitoids, the kinematic analysis show main dextral (~70%) and subordinated sinistral (25–30%) movements (stereogram 1 to 5 of the Fig. 10A; Supplementary Table). Minor normal kinematics were observed (0–5%). The direction of kinematic indicators is mainly NW–SE/10–40°NE (70%) and NE–SW/10–40°SE (30%) oriented. However, in the Hilário Formation of the Lavras do Sul Mining District, the kinematic analysis of volcanogenic rocks are mainly ENE–WSW/10–30°SE oriented (stereogram 6 of the Fig. 10A; (Supplementary Table). The orientation of the mineralized structures was associated with the main N70°W direction.

The intermediate to basic volcanogenic rocks of the Hilário Formation is delimited by N50°E/80–88°SE oriented Cabritos–Perau and N20°E/80–88°NW oriented Segredo faults. The ~E and NW bedding variation in volcanogenic rocks is found in Hilário Formation close to granitoids and Seival Mine, respectively. These changes are related to the original volcano–sedimentary deposition.

In Seival Mine area the volcanogenic rocks of the Hilário Formation have main structures represented by transcurrent and normal faults (stereogram 7 to 12 of the Fig. 10A; Supplementary Table). These faults are oriented NE–SW/70–88°NW (48%) and NW–SE/70–88°NE (48%). Few subhorizontal transcurrent fault (< 30°N–S) with slickenlines were observed (4%) with ~E–W orientation. The structural analysis indicates that most of the lineations are associated with transcurrent faults and show subhorizontal orientation with dextral (44%) and sinistral (30%) kinematics. Only 26% of the slickenlines are subvertical and associated with normal faults. The mineralized fractures and faults show NE–SW and NNE–SSW directions and vertical to subvertical disposition.

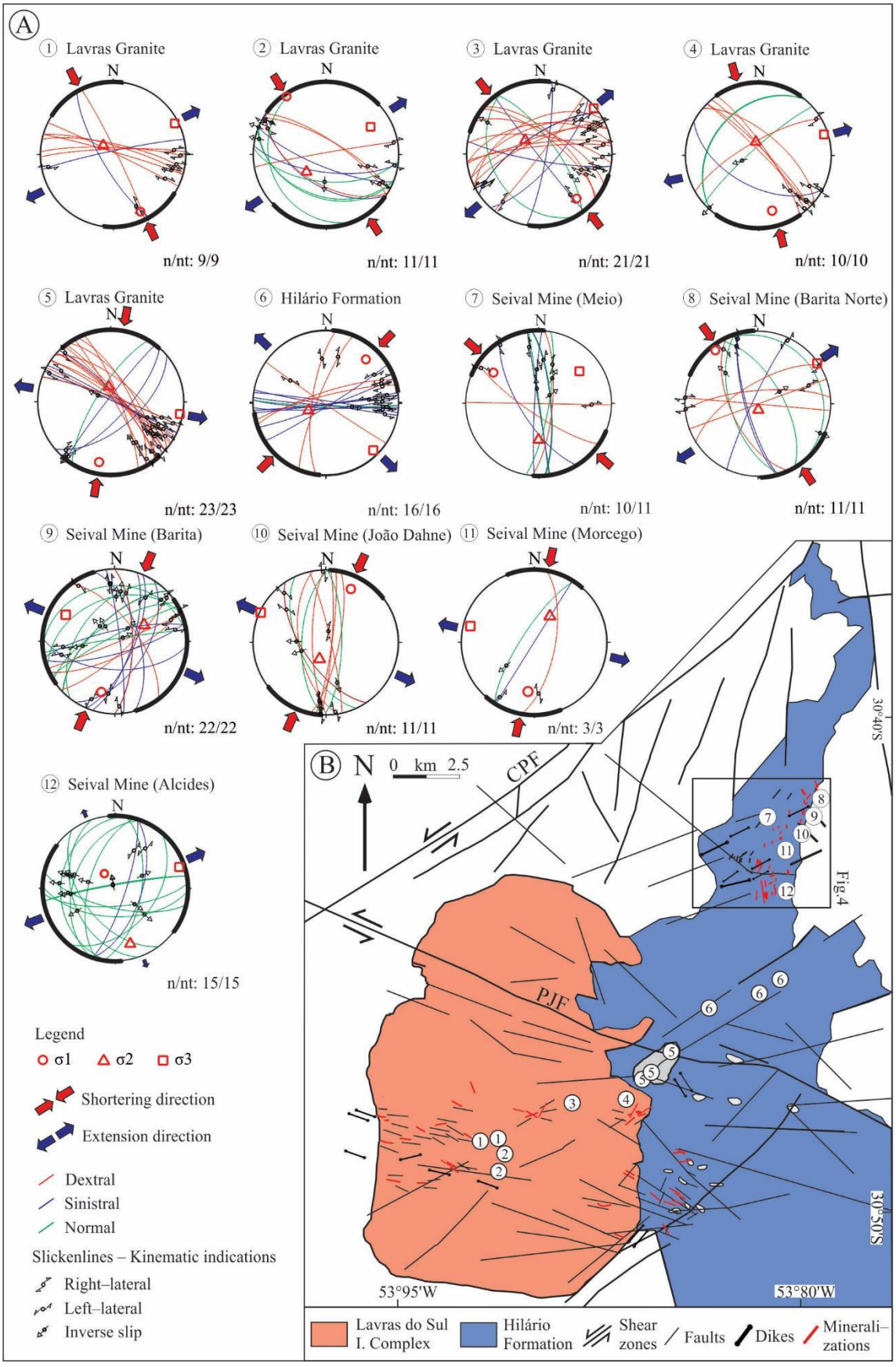
A
1 Lavras Granite
n/nt: 9/9
2 Lavras Granite
n/nt: 11/11
3 Lavras Granite
n/nt: 21/21
4 Lavras Granite
n/nt: 10/10
5 Lavras Granite
n/nt: 23/23
6 Hilário Formation
n/nt: 16/16
7 Seival Mine (Meio)
n/nt: 10/11
8 Seival Mine (Barita Norte)
n/nt: 11/11
9 Seival Mine (Barita)
n/nt: 22/22
10 Seival Mine (João Dahne)
n/nt: 11/11
11 Seival Mine (Morcego)
n/nt: 3/3
12 Seival Mine (Alcides)
n/nt: 15/15
N
Legend
σ1 σ2 σ3
Shortering direction
Extension direction
Dextral
Sinistral
Normal
Slickenlines – Kinematic indications
Right–lateral
Left–lateral
Inverse slip
B
0 km 2.5
CPF
PJF
Fig.4
30°40'S
30°50'S
53°95'W
53°80'W
Lavras do Sul I. Complex
Hilário Formation
Shear zones
Faults
Dikes
Minerali–zations

Figure 10. Structural analysis from Lavras do Sul Mining District and Seival Mine. A) Stereographic projections of faults with slickenside and kinematic indicators: 1 to 5= Lavras do Sul Intrusive Complex; 6= Hilário Formation; 7 to 12: Seival Mine (stress values see Table 1); B) Measured points localization, main structures and simplified geological map of the studied areas.

We recognized two scarce generations of slickenlines in the Seival area (Fig. 11A), similar to slickenlines on fault planes. These slickenlines contain deformed calcite and oriented hematite (Fig. 11B) for both slickenlines generation. The mineral lineation exhibits different structural events marked by kinematic indicators. Subvertical slickenlines (e.g., N05°W/30°NE oriented) cutting the subhorizontal ones (Fig. 11C) (e.g., N66°E/62°NE oriented) show an early transcurrent and late normal displacement marked by NE–SW and NE–SW directions, respectively.

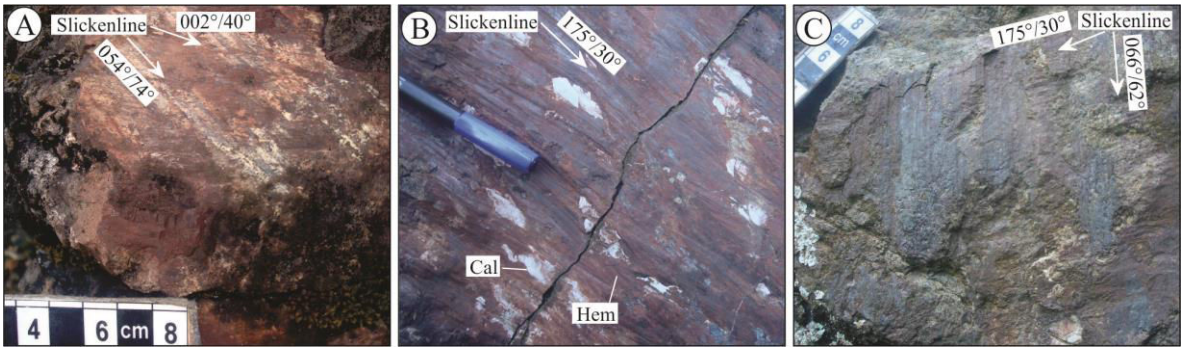

Figure 11. Photography of slickensides from Seival Mine area. A) Two generations of slickenlines with sinistral transcurrent and normal sense of movement filled by hematite–rich in lapilli tuff, Meio Mine; B) Slickenlines with hematite and calcite in lapilli tuff, Meio Mine; C) Two generations of slickenlines with dextral transcurrent and normal sense of movement filled by calcite–hematite in andesite porphyritic lava flows, Morcego Mine. Keys: Hem= Hematite; Cal= Calcite.

4.3 Fractures and veins

The fractures and veins occur along extensional cracks classified as Mode 1 fractures. These fractures are barren and ore–bearing. The extensional barren fractures are similar in Lavras do Sul Mining District and Seival area. The ore–bearing fractures are uniform veins with massive texture. These veins have a thickness with 0.1 to 1 cm of straight to irregular morphology forming a stockwork connectivity with the same orientation as the faults in both areas. The ore–bearing

fractures are mineralized structures with Au–Cu in quartz veins and Cu–Ag in calcite veins in Lavras do Sul Mining District and Seival Mine, respectively.

Vertical– to subvertical fractures were measured in Lavras do Sul Mining District. The barren and ore–bearing fractures are mostly N70–80°W/>60°NE oriented and subordinately N10°W/>60°NE oriented (Fig. 12A). These ore–bearing fractures are filled with quartz.

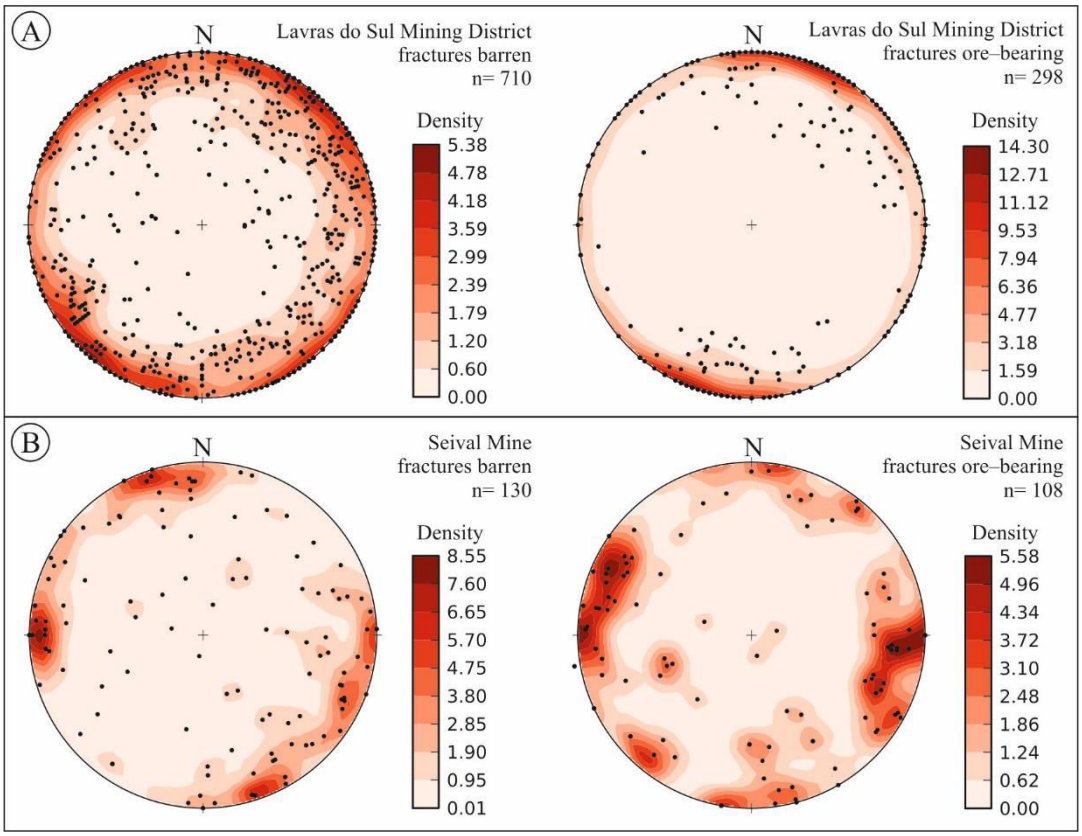

Figure 12. Lower hemisphere stereoplots showing the fractures data of mineralized and non–mineralized. A) Lavras do Sul Mining District: fractures barren with indistinct main direction and ore–bearing with N10°W and N70–80°W directions; B) Seival Mine: fractures barren and ore–bearing with N10°E and N70–80°E directions.

The Seival rocks host mainly subvertical and subordinated subhorizontal fractures. These fractures are N10°E/>60°NW oriented and N70–80°E/>60°NW oriented (Fig. 12B). In addition, the faults are associated with the orientation of copper soil metallic anomalies (Reischl, 1978) and mineralized structures, whereas

the NW/SE oriented structures have no metal concentration indicators. These ore–bearing fractures are filled with calcite, hematite and barite.

5. Discussion

5.1 Tectonic Context

Most of the current tectonic models for southern portion of Brazil consider that the evolution of the Dom Feliciano Belt between 950 Ma and 530 Ma records the closing of the Charrua and Adamastor oceans and the collisional episodes of the Brasiliano Orogeny, evolving the Rio de La Plata and Kalahari cratons (e.g., Ribeiro and Fantinel, 1978; Chemale Jr., 2000; Basei et al., 2008; Saalmann et al., 2010, Philipp et al., 2016a and 2018, Hueck et al., 2018). In this context, the Ediacaran to Cambrian Camaquã Basin has been considered as post–collisional, with its origin related to late–orogenic strike–slip deformation. The stratigraphic record of the deformational events of the basin reveals the recurrence of strike–slip and extensional episodes with no major thrusting (Almeida et al., 2012b). In the Camaquã Basin, the occurrence of three distinct volcanic successions suggests that they were formed associated to movement of deep high–angle shear zones and during a period of enhanced thermal gradient. This hypothesis is confirmed by the presence of several voluminous granitic intrusions coeval to the basins, as the Lavras do Sul Intrusive Complex, Caçapava do Sul and São Sepé granites.

Almeida et al. (2012b) considered that the generation of the Camaquã Basin is not related to extensional collapse of thickened crust caused by the collisional processes that had taken place between 650–620 Ma. For these researchers, the paleostress fields do not support a syn–collisional peripheral foreland basin model for this basin and the evidences suggest that the extensional events responsible for the subsidence cycles and that the strike–slip faulting activities are related to younger and anorogenic deformation (Almeida et al., 2012b).

In our vision, the Camaquã Basin was generated shortly after a major event of collisional orogenic metamorphism. The period of generation of the basin is associated with an intense volcanic activity, being contemporaneous to the development of the Pelotas Batholith, located to the east of the main depocenter of

the basin. The generation of these two large tectonic units of the Dom Feliciano Belt was associated with the activity of the large NE–SW high–angle transcurrent shear zones (Fernandes et al., 1992 and 1995a; Philipp and Machado, 2005; Saalmann et al., 2010; Philipp et al., 2016a). These shear zones were active at high depths up to 560 Ma and were associated with events of compressive deformation and post–collisional orogenic metamorphism as described in the metavolcano–sedimentary associations of the São Gabriel and Tijucas terranes (Cambaizinho, Passo Feio and Porongos complexes) (Saalmann et al., 2006 and 2010; Camozzato et al., 2013a,b; Pertille et al., 2015; Philipp et al., 2016a; Zvirtes et al., 2017).

The recurrence of strike–slip events is related with the third deformational event of regional scale and associated to formation of NE–SW normal F_3 folds in Passo Feio and Porongos complexes as described by Fernandes et al. (1992), Saalmann et al. (2010), Philipp et al. (2016a), Zvirtes et al. (2017) and others researchers. This event was associated with the escape tectonics by Fernandes et al. (1992), and the U–Pb ages of the intrusive syn–tectonic Capané Metagranite (Zvirtes et al., 2015) and Candiotinha Metagranite (Camozzato et al., 2013a, b) show that the metamorphism associated to high–angle ductile shear zones occurred after 580 Ma. These events of deformation and metamorphism are recorded in the basement nuclei (Caçacapa do Sul and Lavras do Sul highlands, Santana da Boa Vista and Vigia domes and Capané Antiform) that separate the sedimentary sub–basin with the successions of the Maricá, Bom Jardim, Santa Bárbara and Guaritas groups. The simultaneous occurrence of the contractional deformation and the metamorphism, associated with the shear zones in deeper portions of the basement and the opening of space with the deposition of the sedimentary rocks of the Camaquã Basin in pull–apart basins, is suggestive of the performance of oblique deformation processes (Philipp et al., 2016a; Zvirtes et al., 2017). Several researchers have suggested that the deposition of the Camaquã Basin occurred under compressive conditions and characterizes the final stage of formation of the Dom Feliciano Belt (Fernandes et al., 1992 and 1995a; Paim et al., 2000; Philipp et al., 2016a).

5.2 Structures of the Lavras do Sul Mining District and Seival Mine

The Camaquã Basin is a structure generated during the post–collisional stage of the Dom Feliciano orogeny (610–540 Ma) (Paim et al., 2000; Janikian et al., 2012; Philipp et al., 2016a). The basin structuring occurred in four main episodes (Paim et al., 2000) controlled by the activation of ductile to brittle–ductile transcurrent shear zones of N40–60°E direction and vertical to subvertical dip (e.g., Ramsay, 1980; Hodgson, 1989; Fossen and Cavalcante, 2017). These shear zones mark the tectonic contact between the different units of Dom Feliciano Belt and represent deep crustal structures (Picada, 1971; Almeida et al., 2012b; Janikian et al., 2012). The deposition cycles associated to each groups of the Camaquã Basin were delimited by regional sinistral transcurrent faults of N40–60°E direction and vertical to subvertical dip. These faults were also responsible for the ascent and control of volcanogenic magmatism related to the development of the Bom Jardim, Santa Bárbara and Guaritas groups and by emplacement of the associated post–collisional granitic magmatism (Philipp et al., 2016a). Fernandes et al. (1992) assigns the transcurrent movements to a escape tectonic model.

The main tectonic structures that control magmatism and sedimentation during the evolution of the Dom Feliciano Belt show NE–SW direction (Fernandes et al., 1995a; Chemale Jr., 2000; Saalmann et al., 2010; Philipp et al., 2016a; Hueck et al., 2018). The compressional direction with N40–60°W dominant stress occurred during the Dom Feliciano orogeny. The Lavras do Sul Mining District area is located in the southern portion of the São Gabriel Terrane, which is delimited from the adjacent terranes by Ibaré Shear Zone (Luzardo and Fernandes, 1990; Philipp et al., 2016a and 2018) and Caçapava do Sul Shear Zone (Fernandes et al., 1995b). Regionally, the Lavras do Sul Mining District area is delimited by vertical to subvertical N50°E oriented shear zones delimited in its northwest portion by the Cabritos–Perau Fault and in its southeast portion by the Caçapava do Sul Shear Zone and Segredo Fault. These fault systems were active during the deposition of the Bom Jardim and Santa Bárbara groups. The structural control of the Camaquã Basin suggests that NE–SW

trending transcurrent fault systems are responsible for the ascent and emplacement of the volcanogenic rocks.

In the Sul–rio–grandense Shield, most of the mineralized areas are controlled mainly by Neoproterozoic tectonic events related to development of the Neoproterozoic Dom Feliciano Belt. Bongiolo et al. (2011) and Gastal et al. (2015) associated brittle structural control to mineralization of Lavras do Sul Mining District. Santos et al. (2012) and Bicca et al. (2013) associated the influence of main compressional stress of NW–SE direction with the Cu and Au mineralization in the Camaquã Mine. Similar control is characterized by predominance of structures with direction of NW–SE and NE–SW in Lavras do Sul Mining District and Seival Mine, respectively. Most of the stereograms with kinematic analysis shows that the maximum principal stress is oriented NW–SE in the Lavras do Sul granitoids and Seival Mine areas (Table 1).

Table 1: Detailed information of main paleostress field orientation related to each deformation event in Lavras do Sul Mining District and Seival Mine.

N°	sigma 1 (σ_1)	sigma 2 (σ_2)	sigma 3 (σ_3)	n/nt	R	R'	Localization
1	155/14	313/75	063/05	09/09	0.5	1.5	Lavras Granite
2	326/04	228/61	058/29	11/11	0.5	1.5	Lavras Granite
3	141/21	313/69	050/03	21/21	0.5	1.5	Lavras Granite
4	166/23	337/67	074/03	10/10	0.5	1.5	Lavras Granite
5	191/17	353/72	100/05	23/23	0.5	1.5	Lavras Granite
6	042/21	248/67	136/09	16/16	0.5	1.5	Hilário Formation
7	305/25	181/49	050/29	10/11	0.5	1.5	Seival Mine - Meio
8	326/06	171/84	056/03	11/11	0.6	1.4	Seival Mine - Barita Norte
9	195/28	062/52	298/23	22/22	0.68	1.32	Seival Mine - Barita
10	025/20	200/70	295/02	11/11	0.73	1.27	Seival Mine - João Dahne
11	187/32	031/55	284/11	3/3	0.5	1.5	Seival Mine - Morcego
12	324/69	165/19	072/07	15/15	0.33	1.67	Seival Mine - Alcides

5.3 Faults at regional scale and paleostress–fields

The lineaments analyzed are associated with a large number of N50°E/80–88°SE, N20°E/80–88°NW and N70°W/80–88°NE faults, including, respectively, the Cabritos–Perau Fault, Segredo Fault and Palma–Jacques Fault. The occurrence of many structures with NE–SW and NW–SE orientations and the intrusive contacts of granitic plutons in volcanogenic rocks of the Hilário Formation suggest that Seival

Mine rocks are older than Lavras do Sul granitoids (Gastal et al., 2015). The ages obtained by the U–Pb method in zircon also confirm this stratigraphic relation (Remus et al., 2009; Janikian et al., 2012). The evaluation of the rheological behavior of the different rock types in relation to the main compressional stress indicates that the volcanogenic rocks of Seival Mine were more deformed and have a higher fracture density. Reciprocally, the dominant occurrences of N70°W/70–88°NE direction structures in Lavras do Sul compared to Seival Mine suggest that the granitoids did not accommodate the strain of NE–SW direction. On the other hand, the NE–SW strain is well marked in these volcanogenic rocks. The emplacement of the Lavras do Sul Intrusive Complex units is related to the opening of space generated by the movement of Cabritos–Perau Fault (N50°E/80–88°SE) and Segredo Fault (N40°E/80–88°NW) as suggested by Picada (1971). The main regional structures and Cu–Au–Ag deposits of the Dom Feliciano Belt are formed by the regional NW–SE compression associated with collisional processes related to the formation of the SW portion of Gondwana (Saalmann et al., 2010; Philipp et al., 2016a; Hueck et al., 2018). The stress orientation in the mineralized areas was obtained from the integration of orientation and kinematic indicators determined in the transcurrent and normal faults that control the mineralizations.

The large number of NE–SW normal faults and fracture systems in Seival compared to Lavras do Sul Mining District area suggest a superposition of two distinct deformational events with main subhorizontal NW–SE and NE–SW oriented compressive maximum stress, respectively. A first interpretation of these stress directions, based on a dominant occurrence in Lavras do Sul Mining District (NW–SE σ1; stereograms 1–5 and 7–8 of the Fig. 10A; Supplementary Table) compared to Seival (NE–SW σ1; stereograms 6 and 9–11 of the Fig. 10A; Supplementary Table), suggests that NE–SW stress was more expressive in the volcanogenic rocks. A second factor would be that subhorizontal thin pyroclastic layers of the lapilli tuff of the Seival Mine have a lower resistance to stress than massive granitoids of Lavras do Sul Mining District, and for this reason recorded more deformation.

The paleostresses calculated are associated with regional movement related to Caçapava do Sul Shear Zone, Cabritos–Perau Fault and Segredo Fault. Therefore, we analyzed separately Lavras do Sul Mining District and Seival Mine as diachronous paleostress fields.

The paleostress field calculation in Lavras do Sul Mining District and Seival Mine areas was based on spatial distribution of fractures and NE–SW oriented fault zones, taking into account the observed slickenlines in transcurrent and normal faults. As before described for the evolution of the Dom Feliciano Belt, the NW–SE direction represents the dominant maximum compressive stress. The paleostress calculated for Lavras do Sul and Seival areas indicates a main subhorizontal compressive sigma (σ1) oriented NW–SE.

The Lavras do Sul granitoids presented a common pattern of paleostress for both areas, characterized by a σ1 of subhorizontal disposition and positioned according to NW–SE direction. This compressive NW–SE stress is indicated in stereograms 1–5 and 7–8 of the Figure 10A for Lavras do Sul Mining District and Seival Mine, respectively. The calculated maximum compressive stress of NW–SE direction is associated with NW–SE mineralized zones in the intrusive granites of Lavras do Sul area and are also recognized in the volcanogenic rocks of the Hilário Formation in Seival area, suggesting that both units were affected by the same tectonic event. The subhorizontal maximum compressive stress of NW–SE direction is more pronounced in granitic rocks occurring predominantly in transcurrent regimes. 95% of slickenlines data from transcurrent faults of the Lavras do Sul Mining District is represented by low dip lineations with dextral or sinistral sense of movement. This maximum compressive stress of NW–SE direction is responsible for the emplacement of monzonite dikes in extensional fractures of predominant N70°W directions.

Two patterns of disposition of the compressional stress–fields were recognized in the volcanogenic rocks of Hilário Formation in Seival Mine area: (i) subhorizontal NW–SE (stereogram 7 and 8 of the Fig. 10A), and (ii) subhorizontal NE–SW (stereogram 9 to 11 of the Fig. 10A), with an important NE–SW and ESE–WNW

extensional component, respectively. The N40–60°E/70–88°NW extensional fractures resulting from this effort, are compatible with N50°E/70–88°NW orientation of the andesitic to trachyandesitic dikes. The NW–SE compression pattern is more recorded in Seival area than in Lavras do Sul Mining District, suggesting that it predates NE–SW compression. In addition, in the Seival area we also found some subvertical extension in the ENE–WSW and NNW–SSE direction (stereogram 12 of the Fig. 10A).

The maximum compressive stress of NW–SE direction was responsible for the activation of the dextral N30–70°W and N30–60°E oriented faults and sinistral N30–60°E oriented faults, just as Cabritos–Perau and Segredo faults feature sinistral movement in a transtension regime (Fig. 13A). In this case, the NE–SW structures would be synthetic Riedel shear faults represented by Cabritos–Perau and Segredo faults (Fig. 13B). This pattern has great importance for the mineralization, since the main pattern of ore–bearing faults and fractures has similar directions, as well as the N50°E/70–88°NW andesitic to trachyandesitic dikes. The presence of hydrothermal alteration faults and dikes suggests these structures are deeper crustal structures and probably served as pathways for the Hilário Formation magma rise. The less pronounced ENE–WSW distension pattern was only found in the southern Seival area. This pattern is dominantly marked by normal faults which overprints of striations in transcurrent faults, suggesting that this must be the last tectonic event (Fig. 13C).

In a few mineralized rocks of the Seival area, fault planes show two slickenlines patterns, suggesting two phases of structural activity. Oblique transcurrent faults are less impressed on the fault plane, indicating an event prior in relation to normal faults with subvertical striation (> 70 º). Oblique transcurrent faults are commonly attributed to compressive stress of NW–SE direction and normal faults were probably generated by a NE–SW distentional regime.

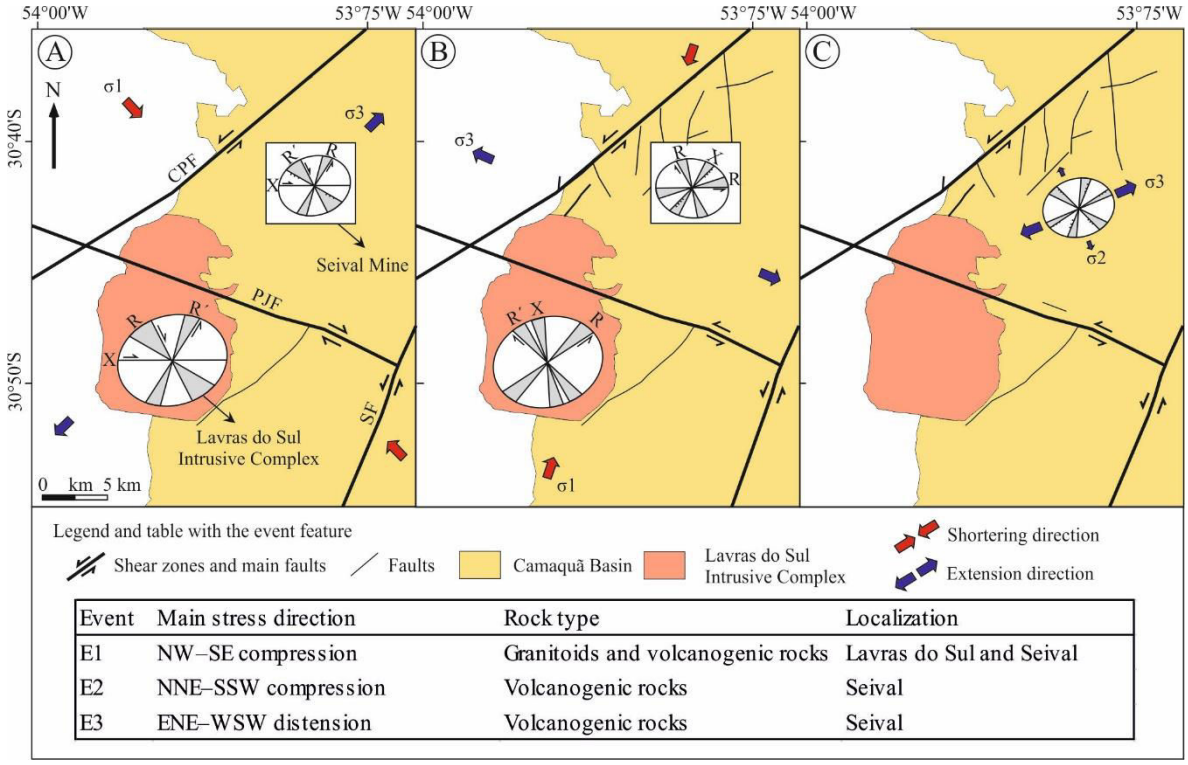

Event	Main stress direction	Rock type	Localization
E1	NW–SE compression	Granitoids and volcanogenic rocks	Lavras do Sul and Seival
E2	NNE–SSW compression	Volcanogenic rocks	Seival
E3	ENE–WSW distension	Volcanogenic rocks	Seival

Figure 13. Deformations events, disposition of the main structures and paleostress fields from Lavras do Sul Mining District and Seival Mine. A) Event 1= Subhorizontal NW–SE compressional paleostress associated to sinistral NE–SW movement of the Cabritos–Perau and Segredo faults and to dextral NW–SE movement related to Palma–Jacques Fault; B) Event 2= Subhorizontal compressional NE–SW paleostress and NW–SE distension associated to sinistral N50°E/80–88°SE oriented Cabritos–Perau and N20°E/80–88°NW oriented Segredo faults and to sinistral N70°W/80–88°NE oriented Palma–Jacques Fault; C) Event 3= Subvertical distention NE–SW and NW–SE in Seival area. Keys: CPF= Cabritos–Perau Fault; SF= Segredo Fault; PJF= Palma–Jacques Fault; R= Riedel; R´= anti–Riedel; X= normal.

5.4 Mineralizations associated with faults and fractures

The mineralized structures with variable orientations are considered contemporaneous based on mineralogy and alteration type. The main maximum compressional stress of NW–SE direction is associated with the development of Caçapava do Sul Shear Zone and generation of Cabritos–Perau Fault, Segredo Fault and Palma–Jacques Fault. It is difficult to define a structural model for mineralized structures. These mineralized structures were formed probably between

600 to 580 Ma ago (Gastal et al., 2006; Janikian et al., 2008; Almeida et al., 2012a) and indicated a period of intense tectonic activity.

The results allowed us to associate the same regional stress with both shear zones and mineralized areas. Au and Cu–Ag mineralizations in Lavras do Sul Mining District and Seival, respectively, are located immediately adjacent to Cabritos–Perau and Palma–Jacques faults. The mineralized structures are associated with dikes and hydrothermal fluids percolation and were probably responsible for the ascent and emplacement of the Lavras do Sul Intrusive Complex (Bongiolo et al., 2011; Gastal et al., 2015), as well as the volcanogenic rocks of the Hilário Formation (Lopes et al., 2014; Fontana et al., 2017). At least two other copper occurrences are associated to these structures (Teixeira, 1937; Toniolo et al., 2007) indicating a fertile structure in the region. A significant regional stress relationship with NW–SE oriented faults and Au–Cu mineralizations has been reported also for Camaquã Mine (e.g., Santos et al., 2012; Bicca et al., 2013).

The mineralized fractures were formed by opening cracks in the rocks. Euhedral or drusiform quartz fill the fractures (Fontana et al., 2017) evidencing the Mode 1 fractures. These fractures and faults allowed hydrothermal fluid percolation in these rocks. The regular to irregular veins are characteristic of porphyry–epithermal (Seedorff et al., 2005; Sillitoe, 2010) or iron oxide copper–gold deposits (IOCG; Dilles and Einaudi, 1992; Sillitoe, 2003) indicating possible models for mineralizations in Lavras do Sul Mining District and Seival Mine. We correlated Lavras do Sul Intrusive Complex and volcanogenic rocks of Seival Mine suggesting a porphyry–epithermal system to the Au–Cu–Ag mineralizations.

In Lavras do Sul Mining District, the maximum compressional stress of NW–SE direction was responsible for vein type–fractures of N70°W/70–88°NE direction, which provided a drain for the circulation of hydrothermal fluids and the Au–Cu deposition. In volcanogenic rocks of Lavras do Sul Mining District Au–quartz veins occur in monzonites (Liz et al., 2009a; Müller et al., 2012). Lamprophyre intrusions of ~590 Ma (Almeida et al., 2012a) occur in the volcanogenic rocks, which indicates influence in regional mineralization (Nardi and Lima, 1988; Mexias et al., 1990a, b

and c). In Seival Mine area the enrichment of Cu and Ag in whole–rock analysis of monzonitic and andesitic to trachyandesitic dikes suggests, probably, those mineralization elements are associated with dike magmatism (Lopes et al., 2014; Fontana et al., 2017).

The relative chronology of regional structures and the influence of the regional maximum compressive stress in the ore location are associated to regional tectonic events. The similar stress of mineralized fractures in the region are related with the evolution and emplacement of Tapera Granite, Lavras do Sul Granite and the volcanogenic rocks of the Hilário Formation of Bom Jardim Group. The probable origin of hydrothermal fluids is associated with monzonitic and andesitic to trachyandesite dikes. The magmatism of Bom Jardim Group is so characterized: (i) high content of water and, consequently, volatiles favoring the hydrotermalism (Lima and Nardi, 1988); (ii) the granitic magmatism structure is characterized by a caldera limited by NE–SW oriented structures (Caçapava do Sul Shear Zone and Cabritos–Perau Fault) and with centered in Lavras do Sul granitoids (Gastal et al., 2015). The similar compressive stress in Lavras do Sul Mining District and Seival Mine suggested this pattern affected regionally the Dom Feliciano Belt. We related the same compressional stress with the generation and emplacement of monzonitic and andesitic to trachyandesitic dikes in Lavras do Sul Mining District and Seival Mine, respectively, suggesting those structures are deeper in the crust and allowed hydrothermal percolation and Au–Cu–Ag mineralization.

6. Conclusion

The analysis of the brittle tectonic activity in the Lavras do Sul Mining District and Seival Mine shows that the Au–Cu mineralizations are associated with the NE–SW and NW–SE transcurrent and normal faults and with extensional vein–type fractures. The fault systems associated with the Caçapava do Sul Shear Zone as well as Cabritos–Perau and Segredo faults formed in a stress field with a subhorizontal NW–SE oriented maximum principal stress direction. The mineralized areas are

associated with the ascent and emplacement of the monzonitic and andesitic to trachyandesitic dikes and with Lavras do Sul Intrusive Complex.

The two studied areas were subjected to the main NW–SE compression stress system; however, the volcanogenic rocks of the Seival Mine region also recorded structures generated under a NE–SW direction stress system. The Palma–Jacques Fault (N70°W) is the main structure related to the Lavras do Sul Mining District, while the Cabritos–Perau Fault (N50°E) and the Segredo Fault (N20°E) are related to the Seival Mine area. These faults systems are associated respectively with the activation of the the Ibaré and Caçapava do Sul shear zones. The relative chronology indicates that NW–SE compression and consequent mineralized fractures are associated with transcurrent movements related to post–collisional period of the Dom Feliciano Belt evolution. The development of these high–angle shear zones suggests escape tectonic activity during the Middle– to Late–Ediacaran period, including the magmatism in the Bom Jardim Group, with intense fluid circulation and ore precipitation associated to andesite dikes emplacement.

Acknowledgements

This study is part of the co–tutela doctoral thesis of Rodrigo Winck Lopes at Universidade Federal do Rio Grande do Sul (Brazil) and Université Côte d´Azur (France). R.P. Philipp expresses thanks for the research grant from the Brazilian National Council for Scientific and Technological Development (CNPq). We wish to thank the CNPq, CAPES and Programa Ciências Sem Fronteiras (Process number: 200081/2014–4) for financial support and Votorantim Metais for allowing access to drill–cores. We wish to thank Luiz F. G. Morales and anonymous reviewers for the review and suggestions as well as and Reinhardt A. Fuck for thorough editorial support. We wish to thank Maria José M. de Mesquita for additional review, and Marcelo Lindenberg, Bruno Petracco and Amós Martini for help in sampling and fieldworks.

REFERENCES

Almeida, F.F.M., Hasuy, Y., 1984. O Pré–Cambriano do Brasil. São Paulo: Edgard Blücher, 378 p.

Almeira, R.P., Janikian, L., Fragoso–Cesar, A.R., Marconato, A., 2009. Evolution of a rift basin dominated by subaerial deposits: The Guaritas Rift, Early Cambrian, Southern Brazil. Sedimentary Geology, 217, 30–51.

Almeida, R.P., Janikian, L., Fragoso–Cesar, A.R., Fambrini, G.L., 2010. The Ediacaran to Cambrian rift system of Southeastern South America: tectonic implications. The Journal of Geology, 118, 145–161.

Almeida, D.P.M., Chemale Jr., F., Machado, A., 2012a. Late to post–orogenic Brasiliano–Pan–African volcano–sedimentary basins in the Dom Feliciano Belt, southernmost Brazil, in: Al–Juboury, A.I. (Ed.), Petrology – New Perspectives and Applications, pp. 73–135.

Almeida, R.P, Santos, M.G.N., Fragoso–Cesar, A.R.S., Janikian, L., Fambrin, G.L., 2012b. Recurring extensional and strike–slip tectonics after the Neoproterozoic collisional events in the southern Mantiqueira province. Anais da Academia Brasileira de Ciências, 84, 347–376.

Angelier, J., 1994. Fault slip analysis and paleostress reconstruction. In: P.L. Hancock (ed.) Continental Deformation, Pergamon, Oxford, pp. 101–120.

Basei, M.A.S., Frimmel, H.E., Nutman, A.P., Preciozzi, F., 2008. West Gondwana amalgamation based on detrital zircon ages from Neoproterozoic Ribeira and Dom Feliciano belts of South America and comparison with coeval sequences from SW Africa. In: Pankhurst, R.J., Trouw, R.A.J., Brito Neves, B.B., de Wit, M.J. (eds). West Gondwana, Pre–Cenozoic correlations across the South Atlantic region. Geological Society, London, Special Publication, 294, 239–256.

Barton, M.D., Johnson, D.A., 2000. Alternative brine sources for Feoxide(–Cu–Au) systems: Implications for hydrothermal alteration and metals. In Hydrothermal iron oxide copper–gold and related deposits: A global perspective (Porter, T.M., editor). Adelaide, Australian Mineral Foundation, pp. 43–60.

Bicca, M.M., Chemale Jr., F., Jelinek, A.R., Oliveira, C.H.E., Guadagnin, F., Armstrong, R., 2013. Tectonic evolution and provenance of the Santa Bárbara

Group, Camaquã Mines region, Rio Grande do Sul, Brazil. Journal of South American Earth Sciences, 48, 173–192.

Bongiolo, E.M., 2002. Mineralização de ouro da região de Lavras do Sul/RS e alteração hidrotermal associada. Masters dissertation, Instituto de Geociências, Universidade Federal do Rio Grande do Sul. Porto Alegre, 131 p.

Bongiolo, E.M., Patrier–Mas, P., Mexias, A.S, Beaufort, D., Formoso, M.L.L., 2008. Spatial and temporal evolution of hydrothermal alteration at Lavras do Sul, Brazil: evidence from dioctahedral clay minerals. Clays and Clay Minerals, 56, 222–243.

Bongiolo, E.M., Renac, C., Mexias, A.S., Gomes, M.E.B., Ronchid, L.H., Patrier–Mase, P., 2011. Evidence of Ediacaran glaciation in southernmost Brazil through magmatic to meteoric fluid circulation in the porphyry–epithermal Au–Cu deposits of Lavras do Sul. Precambrian Research, 189, 404–419.

Borba, A.W., Mizusaki, A.M.P., Silva, D.R.A., Koester, E., Noronha, F.L., Casagrande, J., 2006. Provenance of the Neoproterozoic Maricá Formation (Sul–rio–grandense Shield, southern Brazil): petrographic and Sm–Nd isotopic constraints. Gondwana Research, 9, 464–474.

Borba, A.W., Mizusaki, A.M.P., Santos, J.O.S., McNaughton, N.J., Ono, A.T., Hartmann, L.A., 2008. U–Pb zircon and ^{40}Ar–^{39}Ar K–feldspar dating of syn–sedimentary volcanism of the Neoproterozoic Maricá Formation: constraining the age of foreland basin inception and inversion in the Camaquã Basin of southern Brazil. Basin Research, 20, 359–375.

Camozzato, E., Philipp, R.P., Chemale Jr., F., 2013a. Arquitetura Estrutural do Domo da Vigia e da área Jaíba Torrinhas (RS) como resultado de Colisão Oblíqua Neoproterozoica. In: XIV SIMPÓSIO NACIONAL DE ESTUDOS TECTÔNICOS, Resumos Expandidos – CD Rom.

Camozzato, E., Philipp, R.P., Chemale Jr., F., 2013b. Evolução Tectônica e Geocronologia U–Pb em zircão da terminação sul do Terreno Tijucas (RS, Brasil). In: VII CONGRESO URUGUAYO DE GEOLOGÍA, Sociedad Uruguaya de Geología, Montevideo, Resúmenes Extendidos, 7 p.

Carten, R.B., 1986. Sodium–calcium metasomatism: chemical, temporal, and spatial relationships at the Yerington, Nevada, porphyry copper deposit. Economic Geology, 81, 1495–1519.

Chemale Jr., F., 2000. Evolução Geológica do Escudo Sul–rio–grandense. In: Holz, M., De Ros, L.F., Geologia do Rio Grande do Sul, pp. 13–52.

Chemale Jr., F., Philipp, R.P., Dussin, I., Formoso, M.L.L., Kawashita, K., Berttotti, A.L., 2011. Lu–Hf and U–Pb age determination of the Capivarita Anorthosite, Dom Feliciano belt, Brazil. Precambriam Research, 186, 117–126.

Costa, A.F.U., 1997. Teste e modelagem geofísica das associações litotectônicas précambrianas no Escudo Sul–rio–grandense. PhD Thesis, Instituto de Geociências, Universidade Federal do Rio Grande do Sul. Porto Alegre, 257 p.

Cordani, U.G., Brito–Neves, B.B., D'Agrella–Filho, M., 2003. From Rodinia to Gondwana: A review of the Available Evidence from South America. Gondwana Research, 6, 275–283.

Delvaux, D., Sperner, B., 2003. New aspects of tectonic stress inversion with reference to the TENSOR program. In: Nieuwland, D. (ed.), New insights into structural interpretation and modelling. London, Geological Society of London, Special Publication, 212, 75–100.

Dilles, J.H., Einaudi, M.T., 1992. Wall–rock alteration and hydrothermal flow paths about the Ann Mason porphyry copper deposit, Nevada; a 6–km vertical reconstruction. Economic Geology and the Bulletin of the Society of Economic Geologists, 87, 1963–2001.

Fambrini, G.L., Janikian, L., Almeida, R.P., Fragoso–Cesar, A.R.S., 2005. O Grupo Santa Bárbara (Neoproterozóico III) na sub–bacia Camaquã Central, RS: sistemas deposicionais, paleogeografia e implicações tectônicas. Revista Brasileira de Geologia, 35, 227–238.

Fambrini, G.L., Janikian, L., Almeida, R.P., Fragoso–Cesar, A.R.S., 2007. Evolução Estratigráfica e Paleogeográfica do Grupo Santa Bárbara na Sub–bacia Camaquã Central, RS. Geologia USP – Série Científica, 7, 1–24.

Fernandes, L.A., Tommasi, A., Porcher, C.C., 1992. Deformation patterns in the Southern Brazilian branch of the Dom Feliciano Belt: a reappraisal. Journal of South American Earth Sciences, 5, 77–96.

Fernandes, L.A.D., Menegat, R., Costa, A.F.U., Koester, E., Porcher, C.C., Tommasi, A., Kraemer, G., Ramgrab, G.E., Camozzato, E., 1995a. Evolução tectônica do Cinturão Dom Feliciano no Escudo Sul–rio–grandense: parte I – Uma contribuição a partir do registro geológico. Revista Brasileira de Geologia, 25, 351–374.

Fernandes, L.A.D., Menegat, R., Costa, A.F.U., Koester, E., Tommasi, A., Kraemer, G., Ramgrab, G.E., Camozzato, E., Porcher, C.C., 1995b. Evolução Tectônica do Cinturão Dom Feliciano no Escudo Sul–Rio–grandense: Parte II – Uma contribuição a partir das assinaturas geofísicas. Revista Brasileira de Geologia, 25, 375–384.

Fragoso–Cesar, A.R.S., 1991. Tectônica de Placas no Ciclo Brasiliano: as orogenias dos Cinturões Dom Feliciano e Ribeira no Rio Grande do Sul. PhD Thesis, Instituto de Geociências, Universidade de São Paulo. São Paulo, 366 p.

Fragoso–Cesar, A.R.S., Fambrini, G.L., Almeida, R.P., Pelosi, A.P.M.R., Janikian, L., Riccomini, C., Machado, R., Nogueira, A.C.R., Saes, G.S., 2000. The Camaquã extensional basin: Neoproterozoic to early Cambrian sequences in southernmost Brazil. Revista Brasileira de Geologia, 30, 438–441.

Fragoso–Cesar, A.R.S., Fambrini, G.L., Riccomini, C., Janikian, L., Almeida, R.P., Pelosi, A.P.M.R., Machado, R., 2001. Estruturas induzidas por abalos sísmicos na Formação Santa Bárbara (Neoproterozóico III – Eocambriano), Bacia do Camaquã, RS: o exemplo do Passo da Capela. Revista Brasileira de Geologia, 31, 155–162.

Fontana, E., Mexias, A.S., Renac, C., Nardi, L.V.S., Lopes, R.W., Gomes, M.E.B., Barats, A., 2017. Hydrothermal alteration of volcanic rocks in Seival Mine Cu–mineralization – Camaquã Basin – Brazil (Part I): Chloritization process and geochemical dispersion in alteration halos. Journal of Geochemical Exploration, 177, 45–60.

Fossen, H., Cavalcante, G.C.G., 2017. Shear zones – A review. Earth–Science Reviews, 171, 434–455.

Gastal, M.C.P., Lafon, J.M., 1998. Gênese e evolução dos granitóides metaluminosos de afinidade alcalina da porção oeste do Escudo Sul–riograndense: geoquímica e isótopos de Rb–Sr e Pb–Pb. Revista Brasileira de Geologia, 28, 11–28.

Gastal, M.C., Lafon, J.M., Ferreira, F.J.F., Magro, F.U.S., Remus, M.V.D., Sommer, C.A., 2006. Reinterpretação do Complexo Intrusivo Lavras do Sul – RS, de acordo com os sistemas vulcano–plutônicos de subsidência. Parte I: Geologia, geofísica e geocronologia ($^{207}Pb/^{206}Pb$ e $^{206}Pb/^{238}U$). Revista Brasileira de Geologia, 36, 109–124.

Gastal, M.C., Ferreira. F.J.F., Cunha, J.U., Esmeris, C., Koester, E., Raposo, M.I.B., Rossetti, M.M.M., 2015. Lavras granite emplacement and gold mineralization during the development of the post–collisional volcanoplutonic center, west of the Sul–riograndense Shield: Geophysical and structural data. Brazilian Journal of Geology, 45, 217–241.

Gresse, P.G., Chemale Jr., F., Silva, L.C., Walraven, F., Hartmann, L.A., 1996. Late– to post– orogenic basins of the Pan–African–Brasiliano collision orogen in southern Africa and southern Brazil. Basin Research, 8, 157–171.

Gubert, M.L., Philipp, R.P, Basei, M.A.S., 2016. U–Pb geochronology and tectonic implications for the Neoproterozoic São Gabriel Arc, southernmost Brazil. Journal of South American Earth Sciences, 70, 1–17.

Hatcher, R.D., 1995. Structural geology (2nd edition): Englewood Cliffs, New Jersey, Prentice–Hall, 525 p.

Hartmann, L.A., Chemale Jr., F., Philipp, R.P., 2007. Evolução Geotectônica do Rio Grande do Sul no Pré–Cambriano In: Iannuzzi, R., Frantz, J.C. (Eds). 50 anos de Geologia, pp. 99–123.

Hartmann, L.A., Philipp, R.P., Santos, J.O.S., McNaughton, N.J., 2011. Time frame of 753–680 Ma juvenile accretion during the São Gabriel orogeny, southern Brazil. Gondwana Research, 19, 84–99.

Heilbron, M., Machado, N., 2003. Timing of Terrane Accretion in the Neoproterozoic – Eopaleozoic Ribeira Belt (SE Brazil). Precambrian Research, 125, 87–112.

Hodgson, C.J., 1989. The structure of shear–related, vein–type gold deposits: a review. Ore Geology Reviews, 4, 231–273.

Hueck, M., Oyhantçabal, P., Philipp, R.P., Basei, M.A.S., Siegesmund, S., 2018. The Dom Feliciano Belt in Southern Brazil and Uruguay. Geology of the SW Gondwana. In: Siegesmund, S., Oyhantçabal, P., Basei, M.A.S., Oriolo, S. (Eds.). Regional Geology Review, Springer, pp. 267–303.

Janikian, L., Almeida, R.P., Fragoso–Cesar, A.R.S., Fambrini, G.L., 2003. Redefinição do Grupo Bom Jardim (Neoproterozóico III) em sua área–tipo: litoestratigrafia, paleogeografia e significado tectônico das sucessões vulcano–sedimentares do Supergrupo Camaquã, RS. Revista Brasileira de Geologia, 33, 349–362.

Janikian, L., Almeida, R.P., Fragoso–Cesar, A.R.S., Corrêa, C.R.A., Pelosi, A.P.M.R., 2005. Evolução paleoambiental e sequências deposicionais do Grupo Bom Jardim e Formação Acampamento Velho (Supergrupo Camaquã) na porção norte da Sub–Bacia Camaquã Ocidental. Revista Brasileira de Geologia, 35, 245–256.

Janikian, L., Almeida, R.P., Trindade, R.I.F., Fragoso–Cesar, A.R.S., D´Agrella–Filho, M.S., Dantas, E.L., Tohver, E., 2008. The continental record of Ediacaran volcano–sedimentary successions in southern Brazil and their global implications. Terra Nova, 20, 259–266.

Janikian, L., Almeida, R.P., Fragoso–Cesar, A.R.S., Martins, V.T.S., Dantas, E.L., Tohver, E., McReath, I., D'Agrella–Filho, M.S., 2012. Ages (U–Pb SHRIMP and LA ICPMS) and stratigraphic evolution of the Neoproterozoic volcano–sedimentary successions from the extensional Camaquã Basin, Southern Brazil. Gondwana Research, 21, 466–482.

Kaul, P.F.T., 1975. Distrito aurífero de Lavras do Sul (RS) histórico dos trabalhos de pesquisa e exploração. Revista Mineração Metalurgia, 364, 18–22.

Kaul, P.F.T., 1976. Juntas, falhas e filões e seu relacionamento estrutural na mina Aurora, distrito aurífero de Lavras do Sul, RS. Revista Mineração Metalurgia, 365, 29–33.

Laux, J.H., Lindenmayer, Z.G., Teixeira, J.B.G., Neto, A.B., 2005. Ore genesis at the Camaquã copper mine, a neoproterozoic sediment–hosted deposit in Southern Brazil. Ore Geology Review, 26, 71–89.

Leite, J.A.D., Hartmann, L.A., McNaughton, N.J., Chemale Jr., F., 1998. SHRIMP U/Pb zircon geochronology of Neoproterozoic juvenile and crustal reworked terranes in southernmost Brazil. International Geology Review, 40, 688–705.

Lena, L.O.F., Pimentel, M.M., Philipp, R.P., Armstrong, R., Sato, K., 2014. The evolution of the Neoproterozoic São Gabriel juvenile terrane, southern Brazil based on high spatial resolution U–Pb ages and $\delta^{18}O$ data from detrital zircons. Precambrian Research, 247, 126–138.

Lima, E.F., Nardi, L.V.S., 1998. The Lavras do Sul Shoshonitic Association: implications for origin and evolution of neoproterozoic shoshonitic magmatism in southernmost Brazil. Journal of South American Earth Science, 11, 67–77.

Lima, E.F.L., Sommer, C.A., Nardi, L.V.S., 2007. O vulcanismo Neoproterozóico–Ordoviciano no escudo sul–riograndense: os ciclos vulcânicos da Bacia do Camaquâ. In: Iannuzzi, R., Frantz, J.C. (Eds). 50 anos de Geologia, pp. 79–97.

Liz, J.D., Lima, E.F., Nardi, L.V.S., 2009a. Avaliação de fontes magmáticas de séries shoshoníticas pós–colisionais com base na normalização pela Associação Shoshonítica de Lavras do Sul – aplicação de Sliding Normalization. Revista Brasileira de Geologia, 39, 55–66.

Liz, J.D., Lima, E.F., Nardi, L.V.S., Sommer, C.A., Saldanha, D.L., Pierosan, R., 2009b. Petrologia e sucessão estratigráfica das rochas monzoníticas da associação shoshonítica de Lavras do Sul (RS). Revista Brasileira de Geologia, 39, 244–255.

Lopes, R.W., Fontana, E., Mexias, A.S., Gomes, M.E.B., Nardi, L.V.S., Renac, C., 2014. Caracterização petrográfica e geoquímica da sequência magmática da

Mina do Seival, Formação Hilário (Bacia do Camaquã – Neoproterozoico), Rio Grande do Sul, Brasil. Pesquisas em Geociências, 41, 51–64.

Luzardo, R., Fernandes, L.A.D., 1990. Análise estrutural do Lineamento de Ibaré, Parte I – filitos de Ibaré: greenstone belt ou cobertura cratônica deformada?. Acta Geológica Leopoldensia, 13, 25–36.

Machado, R., Sayeg, H.S., 1992. Aplicação da análise geométrica e cinemática nos falhamentos que condicionaram a bacia molássica do Arroio Boici, RS. In: I WORKSHOP SOBRE AS BACIAS MOLÁSSICAS BRASILIANAS, Boletim de Resumos Expandidos, SBG/UNISINOS, São Leopoldo, RS, pp. 73–76.

Mark, G., Oliver, N.H.S., Carew, M.J., 2006. Insights into the genesis and diversity of epigenetic Cu–Au mineralisation in the Cloncurry district, Mt Isa Inlier, northwest Queensland. Australian Journal of Earth Sciences, 53, 109–124.

Mesquita, M.J.M., Fernandes, L.A.D., 1990. Petrografia dos granitóides deformados na Zona de Cisalhamento Dorsal de Canguçu (Região de Quitéria–Capivarita). Acta Geológica Leopoldensia, 30, 55–74.

Mexias, A.S., Formoso, M.L.L., Meunier, A., Beaufort, D., 1990a. O sistema hidrotermal fóssil de Volta Grande – Lavras do Sul/RS. Parte I – Petrografia do hidrotermalismo. Geochimica Brasiliensis, 4, 139–157.

Mexias, A.S., Formoso, M.L.L., Gomes, M.E.B., Meunier, A., Beaufort, D., Mattos, I., 1990b. O sistema hidrotermal fóssil de Volta Grande – Lavras do Sul/RS. Parte II – Geoquímica das cloritas. Geochimica Brasiliensis, 4, 159–174

Mexias, A.S., Formoso, M.L.L., Meunier, A., Beaufort, D., 1990c. Composition and crystallization of corrensite in volcanic and pyroclastic rocks of Hilário Formation (RS) Brazil. Sciences Géologiques, 88, 135–143.

Mexias, A.S., Berger, G., Gomes, M.E.B., Formoso, M.L.L., Dani, N., Frantz, J.C., Bongiolo, E.M., 2005. Geochemical modelling of gold precipitation conditions in Bloco do Butiá Mine, Lavras do Sul/Brazil. Anais da Academia Brasileira de Ciências, 77, 1–12.

Mexias, A.S., Bongiolo, E.M., Gomes, M.E.B., Formoso, M.L.L., Frantz, J.C., 2007. Alterações hidrotermais e mineralizações nas rochas da Associação Plutono–

Vulcano–Sedimentar da região de Lavras do Sul–RS. Cambriano In: Iannuzzi, R., Frantz, J.C. (Eds). 50 anos de Geologia, pp. 143–159.

Müller, I.F., Nardi, L.V.S., Lima, E.F., Mexias, A.S., 2012. Os diques latíticos portadores de ouro e sulfetos da Associação Shoshonítica de Lavras do Sul – RS: Petrogênese e geoquímica. Pesquisas em Geociências, 39, 173–191.

Nardi, L.V.S., 1984. Geochemistry and petrology of the Lavras Granite Complex, RS, Brazil. PhD Thesis, London University. Londres, 268 p.

Nardi, L.V.S., Lima, E.F., 1988. Hidrotermalismo no Complexo Granítico Lavras e vulcânicas associadas, RS. Revista Brasileira de Geologia, 18, 369–375.

Oliveira, J.M.M.T., Fernandes, L.A.D., 1991. Estágios finais da evolução do Cinturão Dom Feliciano: Tectônica e sedimentação da Formação Arroio dos Nobres. In: III SIMPÓSIO NACIONAL DE ESTUDOS TECTÔNICOS, Boletim de Resumos Extensos, SBG, Rio Claro, SP, pp. 58–59.

Oliveira, J.M.M.T., Fernandes, L.A.D., 1992. Bacias molássicas brasilianas, mito ou realidade? In: I WORKSHOP SOBRE AS BACIAS MOLÁSSICAS BRASILIANAS, Boletim de Resumos Expandidos, SBG/UNISINOS, São Leopoldo, RS, pp. 97–105.

Oyhantçabal, P., Siegesmund, S., Wemmer, K., 2011. The Rio de la Plata Craton: a review of units, boundaries, ages and isotopic signature. International Journal of Earth Sciences, 100, 201–220.

Paim, P.S.G., Scherer, C.M.S., 2007. High–resolution stratigraphy and depositional model of wind– and waterlaid deposits in the ordovician Guaritas rift (Southernmost Brazil). Sedimentary Geology, 202, 776–795.

Paim, P.S.G., Chemale Jr., F., Lopes, R.C., 2000. A Bacia do Camaquã. In: Holz, M., De Ros, L.F., Geologia do Rio Grande do Sul, pp. 231–374.

Paim, P.S.G., Chemale Jr., F., Wildner, W., 2014. Estágios evolutivos da Bacia do Camaquã (RS). Ciência e Natura, 36, 183–193.

Pertille, J., Hartmann, L.A., Philipp, R.P., Petry, T.S., Lana, C.C., 2015. Origin of the Ediacaran Porongos Group, Dom Feliciano Belt, southern Brazilian Shield, with

emphasis on whole rock and detrital zircon geochemistry and U–Pb, Lu–Hf isotopes. Journal of South American Earth Sciences, 64, 69–93.

Philipp, R.P., Mesquita, M.J.M., Gomes, M.E.B., Almeida, D.P.M., 1993. Reconhecimento estrutural e geoquímico dos granitóides Brasilianos na região de Pelotas, RS. Revista Pesquisas em Geociências, Porto Alegre, 20(1), 3–13.

Philipp, R.P., Machado, R., 2005. The Neoproterozoic to Cambrian granitic magmatism of Pelotas Batholith, Southern Brazil. Journal of South American Earth Sciences, 19, 461–478.

Philipp, R.P., Pimentel, M.M., Chemale Jr., F., 2016a. Tectonic evolution of the Dom Feliciano Belt in Southern Brazil: Geological relationships and U–Pb geochronology. Brazilian Journal of Geology, 46, 83–104.

Philipp, R.P., Bom, F.M., Pimentel, M.M., Junges, S.L., Zvirtes, G., 2016b. SHRIMP U–Pb age and high temperature conditions of the collisional metamorphism in the Várzea do Capivarita Complex: implications for the origin of Pelotas Batholith, Dom Feliciano Belt, southern Brazil. Journal of South American Earth Sciences, 66, 197–207.

Philipp, R.P., Pimentel, M.M., Basei, M.A.S., 2018. Tectonic evolution of the São Gabriel Terrane, Dom Feliciano Belt, southern Brazil: the closure of the Charrua Ocean. Geology of the SW Gondwana. In: Siegesmund, S., Oyhantçabal, P., Basei, M.A.S., Oriolo, S. (Eds.), Regional Geology Review, Springer, pp. 243–266.

Picada, R.S., 1971. Ensaio sobre a tectônica do Escudo Sul–Riograndense. Caracterização dos sistemas de falhas. In: XXV CONGRESSO BRASILEIRO DE GEOLOGIA, 25. 1971, Porto alegre. Anais... Porto Alegre, SBG, pp. 167–191.

Ramsay, J.G., 1980. Shear zone geometry: a review. Journal of Structural Geology, 2, 83–100.

Reischl, J.L., 1978. Mineralizações cupriferas associadas a vulcânicas na Mina do Seival. In: XXX CONGRESSO BRASILEIRO DE GEOLOGIA, 30. 1978, Recife. Anais... Recife, SBG, 4, pp. 1568–1582.

Remus, M.V.D., McNaughton, N.J., Hartmann, L.A., Koppe, J.C., Fletcher, I.R., Groves, D.I., Pinto, V.M., 1999. Gold in the Neoproterozoic juvenile Bossoroca

volcanic arc of southernmost Brazil, isotopic constraints on timing and sources. Journal of South American Earth Sciences, 12, 349–366.

Remus, M.V.D., Hartmann, L.A., McNaughton, N.J., Groves, D.I., Reischl, J.L., 2000. A distal magmatic–hydrothermal origin for the Camaquã Cu (Au–Ag) and Santa Maria Pb, Zn (Cu–Ag) deposits, southern Brazil. Gondwana Research, 3, 155–174

Renac, C., Mexias, A.S., Gomes, M.E.B., Ronchi, L.H., Nardi, L.V.S., Laux, J.H., 2014. Isotopic fluid changes in a Neoproterozoic porphyry–epithermal system: the Uruguay mine, southern Brazil. Ore Geology Review, 60, 146–160.

Ribeiro, M., Bocchi, P.R., Figueiredo, F.P.M., Tessari, R.I., 1966. Geologia da quadrícula de Caçapava do Sul, RS, Brasil. Boletim do DNPM/DFPM, 127, 231 p.

Ribeiro, M., Fantinel, L.M., 1978. Associações petrotectônicas do Escudo Sul–Riograndense: I Tabulação e distribuição das associações petrotectônicas do Escudo do Rio Grande do Sul. Ihneríngia, Série Geológica 5, 19–54.

Robertson, J.F., 1966. Revision of the stratigraphy and nomenclature of the rock units in Caçapava e Lavras Region, State of Rio Grande do Sul, Brazil, volume 1. Notas e Estudos, IG/UFRGS, pp. 41–54.

Santos, M.G.M., Almeida, R.P., Fragoso–Cesar, A.R.S., 2012. Paleostress analysis in brittle structures of the Camaquã copper mines. Revista Brasileira de Geologia, 42, 573–584.

Saalmann, K., Remus, M.V.D., Hartmann, L.A., 2006. Tectonic evolution of the Neoproterozoic juvenile São Gabriel Belt, southern Brazil – constraints on Brasiliano orogenic evolution of the La Plata cratonic margin. Journal of South American Earth Sciences, 21, 204–227.

Saalmann, K., Gerdes, A., Lahaye, Y., Hartmann, L.A., Remus, M.V.D., 2010. A multiple accretion at the eastern margin of the Rio de la Plata craton: the prolonged Brasiliano orogeny in southernmost Brazil. International Journal of Earth Sciences, 100, 355–378.

Seedorff, E., Dilles, J.H., Proffett Jr., J.M., Einaudi, M.T., Zurcher, L., Stavast, W.J.A., Johnson, D.A., Barton, M.D., 2005. Porphyry deposits: characteristics and

origin of hypogene features. Society of Economic Geologists, Economic Geology 100th Anniversary Volume, 251–298.

Sillitoe, R.H., 1991. Gold metallogeny of Chile – an introduction. Economic Geology, 86, 1187–1205.

Sillitoe, R.H., 2003. Iron oxide–copper–gold deposits: An Andean view. Mineralium Deposita, 38, 787–812.

Sillitoe, R.H., 2010, Porphyry copper systems. Economic Geology, 105, 3–41.

Silva, L.C., McNaughton, N.J., Armstrong, R., Hartmann, L.A., Fletcher, I.R., 2005. The neoproterozoic Mantiqueira Province and its African connections: a zircon–based U–Pb geochronologic subdivision for the Brasiliano/Pan–African systems of orogens. Precambrian Research, 136, 203–240.

Sommer, C.A., Lima, E.F., Nardi, L.V.S., Figueiredo, A.M.G., Pierosan, R., 2006. Potassic and low–and high–Ti mildly alkaline volcanism in the Neoproterozoic Ramada Plateau, southermost Brazil. Journal of South American Earth Sciences, 18, 237–254.

Teixeira, E., 1937. Cobre no Rio Grande do Sul. DNPM, Divisão de Fomento da Produção Mineral, 22, 29 p.

Toniolo, J.A., Gil, C.A.A., Sander, A., 2007. Projeto BANEO–Metalogenia das Bacias Neoproterozóico–Eopaleozóicas do Sul do Brasil – Bacia do Camaquã. CPRM – Serviço Geológico do Brasil, CD Rom.

Twiss, R.J., Moores, E.M, 1992. Structural geology. University of California, 532 p.

Vedana, L.A., Philipp, R.P., Basei, M.A.S., 2018. Tonian to early Cryogenian synorogenic basin of the São Gabriel Terrane, Dom Feliciano Belt, southernmost Brazil. International Geology Review, 60, 109–133.

Wildner, W., Lima, E.F., Nardi, L.V.S., Sommer, C.A., 2002. Volcanic cycles and setting in the Neoproterozoic III to Ordovician Camaquã Basin succession in southern Brazil: characteristics of post–collisional magmatism. Journal of Volcanology and Geothermal Research, 118, 261–283.

Zvirtes, G., Philipp, R.P., Camozzato, E., Chemale Jr., F., 2015. Metagranito alcalino Capané: evidências de rifteamento e metamorfismo regional orogênico neoproterozóico nos estágios finais de evolução do Cinturão Dom Feliciano. In: IX SIMPÓSIO SUL–BRASILEIRO DE GEOLOGIA, 9, Anais, SBG, Florianópolis, v. 1.

Zvirtes, G., Philipp, R.P., Camozzato, E., Guadagnin, F., 2017. Análise estrutural do Metagranito Capané, Antiforme Capané, Complexo Porongos, Cachoeira do Sul, RS. Revista Pesquisas em Geociências, 44, 05–23.

4.2 Manuscrito II

O manuscrito II foi primeiramente submetido ao *Journal of Geochemical Exploration* em 11/01/2017 e recusado com possível resubmissão em 24/06/2017. O manuscrito foi reescrito e resubmetido em 01/11/2017 para a mesma revista científica. Esta segunda versão passou por uma primeira revisão e foi resubmetida seguindo as correções e sugestões em 23/02/2018. Uma nova revisão foi solicitada e o manuscrito foi resubmetido em 30/08/2018. Após revisão, uma nova versão ainda não submetida foi inserida na presente tese. A tabela suplementar com os dados de microssonda eletrônica é apresentada no ANEXO F.

Assunto **Your manuscript GEXPLO_2017_533_R2 has been sent for review**
Remetente Journal of Geochemical Exploration
Para rodrigo.winck@ufrgs.br
Responder para gexplo-eo@elsevier.com
Data 2018-11-15 23:17

This message was sent automatically. Please do not reply.

Reference: GEXPLO_2017_533_R2
Title: Mineral assemblages and temperature associated with Cu enrichment in the Seival area (Neoproterozoic Camaquã Basin of Southern Brazil)
Journal: Journal of Geochemical Exploration

Dear Mr. Winck Lopes,

I am currently identifying and contacting reviewers who are acknowledged experts in the field. Since peer review is a voluntary service it can take time to find reviewers who are both qualified and available. While reviewers are being contacted, the status of your manuscript will appear in EVISE® as 'Reviewer Invited'.

Once a reviewer agrees to review your manuscript, the status will change to 'Under Review'. When I have received the required number of expert reviews, the status will change to 'Ready for Decision' while I evaluate the reviews before making a decision on your manuscript.

To track the status of your manuscript, please log into EVISE® and go to 'My Submissions' via:
http://www.evise.com/evise/faces/pages/navigation/NavController.jspx?JRNL_ACR=GEXPLO

Kind regards,

Journal of Geochemical Exploration

Have questions or need assistance?
For further assistance, please visit our Customer Support site. Here you can search for solutions on a range of topics, find answers to frequently asked questions, and learn more about EVISE® via interactive tutorials. You can also talk 24/5 to our customer support team by phone and 24/7 by live chat and email.

Mineral assemblages and temperature associated with Cu–enrichment in the Seival area (Camaquã Basin, Neoproterozoic of Southern Brazil)

Rodrigo W. LOPES[1–2], Christophe RENAC[2], André S. MEXIAS[1], Lauro V.S. NARDI[1], Eduardo FONTANA[3], Márcia E.B. GOMES[1], Aurélie BARATS[2]

[1] Universidade Federal do Rio Grande do Sul, Instituto de Geociências, avenida Bento Gonçalves, 9500, 91501–970 Porto Alegre, RS, Brazil
[2] Université Côte d'Azur, CNRS, IRD, Observatoire de la Côte d'Azur, Géoazur UMR 7329, 250 avenue Albert Einstein, 06560, Valbonne, France
[3] Universidade Federal dos Vales do Jequitinhonha e Mucuri, Centro de Geociências, Instituto de Ciência e Tecnologia, Rodovia MGT 367 – Km 583, nº 5000 – Alto da Jacuba, Diamantina, MG, Brazil
E–mail address: rodrigo.winck@ufrgs.br (R.W. Lopes), christophe.renac@unice.fr (C. Renac), andre.mexias@ufrgs.br (A.S. Mexias), lauro.nardi@ufrgs.br (L.V.S. Nardi), eduardo.fontana@ict.ufvjm.edu.br (E. Fontana), marcia.boscato@ufrgs.br (M.E.B. Gomes), aurelie.barats@unice.fr (A. Barats).

Abstract

The Neoproterozoic sequence of volcanic rocks in the Camaquã Basin included in the Lavras do Sul Shoshonitic Association hosts disseminated Cu deposits. The volcanic sequence in the Seival Mine area includes andesitic lava flows, lapilli tuff, volcanic agglomerate and andesitic dikes with pervasive alteration. The hydrothermal alteration is interpreted to be a product of late–magmatic fluids or the mixing of magmatic with meteoric fluids or basinal brines. The late–magmatic hydrothermal system started after volatile oversaturation and degassing in a magmatic system, which was partially segregated into vesicles. The similar REE contents in the andesine–labradorite and albite indicate that the fluid temperatures ranged from 600 to 250 °C. The crystallization of titanite and Fe–clinochlore to Mg–chamosite followed the albitization process. The temperature range associated with the chloritization process was estimated using a chlorite geothermometer and varied from 251 ± 56 to 183 ± 39 °C. The precipitation of Mg–saponite and smectite–rich chlorite/smectite mixed–layers in some andesitic lava flows and the precipitation of quartz, calcite, barite and hematite in fractures suggest fluid circulation with temperatures lower than the chloritization process. The alteration minerals are represented by chlorite and albite associated with pyrite–chalcopyrite, while chlorite/smectite mixed–layers and barite or hematite are associated with bornite–chalcocite–covellite. Thermodynamic calculations confirm the potential coprecipitation of pyrite–chalcopyrite with chlorite and albite. The occurrence of bornite–chalcocite–covellite and barite seems to be favored by low–temperature chlorite/smectite with neutral to mildly acidic water influx. Consequently, albitization and the process of chloritization at high temperatures (> ca. 251 ± 56 °C) can be used as an exploration guide for primary pyrite–chalcopyrite enrichment, and chlorite/smectite at low temperatures (ca. 250 to 50 °C) can be related to bornite–chalcocite–covellite or the process of Cu enrichment.

Keywords: Late–magmatic and hydrothermal alteration; Albitization; Chlorites

1. Introduction

The Neoproterozoic Camaquã Basin and its associated igneous rocks contain significant Au, Cu and Ag ore deposits, such as the Uruguay–São Luiz mines and the Lavras do Sul Mining District (Remus et al., 2000; Bongiolo et al., 2011; Renac et al., 2014). In the central–western section of this basin, volcanogenic (Lopes et al., 2014; Fontana et al., 2017) and plutonic rocks (Mexias et al., 2005) show pervasive alteration described as late–magmatic albitization and hydrothermal alteration with the influx of meteoric fluids (Mexias et al., 1990a, 2005; Bongiolo et al., 2011; Fontana et al., 2017). The largest Cu deposit in this basin is the Camaquã Mine, which is hosted in a Neoproterozoic sedimentary sequence and was exploited from the 18th century until 1996 (Remus et al., 2000; Laux et al., 2005; Renac et al., 2014). This exploited deposit has an ore reserve of ~30.8 Mt with an average Cu grade of ~1.06%, which is manifested as massive veins, stockworks and disseminated chalcopyrite, pyrite, bornite, chalcocite, gold, silver and hematite. The extrusive and intrusive rocks from the Lavras do Sul Mining District (Mexias et al., 2007), which are located on the central–western rim of the Camaquã Basin, host nineteen Au and Au–Cu deposits that were exploited during the same time frame (Bongiolo et al., 2011). The ore zones consist of quartz and sulfide–rich quartz veins (Mexias et al., 2005) associated with wall–rock alteration characterized by ‘sericite’, chlorite, pyrite and chalcopyrite (Bongiolo et al., 2011). In the vicinity of the Lavras do Sul area, the volcanogenic sequence in the Seival area hosts Cu–Ag deposits (Reischl, 1978; Lopes et al., 2014). The different mines yielded ca. 0.20 Mt of Cu–ore with an average grade of ~1.40%. The chalcopyrite, pyrite, chalcocite, bornite and covellite sulfides occurred in association with chlorite, hematite, calcite, barite and quartz disseminated in andesitic lapilli tuff and volcanic agglomerates or along fault planes cutting the volcanic sequence. A recent study on the Seival Mine (Fontana et al., 2017) improved current knowledge about the clay minerals in these ore deposits. Fontana et al. (2017) described the zoning and lithotypes with the predominant occurrence of smectite, chlorite/smectite mixed–layers, chlorite and corrensite, and suggested that the base–metal deposition was related to the late–magmatic process

of albitization and high–temperature hydrothermal alteration. Later low–temperature hydrothermal alteration represented the mixing of magmatic and meteoric fluids. Both albitization and chloritization processes were observed in the granite–related epithermal systems of the Lavras do Sul area (Mexias et al., 2007; Bongiolo et al., 2011) and the Camaquã Mine (Laux et al., 2005; Renac et al., 2014). A similar alteration mineralogy in the vicinity of the Lavras do Sul Intrusive Complex, located 10 km west of the Seival area, suggests that the Lavras do Sul porphyry–epithermal system contributes to the alteration of the andesitic rocks and ore deposition in the Seival area, as also occurs in the Potrerill Cu–Mo porphyry deposits and El Hueso Au epithermal deposits (Sillitoe, 1991; Marsh et al., 1997).

Consequently, this study focused on the chemical signatures of albite and chlorite to smectite in the hydrothermal alteration products. The petrographic and chemical analyses of the minerals were used to estimate the temperatures and bracket temperatures of late–magmatic to hydrothermal alteration. Petrographic observations and temperatures estimated by chlorite geothermometers were introduced into a thermodynamic model. This model was used to reconstruct the chemical conditions favorable to ore deposition in the process of base–metal migration in the Seival area.

2. Geological Setting

2.1 Regional geology

The Mantiqueira Province extends from the southeast of Brazil to Uruguay (Almeida and Hasui, 1984; Silva et al., 2005). In the Gondwana supercontinent, the southern portion of collision between the Rio de La Plata (Brazil) and the Kalahari (Africa) cratons is characterized by the Sul–rio–grandense Shield (Fig. 1A) with Neoproterozoic ages. This collision is represented by the Braziliano Orogeny and the opening of the Camaquã Basin related to the post–collisional stage (Lima and Nardi, 1998; Gastal et al., 2005a, b). The Sul–rio–grandense Shield comprises four geotectonic units: the Taquarembó Terrane, São Gabriel Terrene, Tijucas Terrene, and Pelotas Batholith. Recovering these units, the Camaquã Basin was considered

as a succession of sub–basins (Paim et al., 2000) that contains volcano–sedimentary sequences. The Maricá Group, which is represented by the volcano–sedimentary rocks of the Maricá Formation, is related to a foreland retro arc–basin setting (630–601 Ma; Paim et al., 2000; Borba et al., 2008). The Bom Jardim Group, in which shoshonitic volcanism was emplaced during the strike–slip movement of the basin (600–590 Ma; Janikian et al., 2008), is represented by the Hilário Formation. The late Santa Bárbara Group (574–544 Ma; Sommer et al., 2006; Bicca et al., 2013; Almeida et al., 2012; Janikian et al., 2012; Matté et al., 2016) is mainly represented by the acidic effusive/explosive episodes and minor basic magmatism of the Acampamento Velho Formation and by the sedimentary sequences of the Santa Fé and Santa Bárbara formations (Fig. 1B). The Guaritas Group (547–535 Ma; Almeida et al., 2012; Oliveira et al., 2014) is represented by volcanic rocks of the Rodeio Velho Formation associated with a sedimentary sequence represented by the Pedra Pintada and Guaritas formations related to transtensional tectonic stages (Paim et al., 2000; Almeida et al., 2012). These effusive rocks have basic to intermediate sodic compositions with mildly alkaline to high–K tholeiitic affinities (Almeida et al., 2012).

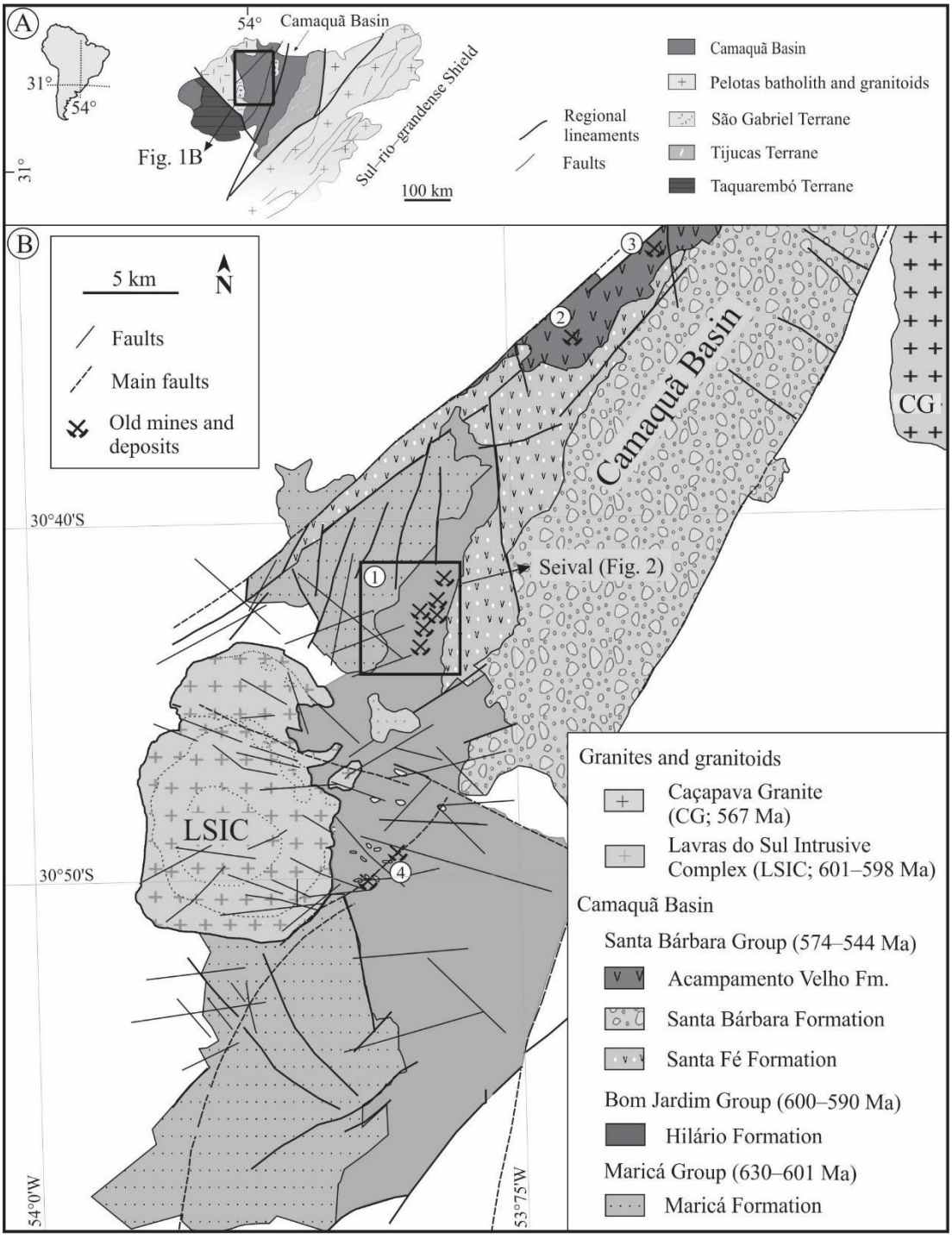

Figure 1. Geological setting of the study area. A) Schematic Sul–rio–grandense Shield map (modified from Hartmann et al., 2007); B) Central–western Camaquã Basin geological map with Seival Mine area and Cu occurrences localization (modified from Toniolo et al., 2007; Gastal et al., 2015). Keys: 1= Seival Mine (Cu and Ag); 2= Silveira Mine (Cu); 3= Crespos Mine (Cu); 4= Volta Grande and Merita Mine (Cu and Au).

The volcano–sedimentary units that occur in the Seival area (Fig. 2) have dominant intermediate compositions with basic and acidic end–members. The Bom Jardim Group, as previously described, consists of the effusive units of the Hilário Formation in the study area (Ribeiro and Fantinel, 1978). The deformation of the Hilário Formation along the Lavras do Sul contact suggests that the Hilário Formation is older than the Lavras do Sul Intrusive Complex (Gastal et al., 2015). The Hilário Formation consists of dominantly andesitic rocks represented by andesitic lava flows, lapilli tuff, volcanic agglomerates, and dikes with a shoshonitic geochemical affinity (Lopes et al., 2014; Fontana et al., 2017). The Ar–Ar radiogenic dating of plagioclase suggests an age of 600 to 590 Ma (Janikian et al., 2008) that might be thermally influenced by intrusive magmas such as dikes or the Lavras do Sul granitoids. The other vesicular lava flows and volcanic clastic materials are represented by the polymictic conglomerates of the Santa Fé Formation. The Acampamento Velho Formation occurs as rhyolite dikes that cross–cut the Hilário Formation.

The granitoids of the Lavras do Sul Intrusive Complex with U–Pb ages varying from 601 to 587 Ma (SHRIMP in zircon, Remus et al., 1999, 2000; Gastal et al., 2006; Liz et al., 2009), comprise a ring structure composed of porphyritic quartz–monzonite granodiorite and syenogranite to monzogranite with monzonitic intrusions in its northeastern margin (Gastal et al., 2006; Liz et al., 2009). In the contact zone between the Lavras do Sul granitoids and the Hilário Formation is a hectometer-thick metamorphic halo (Mexias et al., 1990a, b; Bongiolo et al., 2011) attesting to the thermal influence of granitoids on the volcano–sedimentary pile.

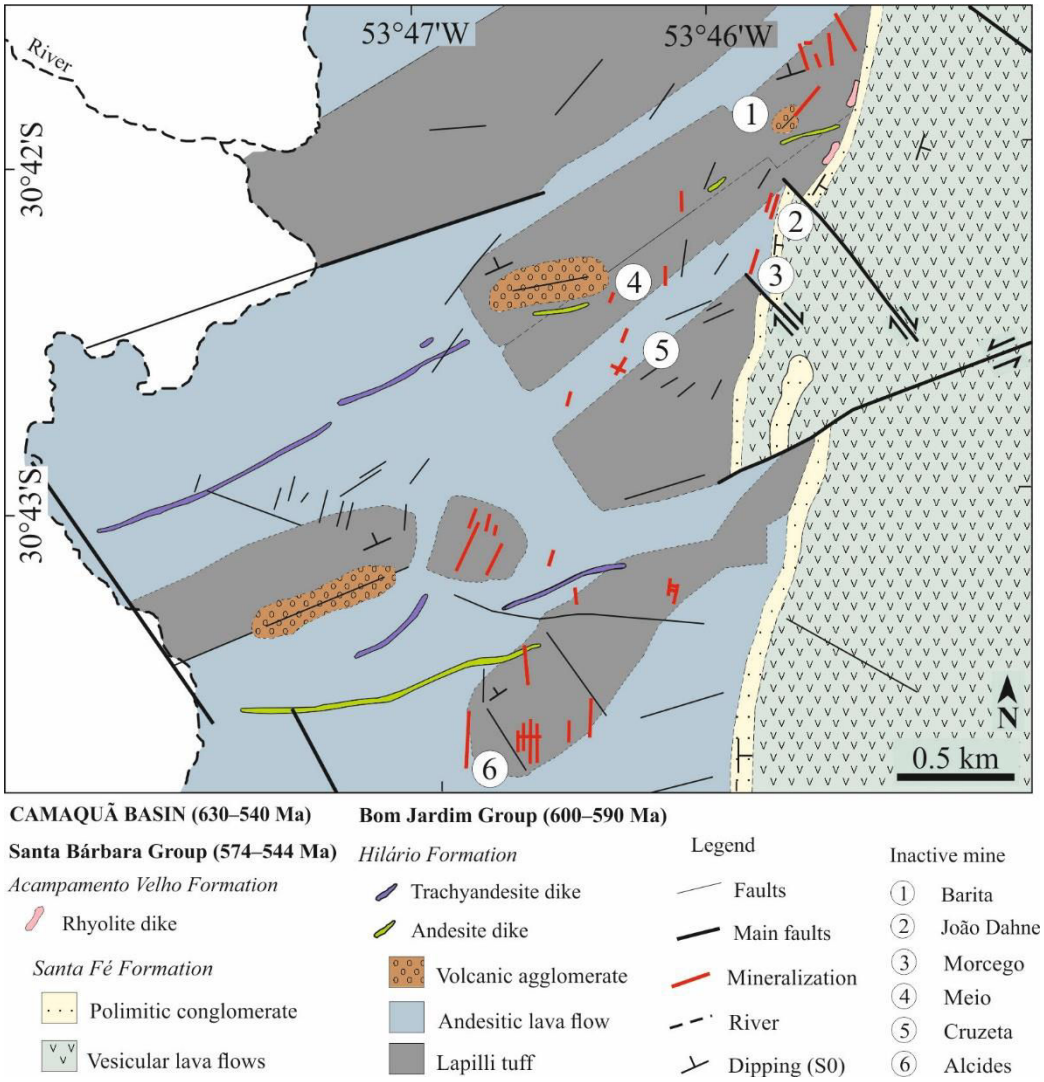

Figure 2. Geological map of the Seival Mine. Sequence of lapilli tuff, andesitic lava flows and volcanic agglomerate with andesitic and trachyandesitic dike (NE direction) from Hilário Formation (HF), polymictic conglomerate and vesicular lava flows from Santa Fé Formation (SFF), rhyolite dikes of Acampamento Velho Formation (AVF), faults, mineralization projections, inactive open pit mines and bore–hole localization (modified from Reischl, 1978; Lopes et al., 2014). Keys: 1= Barita Mine; 2= João Dahne Mine; 3= Morcego Mine; 4= Meio Mine; 5= Cruzeta Mine; 6= Alcides Mine.

2.2 Ore geology

The Seival hosts six inactive Cu–bearing deposits and several prospects. This reserve was estimated at ~0.20 Mt of ore with an average grade of ~1.40% of Cu and 10–70 ppm of Ag (Fig. 3A; Reischl, 1978; Lopes et al., 2014). The ore deposits

in the Seival area were associated with the development of NE–SW-oriented shear zones that cross-cut the Camaquã Basin (Fernandes et al., 1992; Philipp et al., 2016). The emplacement of metallic mineralizations are bracketed between 600 and 580 Ma ago based on the ages of lava flows (Janikian et al., 2008), tectonic activity (Gastal et al., 2015) and the Lavras do Sul magmatism (Gastal et al., 2006; Almeida et al., 2012).

The sulfides are represented by chalcopyrite, bornite, chalcocite and covellite (Fontana et al., 2017) and are part of the main Cu–bearing veins that fill fractures and faults. The alteration halos are related to the distances of mineralized structures (Lopes et al., 2014; Fontana et al., 2017). The mineral association of chlorite, epidote and calcite formed at temperature of ~300 °C (Mexias et al., 1990b; Mexias et al., 2007; Bongiolo et al., 2011) in the volcanogenic rocks of the Hilário Formation close to the Lavras do Sul granitoids.

The mineral assemblages allow for the characterization of hydrothermal zones (Seedorff et al., 2005; Sillitoe, 2010). Propylitic alteration was related to chlorite, C/S mixed–layer, hematite, titanite, calcite, barite and quartz associated with pyrite–chalcopyrite and chalcocite–bornite, while argillic alteration was related to smectite and quartz (Fig. 3B; Lopes et al., 2014; Fontana et al., 2017). Cu enrichment was associated with propylitic alteration and the formation of albite (600 to 250 °C; Fontana et al., 2019) and Mg–chamosite to Fe–clinochlore (251 to 180 °C). The late–hydrothermal veins are composed of barite, calcite and minor proportion of veins with calcite–quartz assemblage . These late precipitations represent the lowest temperatures of hydrothermal alteration (150 to 80 °C; Fontana et al., 2017). In the preserved parts of these inactive mines, mineralization occurs as a stockwork of veins or disseminated in volcaniclastic rocks and andesitic lava flows (Fontana et al., 2017). The faults, mineralized structures and dikes are considered contemporaneous based on the mineralogy and alteration type. Thus, the hydrothermal processes can be associated with the intrusion of NE–SW-oriented andesite (Lopes et al., 2018) and local hydrothermal cells.

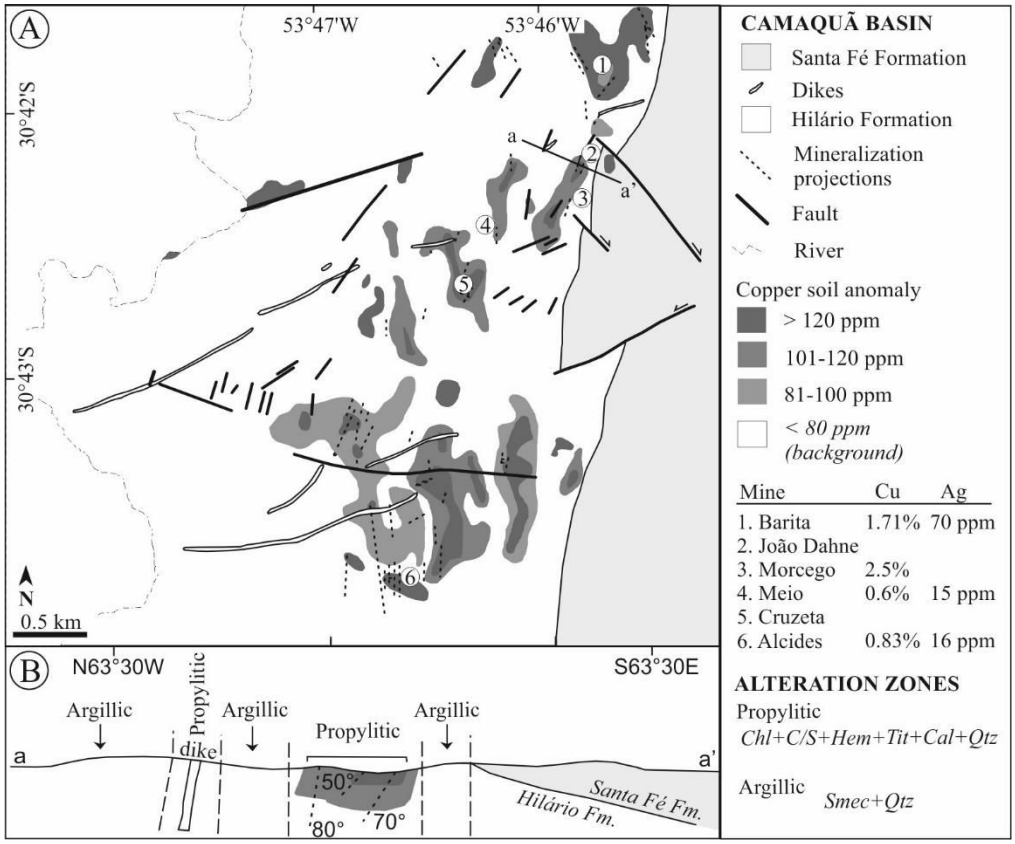

Figure 3. Mineralization in the Seival Mine area. A) Cu soil anomaly (modified from Reischl, 1978) and inactive open pit mines, faults and Cu–mineralization; B) Schematic section of alteration zones in Hilário Formation. Keys: Chl= Chlorite; C/S= Chlorite/smectite mixed–layer; Hem= Hematite; Tit= Titanite; Cal= Calcite; Qtz= Quartz; Cc= Chalcocite; Bn= Bornite; Smec= Smectite.

3. Analytical methods

Field work consisted of sample collection and logging of drill cores. The samples collected were representative of lapilli tuff, amygdaloidal to porphyritic andesitic lava flows and dikes. Petrographic observations of thin sections allowed the description of magmatic and hydrothermally altered crystals. The minerals, after of crushing and sieving, were separated using a magnetic separator, heavy liquids and hand–picking under a binocular microscope. Products of alteration were either collected under a binocular microscope in the altered phenocrysts or identified in the clay–size fraction. These petrographic observations, mineral separation and clay–size fraction were characterized by scanning electron microscopy combined with energy–dispersive spectrometry (SEM–EDS, Zeiss EVO LS15, 20 kV, 2.5 nA with X–Max Oxford EDS

detectors, IAEA Monaco) and X–ray diffraction (Siemens D5000, KαCu, 40 kV and 25 mA, Geoscience Institute–CPGq–UFRGS). X–ray patterns of the clay minerals were obtained in < 0.4 µm clay–size fraction. Major element composition as oxides (SiO_2, TiO_2, Al_2O_3, FeO_{total}, MnO, MgO, CaO, Na_2O, F and K_2O) in minerals from thin section were quantified by electron microprobe (CAMECA, SXFive model equipped with TAP, PET and LIF crystal detectors) at the Geoscience Institute, Universidade Federal do Rio Grande do Sul, Brazil. The beam diameter is about 10 to 4 µm with an acceleration voltage of 15 kV and 15 nA with counting time per element of 10 sec and background counting times of 5 sec per element. Chemical calibrations were performed on albite, jadeite, diopside, sanidine, rutile, rhodonite and hematite standards mounted in epoxy resin. The mineral composition in thin section were calculated of atom per formula unit (a.p.f.u.) assumed the following number of oxygen atoms for ideal compositions of feldspar (32), pyroxene (12), biotite (22), titanite (5), smectite (22), chlorite/smectite mixed–layer (28) and chlorite (28). Charge balance of structural formula was obtained by the adjustment of Fe^{2+} and Fe^{3+} proportions, including for smectite and biotite, where only Fe^{2+} was considered. Analyzes in ten thin sections were performed to follow changes from preserved magmatic minerals to mineral transformed or precipitated by the hydrothermal alteration. Based on major element compositions, chemical changes will then be related to albitization and chloritization processes. The complete dataset of primary and hydrothermal minerals analyzed are available in Supplementary Table A–G.

The major element changes observed in plagioclase were completed by rare earth elements (REE; lanthanides, Y and Sc) analyzes. These REEs have been measured from plagioclase separates preliminary recovered for phenocrysts and the microlithic matrix subsequently recognized with different major element compositions. These REE concentrations were measured from feldspar separates preliminary acid leached with ultrapure HNO_3 (1N) to dissolve traces carbonates and oxides on the surface of the grains separated then clean in ultrapure pure MQ water. Later, cleaned grains were then acid digested in ultrapure HNO_3 (15N) and HF (20N).

Inductively-coupled plasma mass spectrometry analyzed all digested samples diluted in 1% HNO_3 solutions (ICP–MS: Elan DRCII, Perkin Elmer at the University of Nice Sophia–Antipolis). Quantification limits are below 50 ng/L. Element concentration was expressed as ppm and then normalized with respect to chondrite values (McDonough and Sun, 1995). The Eu/Eu*= the values of the Eu anomaly were calculated using $[Eu/Eu^*]= [(Eu_N)/((Sm_N \times Gd_N)^{1/2})]$ formula from Worrall and Pearson (2001).

The different mineralogical and chemical data of magmatic minerals were used with the petrogenetic model (MELTS software modeling; Ghiorso and Sack, 1995) to reconstruct magmatic conditions. The magmatic and hydrothermal minerals were combined in a thermodynamic model (PHREEQC interactive; Parkhurst, 1995) to estimate the favorable conditions for precipitation of hydrothermal phases and sulfides.

4. Results

4.1 Textures and petrographic observations

The host rocks of the Cu deposits in the Seival area are predominantly andesitic lava flows and lapilli tuff (Fig. 4A) to volcanic agglomerates with rounded andesitic pyroclasts. Their aphyric matrixes are dark to glassy and green with disseminated microlites of plagioclase and fragments of pyroxene. Amygdaloidal and porphyritic andesitic lava flows are predominant in the southern and northeastern parts of the Seival area and are in contact with the Santa Fé Formation (Fig. 2). Subvolcanic rocks have andesitic (Fig. 4B) to trachyandesitic compositions with feldspar phenocrysts, dominant pyroxene and scarce biotite phenocrysts.

Most of the rocks are intensively fractured and brecciated, particularly those with higher Cu sulfide contents. The andesitic pyroclasts in the lapilli tuff show vesicles or amygdaloids. The amygdaloidal matrix in the lapilli tuff consists of fragments of igneous plagioclase and pyroxene. The petrographic observations of pyroxene revealed the replacement by clay minerals and calcite or intergranular

spaces filled by clay minerals, quartz, calcite, titanite, pyrite, chalcopyrite, and minor hematite (Fig. 4C).

Porphyritic andesitic lava flows have phenocrysts of plagioclase and clinopyroxene in a trachytic matrix with oriented plagioclase. Andesitic dikes host subhedral grains of feldspars further identified as plagioclase with rims of K–feldspar (Fig. 4D) and phenocrysts of pyroxene. Some trachyandesitic dikes have subhedral phenocrysts of plagioclase, pyroxene and biotite. Some plagioclase and biotite phenocrysts have inclusions of apatite, zircon (50 to 200 µm) and titanite, while the oxidized matrix contains hematite. The titanite grains occur as euhedral grains associated with biotite and pyroxene and as anhedral grains of smaller granular agglomerates in the altered matrix.

As previously described (Lopes et al., 2014; Fontana et al., 2017), the Hilário volcanic sequence in the studied area is pervasively altered to clay minerals, calcite, barite and quartz. The original igneous mafic minerals and different matrixes have a light green material recognized as chlorite/smectite mixed–layer (Fig. 4E). Albite, chlorite and sulfide occur in the more altered rocks with traces of calcite and specular hematite, and euhedral or agglomerates of titanite occur with albite and microscopic euhedral quartz (Fig. 4F).

Less-altered material occurs in the amygdaloidal andesitic lava flows from the south and west. Nevertheless, these lava flows are partially altered to dark clay minerals (Fig. 4G) between crystals or exhibit quartz, pyrite–chalcopyrite and calcite filling vesicles. Petrographic observations indicate the predominance of clay minerals associated with sulfides in the intergranular porosity that are further recognized as chlorite and dominant pyrite–chalcopyrite, or the association of chlorite/smectite mixed–layer (Fig. 4H) with minor pyrite–chalcopyrite and dominant chalcocite–covellite or chalcocite–bornite. The malachite and azurite observed in the different open pits are the product of the recent weathering of Cu–rich sulfides.

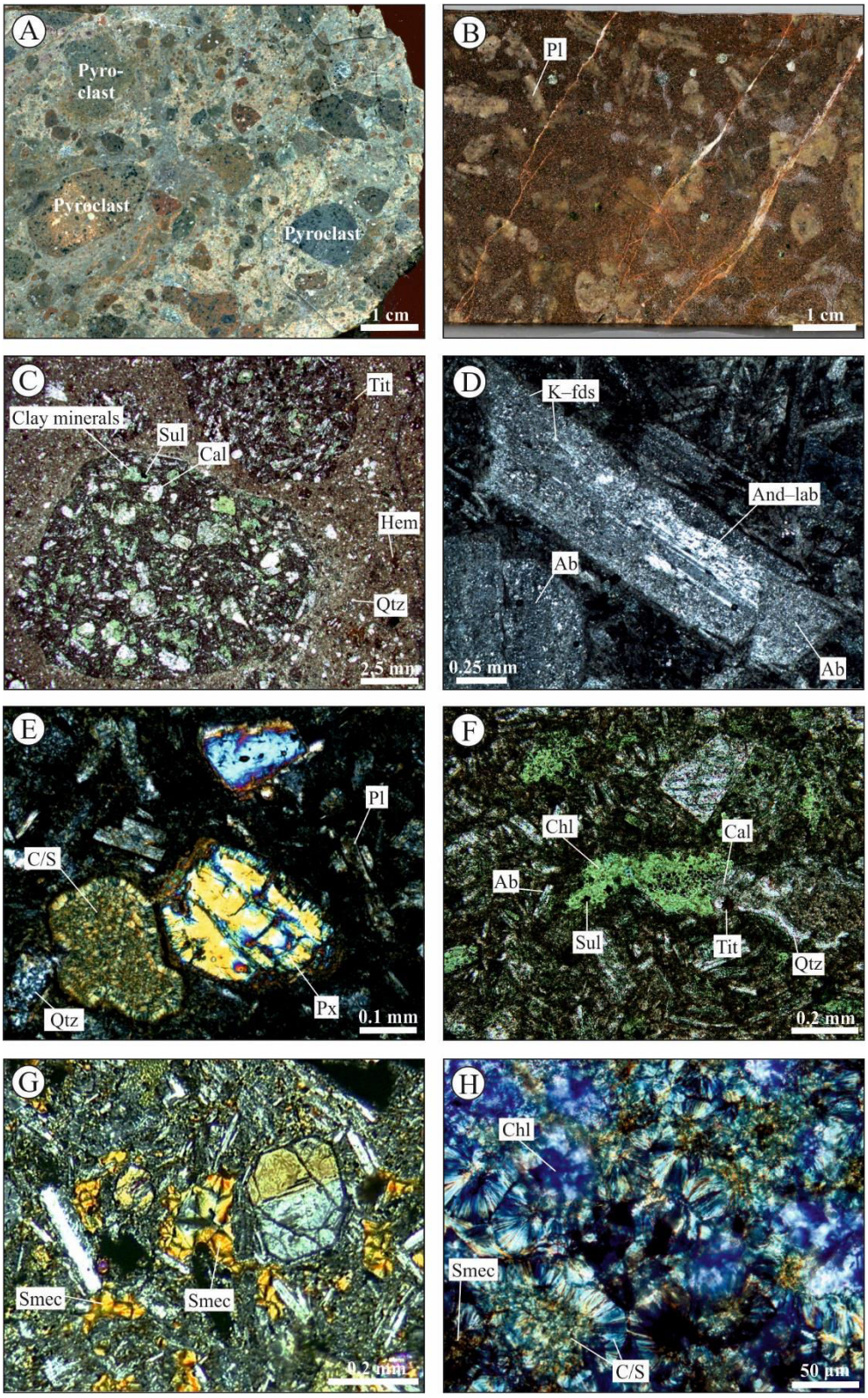

Figure 4. Macroscopic photograph (A and B), photomicrograph in natural (C and F) and polarized light (D, E, G and H). A) Hand sample containing altered pyroclasts of

lapilli tuff; B) Hand sample with plagioclase and altered matrix in andesite dike; C) Pervasive clay minerals alteration in lapilli tuff; D) Zoned phenocryst of plagioclase with indication of unaltered andesine–labradorite and altered plagioclase with albite composition in andesitic dike; E) Clinopyroxene and vesicle fulfilled by smectite–rich chlorite/smectite in less altered amygdaloidal andesitic lava flows; F) Amygdaloidal andesitic lava flows pyroclast of lapilli tuff fulfilled by chlorite, calcite, sulfide, titanite and quartz; G) Smectite in less altered andesitic lava flows; H) Vesicle fulfilled by chlorite/smectite mixed–layers in andesitic lava flows. Keys: Pl= Plagioclase; Sul= Sulfide; Cal= Calcite; Tit= Titanite; Hem= Hematite; Qtz= Quartz; K–fds= K–feldspar; And–lab= Andesine–labradorite; Ab= Albite; C/S= Chlorite/smectite mixed–layer; Px= Pyroxene; Chl= Chlorite, Smec= Smectite.

4.2 Major element compositions of magmatic to late–magmatic minerals and REE compositions of feldspars

Phenocrysts and microlites or crystalloclasts of pyroxene in porphyritic andesitic lava flows and andesitic dikes are augite ($Wo_{0.40–0.47}$ $En_{0.32–0.41}$ $Fs_{0.12–0.28}$; Fig. 5A; Supplementary Table A). According to the structural formula of augite (Table 1), the atomic ratios of [$Mg/(Mg+Fe_{tot})$= 0.67–0.85] are high and those of [Na/(Ca+Na)= 0.02–0.05)] are low.

Prismatic biotite phenocrysts recognized in trachyandesitic dikes are classified as Mg–biotite with the structural formula expressed in Supplementary Table B. The less pristine Mg–biotites show slightly different compositions (Table 1), with increases in Al^{VI} (Fig. 5B) and lower contents of Fe, Mg and Mn (Table 1). The euhedral to agglomerate titanite grains (Fig. 5C; Table 1 and Supplementary Table C) are associated with albite and biotite phenocrysts, and the anhedral grains in the matrix have similar chemical compositions.

The chemical compositions of feldspars were analyzed in thin section. The plagioclase phenocrysts have compositions of andesine–labradorite ($An_{0.43–0.53}$ $Ab_{0.43–0.54}$ $Or_{0.03–0.05}$) (Table 1). Moreover, some of the andesine–labradorite phenocrysts have a thin rim of K–feldspar ($An_{0–0.01}$ $Ab_{0–0.33}$ $Or_{0.66–1}$; Fig. 4B and Fig. 5D; Table 1), further described as Group I. In contrast, the microlites and phenocrysts of plagioclase (Supplementary Table D) from altered lapilli tuff, porphyritic andesitic lava flows and andesitic dikes consist of dominant albite ($An_{0–0.06}$ $Ab_{0.89–1}$ $Or_{0–0.10}$; Table 1), further described as Group II. The feldspar separates

were characterized by X–ray diffraction and observed by SEM–EDS. The separates with traces of illite or quartz were removed from further REE measurements. The total REE content of andesine–labradorite (Group I) and albite (Group II) have similar patterns and are slightly higher in albite. However, the andesine–labradorite have positive Eu anomalies (Group I: Eu/Eu*= 2.94–4.60; Group II: Eu/Eu*= 0.90–1.43; Table 2).

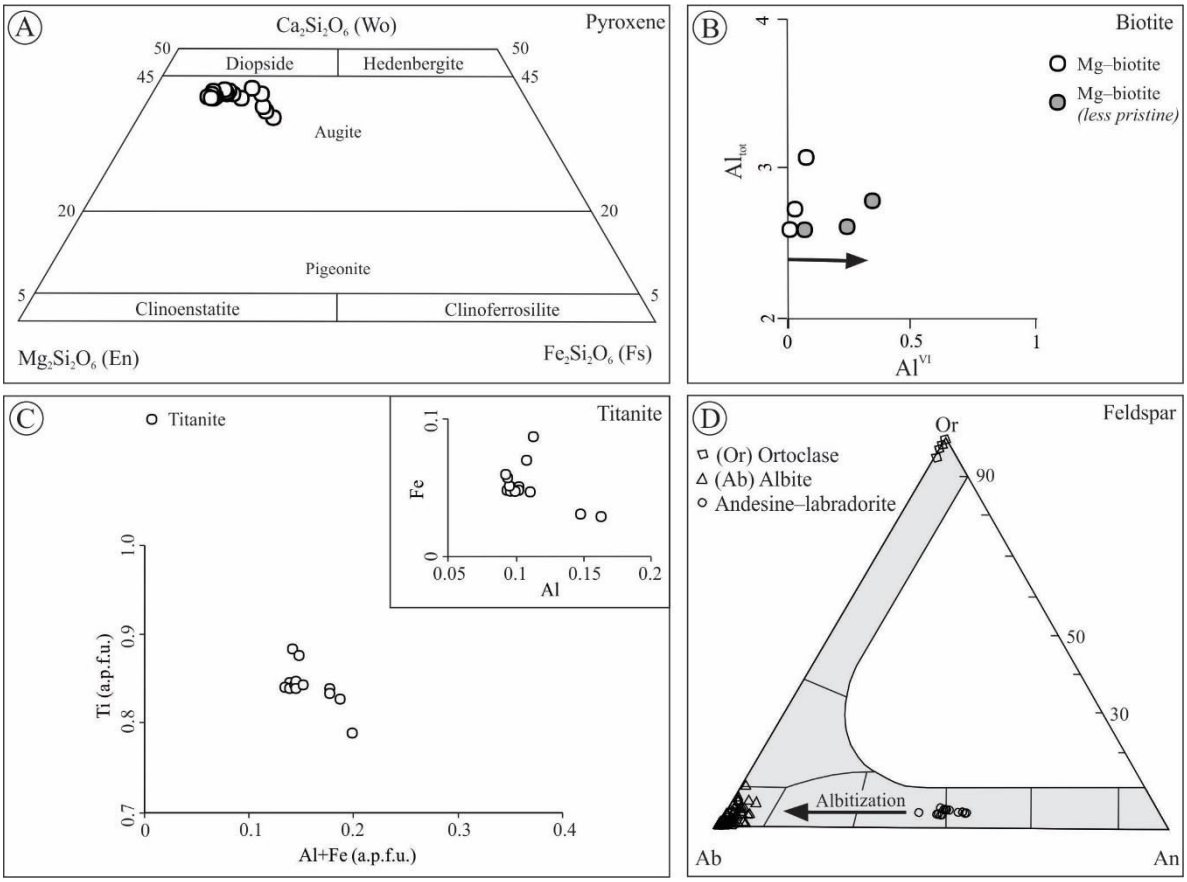

Figure 5. Plots of mineral compositions. A) Ca–Mg–Fe clinopyroxenes showing augite compositions in andesitic lava flows and andesitic dike; B) Biotite (white point) and less pristine biotite (gray point) in the Al_{tot} *vs* Al^{VI} diagram; C) $Al+Fe^{3+}$ *vs* Ti and Al *vs* Fe binary diagram of the hydrothermal titanite compositions (diagram extracted from Cao et al., 2015); D) An–Ab–Or ternary feldspar diagram showing albitization in andesine–labradorite and rims with K–feldspar in some zoned plagioclase (An= Anorthite; Ab= Albite; Or= Orthoclase).

Table 1. Summary of mineral, host rock and structural formula of magmatic, magmatic to late–magmatic and hydrothermal phases. Nomenclature of chlorites after Bayliss (1975).

Host rock	Mineral	Structural formula
Magmatic phase		
Andesitic lava flow and dike: less altered	Augite	$[(Ca_{0.70–0.81}\ Na_{0.01–0,03})\ (Fe^{+2}_{0.15–0.32}\ Mg_{0.86–0.97})\ (Al_{0.06–0.19}\ Ti_{0–0.02}\ Fe^{+3}_{0–0.06})\ (Si_{1.88–1.99})\ O_{12}]$
Trachyandesitic dike: magmatic or pristine	Mg–biotite	$[(Ca_{0.01–0.03}\ Na_{0.09–0.25}\ K_{0.61–1.41})\ (Fe^{+2}_{1.92–2.3}\ Mg_{2.95–3.81}\ Mn_{0.01–0.03}\ Al_{0–0.07}\ Ti_{0.44–0.76})^{VI}\ (Al_{2.61–2.98}\ Si_{5.02–5.39})^{IV}\ O_{20}\ OH_{3.75–3.96}\ F_{0.03–0.25}]$
Trachyandesitic dike: less pristine	Mg–biotite	$[(Ca_{0.01–0.02}\ Na_{0.20–0.24}\ K_{1.22–1.49})\ (Fe^{+2}_{1.79–2.02}\ Mg_{2.72–2.89}\ Mn_{0.01–0.02}\ Al_{0.07–0.33}\ Ti_{0.61–0.75})^{VI}\ (Al_{2.39–2.54}\ Si_{5.46–5.61})^{IV}\ O_{20}\ OH_{3.73–3.85}\ F_{0.15–0.27}]$
Magmatic to late–magmatic phase		
Andesitic dike: euehdral to agglomerates	Titanite	$[(Ca_{0.94–1.02}\ \square_{0.02}\ Ti_{0.79–0.88}\ Al_{0.09–0.16}\ Fe^{3+}_{0.03–0.09}\ Mg_{0–0.03}\ Si_{1.01–1.07}\ O_5)]$
Andesitic dike and lava flow: less altered	Andesine–labradorite	$[(An_{0.43–0.53}\ Ab_{0.43–0.54}\ Or_{0.03–0.05})]$
Andesitic dike	K–feldspar	$[(An_{0.43–0.53}\ Ab_{0.43–0.54}\ Or_{0.03–0.05})]$
Andesitic lava flow and dike: more altered	Albite	$[(An_{0–0.06}\ Ab_{0.89–1}\ Or_{0–0.10})]$
Hydrothermal phase		
* Porphyritic andesitic lava flow: augite replacement	Mg–chamosite to Fe–clinochlore	$[(Ca_{0.04–0.06}\ Na_{0–0.04}\ K_{0.02–0..11})\ (Al_{2.70–3.03}\ Ti_{0–0.01}\ Fe^{3+}_{0.37–0.57}\ Fe^{2+}_{3.61–5.23}\ Mg_{3.07–3.97}\ Mn_{0.01–0.04})^{VI}\ (Si_{5.94–6.24}\ Al_{1.76–2.06})^{IV}\ O_{20}\ (OH)_8]$
** Lapilli tuff: filled vugs	Mg–chamosite	$[(Ca_{0–0.03}\ Na_{0–0.04}\ K_{0–0.11})\ (Al_{2.70–3.11}\ Ti_{0–0.01}\ Fe^{3+}_{0.31–0.46}\ Fe^{2+}_{4.38–5.14}\ Mg_{3.17–3.50}\ Mn_{0.01–0.02})^{VI}\ (Si_{5.62–6.01}\ Al_{1.99–2.38})^{IV}\ O_{20}\ (OH)_8]$
*** Andesitic dikes: matrix	Mg–chamosite to Fe–clinochlore	$[(Ca_{0.03–0.12}\ Na_{0–0.03}\ K_{0.01–0.05})\ (Al_{1.63–2.13}\ Ti_{0–0.01}\ Fe^{3+}_{0.1–0.28}\ Fe^{2+}_{4.26–5.49}\ Mg_{4.4–4.74}\ Mn_{0.03–0.08})^{VI}\ (OH)_4\ (Si_{6.20–6.62}\ Al_{1.38–1.80})^{IV}\ O_{20}\ (OH)_8)]$
Amygdaloidal andesitic lava flow: less altered rocks	Mg–saponite	$[(Ca_{0.18–0.31}\ Na_{0.02–0.05}\ K_{0.02–0.07})\ (Al_{0.06–0.23}\ Ti_{0–0.01}\ Fe^{+2}_{1.35–1.78}\ Mg_{4.50–4.81}\ Mn_{0.02–0.03})^{VI}\ (Si_{6.41–6.98}\ Al_{1.02–1.59})^{IV}\ O_{20}\ (OH)_2]$
Amygdaloidal andesitic lava flow: less altered rocks	Chl–rich C/S mixed–layer	$[(Ca_{0.05–0.16}\ Na_{0–0.09}\ K_{0.01–0.05})\ (Al_{1.59–1.93}\ Ti_{0–0.01}\ Fe^{3+}_{0.18–0.49}\ Fe^{2+}_{2.68–3.77}\ Mg_{5.70–6.37}\ Mn_{0.03–0.05})^{VI}\ (Si_{6.53–7.23}\ Al_{0.77–1.47})^{IV}\ O_{20}\ (OH)_8]$
Porphyritic andesitic lava flow: more altered rock	Chl–rich C/S mixed–layer	$[(Ca_{0.05–0.07}\ Na_{0.02–0.06}\ K_{0.01–0.03})\ (Al_{2.21–2.46}\ Ti_{0–0.02}\ Fe^{3+}_{0.46–0.61}\ Fe^{2+}_{2.19–2.74}\ Mg_{5.59–5.86}\ Mn_{0.06–0.07})^{VI}\ (Si_{6.52–6.75}\ Al_{1.25–1.48})^{IV}\ O_{20}\ (OH)_8]$

Table 2. Measured REE analyzes and normalized values to McDonough and Sun (1995) in separate plagioclase grains of the Seival Mine, andesitic lava flows located outside of the area (black line) and whole–rock analyzes (Lopes et al., 2014). Keys: And= Andesitic lava flows; AD= Andesitic dike; Outs. area= Andesitic lava flows located of outside studied area; Light REE= La to Sm; Heavy REE= Eu to Lu; ΣREE= Sum of total concentration of not normalized rare earth elements; Eu/Eu*= The value of the normalized Eu anomaly calculated by the formula [Eu/Eu*]= [(Eu_N)/((Sm_N x Gd_N)$^{1/2}$)] from Worrall and Pearson (2001).

Sample (mg/kg)	RFM 55 – And	WL 13 – And	WL 19 – And	FM 13 – AD	DD 62 – AD
Y	9.18	3.15	2.26	0.23	1.61
La	28.39	7.70	5.47	1.66	6.18
Ce	55.31	19.25	16.08	2.68	15.41
Pr	8.15	2.29	2.06	0.32	1.65
Nd	32.46	8.71	8.07	1.14	6.10
Sm	5.85	2.12	2.25	0.18	1.77
Eu	2.28	0.60	0.67	0.17	1.79
Gd	5.55	1.94	1.92	0.18	1.89
Tb	0.74	0.26	0.26	0.02	0.21
Dy	3.07	1.11	1.05	0.07	0.78
Ho	0.65	0.23	0.21	0.02	0.15
Er	1.80	0.59	0.56	0.04	0.40
Tm	0.28	0.09	0.09	0.01	0.06
Yb	1.46	0.45	0.45	0.03	0.29
Lu	0.35	0.12	0.12	0.01	0.08
Normalization standard CI chondrite (McDonough and Sun, 1995)					
La	119.77	32.50	23.10	6.99	26.07
Ce	90.23	31.40	26.23	4.37	25.14
Pr	87.81	24.68	22.19	3.41	17.80
Nd	71.04	19.06	17.66	2.49	13.35
Sm	39.55	14.32	15.20	1.20	11.98
Eu	40.48	10.57	11.87	3.04	31.85
Gd	27.90	9.74	9.66	0.89	9.50
Tb	20.44	7.31	7.15	0.55	5.73
Dy	12.48	4.50	4.26	0.30	3.16
Ho	11.83	4.12	3.83	0.27	2.71
Er	11.27	3.69	3.53	0.26	2.51
Yb	9.09	2.80	2.81	0.20	1.82
Lu	14.27	4.72	4.88	0.28	3.09
ΣLREE	130.16	40.07	33.93	5.98	31.11
ΣHREE	16.18	5.39	5.33	0.55	5.65
ΣREE	155.52	48.61	41.52	6.76	38.37
Eu/Eu*	1.22	0.90	0.98	2.94	2.99

Continuation of Table 2

Sample (mg/kg)	RFM 66 – AD	FM 33 – AD	FM 32 – AD	DD 76 – AD	RFM 68 – Outs. Area
Y	1.63	0.41	1.36	11.03	1.24
La	9.95	2.16	4.30	31.66	8.09
Ce	17.54	5.57	14.19	60.18	13.61
Pr	1.90	0.66	1.89	7.79	1.46
Nd	6.54	2.51	7.31	29.43	5.04
Sm	1.51	0.45	2.61	6.47	0.82
Eu	2.36	0.17	0.82	3.05	1.75
Gd	1.62	0.37	2.19	6.50	0.90
Tb	0.17	0.04	0.28	0.81	0.09
Dy	0.58	0.16	1.04	3.20	0.30
Ho	0.11	0.03	0.20	0.63	0.06
Er	0.31	0.09	0.54	1.64	0.16
Tm	0.04	0.01	0.08	0.24	0.02
Yb	0.22	0.07	0.39	1.21	0.11
Lu	0.05	0.02	0.12	0.29	0.03
Normalization standard CI chondrite (McDonough and Sun, 1995)					
La	42.00	9.10	18.16	133.60	34.12
Ce	28.62	9.09	23.15	98.18	22.21
Pr	20.48	7.12	20.42	83.91	15.70
Nd	14.32	5.48	16.01	64.40	11.03
Sm	10.22	3.02	17.66	43.73	5.53
Eu	41.95	2.98	14.55	54.09	31.07
Gd	8.14	1.88	10.98	32.67	4.50
Tb	4.63	1.22	7.73	22.49	2.41
Dy	2.35	0.64	4.24	13.02	1.21
Ho	2.03	0.57	3.70	11.45	1.04
Er	1.94	0.56	3.39	10.26	0.98
Yb	1.37	0.43	2.43	7.54	0.69
Lu	2.15	0.69	4.67	11.91	1.06
ΣLREE	37.44	11.35	30.30	135.53	29.02
ΣHREE	5.46	0.96	5.66	17.57	3.42
ΣREE	44.53	12.72	37.32	164.13	33.68
Eu/Eu*	4.60	1.25	1.04	1.43	6.23

4.3 Mineralogy and major elemental compositions of clay minerals

Petrographic observations show “green clays” replacing pyroxene, biotite or feldspars that fill vesicles and intergranular porosity. Similar to Fontana et al. (2017), using X–ray diffraction techniques on clay–size fractions allowed for the identification of dominant trioctahedral smectite and smectite–rich (C/S) in less altered andesitic lava flows, as well as chlorite–rich chlorite/smectite mixed–layer and chlorite in more altered andesitic lava flows and lapilli tuff. The occurrence of different clay minerals for similar andesitic lithotypes suggests that hydrothermal alteration is not completely related to the primary magmatic mineralogy but to the influx of external fluid. The in–situ electron microprobe analyses allowed for the identification of the composition of the large chlorite flakes (Fig. 6) in the cleavage of andesine–labradorite and albite and the replacement of augite phenocrysts or micrometer vugs in the andesitic dikes with a light green color (Table 1). Based on the $Fe^{2+}/(Fe^{2+}+Mg)$ ratio, these chlorites have compositions of Fe–clinochlore to Mg–chamosite (Supplementary Table E). The observed $Fe^{2+}/(Fe^{2+}+Mg)$ atomic ratios between 0.47 and 0.64 suggest that values < 0.5 are Fe–clinochlore and those of > 0.5 are Mg–chamosite. These two types of chlorite were also recognized in a regional epithermal system (Fig. 7; Mexias et al., 1990b; Bongiolo et al., 2011) and distal–epithermal halo from the Camaquã Mine (Fig. 7; Troian et al., 2010; Renac et al., 2014). Low $Fe^{2+}/(Fe^{2+}+Mg)$ proportions are structurally compensated by tetrahedral and octahedral aluminum (Al^{IV}= 1.7 to 3.4; Al^{VI}= 2.7 to 3.11). The Fe–clinochlore to Mg–chamosite in andesitic lava flows and lapilli tuff have lower Fe^{2+}+Mg atomic proportions (7.5 to 8.5; atomic ratios of $Fe^{3+/}Fe_{tot}$= 0.01 to 0.06) than in andesitic dikes (Fe^{2+}+Mg= 9 to 10.1; atomic ratio of Fe^{3+}/Fe_{tot}= 0.05). However, the chloritization of augite and filling of vugs reflect increasing contents of Fe+Al and Fe+Mg total contents in lapilli tuff and andesitic dikes, respectively. In addition, the Fe–clinochlore to Mg–chamosite compositions are very similar (Fig. 8A; Table 1) and were described using the same structural formula.

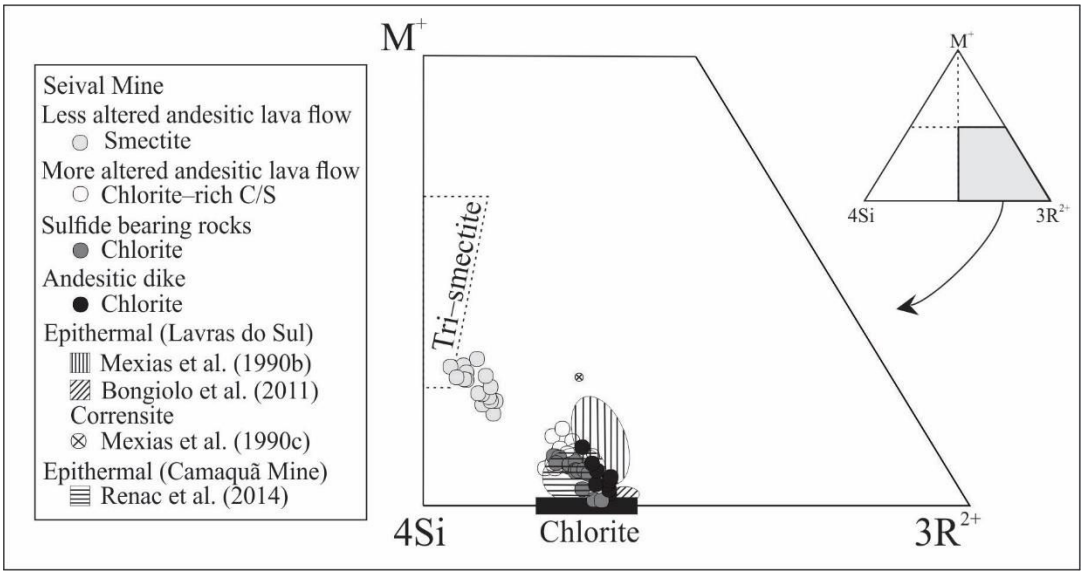

Figure 6. Chemical compositions of a series of saponite, chlorite and chlorite/smectite mixed–layers in projection M^+, 4Si and $3R^{2+}$ (Velde, 1985; adapted from Inoue et al., 1984) with detail showing the smectite, chlorite–rich C/S mixed–layer (C/S) and chlorite compositions from Seival Mine, as well as comparison between chlorites analyzes from epithermal Lavras do Sul (Mexias et al., 1990b,c; Bongiolo et al., 2011) and Camaquã Mine (Renac et al., 2014).

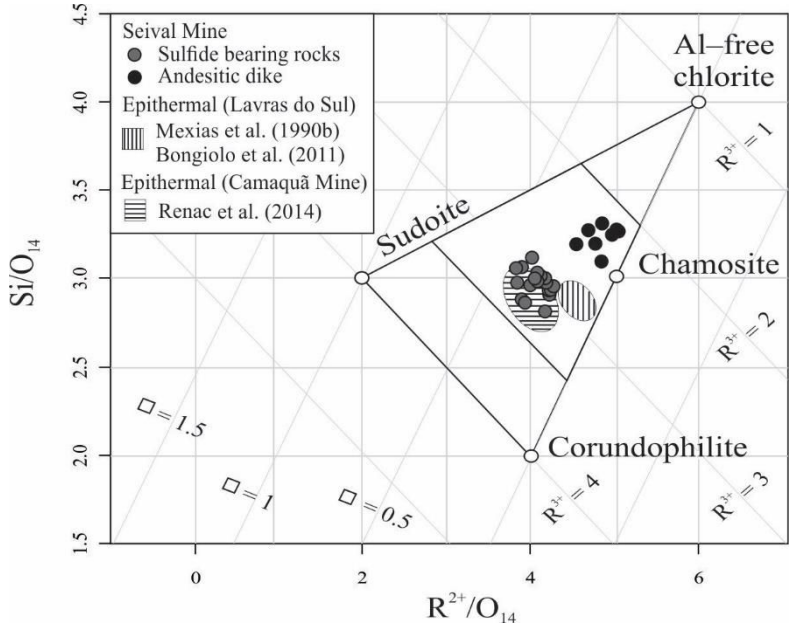

Figure 7. Atomic proportions of chlorites in vein and matrix of andesitic dikes presented in Wiewiora and Weiss diagram (1990), of Si and divalent transition metals normalized to chlorite atom per formula (28 oxygen total anions atoms) in

comparison with epithermal system from Lavras do Sul (Mexias et al., 1990b; Bongiolo et al., 2011) and Camaquã Mine (Renac et al., 2014).

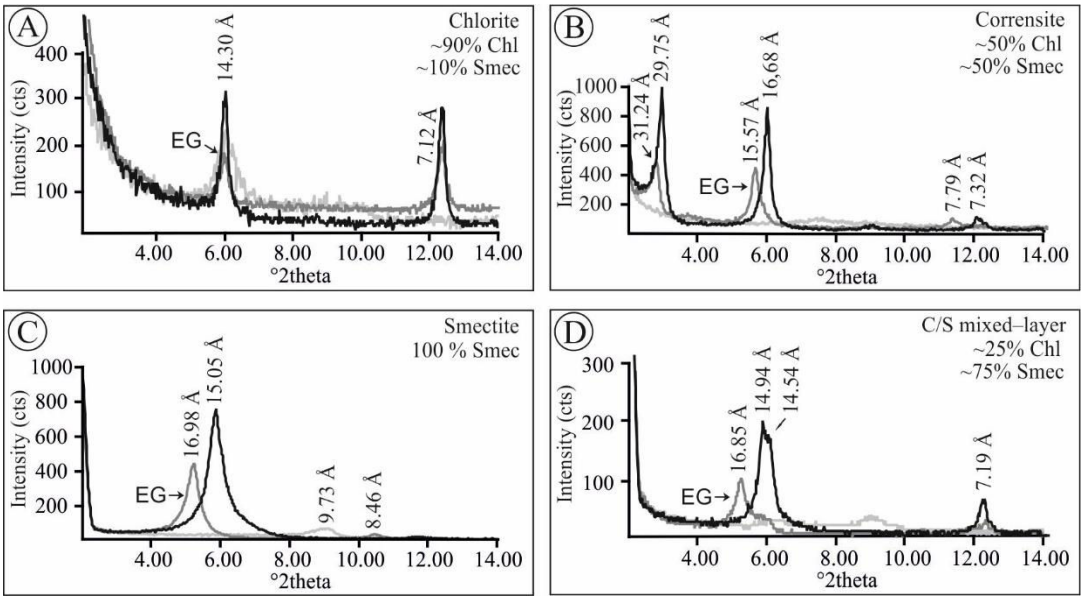

Figure 8. X–ray diffraction patters of < 0.4 µm clay–size fraction of chlorite (A), corrensite (B), smectite (C) and chlorite/smectite mixed–layer (D). Keys: Air dried (black line); EG= Ethylene glycol solvation (gray line); Heating treatment (light gray line).

The occurrence of dominant chlorite/smectite, trioctahedral smectite and corrensite recognized by their dark green color and identified using X–ray diffraction (Fig. 8) was confirmed by electron microprobe measurements. The smectite–rich chlorite/smectite, smectite (Supplementary Table F) and corrensite (Fig. 8B and Figs. 9A–B) represent the dominant hydrothermal phase of andesitic lava flows and andesitic dikes. The dominant trioctahedral smectite (Fig. 8C) has a Mg–saponite composition (Table 1). The dominant chlorite–rich chlorite–smectite (Fig., 8D; Supplementary Table G) with micrometer-scale fan–shaped particles (Fig. 4C) occurs in altered porphyritic and amygdaloidal andesitic lava flows. The chlorite–rich chlorite–smectite have Al^{VI} and ^{IV} contents (Al_{tot} 2.21+ 1.25 to 2.46+ 1.48 a.p.f.u.) that are higher in the porphyritic andesitic lava flows than the chlorite–rich chlorite–smectite (Al_{tot}= 1.59+ 0.77 to 1.93+ 1.47) in the amygdaloidal andesitic lava flows. The proportion of Fe and its valency balance are represented by changes in

tetrahedral and octahedral Al. The chlorite–rich chlorite–smectite structural formulas vary between porphyritic and amygdaloidal andesitic lava flows (Table 1).

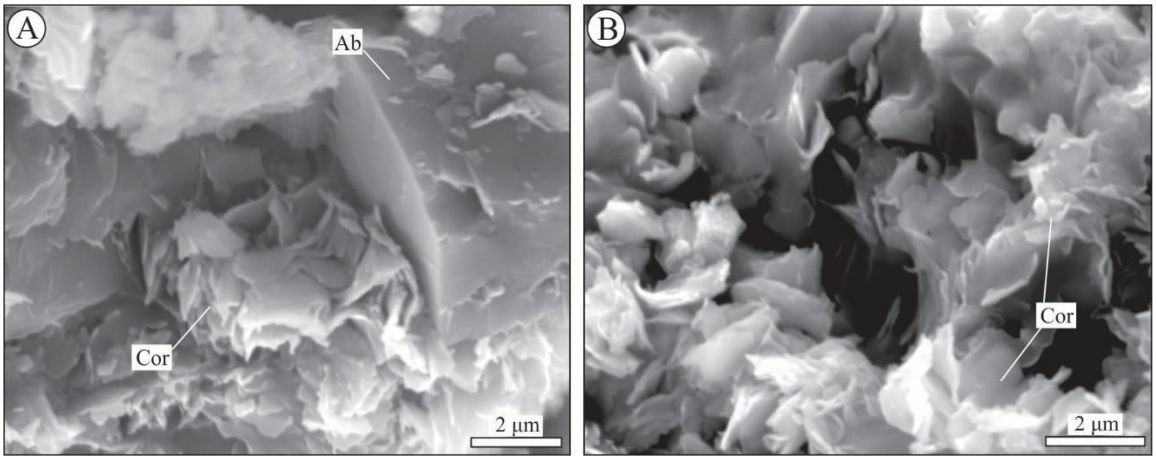

Figure 9. S.E.M. images obtained from drill hole fresh rock sample fragment of amygdaloidal andesitic lava flows described by Fontana et al. (2017). A) Albite fragment associated with corrensite clay minerals of the andesitic lava flows matrix; B) Detail of corrensite morphology of the altered andesitic lava flows matrix. Keys: Ab= Albite; Cor= Corrensite.

It is possible to confirm the association of albite and chlorite minerals with Cu enrichment. The magmatic and post–magmatic stages were related to albite and chlorite crystallization, while chlorite, chlorite/smectite mixed–layer and the destabilization of sulfides were related to the precipitation of chalcocite–bornite. These mineral associations suggest a sequence of crystallization and hydrothermal alteration over time.

5. Discussion

5.1 Chemistry of magmatic and late–magmatic minerals

The volcanogenic rocks in the Seival area are interpreted as part of the Lavras do Sul Shoshonitic Association (Lima and Nardi, 1998), which are related to the Lavras do Sul granitoids and lamprophyres. The occurrence of lamprophyres (Lima and Nardi, 1998; Almeida et al., 2012), andesitic dikes and various volcanic events in the region suggests long and intense episodes of magmatism in the Seival area constrained by the dating of zircon (Almeida et al., 2012; Janikian et al., 2012)

between 600 ± 2 to 590 ± 6 Ma. The mineralogy of andesitic rocks with andesine–labradorite, augite and Mg–biotite phenocrysts and their whole–rock compositions (Lima and Nardi, 1998; Sommer et al., 2006; Lopes et al., 2014) suggest a petrogenetic link with the Lavras do Sul Shoshonitic Association.

Petrogenetic modeling (MELTS Software: Ghiorso and Sack, 1995) used with whole–rock compositions (Lopes et al., 2014) estimates a liquidus temperature of ca. 1080 °C. The modeling shows a sequence of crystallization initiated by calcic plagioclase followed by low–Ca–pyroxene, late orthoclase and high–Ca pyroxene or biotite (ca. 800 °C). The stages below 800 °C include late–magmatic minerals formed by volatile-rich melt (c.f. Dixon et al., 1995). In this context, the biotites observed with the higher Al^{IV} contents of less pristine biotite compared with the biotite phenocrysts might represent two stages of biotite crystallization or slightly altered crystals. The late–magmatic stage initiated at solidus temperatures (800 to 500 °C) with volatile oversaturation and the degassing of the melt (c.f. Dixon et al., 1995). This interpretation is reinforced by the oxygen isotopic values of andesine–labradorite ($\delta^{18}O_{\text{andesine–labradorite}}$: 6.6 to 8.2 ‰; Fontana et al., 2019) showing the magmatic signature of fluids in equilibrium with feldspars (Taylor, 1987) evolving toward the mixing of meteoric and magmatic fluids for albite ($\delta^{18}O_{\text{albite}}$: 14.2 to 16.2 ‰; Fontana et al., 2019). Consequently, presume that observed Mg–biotite formation, euhedral F–rich titanite grains and albite are related to late–magmatic crystallization and albitization processes of andesine–labradorite. According to thermodynamic modelling and the literrature (c.f. Higgins and Ribb, 1976; Franz and Spear, 1985; Enami et al., 1993; Tropper et al., 2002; Harlov et al., 2006; Hövelmann et al., 2010; Kaur et al., 2012) this albitization process occurs at temperatures below 800 °C, presumably from ca. 600 to 250 °C. The widely observed albite suggests a magmatic to high–temperature hydrothermal system (epithermal–porphyry: Richards, 2003; Sillitoe, 2010 or Iron Oxide–Copper–Gold; Sillitoe, 2003; Williams et al., 2005; Groves et al., 2010). The alkaline and acidic fluids in these systems are related to the albitization process and K–rich alteration (Perez and Boles, 2005; Boulvais et al., 2007) that, to some degree, participated or started the leaching of

base metals from the lava (Moody et al., 1985; Perez and Boles, 2005; Hövelmann et al., 2010; Kontonikas–Charos et al., 2014). Non-magmatic basinal brine has also reported in the albitization process (Barton and Johnson, 1996 and 2000), such as in the Nevada porphyry, IOCG deposits (Carten, 1986; Dilles and Einaudi, 1992; Dilles et al., 2000; Sillitoe, 2003; Mark et al., 2006; Kendrick et al., 2007) or Chilean "Manto–type" deposits, such as Michilla, with the mixing of magmatic and basinal brine (Barton, 2014). In the Seival area, the change of andesine–labradorite ($An_{0.43–0.53}$ $Ab_{0.43–0.54}$ $Or_{0.03–0.05}$) to albite ($An_{0–0.06}$ $Ab_{0.89–1}$ $Or_{0–0.10}$) with rare K–feldspar rims on andesine–labradorite or rare illite attest to the circulation of alkaline fluid. Moreover, the sizes of the quartz and calcite crystals with liquid inclusions did not allow fluid inclusion microthermometry to recognize high–density fluid, as in IOCG-type deposits (Reeve et al., 1990; Davidson and Large, 1998). Nevertheless, the REE patterns of the plagioclase separates (Groups I and II) are not similar to the whole–rock patterns (Fig. 10; Lopes et al., 2014) with positive Eu positive anomalies (Eu/Eu*= >1; Table 2) that are higher in the andesine–labradorite–rich grains (group I) than albite (group II; Fig. 10A–B). These changes can be related to apatite inclusions in plagioclase, as mentioned in the petrography section, since these samples were acid-leached to remove traces of carbonates, Ca–phosphates and Fe oxides (Fontana et al., 2017). Consequently, the similar □REE contents with LREE and HREE variations from albites and andesine–labradorite suggest a similar source of REE (□REE) that was not affected by fluid dilution, such as that by meteoric fluids. Therefore, the albitization process in the Hilário Formation was related to the neutral to mildly acidic water circulation of Na–rich magmatic fluid, such as late–magmatic glass interactions with outgassing magmatic fluids (CO_2 and H_2O), but these data cannot decipher between a magmatic to late–magmatic crystallization with the mixing of magmatic fluids and brine (e.g. IOCG: Barton and Johnson, 1996 and 2000).

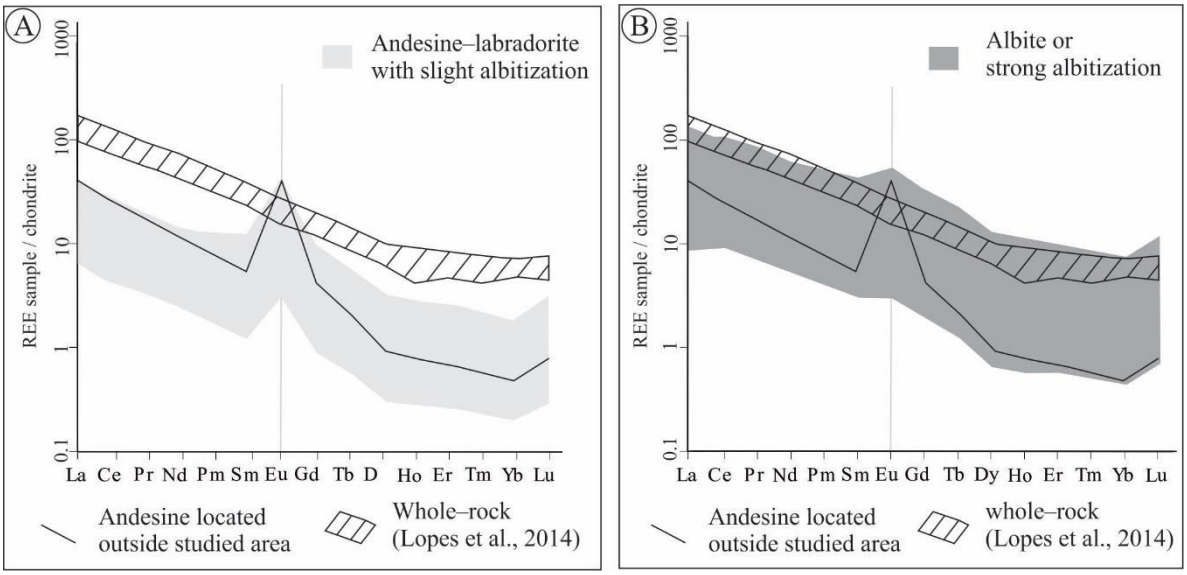

Figure 10. REE normalized patterns by the chondrite values (McDonough and Sun, 1995). A) Andesine–labradorite with slight albitization of group I; B) Albite–rich plagioclases of group II.

No mineralization model has yet been proposed for the Seival Mine. Fontana et al. (2017) indicated mineralization associated with magmatic and meteoric fluids. The aligned Cu–Ag ore bodies and disseminated mineralizations (see Figure 3) with similar mineral assemblages (albite, chlorite, chlorite/smectite mixed–layers, chalcocite–bornite, barite, and minor calcite, hematite and quartz) could be typical of epithermal deposits (Sillitoe, 2010) associated with the geothermal influence of andesitic dikes or the Lavras do Sul granitoids. These observations and interpretations suggest that Seival would be a superficial part of the Lavras do Sul porphyry (Mexias et al., 2007; Bongiolo et al., 2011). We assumed that low–hematite contents in the Seival area associated with calcite in small veins and ore deposits without an iron–oxide caprock are clues discarding the hypotheses of an IOCG type deposit or a metallic enrichment related to weathering profile such as Gossan genetic model of ore deposits.

5.2 Clay minerals and chlorite during hydrothermal stages

The hydrothermal stages associated with saponite, chlorite/smectite and chlorite precipitations surrounding albite suggest hydrothermal fluids of below 350

°C. Previous studies (Lopes et al., 2014; Fontana et al., 2017) characterized the occurrence of Fe–Cu–rich sulfides associated with chlorite/smectite. The association of Cu–rich sulfides with Fe –Al –Mg rich chlorite/smectite suggests that the Fe^{2+}, Mg and Al contents of the clay minerals are related to ore deposition (Wilkinson et al., 2015; Yoneda et al., 2016). Nevertheless, the origin, chemistry and temperature of the fluids are not well characterized.

In the Seival area, crystallography realized by X–ray diffraction and mineral chemistry obtained by electron electron microprobe analyses identified Mg–saponite (smectite), chlorite/smectite mixed–layer and corrensite infilling the porosity or intergranular spaces. The occurrence of dominant clay minerals with Mg–saponite, chlorite/smectite and corrensite in different lithotypes was interpreted as a lithological control of alteration rather than being derived from local equilibrium (Fontana et al., 2017). The comparison of the major element compositions of magmatic minerals (Part 4.2), clay mineral (part 4.3) and whole–rock samples (Lopes et al., 2014) provided information to support this hypothesis. The predominant Fe– Mg–rich clay minerals and their Fe_{tot}/Fe_{tot}+Mg atomic ratios compared to augite (0.14 to 0.27) and biotite (0.37 to 0.44) indicate that Mg–saponite (0.22 to 0.27) and chlorite/smectite mixed–layers may be derived from the alteration of magmatic minerals and glass. In contrast, the high Fe–clinochlore to Mg–chamosite ratio (0.47 to 0.63; Supplementary Table E) suggests the addition of Fe and Mg during the chloritization process. This interpretation as confirmed by mass–balance calculations performed by Fontana et al. (2019).

We estimated the temperatures of chlorites using chemical thermometers (Inoue et al., 2009; Bourdelle and Cathelineau, 2015). These thermometers are the only available temperature constraint considering the small sizes of the fluid inclusions (Fontana et al., 2017). We discarded the chemical thermometer of chlorite related to metamorphic conditions and selected one determined in similar lithotypes and pressure conditions. The chosen chemical thermometers use a structural formula with an uncertainty dominantly controlled by the Fe valency and different octahedral layers. Assuming an error of 20% in the Fe distribution, the uncertainty is

approximately 50 °C in both calculations. The calculated temperatures of Fe–clinochlore to Mg–chamosite (Supplementary Table E) vary from 129 to 275 °C in the lapilli tuff–andesite (median= 183 ± 39 °C; n= 18) and 172 to 312 °C in andesitic dikes (median= 251 ± 56 °C; n= 8). Moreover, the compositional changes in chlorite in the Seival area compared to those in the Lavras do Sul area (Mexias et al., 1990b; Bongiolo et al., 2011) or the Camaquã Mine (Renac et al., 2014) yield comparable temperatures. These different uncertainties (± 50 °C) and calculated temperatures reflect chloritization below of the minimum temperature of albitization. The higher temperature of chlorite associated with andesitic dikes suggests a temperature related to intrusive bodies or different thermal gradients between lapilli tuff and andesitic dikes.

5.3 Hydrothermal evolution and thermodynamic modeling

The chlorite and chlorite/smectite mixed–layers associated with sulfides are typical mineralogical assemblages of hydrothermal deposits (Barnes, 1979; Pirajno, 2009; Sillitoe, 2010). In the Seival area, different Fe–Cu –rich sulfide assemblages occur in the intergranular space or are mixed with clay minerals (Fontana et al., 2017).

Hydrothermal alteration minerals are associated with a sequence of precipitations rather than a paragenetic assemblage, as occurs in metamorphic reactions. Therefore, thermodynamic modeling can be erroneous when based on the assumption of an output represented by all of the hydrothermal phases observed. Consequently, we tested the different equilibrium conditions of the hydrothermal stage (below 350 °C) with thermodynamic modeling (PHREEQC interactive; Parkhurst, 1995, rather than SUPCRIT or the equivalent CHONZ Rpackage). The PHREEQC thermodynamic models primarily use minerals with an initial water content and propose secondary minerals as outputs with the new composition of the final fluid. In our case, reactions involved observed magmatic minerals observed (feldspars: andesine–labradorite and albite and Ca–pyroxene: augite) and late–magmatic minerals (biotite, titanite, Fe–titanium oxides and silica–rich glass)

reacting with initial fluid (low–concentration water similar to rainfall, Salve et al., 2008), and carbonic fluids (CO_2 as recognized in fluid inclusions (Fontana et al., 2017). The temperature domain of these calculations was bracketed by the albitization process (< 350 °C) and the calculations of the chlorite thermometer (120 to 320 °C). Each calculation considers a molar proportion of water a hundred times higher than those of minerals and fluids for varying pH values and temperatures below 350 °C. Consequently, the thermodynamic changes in calculated fluids and the dissolution or precipitation of primary and secondary minerals equilibrated at 350, 300, 250, 200 and 150 °C with pH and Eh were adjusted for charge balance and redox conditions. These preliminary calculations indicate multiple solutions with more products than were identified in the altered rocks. Therefore, we forced the software to uniquely consider results with chlorite, calcite, quartz and Fe–Cu rich sulfide or barite, which are here assumed to be products of hydrothermal reactions, without any constraints related to their precipitation or dissolution.

These thermodynamic calculations were obtained for neutral (pH: 7) and acidic (pH: 4) initial water conditions. Regardless of the considered temperature, all final waters remained neutral for an initial fluid with a neutral pH (pH: 7 to 7.3), whereas acidic waters changed to a neutral pH (pH 4 to 7.3).

The high–temperature (350 °C) calculations indicate the coprecipitation of albite and titanite with the total consumption of the Ca–rich feldspars and pyroxene, but no minor chlorite or smectite. The conservation of some pyroxene and andesine–labradorite observed in the petrography and the lack of clay minerals suggests unrealistic solutions for hydrothermal alteration forming albite with titanite and chlorite. Consequently, we forced the precipitation of chlorites in a second data set.

– For temperatures between 350 and 250 °C, the chlorite, quartz and calcite associated with pyrite and chalcopyrite can be formed, whereas silica–rich glass, titanite and Ti–magnetite are consumed anorthite, albite and pyroxene are partially dissolved.

– For temperatures between 250 and 150 °C, neutral or acid water dissolved magmatic minerals with predicted precipitations of chlorite, barite, calcite, quartz and

hematite with bornite–chalcocite. Mg–saponite (smectite) was precipitated below 200 °C.

– Below 150 °C, the lower activities of Fe^{2+} with decreasing $HS^-/(HS^-+SO_4)$ molar ratios increased the saturation with respect to chalcocite and sulfate and Fe oxides, such as barite and hematite. These calculations confirm that pyrite and chalcopyrite were probably precipitated from a dominant magmatic fluid at temperatures between 350 to 250 °C. The further mixing of the magmatic fluid with meteoric water or basinal brine at temperatures varying from 250 to 150 °C promoted chalcocite–bornite deposition. Considering the domain of barite saturation and the lack of supergene alteration or gossan profiles in this region, the lower temperature of the Cu enrichment of sulfide ranged from 150 to 50 °C.

6. Conclusions

The Seival area contains hydrothermal Cu–sulfide deposits hosted in volcanic rocks with a shoshonitic affinity. Interpretations based on mineralogical and chemical data suggest that volatile–rich magma produced Mg–biotite, followed by late–magmatic alteration with titanite and the albitization of andesine–labradorite (650 to 250 °C), as suggested by the REE contents of albite. Thermodynamic modeling indicates that late albitization (ca. < 350 °C) was associated with the formation of primary pyrite–chalcopyrite, or that high–temperature chloritization (350 to 250 °C) was associated with bornite–chalcocite. Moreover, the Fe_{tot}/Fe_{tot}+Mg atomic ratios of Fe–clinochlore to Mg–chamosite suggest that fluids altered the pyroxene or residual material with the addition of external Fe compared to smectite precipitation. The high Fe_{tot}/Fe_{tot}+Mg atomic ratios and high Fe^{2+}/Fe^{3+} atomic ratios of these chlorites suggest an Fe–rich and reduced fluid in agreement with the migration of Fe, Cu and S species producing sulfides. However, the origin of fluid, whether the mixing of magmatic and meteoric fluids or basinal brines (IOCG, Chilean 'Manto type'), was not identified. Nevertheless, the chloritization process occurred from 312 to 120 °C. Despite the errors related to chlorite thermometers, the ranges of temperatures in the lapilli tuff (275 to 129 °C; median= 183 ± 39 °C) and andesitic

dikes (312 to 172 °C, median= 251 ± 56 °C) suggest the existence of changing thermal gradients related to the cooling of the lava pile or intrusive dike and fluids with different temperatures at different times.

The lowest-temperature stage was related to the widespread formation of Mg–saponite and smectite–rich C/S (200 to 50 °C). The formations of chlorites, chlorite/smectite mixed–layers and Mg–saponite were related to the influx of fluids (meteoric water or basinal brine) at lower thermal fluxes associated with the sulfide assemblage of bornite–chalcocite, chalcocite, and barite with the increasing concentration of sulfate. Consequently, the petrographic association of albite and chlorite with pyrite and chalcopyrite suggests that the albitization to chloritization stage and structural control may be prospective guides for Cu fertile magmatic systems. The chlorite/smectite mixed–layers emphasized favorable Cu–enriched zones, such as fluid circulation in faults or along dikes and percolation in the porosity of the lapilli tuff.

Acknowledgements

This study is part of the cotutelle doctoral thesis of Rodrigo Winck Lopes at Universidade Federal do Rio Grande do Sul and Université Côte d´Azur. We wish to thank the Conselho Nacional do Desenvolvimento e Pesquisa (CNPq), CAPES and Programa Ciências Sem Fronteiras (Process number: 200081/2014–4) for financial support. We thank Votorantim Metais for allowing access to drill–cores. We thank Robert Ayuso, Karel Breiter, Douglas Kreiner, Bruno Lemiere and anonymous reviewer for their constructive remarks during the reviewing and editing processes. We wish to thank Everton Bongiolo and Maria José Mesquita for additional revision. We wish to thank the members of the research group Marcelo Lindenberg, Bruno Petracco and the technician laboratory: Denise Canarim, Susan Drago, Edgar Bercht and Lucas Jantsch.

References

Almeida, F.F.M., Hasuy, Y., 1984. O Pré–Cambriano do Brasil (Portuguese – Brazil). São Paulo: Edgard Blücher, 378 p.

Almeida, D.P.M, Chemale Jr., F., Machado, A., 2012. Late to Post–Orogenic Brasiliano–Pan–African volcano–sedimentary basins in the Dom Feliciano Belt, Southernmost Brazil, in: Al–Juboury, A.I. (Ed.), Petrology – New Perspectives and Applications, pp. 73–135.

Barnes, H.L., 1979. Geochemistry of Hydrothermal Ore Deposits. Second Edition, Wiley–Interscience, Inc., New York, 798 p.

Barton, M.D., Johnson, D.A., 1996. Evaporitic source model for igneous–related Fe oxide–(REE–Cu–Au–U) mineralization. Geology, 24, 259–262.

Barton, M.D., Johnson, D.A., 2000. Alternative brine sources for Feoxide(–Cu–Au) systems: Implications for hydrothermal alteration and metals. In: Hydrothermal iron oxide copper–gold and related deposits: A global perspective (Porter, T.M., editor). Adelaide, Australian Mineral Foundation, pp. 43–60.

Barton, M.D., 2014. Iron oxide(–Cu–Au–REE–P–Ag–U–Co) systems. Treatise on Geochemistry, 13, 515–541.

Bayliss, P., 1975. Nomenclature of the trioctahedral chlorites. The Canadian Mineralogist, 13, 178–180.

Bicca, M.M., Chemale Jr., F., Jelinek, A.R., Oliveira, C.H.E., Guadagnin, F., Armstrong, R., 2013. Tectonic evolution and provenance of the Santa Bárbara Group, Camaquã Mines region, Rio Grande do Sul, Brazil. Journal of South American Earth Sciences, 48, 173–192.

Bongiolo, E.M., Renac, C., Mexias, A.S., Gomes, M.E.B., Ronchi, L.H., Patrier–Mase, P., 2011. Evidence of Ediacaran glaciation in southernmost Brazil through magmatic to meteoric fluid circulation in the porphyry–epithermal Au–Cu deposits of Lavras do Sul. Precambrian Research, 189, 404–419.

Borba, A.W., Mizusaki, A.M.P., Santos, J.O.S., McNaughton, N.J., Ono, A.T., Hartmann, L.A., 2008. U–Pb zircon and ^{40}Ar–^{39}Ar K–feldspar dating of syn–sedimentary volcanism of the Neoproterozoic Maricá Formation: constraining the

age of foreland basin inception and inversion in the Camaquã Basin of southern Brazil. Basin Research, 20, 359–375.

Boulvais, P., Ruffet, G., Cornichet, J., Mermet., M., 2007. Cretaceous albitization and dequartzification of Hercynian peraluminous granite in the Salvezines Massif (French Pyrénées). Lithos, 93, 89–106.

Bourdelle, F., Cathelineau, M., 2015. Low–temperature chlorite geothermometry: a graphical representation based on a T–R^{2+} diagram. European Journal of Mineralogy, 27, 617–626.

Cao, M.J., Qin, K.Z., Li, G.M., Evans, N.J., Jin, L.Y., 2015. Abiogenic Fischer–Tropsch synthesis of methane at the Baogutu reduced porphyry copper deposit, western Junggar, NW China. Geochimica et Cosmochimica Acta, 141, 179–198.

Carten, R.B., 1986. Sodium–calcium metasomatism; chemical, temporal, and spatial relationships at the Yerington, Nevada, porphyry copper deposit. Economic Geology, 81, 1495–1519.

Davidson, G.J., Large, R.R., 1998. Proterozoic copper–gold deposits. AGSO Journal of Australian Geology and Geophysics, 17, 105–113.

Dilles, J.H., Einaudi, M.T., 1992. Wall–rock alteration and hydrothermal flow paths about the Ann Mason porphyry copper deposit, Nevada; a 6–km vertical reconstruction. Economic Geology and the Bulletin of the Society of Economic Geologists, 87, 1963–2001.

Dilles, J.H., Einaudi, M.T., Proffett, J.M., Barton, M.D., 2000. Overview of the Yerington porphyry copper district: magmatic to nonmagmatic sources of hydrothermal fluids, their flow paths, alteration affects on rocks, and Cu–Mo–Fe–Au ores. Society of Economic Geologists, Post–Meeting Field Conference, 32, 55–66.

Dixon, J.E., Stolper, E.M., Holloway, J.R., 1995. An experimental study of water and carbon dioxide solubilities in mid–ocean ridge basaltic liquids. Part 1: Calibration and solubility models. Journal of Petrology, 36, 1607–1631.

Enami, M., Suzuki, K., Liou, J.G., Bird, D.K., 1993. Al–Fe^{3+} and F–OH substitution in titanite and constraints on their P–T–dependence. European Journal of Mineralogy, 5, 219–231.

Fernandes, L.A., Tommasi, A., Porcher, C.C., 1992. Deformation patterns in the Southern Brazilian branch of the Dom Feliciano Belt: a reappraisal. Journal of South American Earth Sciences, 5, 77–96.

Fontana, E., Mexias, A.S., Renac, C., Nardi, L.V.S., Lopes, R.W., Gomes, M.E.B., Barats, A., 2017. Hydrothermal alteration of volcanic rocks in Seival Mine Cu–mineralization – Camaquã Basin – Brazil (Part I): Chloritization process and geochemical dispersion in alteration halos. Journal of Geochemical Exploration, 177, 45–60.

Fontana, E., Renac, C., Mexias, A.S., Barats, A., Gerbe, M.C., Lopes, R.W., Nardi, L.V.S., 2019. Mass balance and origin of fluids associated to smectite and chlorite/smectite alteration in Seival Mine Cu–Mineralization – Camaquã Basin – Brazil (Part II). Journal of Geochemical Exploration, 196, 20–32.

Franz, G., Spear, F.S., 1985, Aluminous titanite (sphene) from the eclogite zone, south–central Tauern Window, Austria. Chemical Geology, 50, 33–46.

Gastal, M.C.P., Lafon, J.M., Hartmann, L.A., Koester, E., 2005a. Sm–Nd isotopic compositions as a proxy for magmatic processes during the Neoproterozoic of the southern Brazilian shield. Journal of South American Earth Sciences, 18, 255–276.

Gastal, M.C.P., Lafon, J.M., Hartmann, L.A., Koester, E., 2005b. Sm–Nd isotopic investigation of Neoproterozoic and Cretaceous igneous rocks from southern Brazil: a study of magmatic processes. Lithos, 82, 345–377.

Gastal M.C., Lafon, J.M., Ferreira, F.J.F., Magro, F.U.S., Remus, M.V.D., Sommer C.A., 2006. Reinterpretação do Complexo Intrusivo Lavras do Sul – RS, de acordo com os sistemas vulcano–plutônicos de subsidência. Parte I: Geologia, geofísica e geocronologia ($^{207}Pb/^{206}Pb$ e $^{206}Pb/^{238}U$). Revista Brasileira de Geologia (Portuguese – Brazil), 36, 109–124.

Gastal, M.C., Ferreira. F.J.F., Cunha, J.U., Esmeris, C., Koester, E., Raposo, M.I.B., Rossetti, M.M.M., 2015. Lavras granite emplacement and gold mineralization during the development of the post–collisional volcano–plutonic center, west of the

Sul–riograndense Shield: Geophysical and structural data. Brazilian Journal of Geology, 45, 217–241.

Ghiorso, M.S., Sack, R.O., 1995. Chemical mass transfer in magmatic processes IV. A revised and internally consistent thermodynamic model for the interpolation and extrapolation of liquid–solid equilibria in magmatic systems at elevated temperatures and pressures. Contributions to Mineralogy and Petrology, 119, 197–212.

Groves, D.I.P., Bierlein, F.P., Meinert, L.D., Hitzman, M.W., 2010. Iron oxide copper–gold (IOCG) deposits through Earth history; implications for origin, lithospheric setting, and distinction from other epigenetic iron oxide deposits. Economic Geology, 105, 641–654.

Harlov, D.E., Tropper, P., Seifert, W., Nijland, T., Förster, H.–J., 2006. Formation of Al–rich titanite ($CaTiSiO_4O$–$CaAlSiO_4OH$) reaction rims on ilmenite in metamorphic rocks as a function of fH_2O and fO_2. Lithos, 88, 72–84.

Hartmann, L.A., Chemale Jr., F., Philipp, R.P., 2007. Evolução Geotectônica do Rio Grande do Sul no Pré–Cambriano. In: Iannuzzi, R., Frantz, J.C. (Eds). 50 anos de Geologia (Portuguese – Brazil). Porto Alegre: Ed. Universidade/UFRGS, pp. 99–123.

Higgins, J.B., Ribbe, P.H., 1976. The crystal chemistry and space groups of natural and synthetic titanites. American Mineralogist, 61, 878–888.

Hövelmann, J., Putnis, A., Geisler, T., Schmidt, B.C., Golla–Schindler, U., 2010. The replacement of plagioclase feldspars by albite: observations from hydrothermal experiments. Contributions to Mineralogy and Petrology, 159, 43–59.

Inoue, A., Utada, M., Nagata, H., Watanabe, T., 1984. Conversion of trioctahedral smectite to interstratified chlorite/smectite in Pliocene acidic pyroclastic sediments of the Ohyu district, Akita Prefecture, Japan. Clay Science, 6, 103–106.

Inoue, A., Meunier, A., Patrier–Mas, P., Rigault, C., Beaufort, D., Vieillard, P., 2009. Application of chemical geothermometry to low–temperature trioctahedral chlorites. Clays and Clay Minerals, 57, 371–382.

Janikian, L., Almeida, R.P., Trindade, R.I.F., Fragoso–Cesar, A.R.S., D´Agrella–Filho, M.S., Dantas, E.L., Tohver, E., 2008. The continental record of Ediacaran volcano–sedimentary successions in southern Brazil and their global implications. Terra Nova, 20, 259–266.

Janikian, L., Almeida, R.P., Fragoso–Cesar, A.R.S., Martins, V.T.S., Dantas, E.L., Tohver, E., McReath, I., D'Agrella–Filho, M.S., 2012. Ages (U–Pb SHRIMP and LA ICPMS) and stratigraphic evolution of the Neoproterozoic volcano–sedimentary successions from the extensional Camaquã Basin, Southern Brazil. Gondwana Research, 21, 466–482.

Kaur, P., Chaudhri, N., Hofmann, A., Raczek, I., Okrusch, M., Skora, S., 2012. Two–Stage, extreme albitization of A–type granites from Rajasthan, NW India. Journal of Petrology, 53, 919–948.

Kendrick, M.A., Mark, G., Phillips, D., 2007. Mid–crustal fluid mixing in a Proterozoic Fe oxide–Cu–Au deposit, Ernest Henry, Australia: Evidence from Ar, Kr, Xe, Cl, Br and I. Earth and Planetary Science Letters, 256, 328–343.

Kontonikas–Charos, A., Ciobanu, C.L., Cook, N.J., 2014. Albitization and redistribution of REE and Y in IOCG systems: Insights from Moonta–Wallaroo, Yorke Peninsula, South Australia. Lithos, 208–209, 178–201.

Laux, J.H., Lindenmayer, Z.G., Teixeira, J.B.G., Neto, A.B., 2005. Ore genesis at the Camaquã copper mine, a neoproterozoic sediment–hosted deposit in Southern Brazil. Ore Geology Review, 26, 71–89.

Lima, E.F., Nardi, L.V.S., 1998. The Lavras do Sul Shoshonitic Association: implications for origin and evolution of neoproterozoic shoshonitic magmatism in southernmost Brazil. Journal of South American Earth Science, 11, 67–77.

Liz, J.D., Lima, E.F., Nardi, L.V.S., Sommer, C.A., Saldanha, D.L., Pierosan, R., 2009. Petrologia e sucessão estratigráfica das rochas monzoníticas da associação shoshonítica de Lavras do Sul (RS). Revista Brasileira de Geologia (Portuguese – Brazil), 39, 244–255.

Lopes, R.W., Fontana, E., Mexias, A.S., Gomes, M.E.B., Nardi, L.V.S., Renac, C., 2014. Caracterização petrográfica e geoquímica da sequência magmática da

Mina do Seival, Formação Hilário (Bacia do Camaquã – Neoproterozoico), Rio Grande do Sul, Brasil. Pesquisas em Geociências (Portuguese – Brazil), 41, 51–64.

Lopes, R.W., Mexias, A.S., Philipp, R.P., Bongiolo, E.M., Renac, C., Bicca, M.M., Fontana, E., 2018. Au-Cu-Ag mineralization controlled by brittle structures in Lavras do Sul Mining District and Seival Mine deposits, Camaquã Basin, southern Brazil. Journal of South American Earth Sciences, 88, 197–215.

Marsh, T.M., Einaudi, M.T., McWilliams, M., 1997. $^{40}Ar/^{39}Ar$ geochronolgy of Cu–Au and Au–Ag mineralization in the Potrerillos district, Chile. Economic Geology, 92, 784-806.

Mark, G., Oliver, N.H.S., Carew, M.J., 2006. Insights into the genesis and diversity of epigenetic Cu–Au mineralization in the Cloncurry district, Mt Isa Inlier, northwest Queensland. Australian Journal of Earth Sciences, 53, 109–124.

Matté, V., Sommer, C.A., Lima, E.F., Philipp, R.P., Basei, M.A.S., 2016. Post–collisional Ediacaran volcanism in oriental Ramada Plateau, southern Brazil. Journal of South American Earth Sciences, 71, 201–222.

McDonough, W.F., Sun, S.S., 1995. Composition of the Earth. Chemical Geology, 120, 223–253.

Mexias, A.S., Formoso, M.L.L., Meunier, A., Beaufort, D., 1990a. O sistema hidrotermal fóssil de Volta Grande – Lavras do Sul/RS. Parte I – Petrografia do hidrotermalismo. Geochimica Brasiliensis (Portuguese – Brazil), 4, 139–157.

Mexias, A.S., Formoso, M.L.L., Gomes, M.E.B., Meunier, A., Beaufort, D., Mattos, I., 1990b. O sistema hidrotermal fóssil de Volta Grande – Lavras do Sul/RS. Parte II – Geoquímica das cloritas. Geochimica Brasiliensis (Portuguese – Brazil), 4, 159–174

Mexias, A.S., Formoso, M.L.L., Meunier, A., Beaufort, D., 1990c. Composition and crystallization of corrensite in volcanic and pyroclastic rocks of Hilário Formation (RS) Brazil. Sciences Géologiques, 88, 135–143.

Mexias, A.S., Berger, G., Gomes, M.E.B., Formoso, M.L.L., Dani, N., Frantz, J.C., Bongiolo, E.M., 2005. Geochemical modelling of gold precipitation conditions

in Bloco do Butiá Mine, Lavras do Sul/Brazil. Anais da Academia Brasileira de Ciências (Portuguese – Brazil), 77, 1–12.

Mexias, A.S., Bongiolo, E.M., Gomes, M.E.B., Formoso, M.L.L., Frantz, J.C., 2007. Alterações hidrotermais e mineralizações nas rochas da Associação Plutono–Vulcano–Sedimentar da região de Lavras do Sul–RS. In: Iannuzzi, R., Frantz, J.C. (Eds). 50 anos de Geologia (Portuguese – Brazil). Porto Alegre: Ed. Universidade/UFRGS, pp. 143–159.

Moody, J.B., Jenkins, J.E., Meyer, D., 1985. An experimental investigation of the albitization of plagioclase. Canadian Mineralogist, 23, 583–596.

Oliveira, C.H.E., Chemale Jr., F., Jelinek, A.R., Bicca, M.M., Philipp, R.P., 2014. U–Pb and Lu–Hf isotopes applied to the evolution of the late to post–orogenic transtensional basins of the Dom Feliciano belt, Brazil. Precambrian Research, 246, 240–255.

Paim, P.S.G., Chemale Jr., F., Lopes, R.C., 2000. A Bacia do Camaquã. In: Holz, M.; De Ros, L. F. (Ed.). Geologia do Rio Grande do Sul (Portuguese – Brazil). Porto Alegre: Ed. Universidade/UFRGS, pp. 231–374.

Parkhurst, D.L, 1995. User's guide to PHREEQC–A computer program for speciation, reaction–path, advective–transport, and inverse geochemical calculations. U.S. Geological Survey Water–Resources Investigations Report, 95–4227, 143 p.

Perez, R.J., Boles, J.R., 2005. An empirically derived kinetic model for albitization of detrital plagioclase. American Journal of Science, 305, 312–343.

Philipp, R.P., Pimentel, M.M., Chemale Jr., F., 2016. Tectonic evolution of the Dom Feliciano Belt in Southern Brazil: Geological relationships and U–Pb geochronology. Brazilian Journal of Geology, 46, 83–104.

Pirajno, F., 2009, Hydrothermal processes and mineral systems. Springer, 1250 p.

Reeve, J.S., Cross, K.C., Smith, R.N., Oreskes, N., 1990. Olympic Dam copper–uranium–gold–silver deposit, in Hughes, F. E., ed., Geology of the mineral

deposits of Australia and Papua New Guinea: Melbourne, Australasian Institute of Mining and Metallurgy, pp. 1009–1035.

Reischl, J.L., 1978. Mineralizações cupriferas associadas a vulcânicas na Mina do Seival. In: XXX Congresso Brasileiro De Geologia (Portuguese – Brazil), Recife. Anais, SBG, 4, 1568–1582.

Remus, M.D.V., Hartmann, L.A., McNaughhton, M.J., Fletcher, I.R., 1999. Shrimp U–Pb zircon ages of volcanism from the São Gabriel Block, southern Brazil. In: Simpósio sobre vulcanismo e ambientes associados, 1. Boletim de Resumos, 83 p.

Remus, M.V.D., Hartmann, L.A., McNaughton, N.J., Groves, D.I., Reischl, J.L., 2000. A distal magmatic–hydrothermal origin for the Camaquã Cu (Au–Ag) and Santa Maria Pb, Zn (Cu–Ag) deposits, southern Brazil. Gondwana Research, 3, 155–174.

Renac, C., Mexias, A.S., Gomes, M.E.B., Ronchi, L.H., Nardi, L.V.S., Laux, J.H., 2014. Isotopic fluid changes in a Neoproterozoic porphyry–epithermal system: the Uruguay mine, southern Brazil. Ore Geology Review, 60, 146–160.

Ribeiro, M., Fantinel, L.M., 1978. Associacões petrotectônicas do Escudo Sul–Riograndense: I Tabulação e distribuicão das associações petrotectônicas do Escudo do Rio Grande do Sul. Inheringia Serviço Geológico (Portuguese – Brazil), 5, 19–54.

Richards, J.P., 2003. Tectono–magmatic precursors for porphyry Cu–(Mo–Au) deposit formation. Economic Geology, 98, 1515−1533.

Salve, P.R., Maurya, A., Wate, S.R., Devotta, S., 2008. Chemical composition of major ions in rainwater. Bulletin of Environmental Contamination and Toxicology, 80, 242–246.

Seedorff, E., Dilles, J.H., Proffett Jr., J.M., Einaudi, M.T., Zurcher, L., Stavast, W.J.A., Johnson, D.A., Barton, M.D., 2005. Porphyry deposits: characteristics and origin of hypogene features. Society of Economic Geologists, Economic Geology 100th Anniversary Volume, 251–298.

Sillitoe, R.H., 1991. Gold metallogeny of Chile – an introduction: Economic Geology, 86, 1187–1205.

Sillitoe, R.M., 2003. Iron oxide–copper–gold deposits: An Andean view. Mineralium Deposita, 38, 787–812.

Sillitoe, R.H., 2010, Porphyry copper systems. Economic Geology, 105, 3–41.

Silva, L.C., McNaughton, N.J., Armstrong R., Hartmann, L.A., Fletcher, I.R., 2005. The neoproterozoic Mantiqueira Province and its African connections: a zircon based U–Pb geochronologic subdivision for the Brasiliano/Pan–African systems of orogens. Precambrian Research, 136, 203–240.

Sommer, C.A., Lima, E.F., Nardi, L.V.S., Figueiredo, A.M.G., Pierosan, R., 2006. Potassic and Low–and High–Ti mildly alkaline volcanism In the Neoproterozoic Ramada Plateau, Southermost Brazil. Journal of South American Earth Sciences, 18, 237–254.

Taylor, B.E., 1987. Stable isotope geochemistry of ore–forming fluids. In: Kyser, T.K. (Ed.), Stable isotope geochemistry of low temperature processes. Mineralogical Association of Canada, Short Course Handbook, 13, 337–445.

Toniolo, J.A., Gil, C.A.A., Sander, A., 2007. Projeto BANEO–Metalogenia das Bacias Neoproterozóico–Eopaleozóicas do Sul do Brasil – Bacia do Camaquã. CPRM – Serviço Geológico do Brasil (Portuguese – Brazil), CD Rom.

Troian, G.C., Mexias, A.S., Gomes, M.E.B., Canarim, D., Patricia Patrier–Mas, P., Renac, C., 2010. Cloritização na Mina Uruguai, Minas do Camaquã, RS, Brasil. Pesquisas em Geociências (Portuguese – Brazil), 37, 173–190.

Tropper, P., Manning, C.E., Essene, E.J., 2002. The substitution of Al and F in titanite at high pressure and temperature: experimental constraints on phase relations and solid solution properties. Journal of Petrology, 43, 1787–1814.

Velde, B., 1985. Clay minerals: a physico–chemical explanation of their occurrence. Developments in Sedimentology, 40, Elsevier, Amsterdam, 427 p.

Wiewióra, A., Weiss, Z., 1990. Crystallochemical classifications of phyllosilicates based on the unified system of projection of chemical composition: II The chlorite group. Clay Minerals, 25, 83–92.

Wilkinson, J.J., Chang, Z., Cooke, D.R., Baker, M.J., Wilkinson, C.C., Inglis, S., Chen, H., Gemmell, J.B., 2015. The chlorite proximitor: A new tool for detecting porphyry ore deposits. Journal of Geochemical Exploration, 152, 10–26.

Williams, P.J., Barton, M.D., Johnson, D.A., Fontboté, L., de Haller, A., Mark, G., Oliver, N.H.S., Marschik, R., 2005. Iron oxide copper–gold deposits: Geology, Space–time distribution, and possible modes of origin. Economic Geology, 100th Anniversary Volume, 371–405.

Worrall, F., Pearson, D.G., 2001. Water–rock interaction in an acidic mine discharge as indicated by rare earth element patterns. Geochimica et Cosmochimica Acta, 65, 3027–3040.

Yoneda, T., Watanabe, T., Sato, T., 2016. Mineralogical aspects of interstratified chlorite–smectite associated with epithermal ore veins: A case study of the Todoroki Au–Ag ore deposit, Japan. Clay Minerals, 51, 653–674.

4.3 Manuscrito III

O manuscrito III foi submetido ao *Brazilian Journal of Geology* em 13/09/2018. O manuscrito submetido foi inserido na presente tese.

Submission Confirmation

Print

Thank you for your submission

Submitted to
Brazilian Journal of Geology

Manuscript ID
BJGEO-2018-0102

Title
Composition and REE analysis of barite from Seival Mine Cu–Ag deposits (Camaquã Basin, Neoproterozoic of Southern Brazil)

Authors
Lopes, Rodrigo
Mexias, André
Renac, Christophe
Boscato Gomes, Marcia
Fontana, Eduardo
Barats, Aurélie

Date Submitted
13-Sep-2018

Author Dashboard

Composition and REE analysis of barite from Seival Mine Cu–Ag deposits (Camaquã Basin, Neoproterozoic of Southern Brazil)

R.W. Lopes[1,2]*, A.S. Mexias[1], C. Renac[2], M.E.B. Gomes[1], E. Fontana[3], A. Barats[2]

[1] Instituto de Geociências, Universidade Federal do Rio Grande do Sul, avenida Bento Gonçalves, 9500, 91501–970 Porto Alegre, RS, Brazil. E–mails: rodrigo.winck@ufrgs.br, andre.mexias@ufrgs.br, marcia.boscato@ufrgs.br

[2] Université Côte d'Azur, CNRS, OCA, IRD, Géoazur, 250 rue Albert Einstein, Sophia Antipolis 06560, Valbonne, France. E–mails: christophe.renac@unice.fr, aurelie.barats@unice.fr

[3] Universidade Federal dos Vales do Jequitinhonha e Mucuri, Centro de Geociências, Instituto de Ciência e Tecnologia, Rodovia MGT 367 – Km 583, nº 5000 – Alto da Jacuba, Diamantina, MG, Brazil. E–mail: eduardo.fontana@ict.ufvjm.edu.br
* Corresponding author.

ABSTRACT

Barite, calcite and minor hematite are associated with ore deposits in the Camaquã Basin and related to late–magmatic to low–temperature hydrothermal stage. The Electron Microprobe and Rare Earth Elements (REE) analyzes in the barite crystals were measured to reconstruct low–temperature hydrothermal conditions. The albitization of plagioclase (andesine–labradorite) was associated with part or portion of barium and the sulfide destabilization may have provided sulfur to the fluid responsible for the precipitation of barite (<150 °C). The late precipitation of barite and their major, trace and REE contents suggest a source of metal related to albitization relayed by chloritization associated with an increasing proportion of meteoric water. The influx of meteoric fluid (REE contents) has provided Eh–pH and oxidation conditions changing from dominant H_2S–rich fluid (chalcocite, covellite) toward dominant SO_4–rich fluids associated with precipitation of barite. Based on the difference of barium content of magmatic andesine–labradorite and albite, a volume of altered andesite of 1 m^3 is necessary to produce 1.6 kg of barite. The volume of altered andesite through of the hydrothermal process (albitization, chloritization and sulfide destabilization) corresponds to 0.06 % and occurs in the last veins of the Seival area.

KEYWORDS: Barites; REE geochemistry; Hydrothermal alteration; Camaquã Basin mineralizations.

RESUMO

Barita, calcita e hematita são associadas a depósitos de minério na Bacia do Camaquã e relacionadas ao estágio tardi-magmático a hidrotermal de baixa-temperatura. As análises de Microssonda Eletrônica e Elementos Terras Raras (ETR) nos cristais de barita foram medidas para reconstruir as condições hidrotermais de baixa temperatura. Albitização do plagioclásio (andesina-labradorita) foi associada com parte ou porção de bário e a desestabilização do sulfeto deve ter fornecido enxofre para o fluido responsável pela precipitação de barita (<150°C). A precipitação tardia de barita e seus conteúdos de elementos maiores, traços e ETR sugerem uma fonte de metal relacionada a albitização e retransmitido por cloritização associada com uma crescente proporção de água meteórica. O influxo de fluido meteórico (conteúdo de ETR) tem providenciado mudanças nas condições de Eh-pH e oxidação de fluido dominante H_2S-rico (calcocita, covelita) para fluido com SO_4-rico dominante associado com precipitação de barita. Baseado na diferença do conteúdo de bário de andesina-labradorita magmática e albita, um volume de 1 m^3 de andesito alterado é necessário para produzir 1,6 kg de barita. O volume de andesito alterado através do processo hidrotermal (albitização, cloritização e desestabilização de sulfetos) corresponde a 0,06 % e ocorre nos últimos veios na área do Seival.

PALAVRAS-CHAVES: Baritas; Geoquímica de ETR; Alteração hidrotermal; Mineralizações na Bacia do Camaquã.

1. INTRODUCTION

In hydrothermal and supergene contexts, the precipitation of barite is associated with low–temperature fluids (<150 °C; Hanor, 2000). The extremely low–solubility of barite (Deer et al., 1992; Jamieson et al., 2016) makes this mineral resistant to weathering and reconstruction of low–temperature conditions. Therefore, the crystallization of barite promoted by barium and SO_4^{2-} fluids records alteration of Ba–rich feldspar and pyroxene (Sorrell, 1962; Green, 1980; Mehnert and Büsch, 1981; Deer et al., 1992; Chang et al., 1996) and sulfate from seawater (Goldberg, 1969; Piper, 1974; Michard et al., 1984; Elderfield, 1988; Martin et al., 1995) or oxidation of sulfides (Brimhall and Crerar, 1987; Vaugham and Craig, 1997).

Barite precipitation in the Camaquã Basin is associated with vein–type or disseminated Cu–Pb–Zn–rich sulfide forming ore deposits (Bettencourt, 1976; Remus et al., 2000; Toniolo et al., 2004; Renac et al., 2014). In this case, the precipitation of sulfides and gangue minerals as barite and calcite were related to late–magmatic to low–temperature hydrothermal stage. In the Seival area, metallic

enrichment was associated with albitization of andesine–labradorite (650 to 250 °C; Fontana et al., 2017) and chloritization of pyroxene (312 to 120 °C). Barite, calcite and minor hematite fill fractures and residual porosity of andesite lavas (Lopes et al., 2014; Fontana et al., 2017) and represent the latest aqueous–fluid circulation interpreted as low–temperature meteoric fluids (Fontana et al., 2017). In the literature, hydrothermal–volcanic systems with barite and calcite may have different trace element concentrations and Rare Earth Element (REE) patterns from continental–hydrothermal barite to seawater (Michard, 1989). Few studies concern barite origin and its formation conditions (Guichard et al., 1979; Michard, 1989; Barrett et al., 1990; Martin et al., 1995). Major, trace and REE contents may contribute to the understanding of metal source related to alteration of surrounding volcanogenic rocks or external fluids (eg., Guichard et al., 1979; Morgan and Wandless, 1980; Jurkovic et al., 2010; Zarasvandi et al., 2014). We studied major elements and REE contents of barite to propose an origin of low–temperature fluid in the Seival area.

2. GEOLOGICAL SETTINGS

2.1 REGIONAL GEOLOGY

The Mantiqueira Province extends from northeast Brazil to Uruguay as a Gondwanian–orogenic system with Neoproterozoic age, formed during collision between La Plata and Kalahari cratons (Almeida and Hasui, 1984; Saalmann et al., 2005) (Fig. 1A). Its southernmost portion in Brazil receives the denomination of Sul–rio–grandense Shield. This shield was subdivided in two geotectonic units: (i) Rio de La Plata Craton and Dom Feliciano Belt (Chemale Jr., 2000; Hartmann et al., 2007; Philipp et al., 2016) (Fig. 1B). The Seival area is a zone of volcanogenic rocks associated with the Bom Jardim Group (600–590 Ma; Lima et al., 2007; Janikian et al., 2008 and 2012) from the Camaquã Basin (630–540 Ga; Chemale Jr., 2000; Paim et al., 2000) (Fig. 2) related to the final evolution of the Dom Feliciano Belt (Chemale Jr., 2000; Paim et al., 2000; Philipp et al 2016; Lopes et al., 2018). The Hilário Formation (600–590 Ma; Janikian et al., 2008) belongs to the Bom Jardim Group

deposition (Paim et al., 2000). These volcanogenic rocks were associated with the Lavras do Sul Intrusive Complex (601 to 598 Ma; Nardi, 1984; Lima and Nardi, 1998; Remus et al., 1999; Remus et al. 2000; Gastal et al., 2006; Liz et al. 2009; Fontana et al., 2017; Lopes et al., 2018).

The fractures and dikes in the Seival area are associated with tectonic reworking related to shear zones and deformation episodes that allowed the development of intense fracturing and, consequently, fluid percolation. Lopes et al. (2018) indicated the ore deposition associated with the development of these shear zones with NE–SW and NW–SE directions in the Sul–rio–grandense Shield. The mineralization structures have NE–SW direction and barite veins occur mainly in fractures of N–S direction.

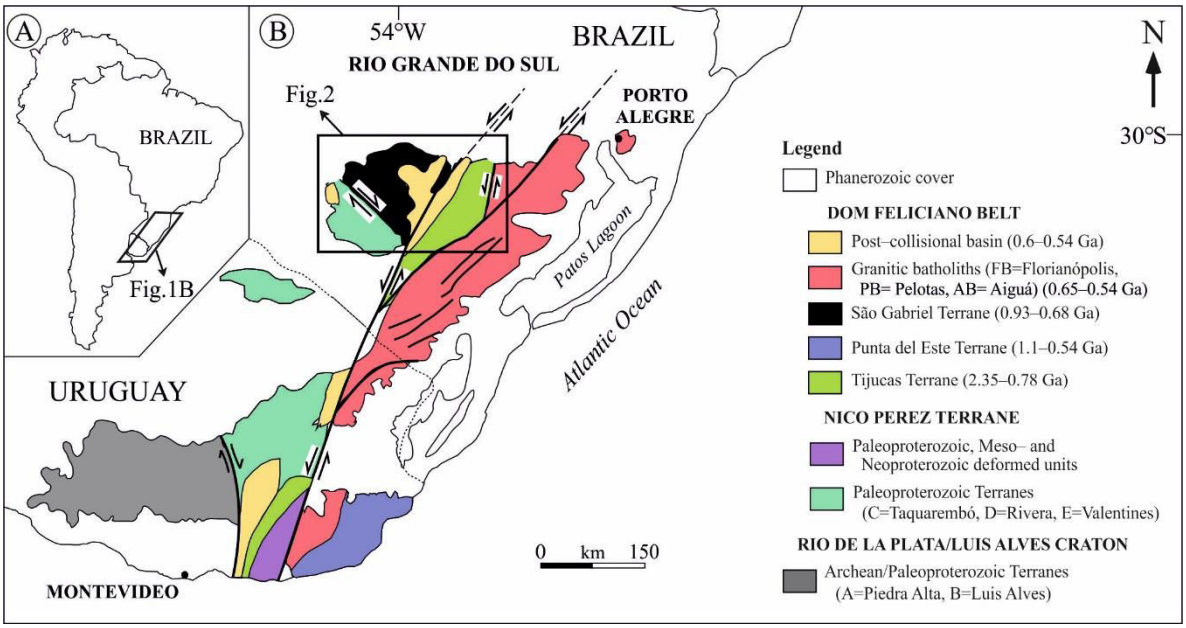

Figure 1. A) Sul–rio–grandense and Uruguay shields location in South America; B) Geotectonic units of the Sul–rio–grandense and Uruguay shields (from Hartmann et al., 2007; Oyhantçabal et al., 2011; Philipp et al., 2016a).

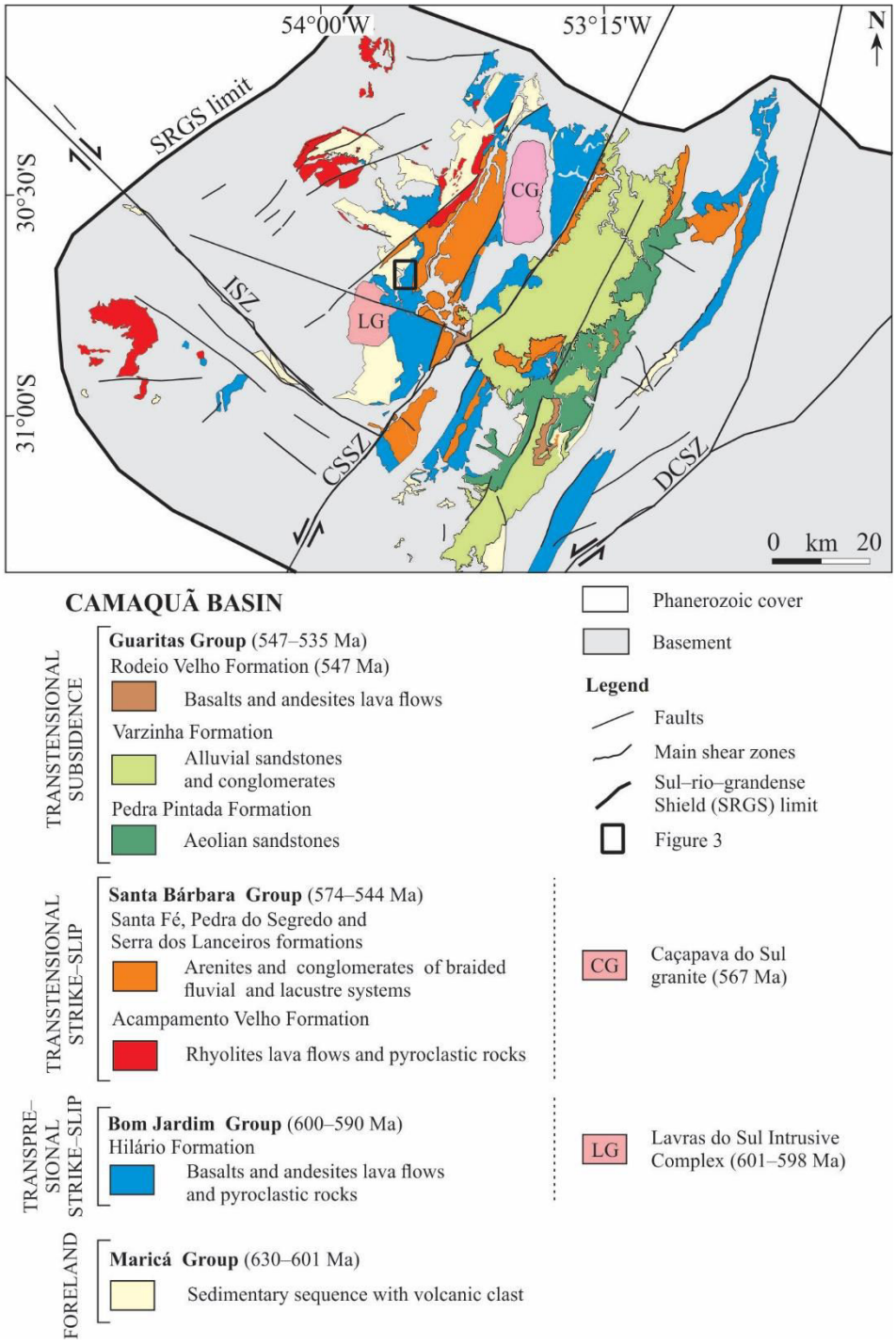

Figure 2. Geological map of the Camaquã Basin and associated granites (modified from Wildner et al., 2002; Toniolo et al., 2007). Granitoids: LG = Lavras do Sul Intrusive Complex; CG = Caçapava do Sul granite; Shear zones: ISZ = Ibaré; CSSZ = Caçapava do Sul; DCSZ = Dorsal do Canguçu.

2.2 TEXTURE AND MINERALOGY

Volcanogenic rocks and andesitic to trachyandesitic dikes (Lopes et al., 2014; Fontana et al., 2017) of the Seival area (Fig. 3) host Cu–Ag mineralizations surrounded by extensive hydrothermal halos, ca. 0.20 Mt of Cu with an average grade of ~1.40 % (Reischl, 1978; Lopes et al., 2018). This sequence is represented by lapilli tuff supported in a matrix of vesicular fine ash with crystals of plagioclase, pyroxene, quartz, opaque minerals and porosity with clasts of several volcanic materials, generally vesicular andesite rocks (Lopes et al., 2014; Fontana et al., 2017). Andesite lava flows have phenocrysts of plagioclase and clinopyroxene dispersed in a trachytic matrix with oriented plagioclase and pyroxene (Lopes et al., 2014). Volcanic agglomerates contain rounded volcanic clast and occur associated with faults and fractures. Andesitic and trachyandesitic dikes have subhedral phenocrysts of plagioclase and pyroxene in a trachytic matrix with oriented plagioclase. Relicts of pyroxene phenocrysts are scarce and most were partially or totally replaced by clay minerals and calcite, sometimes keeping its original shape. The andesitic dikes have albitized plagioclase phenocrysts, while some of them preserved a magmatic chemistry in the center or some preserved part of crystals. The andesitic to trachyandesitic dikes are also associated with NE–SW oriented structures (Lopes et al., 2014; Fontana et al., 2017; Lopes et al., 2018).

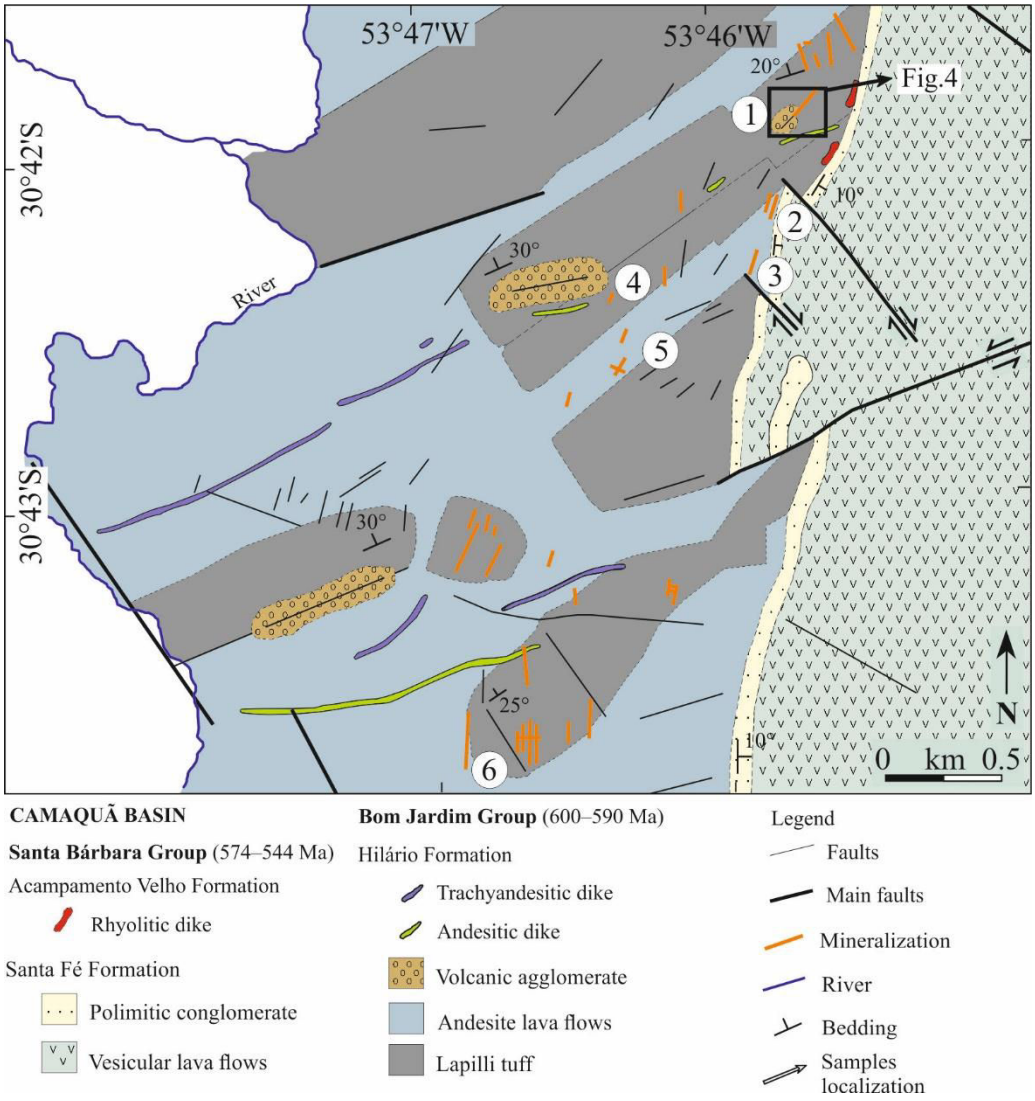

Figure 3. Seival Mine geological map. Sequence of lapilli tuff, volcanic agglomerate and andesite lava flows with andesitic and trachyandesitic dikes (NE direction) of the Hilário Formation (modified from Reischl, 1978; Lopes et al., 2014). Keys: 1= Barite; 2= João Dahne; 3= Morcego; 4= Meio; 5= Cruzeta; 6= Alcides.

3. METHODOLOGY

The samples of field and drill–core consist of volcanogenic rocks with hydrothermal alteration. The selected veins of barite are hosted in the lapilli tuff and andesite lava flows from one and five locations, respectively. We prepared grain mounts and thin sections of barite for petrography and Electron Microprobe (EMPA) analysis. Further on, the mono–mineral content of separates were checked by X–

ray diffraction (Siemens D5000, KαCu, 40 kV and 25 mA; Lopes et al., 2014) at the *Geoscience Institute* (CPGq IGEO–UFRGS).

The X–ray diffraction of powdered samples and EMPA analysis identified their crystallography and mineral compositions. The major and trace element compositions of the plagioclase and barite were examined on a CAMECA, SXFive Electron Probe Micro Analyzer (EPMA) equipped with 5 wavelength dispersive spectrometers with TAP, PET and LIF crystal detector at the *Geoscience Institute* (CPGq IGEO–UFRGS). The analytical procedure used standard conditions optimized to silicate (plagioclase) analysis, using a 5 µm defocused beam, with an acceleration voltage of 15 kV and beam current of 10 nA with peak counting time of 10 sec and two background measurements with counting times of 5 sec. Analytical procedure measurements for barite used LPET detector with a 5 µm defocused beam (beam 15 kV, 100 nA, peak and background counting times of 30 and 10 s, respectively). First, the Na content was measured to minimize its loss by volatilization with increasing time of analysis. Standards were calibrated with synthetic and standard minerals with various diffracting crystals, as follows: albite to Na on TAP, diopside to Mg on TAP, $CaSiO_3$ to Si and Ca on TAP and LPET respectively, sanidine to Al and K on TAP and LPET respectively, rutile to Ti on LPET, hematite to Fe on LLIF and rhodonite to Mn on LLIF. We also used barite to S and Ba on LPET, celestite to Sr on LPET, anhydrite to Ca on LPET in the barite analysis. Measured X–ray intensities were ZAF–corrected. Procedures used to Ba detection on plagioclase were: a backscatter–electron image to detect Ba in plagioclase grain, the procedure to measure Ba contents used first a measurement of background intensity on each side of Ba peak and Ba measurement in the selected area. Traces of Ba in plagioclase standard and samples were calibrated using a Ba–poor feldspar (orthoclase, Ba: 0.12 %). The TiO_2 and Al_2O_3 contents were simultaneously measured to reduce the interference of overlapping peaks (TiKα–BaLα1 and AlKα–BaLα3) on Ba measurements. Limits of detection varied from 206 to 2019 ppm (n= 33); equivalent to standard error of 0.02 % (2σ).

The REE contents were determined in concentrates of veins of barite and calcite. The calcite (< 100 mg) was digested with 10 % HNO_3 (ultra–pure). Barite was digested (500 to 250 mg) using ten times more $NaCO_3$–ultrapure (Merck 99.999% pure) through the flux–based fusing method, as described by Barbieri et al. (1982) and Breit et al. (1985). Barite – $NaCO_3$ mixture was loaded in a Pt–crucible (20 mL crucibles) with an addition of 1 mL Lithium–Iodide (LiI), enhancing the recovery of the fused material from the Pt–crucibles. This LiI was removed by evaporation during the fusing process. The mixture was heated for 10 hours in a muffle furnace (1100 °C). The cooled material was grounded into a very fine powder using an agate grinder. This powder was dissolved in a cleaned Teflon beaker with distilled water (UHQ). The residues (Na_2CO_3 and $BaCO_3$) and sulfate–free solution were heated in 10 mL of HCl and then evaporated to dryness and dissolved in HNO_3 (1 M). The dissolved material went through C_{18} Sep–Pak cartridges (Shabani et al., 1992) to reduce barium and strontium amount. In this resin, we expected that all barium would be transported through the column without being bonded to the bis (2–ethylhexyl) orthophosphoric acid. The cartridge was rinsed (10 mL of 0.01 M HCl) then its content was eluated with HCl (30 mL, 6 M).

The digested solutions were analyzed by ICP–MS (Elan DRCII, Perkin Elmer) at *GEOAZUR* (Université Côte d'Azur). Quantification limits were below 50 ng/L. The REEs were determined by ICP–MS measurements of a digested sulfate–sulfide mineral, thereby correcting for the interference of $^{135}Ba^{16}O$ on ^{153}Eu using the 'doubly charged' technique (Barrett et al., 1990; Jarvis et al., 1989). The use of a Ba–REE–spiked solution (1.5 mg L^{-1}) allowed the determination of an optimal elution time for a REE recovering rate of 87 %. The elements concentrations were expressed as ppm (mg kg^{-1}) and normalized by chondrite values (McDonough and Sun, 1995).

4. RESULTS

4.1 STRUCTURAL GEOLOGY AND CRYSTALLIZATION SEQUENCE

Barite and calcite veins occur located in the same geological context of faults and fractures hosted in the volcanogenic rocks associated with Cu–Ag

mineralizations. The Barita Mine (the main barite location) is the main occurrence of barite in the area, where subvertical fault plans (N10°E/70–88°NW oriented, N10°W/70–88°NE oriented and N40–60°E/70–88°NW oriented) (Fig. 4) host series of 0.1 to 0.5 cm veinlets filled by barite and Cal–3. Outside the Barita Mine, the veinlets are smaller with a filling of Cal–3 and quartz.

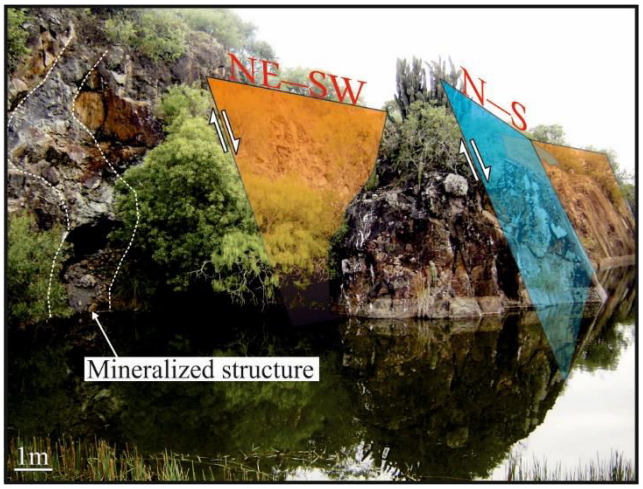

Figure 4. Photography of the Barita Mine (the main barite location) with mineralized structure and NE–SW and N–S oriented faults in the Seival area.

The magmatic crystallization of andesitic lava flows and lapilli tuff is represented by augite and andesine–labradorite. The vesicular andesite lava flows are filled by calcite (Cal–1; Fontana et al., 2017). The pyrite and the chalcopyrite were considered as a late–magmatic hydrothermal alteration associated with calcite (Cal–2; Fontana et al., 2017), minor hematite (Hem–1) and quartz. The hydrothermal phase is separated in two stages with high and low temperatures. The first hydrothermal phase is characterized by albite, chlorite, titanite, calcite (Cal–2) and quartz associated with chalcopyrite, chalcocite and bornite. The second stage is related to veins with barite, calcite (Cal–3; Fontana et al., 2017), minor hematite (Hem–2) and quartz precipitation hosted in fractures and faults of the volcanogenic rocks.

4.2 TEXTURES AND PETROGRAPHIC OBSERVATIONS

The veins and veinlets of barite and calcite take place in fractured and hydrothermal altered zone with rims or halos with hematite (Hem–2), chlorite and chlorite/smectite mixed–layers and remains of Cu–Ag ore represented by disseminated crystals of Fe– and Cu–rich sulfides (Fontana et al., 2017). In veins and veinlets, macroscopic observations show white to pinkish barite occur as aggregates of tabular and prismatic crystals with subhedral to euhedral forms (Fig. 5A). A special attention has been paid to barite crystals and mineral inclusion in barite. These mineral inclusions in larger barite are calcite with oxidized sulfides and hematite. In calcite–rich veins the petrography confirmed the association of dominant calcite–filled (Cal–3) fractures (Fig. 5B) with quartz (Fig. 5C), a smaller proportion of barite or malachite particularly in the mineralized zones (Fig. 5D) with Cu–sulfides such as chalcocite (Fig. 5E) and bornite (Fig. 5F).

The petrographic observations show barite crystals with calcite inclusions and indicate the predominance of clay minerals associated with sulfides. The associations of barite and Cal–3 do not represent mineral assemblages since no grain intergrowth of these minerals was observed. Barite is cutted by Cal–3 veins (Fig. 6A), which also occur in the contact between barite veins and host rock (Fig. 6B). Cal–3 also occurs within joints of barite crystals. This Cal–3 is associated with sulfides grains, hematite and white mica. The sulfides were identified as chalcocite. These sulfides are filling vesicles and the intergranular porosity of the volcanogenic rock (Fig. 6C). The chalcocite grains are concentrated in the Cal–3 veins and in a few millimeters of contact between barite and Cal–3 veins (Fig. 6D). The malachite and azurite were observed in the different Cu occurrences and were considered as a product of the recent weathering of Cu–sulfides.

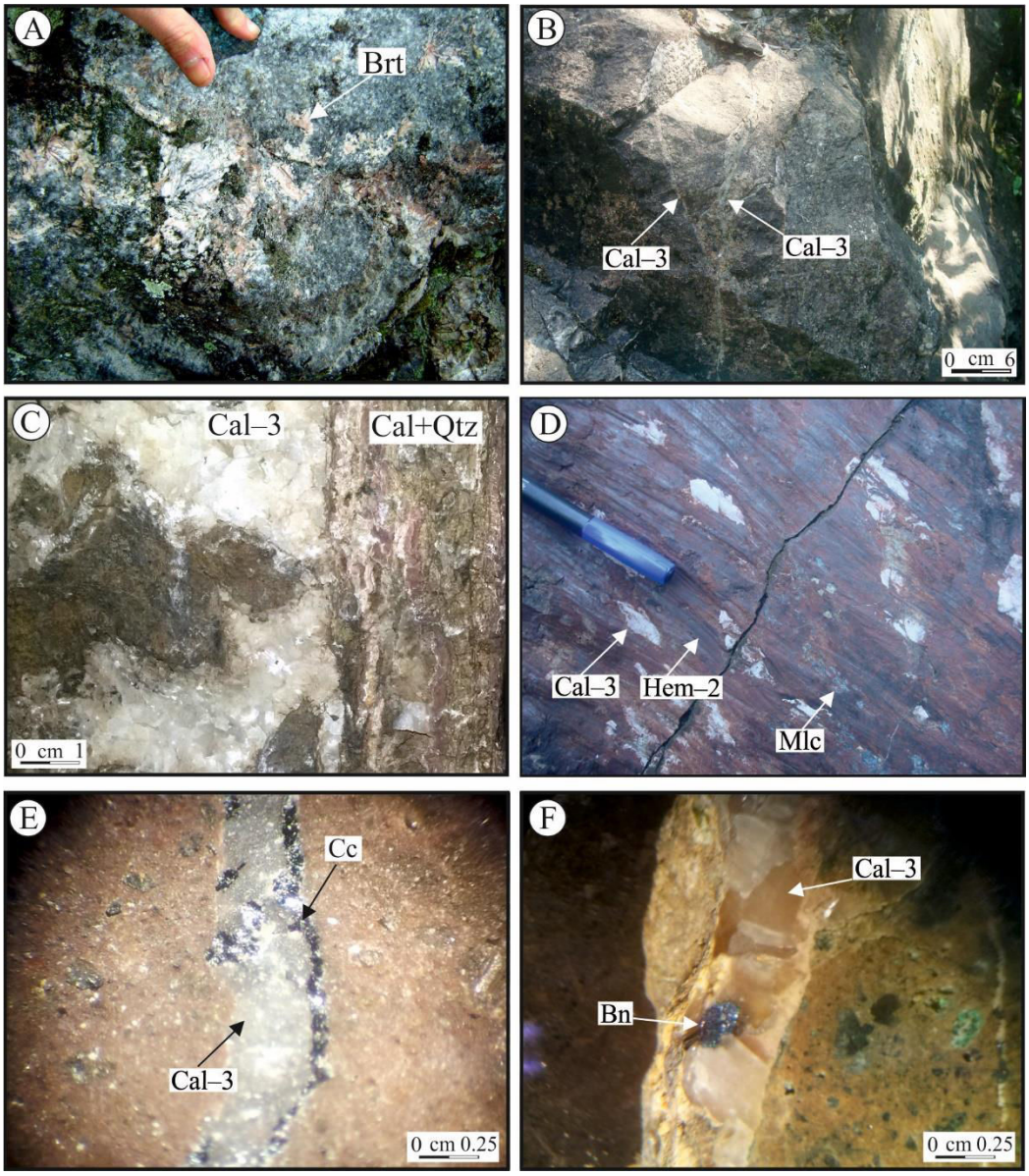

Figure 5. Barite and calcite (Cal–3; Fontana et al., 2017) in Seival area. (A) White to pinkish barite and aggregates of tabular and prismatic crystals; (B) Calcite (Cal–3) veins in mineralized structures; (C) Two generations of calcite (Cal–3) and calcite–quartz veins; (D) Association of malachite, calcite (Cal–3) and hematite (Hem–2); (E) Hand sample of lapilli tuff with calcite (Cal–3) vein and remobilized chalcocite; (F) Hand sample of andesite lava flow with calcite (Cal–3) vein and bornite. Keys: Brt= Barite; Qtz= Quartz; Cal= Calcite; Hem= Hematite; Mlc= Malachite; Cc= Chalcocite; Bn= Bornite.

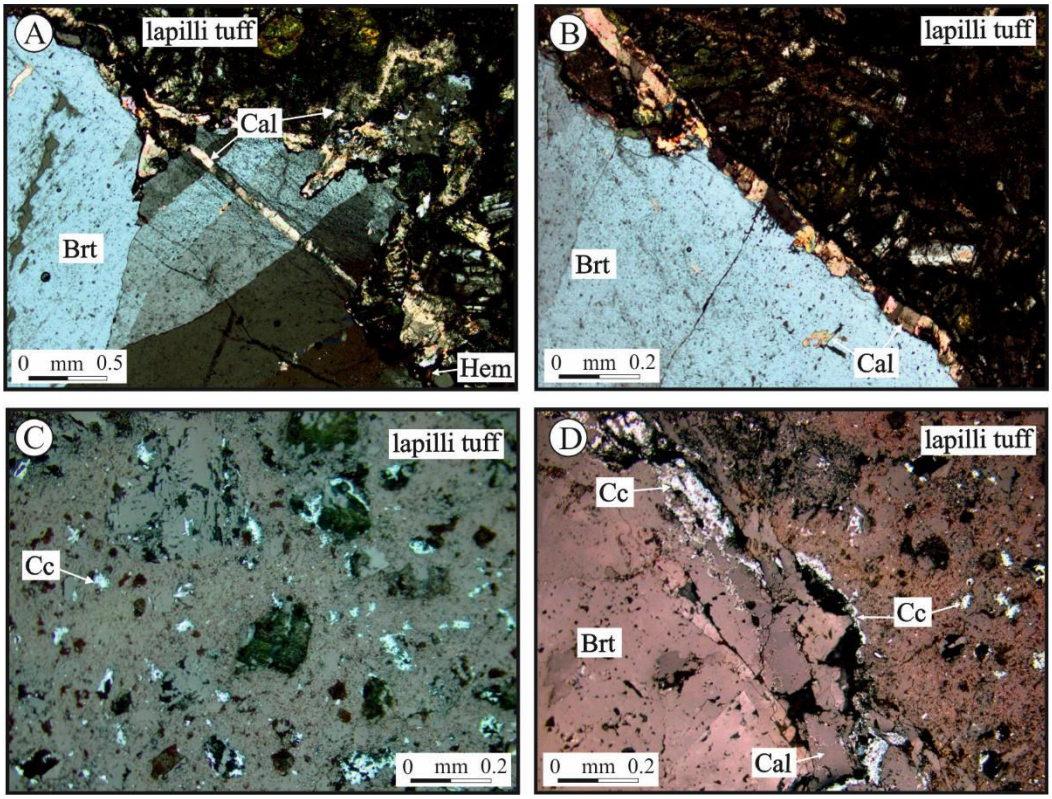

Figure 6. (A) Polarized light photography showing barite vein cutted by Cal–3 vein; (B) Polarized light photography barite vein with included Cal–3 vein; (C) Reflected light photography of chalcocite in lapilli tuff matrix; (D) Reflected light photography with association of Cal–3 vein and chalcocite . Keys: Brt= Barite; Cal= Cal–3 (calcite); Hem= Hematite; Cc= chalcocite.

Crystallographic parameters of the $BaSO_4$–$SrSO_4$ solid–solution were indirectly determined using the relationship of $SrSO_4$ content in barites shows by Abidi et al. (2012). The X–ray diffraction method in barites confirmed barites in the separates of REE analysis with Sr content (part 4.3). The main peak (d–spacing) is 3.43 Å and occurs in position 25.90 °2 theta (Cu) in barite samples (Fig. 7).

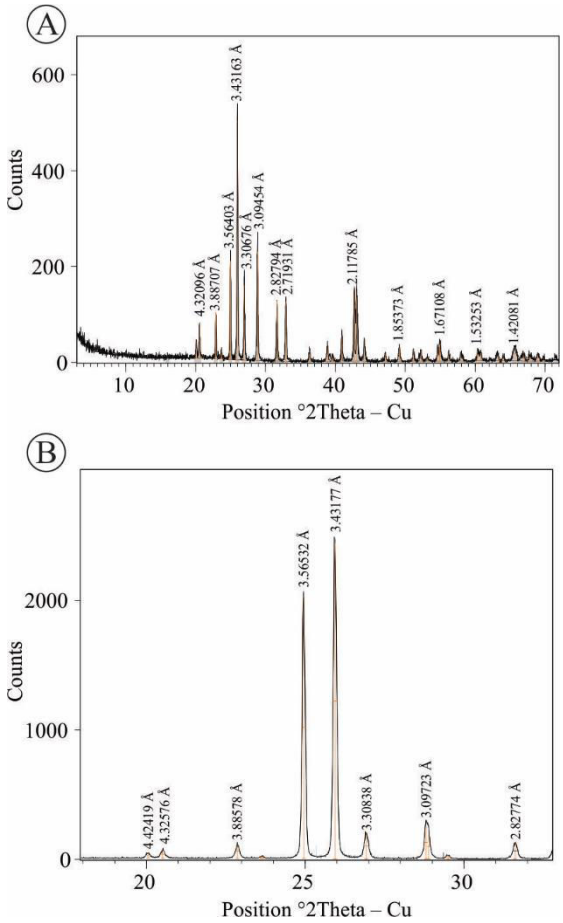

Figure 7. X–ray powder diffraction method in barites separate.

4.3 BARITE AND BARIUM COMPOSITIONS IN PLAGIOCLASE

The EMPA analysis tested barium variation in the plagioclase. The content of Na (0.02 to 0.16 atomic weight %), S (13.08 to 14.05 atomic weight %), Ba (56.87 to 59.10 atomic weight %), Sr (0.02 to 1.01 atomic weight %) and O (26.42 to 27.94 atomic weight %) is showed in Table 1. The contents of Si, Mg, Al, K, Ca, Ti, Cu, Mn and Fe are low–content or trace (< 0.2 atomic weight %) in the analyzes. Low concentration of Sr marked barite end–member of barite–celestine solid solution series.

Table 1. Representative barite chemical compositions from Seival Mine.

Point	1	2	3	4	5	6	7	8	9
SiO_2 (wt %)	0	0	0.02	0.01	0	0	0.01	0	0.01
TiO_2	0.02	0	0	0	0	0.04	0	0	0.05
Al_2O_3	0	0.03	0	0	0	0	0	0.04	0
FeO	0	0.01	0	0.05	0	0	0	0	0.04
MnO	0	0.05	0	0	0	0	0	0.03	0.07
MgO	0	0	0	0	0	0	0	0	0
CaO	0.01	0	0	0.03	0	0	0.08	0.01	0
Na_2O	0.09	0.09	0.18	0.10	0.05	0.09	0.14	0.18	0.12
K_2O	0.04	0	0	0	0	0	0.02	0	0
BaO	64.22	64.83	64.89	65.21	65.78	65.99	65.33	64.08	64.86
SrO	0.50	0.31	0.12	0.50	0.40	0.12	0.03	1.20	0.20
CuO	0.11	0	0	0.01	0	0.07	0.06	0.05	0
SO_3	34.96	34.17	33.97	34.17	34.23	34.14	33.25	34.44	34.76
Sum	99.95	99.49	99.18	100.08	100.46	100.45	98.92	100.03	100.11
Si (wt %)	0	0	0.01	0	0	0	0	0	0
Ti	0.01	0	0	0	0	0.03	0	0	0.03
Al	0	0.01	0	0	0	0	0	0.02	0
Fe	0	0.01	0	0.04	0	0	0	0	0.03
Mn	0	0.04	0	0	0	0	0	0.02	0.06
Mg	0	0	0	0	0	0	0	0	0
Ca	0.01	0	0	0.02	0	0	0.05	0.01	0
Na	0.06	0.06	0.13	0.07	0.03	0.06	0.11	0.13	0.09
K	0.04	0	0	0	0	0	0.02	0	0
Ba	57.52	58.07	58.12	58.41	58.92	59.10	58.51	57.39	58.09
Sr	0.42	0.26	0.10	0.42	0.34	0.10	0.02	1.01	0.17
Cu	0.08	0	0	0.01	0	0.05	0.05	0.04	0
S	14.00	13.69	13.6	13.68	13.71	13.67	13.32	13.79	13.92
O	27.80	27.35	27.22	27.42	27.46	27.43	26.84	27.61	27.72
Sum	99.94	99.49	99.18	100.07	100.46	100.44	98.92	100.02	100.11

Continuation of Table 1.

Point	10	11	12	13	14	15	16	17	18
SiO_2 (wt %)	0	0	0.05	0.02	0	0.03	0.01	0.05	0.02
TiO_2	0.02	0	0	0.05	0	0.02	0.02	0	0.04
Al_2O_3	0	0	0	0.06	0	0	0	0	0
FeO	0	0	0.05	0.09	0.04	0	0.01	0	0
MnO	0	0.04	0.03	0	0	0	0	0	0
MgO	0	0	0	0	0	0	0.02	0	0
CaO	0	0	0.01	0	0.01	0.03	0.03	0.01	0
Na_2O	0.03	0.09	0.17	0.15	0.09	0.15	0.12	0.06	0.05
K_2O	0	0.01	0	0	0	0	0	0.01	0.01
BaO	65.55	64.80	65.05	65.23	65.28	65.28	63.50	65.24	65.71
SrO	0.03	0.63	0.55	0.12	0.33	0.05	1.14	0.06	0.09
CuO	0	0.05	0	0.05	0.06	0.13	0	0.06	0
SO_3	34.43	34.77	34.33	33.72	34.17	34.14	34.78	33.88	34.06
Sum	100.06	100.39	100.24	99.49	99.98	99.83	99.63	99.37	99.98
Si (wt %)	0	0	0.02	0.01	0	0.01	0.01	0.02	0.01
Ti	0.01	0	0	0.03	0	0.01	0.01	0	0.03
Al	0	0	0	0.03	0	0	0	0	0
Fe	0	0	0.04	0.07	0.03	0	0.01	0	0
Mn	0	0.03	0.03	0	0	0	0	0	0
Mg	0	0	0	0	0	0	0.01	0	0
Ca	0	0	0.01	0	0.01	0.02	0.02	0.01	0
Na	0.02	0.07	0.12	0.11	0.06	0.11	0.09	0.05	0.04
K	0	0.01	0	0	0	0	0	0.01	0.01
Ba	58.71	58.04	58.26	58.43	58.47	58.47	56.87	58.43	58.85
Sr	0.02	0.53	0.47	0.10	0.28	0.05	0.96	0.05	0.07
Cu	0	0.04	0	0.04	0.05	0.10	0	0.04	0
S	13.79	13.93	13.75	13.50	13.68	13.67	13.93	13.57	13.64
O	27.51	27.75	27.55	27.17	27.40	27.39	27.72	27.19	27.33
Sum	100.06	100.40	100.25	99.49	99.98	99.83	99.63	99.37	99.98

Continuation of Table 1.

Point	19	20	21	22	23	24	25	26	27
SiO_2 (wt %)	0	0.05	0	0.05	0.02	0.04	0	0.02	0
TiO_2	0.01	0	0.01	0	0	0.04	0	0.01	0
Al_2O_3	0	0.01	0	0	0	0	0	0.01	0
FeO	0.01	0	0.04	0	0	0.04	0.05	0	0
MnO	0	0	0.03	0	0	0	0	0	0
MgO	0	0	0	0	0	0	0	0	0
CaO	0	0	0	0.03	0	0	0	0	0.01
Na_2O	0.12	0.04	0.11	0.05	0.13	0.07	0.12	0.13	0.12
K_2O	0	0	0	0	0	0	0.01	0	0
BaO	65.19	65.76	64.71	65.14	65.22	65.24	64.29	65.46	65.18
SrO	0.33	0.11	0.58	0.31	0.38	0.27	0.57	0.31	0.17
CuO	0.04	0.09	0	0.06	0	0	0	0.08	0.01
SO_3	34.38	34.64	34.21	35.08	34.10	34.69	33.89	34.14	33.91
Sum	100.08	100.7	99.69	100.72	99.85	100.39	98.93	100.16	99.40
Si (wt %)	0	0.02	0	0.02	0.01	0.02	0	0.01	0
Ti	0.01	0	0.01	0	0	0.03	0	0.01	0
Al	0	0.01	0	0	0	0	0	0	0
Fe	0.01	0	0.03	0	0	0.03	0.04	0	0
Mn	0	0	0.02	0	0	0	0	0	0
Mg	0	0	0	0	0	0	0	0	0
Ca	0	0	0	0.02	0	0	0	0	0
Na	0.09	0.03	0.08	0.04	0.10	0.05	0.09	0.10	0.09
K	0	0	0	0	0	0	0.01	0	0
Ba	58.38	58.90	57.96	58.34	58.42	58.43	57.58	58.63	58.38
Sr	0.27	0.09	0.49	0.26	0.32	0.23	0.48	0.26	0.14
Cu	0.04	0.07	0	0.05	0	0	0	0.07	0.01
S	13.77	13.87	13.70	14.05	13.66	13.89	13.57	13.67	13.58
O	27.51	27.70	27.40	27.94	27.36	27.72	27.16	27.42	27.20
Sum	100.08	100.69	99.69	100.72	99.87	100.40	98.93	100.17	99.40

Continuation of Table 1.

Point	28	29	30	31	32	33	34	35
SiO_2 (wt %)	0	0	0.02	0	0.03	0	0.03	0
TiO_2	0.07	0	0	0.03	0.02	0	0.06	0
Al_2O_3	0	0	0	0	0	0	0	0
FeO	0.02	0	0.02	0.05	0.08	0	0.03	0.03
MnO	0	0	0	0	0.09	0	0	0
MgO	0	0	0	0	0	0	0	0
CaO	0	0.03	0.01	0.01	0	0	0.02	0
Na_2O	0.09	0.13	0.15	0.12	0.08	0.09	0.13	0.22
K_2O	0	0	0	0	0	0	0.01	0
BaO	64.86	64.71	64.99	64.69	65.31	64.56	64.49	64.05
SrO	0.43	0.54	0.40	0.16	0.38	0.54	1.09	0.94
CuO	0.04	0	0.08	0	0	0.11	0	0.01
SO_3	34.87	33.83	34.61	32.67	34.04	34.89	34.71	34.71
Sum	100.38	99.24	100.28	97.73	100.03	100.19	100.57	99.96
Si (wt %)	0	0	0.01	0	0.01	0	0.01	0
Ti	0.04	0	0	0.02	0.01	0	0.03	0
Al	0	0	0	0	0	0	0	0
Fe	0.02	0	0.01	0.04	0.06	0	0.02	0.02
Mn	0	0	0	0	0.07	0	0	0
Mg	0	0	0	0	0	0	0	0
Ca	0	0.02	0.01	0.01	0	0	0.01	0
Na	0.07	0.10	0.11	0.09	0.06	0.07	0.10	0.16
K	0	0	0	0	0	0	0.01	0
Ba	58.09	57.96	58.21	57.94	58.49	57.82	57.76	57.36
Sr	0.36	0.46	0.33	0.14	0.32	0.46	0.92	0.79
Cu	0.03	0	0.07	0	0	0.09	0	0.01
S	13.96	13.55	13.86	13.08	13.63	13.97	13.90	13.90
O	27.81	27.16	27.66	26.42	27.37	27.78	27.80	27.71
Sum	100.38	99.25	100.27	97.74	100.02	100.19	100.56	99.95

We measured the barium compositions in the plagioclases with slight albitization and strong albitization to verify the barium variation (Fig. 8A). The andesine–labradorite and albite compositions (Fig. 8B) showed different content of barium. The andesine–labradorite has 0.11 to 0.14 atomic weight % (Table 2) of barium and the albite has < 0.02 atomic weight % (Table 2).

Table 2. Representative barium compositions with a standard deviation of 0.02 weight % in andesine–labradorite and albite. Keys: DL= detection limits; And–lab= Andesine–labradorite.

Point	1	2	3	4	5	6	7	8	9
BaO (wt %)	0.12	0.02	0.13	0.14	0.14	0.15	0.15	0.13	0.13
Ba (wt %)	0.11	0.02	0.11	0.13	0.13	0.14	0.13	0.11	0.12
O	0.01	0	0.01	0.01	0.01	0.02	0.02	0.01	0.01
Sum	0.12	0.02	0.13	0.14	0.14	0.15	0.15	0.13	0.13
DL (ppm)	217	206	218	216	217	215	218	218	217
Composition	and–lab	albite	and–lab	and–lab	and–lab	and–lab	and–lab	and–lab	and–lab

Point	10	11	12	13	14	15	16	17	18
BaO (wt %)	0.14	0.13	0.13	0.14	0.13	0.14	0.12	0.12	0.12
Ba (wt %)	0.13	0.11	0.12	0.13	0.11	0.13	0.11	0.11	0.10
O	0.02	0.01	0.01	0.01	0.01	0.01	0.01	0.01	0.01
Sum	0.14	0.13	0.13	0.14	0.13	0.14	0.12	0.12	0.12
DL (ppm)	219	217	219	216	217	217	217	219	218
Composition	and–lab	and–lab	and–lab	and–lab	and–lab	and–lab	and–lab	and–lab	and–lab

Point	19	20	21	22	23	24	25	26	27
BaO (wt %)	0	0	0.01	0.01	0.01	0.01	0.14	0.14	0.12
Ba (wt %)	0	0	0.01	0.01	0.01	0.01	0.12	0.13	0.11
O	0	0	0	0	0	0	0.01	0.02	0.01
Sum	0	0	0.01	0.01	0.01	0.01	0.14	0.14	0.12
DL (ppm)	210	209	206	207	209	209	216	215	218
Composition	albite	albite	albite	albite	albite	albite	and–lab	and–lab	and–lab

Point	28	29	30	31	32	33
BaO (wt %)	0.13	0.11	0.14	0.14	0.12	0.14
Ba (wt %)	0.12	0.10	0.12	0.12	0.11	0.13
O	0.01	0.01	0.01	0.01	0.01	0.01
Sum	0.13	0.11	0.14	0.14	0.12	0.14
DL (ppm)	219	217	215	216	217	215
Composition	And–lab	And–lab	And–lab	And–lab	And–lab	And–lab

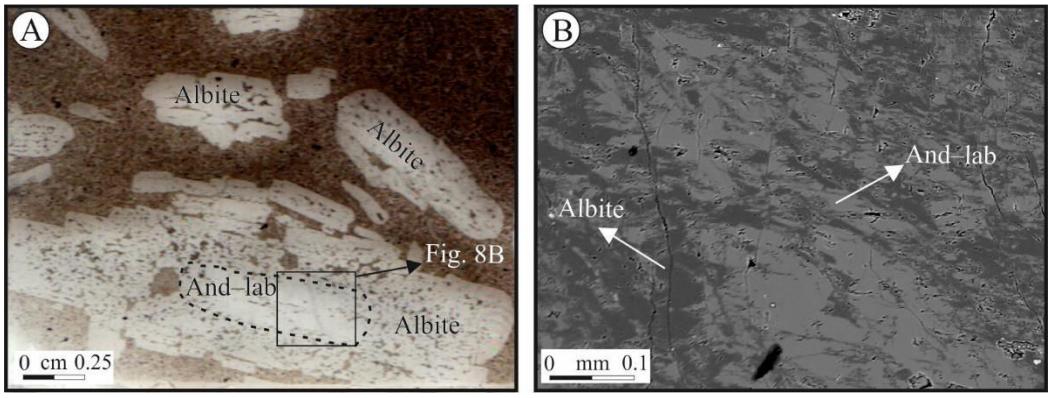

Figure 8. (A) Thin section natural photography of sample from andesitic dikes with phenocrysts of original plagioclase in the center and altered in boundaries; (B) Scanning electron microscope (SEM) backscattered image showing detail of central part andesine–labradorite crystal altered to albite. Keys: And–lab= Andesine–labradorite.

4.4 REE OF BARITE, CALCITE AND WHOLE–ROCK

The concentrations of REE in barite, calcite (Cal–3) and whole–rock (Lopes et al., 2014) samples are showed in Table 3. The total concentrations of REE in barite (ΣREE not normalized) vary from 769.76 to 2476.35 ppm; whereas calcites range from 1.06 to 14.18 ppm and whole–rock from 10.97 to 16.05 ppm. The La/Lu_N normalized ratio representing Light Rare Earth Elements (LREE) compared to Heavy Rare Earth Element (HREE) enrichment varies in barites from 0.04 to 0.11; whereas in calcite and whole–rocks they range from 3.61 to 201.15 and 18.43 to 28.25, respectively. The elevated REE patterns of the barite compared to the flatten calcite and whole–rocks is associated with similar Ce/La_N and Ce/Ce* normalized ratio (Table 3). The very high Eu estimated concentration was probably due to the interference effect of barium despite resin separation, using “doubly charged” technique to interference corrections (Jarvis et al, 1989).

Table 3. Concentrations of Rare Earth Elements and normalization values (McDonough and Sun, 1995) to barite, calcite and whole–rock samples from Seival Mine. Light REE (LREE: La to Sm); Heavy REE (HREE: Eu to Lu); ΣREE= sum of total concentration of Rare Earth Elements; Ratio= ΣLREE/ΣHREE; Eu/Eu*= The value of the normalized Eu anomaly calculated by the formula $[Eu/Eu^*]= [(Eu_N)/((SmN \times Gd_N)^{1/2})]$; Ce/Ce*= Value of Ce anomaly calculated by formula $Ce/Ce^*= [(Ce_N)/((La_N \times Pr_N)^{-1/2})]$ (Worrall and Pearson, 2001).

Sample	Barite–1	Barite–1	Barite–2	Barite–2	Barite–3	Barite–3
La	86.52	145.21	320.19	434.23	349.26	392.31
Ce	4.87	9.15	537.36	715.51	589.22	703.31
Pr	1.80	4.21	64.67	91.12	73.32	84.00
Nd	3.77	32.52	301.24	434.40	342.71	388.55
Sm	60.31	124.24	158.28	235.49	168.24	183.60
Gd	89.54	166.28	188.35	277.70	191.51	206.22
Tb	1.62	2.22	7.63	10.88	8.54	9.40
Dy	0.94	2.33	20.96	32.54	24.02	26.97
Ho	2.13	2.90	5.31	7.93	6.11	6.60
Er	0.99	1.69	9.02	13.80	9.69	11.29
Tm	19.08	33.52	31.80	55.74	43.36	44.47
Yb	482.18	867.50	810.22	1510.56	1122.64	1146.07
Lu	173.28	338.02	313.93	567.20	441.69	453.45
Normalization standard, chondrite (McDonough and Sun, 1995)						
La_N	365.04	612.72	1351.02	1832.21	1473.68	1655.30
Ce_N	7.94	14.92	876.61	1167.23	961.21	1147.32
Pr_N	19.36	45.40	696.85	981.93	790.05	905.18
Nd_N	8.25	71.16	659.16	950.54	749.92	850.23
Sm_N	407.52	839.46	1069.46	1591.15	1136.77	1240.55
Gd_N	449.97	835.57	946.49	1395.48	962.34	1036.29
Tb_N	44.89	61.50	211.24	301.47	236.57	260.31
Dy_N	3.80	9.45	85.22	132.27	97.62	109.63
Ho_N	39.08	53.15	97.32	145.24	111.90	120.86
Er_N	6.20	10.59	56.36	86.27	60.57	70.58
Yb_N	2994.91	5388.18	5032.43	9382.36	6972.92	7118.45
Lu_N	7043.82	13740.68	12761.21	23057.07	17954.69	18433.04
ΣLREE	157.26	315.33	1381.74	1910.75	1522.75	1751.77
ΣHREE	3415.84	6230.46	5220.81	8382.72	5843.07	6234.66
ΣREE	3573.09	6545.79	6602.55	10293.47	7365.82	7986.43
Ratio	0.05	0.05	0.26	0.23	0.26	0.28
La/Lu_N	0.05	0.04	0.11	0.08	0.08	0.09
Ce/La_N	0.02	0.02	0.65	0.64	0.65	0.69
Ce/Ce*	0.09	0.09	0.90	0.87	0.89	0.94

Continuation of Table 3.

Sample	Calcite–1	Calcite–2	Calcite–3	Calcite–4	Calcite–5
La	4.63	26.89	49.46	9.09	1.15
Ce	9.59	40.63	140.29	14.79	1.70
Pr	1.12	3.82	13.69	1.78	0.18
Nd	5.39	16.60	54.93	10.42	0.91
Sm	0.89	2.20	11.16	2.68	0.16
Gd	0.95	2.60	10.86	3.66	0.25
Tb	–	–	–	–	–
Dy	0.22	0.42	1.74	2.89	0.23
Ho	0.03	0.05	0.20	0.52	0.05
Er	0.10	0.24	0.91	1.71	0.23
Tm	0.01	0.01	0.04	0.20	0.03
Yb	0.05	0.11	0.39	1.39	0.24
Lu	0.01	0.01	0.04	0.19	0.03
Normalization standard, chondrite (McDonough and Sun, 1995)					
La_N	19.53	113.44	208.67	38.34	4.84
Ce_N	15.65	66.28	228.85	24.12	2.77
Pr_N	12.07	41.13	147.49	19.20	1.95
Nd_N	11.79	36.33	120.19	22.81	1.98
Sm_N	6.00	14.84	75.44	18.11	1.08
Gd_N	4.77	13.06	54.56	18.40	1.27
Tb_N	–	–	–	–	–
Dy_N	0.90	1.70	7.07	11.76	0.95
Ho_N	0.50	0.94	3.59	9.44	1.00
Er_N	0.63	1.47	5.69	10.69	1.45
Yb_N	0.32	0.71	2.42	8.66	1.48
Lu_N	0.25	0.56	1.72	7.73	1.34
ΣLREE	21.62	90.13	269.52	38.76	4.09
ΣHREE	1.62	4.02	17.35	11.12	1.13
ΣREE	23.24	94.15	286.87	49.88	5.22
Ratio	13.31	22.42	15.53	3.49	3.63
La/Lu_N	77.34	201.15	121.48	4.96	3.61
Ce/La_N	0.80	0.58	1.10	0.63	0.57
Ce/Ce*	1.02	0.97	1.30	0.89	0.90

Continuation of Table 3.

Sample	WR	WR	WR	WR
La	35.40	50.20	62.60	44.40
Ce	72.80	97.70	102.20	83.70
Pr	8.37	11.53	11.38	10.89
Nd	34.60	43.20	39.20	42.60
Sm	6.07	7.78	6.91	8.40
Gd	4.29	6.14	5.00	6.53
Tb	0.52	0.75	0.63	0.79
Dy	2.86	3.72	3.30	3.92
Ho	0.45	0.68	0.59	0.73
Er	1.23	1.69	1.53	1.88
Tm	0.18	0.23	0.22	0.26
Yb	1.26	1.58	1.48	1.69
Lu	0.18	0.23	0.23	0.25
Normalization standard, chondrite (McDonough and Sun, 1995)				
La_N	149.37	211.81	264.14	187.34
Ce_N	118.76	159.38	166.72	136.54
Pr_N	90.19	124.25	122.63	117.35
Nd_N	75.71	94.53	85.78	93.22
Sm_N	41.01	52.57	46.69	56.76
Gd_N	21.56	30.85	25.13	32.81
Tb_N	14.40	20.78	17.45	21.88
Dy_N	11.63	15.12	13.41	15.93
Ho_N	8.24	12.45	10.81	13.37
Er_N	7.69	10.56	9.56	11.75
Yb_N	7.83	9.81	9.19	10.50
Lu_N	7.32	9.35	9.35	10.16
ΣLREE	157.24	210.41	222.29	189.99
ΣHREE	12.56	16.94	14.72	18.41
ΣREE	169.80	227.35	237.01	208.40
Ratio	12.52	12.42	15.10	10.32
La/Lu_N	20.41	22.65	28.25	18.43
Ce/La_N	0.80	0.75	0.63	0.73
Ce/Ce*	1.02	0.98	0.93	0.92

The REE content in the barite showed two distinct patterns (Fig. 9A). The first pattern (Brt2 and Brt3) is similar in LREE and HREE. The second pattern (Brt1) is depleted in LREE (Ce, Pr and Nd) and HREE (Dy and Er) compared to the first group. The analyzes with Ce/La= ~1.7 (not normalized calculi) are similar to those formed in continental barite (Guichard et al., 1979; Barrett et al., 1990; Martin et al., 1995), higher than negative Ce anomalies in the barites of the seawater (Ce/La= ~0.5) (Goldberg, 1969; Guichard et al., 1979). The calcite REE contents showed patterns similar to whole–rocks analyzes. The depleted REE contents in calcite are associated with samples located in the mineralized areas. The wide variation of La/Lu_N ratios in calcite indicates a progressive enrichment of LREE (Fig. 9B). The whole–rock REE patterns are similar to those in albitization and chloritization alteration (Lopes et al., 2014; Fontana et al., 2017) (Fig. 9C). The comparison between the REE patterns in the barite and albitized rocks evidenced enrichment in the barite (Fig. 9D), probably related to pyroxene chloritization, providing REE to hydrothermal fluid. These REE patterns are similar to those found by Michard et al. (1989), which showed barites of high–temperature acidic waters origin (pH < 6; T > 230 °C) from submarine hydrothermal vents on the East Pacific Rise.

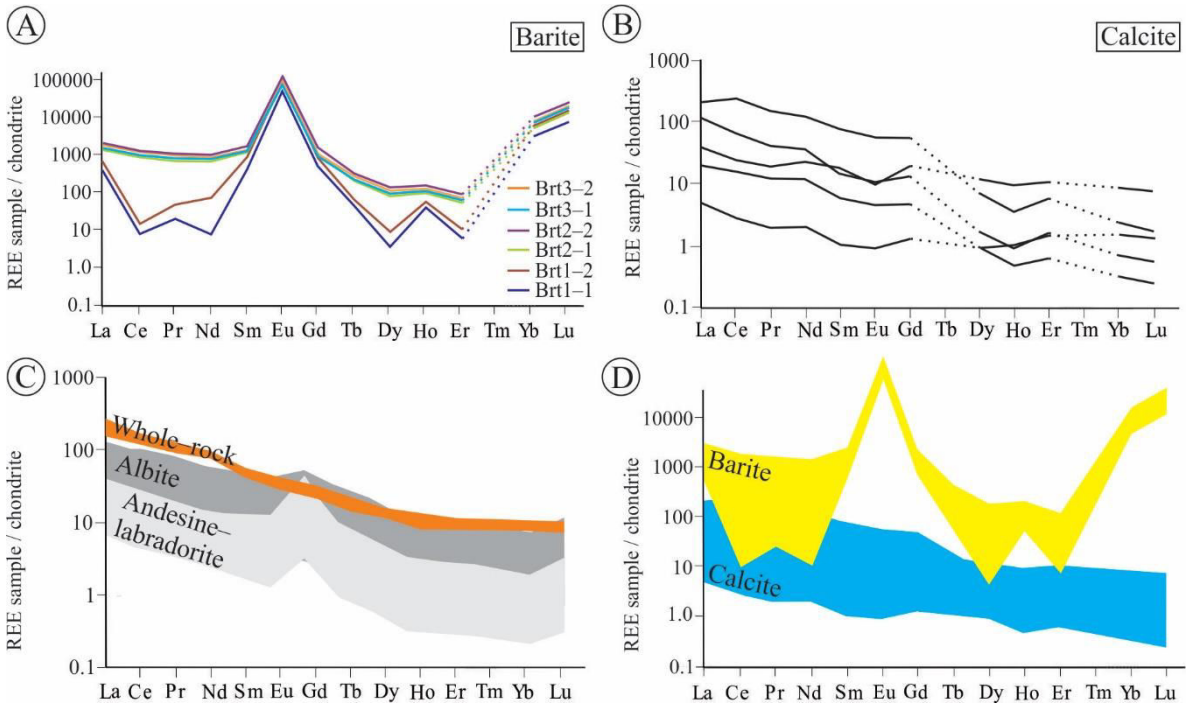

Figure 9. REE patterns normalized by the chondrite values (McDonough and Sun, 1995). (A) Two patterns of barite with REE enrichment; (B) Calcite (Cal–3) veins with variable patterns; (C) Andesine–labradorite, albite and whole–rock patterns (Lopes et al., 2014; Fontana et al., 2017); (D) Comparison of barite and calcite patterns evidencing REE enrichment in barite. Keys: And–lab= Andesine–labradorite.

5. DISCUSSION

5.1 EVOLUTION OF HYDROTHERMAL ALTERATION

The Andesitic volcano–sedimentary rocks from Seival area comprise andesine–labradorite and augite phenocrysts (Lopes et al., 2014; Fontana et al., 2017) indicating magma chamber crystallization. From magma ascent to lava flow emplacement, outgassing through melting has precipitated microlithic plagioclase and magmatic sulfide. The thermodynamic modeling and stable isotopes analysis (Fontana Ph.D.) of less to more altered lavas indicate late–magmatic and incursion of meteoric fluids associated with albitization process (650 to 250 °C; Hövelmann et al., 2010; Huang et al., 2009) followed by chloritization (310 to 120 °C; Lopes et al., 2014; Fontana et al., 2017).

The fractures and veins filled with barite, calcite (Cal–3) and quartz do not represent a paragenetic assemblage but a sequential precipitation, most probably

related to meteoric–fluid influx. The anhedral sulfide grains (chalcocite–bornite) or specular hematite in barite crystals suggest fluids with changes of HS^- and SO_4 proportion and oxygen fugacity. The precipitation of a large amount of barite is related to high–Ba–SO_4 activities and very negative Gibbs–free enthalpy of barite compared to calcite (Cal–3) and minor hematite (Hem–2) (Lawrence Livermore National Laboratory, thermodynamic database). However, the source of barium and sulfur can be associated with either volcanic rocks or seawater. The barium content in andesine–labradorite (0.12 atomic wt %) is higher than in albite (below detection limit), which indicates that albitization process leached barium. The main peak (3.43 Å) in barites shows strontium content in the barite structure, rather than a mixture of barite and celestine ($SrSO_4$). We compared these values to found by Abidi et al. (2012), while possible < 0.5 % of Sr in the barite structure.

We used the Ba–molar content in andesine–labradorite [0.061 molar %= 0.12 % $_{\text{Ba in andesine–labradorite}}$ x 137.3 g mol^{-1} $_{Ba}$ / 268.62 g mol^{-1} $_{\text{andesine}}$] to estimate the amount of feldspar required to produce a mole of barite [34.61 molar % = (58.84 g mol^{-1} $_{\text{Ba in barite}}$ x 137.3 g mol^{-1} $_{Ba}$)/233.39 g mol^{-1} $_{\text{Barite}}$]. The result is 564.35 moles (34.61 / 0.061) of feldspar for one mole of barite (233.39 g; density: 4.23, equivalent to 5.5 x10^{-5} m^3), which represents 151.7 kg of feldspar (564.35 moles x 268.62 g) in a volume of 0.058 m^3 (151.7 kg / density: 2.6). Consequently, the albitization of 1m^3 with formation of pure albite would produce 9.5 x10^{-4} m^3 of barite (5.5x10^{-5} /0.058 m^3).

We also used the same formula of Ba–molar content in seawater [0.006 to 0.023 molar %= 0.0008 to 0.0031 % $_{\text{Ba in seawater}}$ x 137.3 g mol^{-1} $_{Ba}$ / 18.01 g mol^{-1} $_{\text{seawater}}$] to estimate the amount of seawater required to produce a mole of barite (34.61 molar %). The result shows 5768.33 to 1500.78 moles of seawater (34.61/ 0.006 to 0.023) for one mole of barite (18.01 g; density: 1.035, equivalent to 1.7 x10^{-5} m^3), which represents 320.28 to 83.33 liters of seawater (5768.33 to 1500.78 moles / 18.01 g) in a volume of 0.309 m^3 (151.7 kg / density: 2.6). As a result, influx of 1 m^3 of seawater would produce 5.5 x10^{-3} m^3 of barite (1.7 x10^{-5} m^3 / 0.309 m^3).

5.2 SOURCE OF BARIUM, SULFUR AND RARE EARTH ELEMENTS IN BARITE

This chapter features a characterization of alteration mineral assemblages generated in different temperatures of hydrothermal fluids that occur in the Seival area. An order of crystallization was defined, as well as mineral associations of each thermal step of the alteration process, with the purpose of understanding the physical–chemical evolution of the hydrothermal system and Cu–enriched phases.

Volcanogenic rocks from the Seival area are characterized by a magmatic phase including pyroxene (augite) and plagioclase (andesine–labradorite) (Lopes et al., 2014; Fontana et al., 2017). Deposition of primary sulfide (pyrite and chalcopyrite) was considered as a late–magmatic hydrothermal alteration precipitated in temperatures around ~350°C (Fig. 10A). Moreover, Cal–II (Fontana et al., 2017), Hem–I and quartz are associated with relicts or pseudomorphic of pyroxene and plagioclase.

The albitization of plagioclase, chloritization of pyroxene and destabilization of primary sulfides occur associated with the same hydrothermal fluids (Lopes et al., 2014; Fontana et al., 2017) with temperatures of ~250 °C. The barium is not detected in albitized portions of andesine–labradorite (see part 4.3) and, therefore, part or portion of barium in barite crystallization is linked to the albitization of plagioclase (andesine–labradorite).

Crystallization of barite (1 mole) might be produced by the albitization of 483 moles of andesine–labradorite (0.12 weight % of Ba). The albitization of $1m^3$ of andesite lava flows (density of 2.6 g/cm^3) with 30 % of andesine–labradorite would allow precipitation of 360 cm^3 of barite, equivalent to 1.6 kg of barite (d= 4.48 g/cm^3). Hence, an estimated reserve of ~0.20 Mt of andesitic albitized rock can produce 123 ton of barite, representing 0.06 % in the altered rock. This low volume of barite generated through the albitization probably does not represent the whole barium source but indicates a certain amount which contributes to the formation of barite.

However, barite crystallization occurring after albite and chlorite (Hövelmann et al., 2010; Fontana et al., 2017) indicates a late and low–temperature precipitation. Moreover, the previous calculation is valid for the source of barium but do not present

the source of sulfate. The origin and evolution of fluids through fluid–rock interaction has been bracketed by oxygen isotopic analysis in plagioclases and sulfur isotopic analysis in chalcocite–bornite and barite (Fontana, 2017). These oxygen isotopes in plagioclase calculated with temperatures of 600 to 350 °C (Fontana, 2017) suggest an albitization dominantly related to a Na–rich magmatic–fluid (CO_2 and H_2O), whereas sulfur isotopes combined with chlorite thermometer indicate low–temperature alteration ca. ~250 °C (Hövelmann et al., 2010; Huang et al., 2009; Bongiolo et al., 2011; Renac et al., 2014).

The chloritization of pyroxene occurs associated with the presence of Cal–II (Fontana et al., 2017), titanite and quartz with temperatures between 280 to 130 °C (Lopes et al., 2014; Fontana et al., 2017). The chloritization of augite can furnish REE (Green, 1980) mainly to barite (Fig. 9A). In the Seival area, copper–sulfides crystallization were associated with chlorite and chlorite/smectite mixed–layers (~250 °C) (Kameda et al., 2011; Schleicher et al., 2012). The alteration with chlorite/smectite mixed–layers precipitation was related to destabilization of primary sulfides with increasing activity of Cu and S compared to Fe (Pyrite + Chalcopyrite → Bornite) and an increasing content of dissolved CO_2 in fluids for the precipitation of calcite associated with chalcocite. The association of barite and hematite attests oxidation of iron (II to III) and the change from H_2S and HS^- dominant fluid to a SO_4^{2-} rich fluid (Brimhall and Crerar, 1987; Vaugham and Craig, 1997; Dill, 2015; Vaughan and Corkhill, 2017). Similar to Church and Wolgemuth (1972) and Hanor (2000) works these changes are related to increase of oxygen activity and pH changes (Chiba and Sakai, 1985; Renac et al.. 2014) most probably associated with meteoric water and weathering (Fontana et al., 2017).

Barite is spatially associated with Cu–Ag mineralizations, but it did not crystallize at the same time (Fig. 10B). Barite and Cal–III crystallization was interpreted as a low–temperature mineral association (Hogarth et al., 1985). The relation of barite and mineralized fractures suggests barite crystallization temperatures < 157 °C (ca. chlorite temperature; Lopes et al., 2014; Fontana et al., 2017). In this case, barite precipitation may have been generated by hydrothermal

fluids at low temperatures (ca. < 100° C; Hanor, 2000). In other deposits in the Camaquã Basin, similar barite occurrences were observed with estimated temperatures in oxygen isotopes and fluid inclusions between 125 to 115 °C (e.g., Cerro dos Martins; Toniolo et al., 2004) and 180 to 80 °C (e.g., the Camaquã Mine; Bettencourt, 1976; Ronchi et al., 2000; Renac et al., 2014).

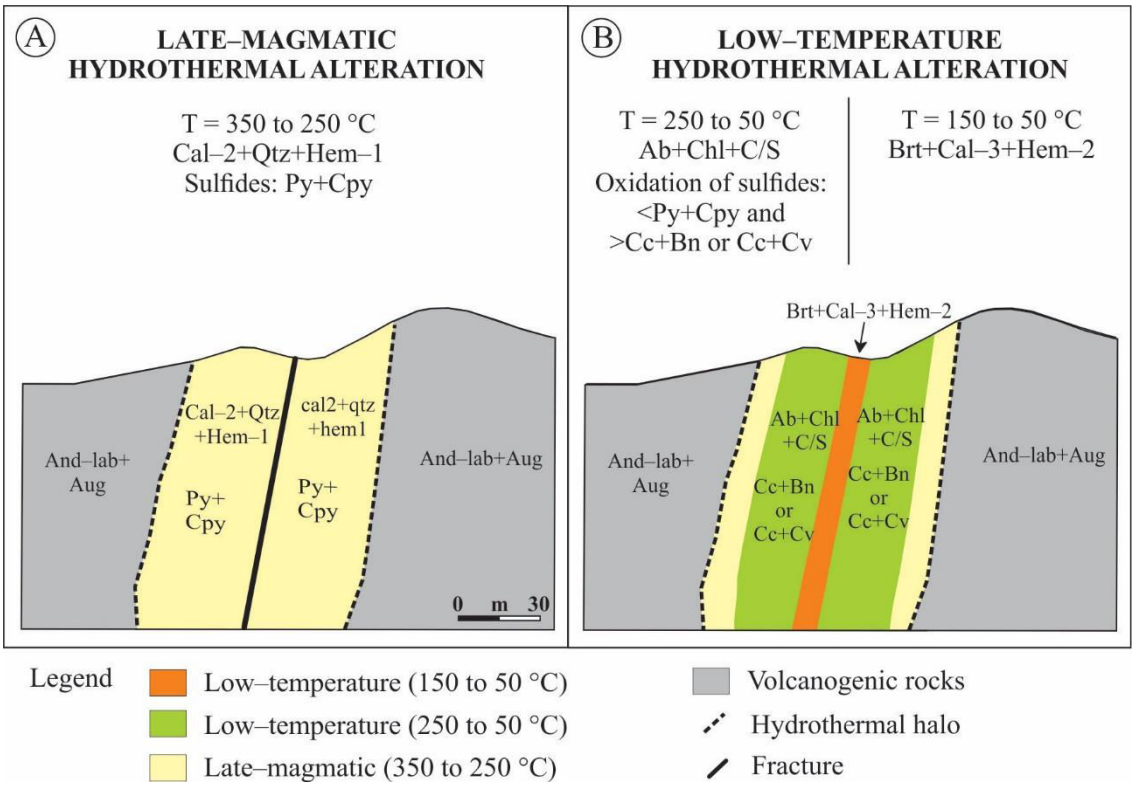

Figure 10: Evolution of hydrothermal alteration in the Seival area. (A) Late–magmatic alteration characterized by Cal–2+Qtz+Hem–1 and Py+Cpy (350 to 250 °C); (B) Low–temperature hydrothermal alteration characterized by association of Ab+Chl+C/S and Cc+Bn ou Cc+Cv (250 to 50 °C) and association of Brt+Cal–3+Hem–2 (150 to 50 °C). Keys: And–lab= Andesine–labradorite; Aug= Augite; Cal= Calcite; Qtz= Quartz; Hem= Hematite; Py= Pyrite; Cpy= Chalcopyrite; Ab= Albite; Chl= Chlorite; C/S= Chlorite/smectite mixed–layers; Cc= Chalcocite; Bn= Bornite; Cv= Covellite; Brt= Barite.

Therefore, the fluid related to albitization, chloritization and destabilization of sulfides was probably a mixing of magmatic and meteoric fluid. However, the fluid responsible for the formation of barite, Cal–III and Hem–II was dominantly meteoric. The albitization of plagioclase provided barium to the hydrothermal fluid due to the availability of S favored by destabilization of primary sulfides, forming barite and

Hem–II in the last stages of hydrothermal alteration and with REE enrichment in barite. We related these change to the low–temperature stage represented by barite, Cal–III (Fontana et al., 2017) and Hem–II, indicating high oxygen fugacity.

Seival mineralizations (Cu–Ag) occur mainly in subvertical fractures. These fractures are also filled by barite with ~N–S orientation (Lopes et al., 2018). Therefore, the deeper structures allowed reactivation and reinjection of hydrothermal fluid and consequent precipitation of barite in the last veins of Seival area.

5.3 REE PATTERNS

The studies on barite for REE geochemistry have been applied for the understanding of barite origin, hydrothermal process and source of fluids (e.g., Guichard et al., 1979; Barrett et al., 1990; Martin et al., 1995). These barites with different patterns suggest variation of the REE contents associated with hydrothermal alteration. Moreover, in Brt1 samples the negative anomalies of Ce can be associated with marine barite (Hogdahl et al., 1968; Guichard et al., 1979) or hydrothermal activities in seawater (Ehya, 2012). These Ce negative anomalies suggest neutral pH rather than more basic like in seawater. The samples Brt1 and Brt2 have no Ce anomalies and confirm meteoric water. Barite analyzes have a large positive Eu anomaly (Fig. 9A). The hydrothermal fluid keeps Eu anomalies positive once Eu is stable under reduced and high–temperature conditions (Sveijensky, 1984; Barrett et al., 1990), as in the continental barite (Guichard et al., 1979). Morgan and Wandless (1980) indicate Eu with similar size of barium or strontium accommodates in the barite structure.

In a previous study of the Seival area, the REE chemistry characterization in the andesine–labradorite and the albite–rich separates showed two groups with different REE contents (Lopes et al., 2014; Fontana et al., 2017). The Group I was characterized by andesine–labradorite partially replaced by albite (weak albitization; Fig. 9C)) and the Group II includes plagioclases totally replaced by albite (Fig. 9C). Moreover, the REE patterns of andesine–labradorite ($\Sigma REE_{andesine–labradorite}$= ~20 ppm) and albite ($\Sigma REE_{albite}$= ~40 ppm) have similar aspects in comparison to the

REE–enriched barite (ΣREE_{barite}= ~1631.01) (Fig. 9D). Therefore, the barite high REE values do not derive from albitization. The plagioclase maintains REE values even with the albitization process. The probable source of REE in barites is the chloritization of pyroxene (Green, 1980) or external fluid, and the source of barium is the albitization of primary plagioclase (andesite–labradorite).

6. CONCLUSIONS

The low–temperature hydrothermal alteration was characterized by barite, calcite and minor hematite located in the same geological context of Cu–Ag mineralizations hosted in volcanogenic rocks from Seival Mine. Barite occurs with NE–SE and NNE–SSW directions in faults and fractures. The EMPA analysis in altered (albite) and not altered (andesine–labradorite) portions of plagioclase showed albite without barium content. The change of H_2S^- dominant fluid to SO_4^{2-}–rich fluid probably occurs with influence of meteoric and oxidant fluid and represents sulfur source promoted by destabilization of primary sulfides (pyrite and chalcopyrite), with formation of chalcocite–bornite or chalcocite–covellite and barite, calcite and hematite. Consequently, barite, calcite and minor hematite were formed in low temperature (< 157 °C) and in more oxidant conditions than albite, chlorite–smectite and Cu–rich sulfides.

The REE geochemistry in concentrates of barite, calcite and whole–rock shows very high values of ΣREE in barites, evidencing that REE released from chloritization of pyroxene may be concentrated in the barites related to the affinity of SO_4 group to accommodate REE in $BaSO_4$ structure. The two patterns of barite were related to LREE depleted, negative anomalies of Ce, Pr and Nd and strong depletion of HREE (Dy), indicating association with hydrothermal alteration. These REE patterns are compatible with low–temperature hydrothermal barites.

ACKNOWLEDGMENTS

This study is part of the co–tutela doctoral thesis of Rodrigo Winck Lopes at Universidade Federal do Rio Grande do Sul and Université Côte d´Azur. We wish to

thank the Conselho Nacional do Desenvolvimento e Pesquisa (CNPq), CAPES and the Programa Ciências Sem Fronteiras (Process number: 200081/2014–4) for financial support. We wish to thank Everton Marques Bongiolo for revision and correction of an early version of this manuscript. We wish to thank the technician laboratory Denise Canarim, Susan Drago, Lucas Gomes, Edgar Bercht and Lucas Jantsch.

REFERENCES

Abidi R., Slim–Shimi N., Marignac C., Hatira N., Gasquet D., Renac C., Soumarin A., Gleeson S. 2012. The origin of sulfate mineralization and the nature of the BaSO4–SrSO4 solid–solution series in the Ain Allega and El Aguiba ore deposits, Northern Tunisia. *Ore Geology Reviews*, 48:165–179.

Almeida F.F.M., Hasuy Y. 1984. *O Pré–Cambriano do Brasil*. São Paulo: Edgard Blücher, 378 p.

Barrett T.J., Jarvis I., Jarvis K.E. 1990. Rare earth element geochemistry of massive sulfides sulfates and gossans on the Southern Explorer Ridge. *Geology*, 18:583–586.

Barbieri M., Masi U., Tolomeo L. 1982. Strontium geochemistry in the epithermal barite deposits from the Apuan Alps (Northern Tuscany, Italy). *Chemical Geology*, 35:351–356.

Bettencourt J.S. 1976. Mineralogia, inclusões fluídas e isótopos estáveis de oxigênio e enxofre da Mina de Cobre de Camaquã RS. In: XXIX Congresso Brasileiro de Geologia, 1976. *Boletim de Resumos do XXIX Congresso Brasileiro de Geologia.* Belo Horizonte, MG, p. 340–341.

Bongiolo E.M., Renac C., Mexias A.S., Gomes M.E.B., Ronchi L.H., Patrier–Mase P. 2011. Evidence of Ediacaran glaciation in southernmost Brazil through magmatic to meteoric fluid circulation in the porphyry–epithermal Au–Cu deposits of Lavras do Sul. *Precambrian Research*, 189, 404–419.

Breit G.N., Simmons E.C., Goldhaber M.B. 1985. Dissolution of barite for the analysis of strontium isotopes and other chemical and isotopic variations using aqueous sodium carbonate. *Chemical Geology*, 52:333–336.

Brimhall G.H., Crerar D.A. 1987. Ore fluids: magmatic to supergene. In: P. H. Ribbe (ed.) Thermodynamic modeling of geological materials: minerals, fluids and melts. *Reviews in mineralogy*, 17:235–321.

Chang L.L.Y., Howie R.A., Zussman J. 1996. *Rock– Forming Minerals. Non–Silicates: Sulfates, Carbonates, Phosphates, Halides.* Geological Society, London, 383 p.

Chemale Jr. F. 2000. *Evolução Geológica do Escudo Sul–rio–grandense*. In: Holz, M., De Ros, L. F., Geologia do Rio Grande do Sul. Porto Alegre: Ed. Universidade/UFRGS, p. 13–52.

Chiba H., Sakai H. 1985. Oxygen isotope exchange between dissolved sulfate and water at hydrothermal temperatures. *Geochimica et Cosmochimica Acta*, 49:993–1000.

Church T.M., Wolgemuth K. 1972. Marine barite saturation. *Earth and Planetary Science Letters*, 15, 35–44.

Deer W.A., Howie R.A., Zussman J. 1992. An Introduction to the Rock Forming Minerals, 2nd ed., Longman. London, 696 p.

Dill H.G. 2015. Supergene Alteration of Ore Deposits: From Nature to Humans. *Elements*, 11:201–206.

Ehya F. 2012. Rare earth element and stable isotope (O, S) geochemistry of barite from the Bijgan deposit, Markazi Province, Iran. *Mineralogy Petrology*, 104:81–93.

Elderfield H. 1988. The oceanic chemistry of the rare earth elements. *Philosophical Transactions of the Royal Society of London*, A325:105–126.

Fontana E. 2017. *Hidrotermalismo e mineralizações das rochas vulcânicas da Mina do Seival: Evolução geoquímica e isotópica ($\delta^{34}S$, $\delta^{18}O$ e $\delta^{13}C$) dos fluidos e sua correlação com outros depósitos de minérios epitermais da Bacia do Camaquã – Rio Grande do Sul – Brasil.* PhD Thesis, Porto Alegre. UFRGS, 201 p.

Fontana E., Mexias A.S., Renac C., Nardi L.V.S., Lopes R.W., Gomes M.E.B., Barats A. 2017. Hydrothermal alteration of volcanic rocks in Seival Mine Cu–mineralization – Camaquã Basin – Brazil (Part I): Chloritization process and geochemical dispersion in alteration halos. *Journal of Geochemical Exploration*, 177:45–60.

Gastal M.C., Lafon J.M., Ferreira F.J.F., Magro F.U.S., Remus M.V.D., Sommer C.A. 2006. Reinterpretação do Complexo Intrusivo Lavras do Sul – RS, de acordo com os sistemas vulcano–plutônicos de subsidência. Parte I: Geologia, geofísica e geocronologia ($^{207}Pb/^{206}Pb$ e $^{206}Pb/^{238}U$). *Brazilian Journal of Geology*, 36:109–124.

Goldberg E.D., Somayajulu B.L.K., Galloway J., Kaplan I.R., Faure G. 1969. Differences between barites of marine and continental origins. *Geochimica Cosmochimica Acta*, 33:287–289.

Green D.H. 1980. Island arc and continent building magmatism – A review of petrogenic models based on experimental petrology and geochemistry. *Tectonophysics*, 63:367–385.

Guichard F., Church T.M., Treuil M., Jaffrezic H. 1979. Rare earths in barites: distribution and effects on aqueous partitioning. *Geochimica Cosmochimica Acta*, 43:983–997.

Hanor J.S. 2000. *Barite–celestine geochemistry and environments of formation*. In: Reviews in Mineralogy & Geochemistry – Sulfate Minerals (Eds C.N. Alpers, J.L. Jambor and D.K. Nordstrom), Mineralogical Society of America. Washington, p. 193–275.

Hartmann L.A., Chemale F., Philipp R.P. 2007. *Evolução Geotectônica do Rio Grande do Sul no Pré–Cambriano.* In: Iannuzzi, R., Frantz, J. C., Geologia do Rio Grande do Sul. Porto Alegre, p. 99–123.

Hogarth D.D., Hartree R., Loop J., Solberg T.N. 1985. Rare–earth element minerals in four carbonatites near Gatineau, Quebec. American Mineralogist, 70:1135–1142.

Hogdahl O.T., Melsom S., Bowen V.T. 1968. *Neutron activation analysis of lanthanide elements in sea water.* In Advances in Chemistry. Journal of the American Chemical Society, 73, Chap. 19, 308 p.

Hövelmann J., Putnis A., Geisler T., Schmidt B.C., Golla–Schindler U. 2010. The replacement of plagioclase feldspars by albite: observations from hydrothermal experiments. *Contributions to Mineralogy and Petrology*, 159, 43–59.

Huang F., Lundstrom C.C., Glessner, J., Ianno A., Boudreau A., Lia J., Ferré E.C., Marshak S., DeFrates J. 2009. Chemical and isotopic fractionation of wet andesite in a temperature gradient: Experiments and models suggesting a new mechanism of magma differentiation. *Geochimica et Cosmochimica Acta*, 73:729–749.

Jamieson J.W., Hanningtone M.D., Tivey M.K., Hansteen T., Williamson N.M., Stewart M., Fietzke J., Butterfield D., Frische M., Allen L., Cousens B., Langer J. 2016. Precipitation and growth of barite within hydrothermal vent deposits from the Endeavour Segment, Juan de Fuca Ridge. *Geochimica et Cosmochimica Acta*, 173:64–85

Janikian L., Almeida R.P., Trindade R.I.F., Fragoso–Cesar A.R.S., D´Agrella–Filho M.S., Dantas E.L., Tohver E. 2008. The continental record of Ediacaran volcano–sedimentary successions in southern Brazil and their global implications. *Terra Nova*, 20:259–266.

Janikian L., Almeida R.P., Fragoso–Cesar A.R.S., Martins V.T.S., Dantas E.L., Tohver E., McReath I., D'Agrella–Filho M.S. 2012. Ages (U–Pb SHRIMP and LA ICPMS) and stratigraphic evolution of the Neoproterozoic volcano–sedimentary successions from the extensional Camaquã Basin, Southern Brazil. *Gondwana Research*, 21:466–482.

Jarvis K.E., Gray A.L., McCurdy E. 1989. Avoidance of spectral interference on Europium in Inductively Coupled Plasma Mass Spectrometry by sensitive measurement of the doubly charged ion. *Journal of Analytical Atomic Spectrometry*, 4:743–747.

Jurkovic I., Garasic V., Hrvatovic H. 2010. Geochemical characteristics of barite occurrences in the Palaeozoic complex of south–eastern Bosnia and their relationship to the barite deposits of the mid–BosnianSchist Mountain. *Geologia Croatica*, 63:241–258.

Kameda, J., Ujiie, K., Yamaguchi, A., Kimura, G., 2011. Smectite to chlorite conversion by frictional heating along a subduction-zone thrust. *Earth and Planetary Science Letters*, 305:161–170.

Lima E.F., Nardi L.V.S. 1998. The Lavras do Sul Shoshonitic Association: implications for origin and evolution of neoproterozoic shoshonitic magmatism in southernmost Brazil. *Journal of South American Earth Sciences,* 11:67–77.

Lima E.F.L., Sommer C.A., Nardi L.V.S. 2007. *O vulcanismo Neoproterozóico–Ordoviciano no escudo sul–riograndense: os ciclos vulcânicos da Bacia do Camaquã*. In: Iannuzzi, R.; Frantz, J. C. (Eds). 50 anos de Geologia: Instituto de Geociências. Contribuições. Porto Alegre, p. 79–97.

Liz J.D., Lima E.F., Nardi L.V.S. 2009. Avaliação de fontes magmáticas de séries shoshoníticas pós–colisionais com base na normalização pela Associação Shoshonítica de Lavras do Sul – aplicação de Sliding Normalization. *Brazilian Journal of Geology*, 39:55–66.

Lopes R.W., Fontana E., Mexias A.S., Gomes M.E.B., Nardi L.V.S., Renac C. 2014. Caracterização petrográfica e geoquímica da sequência magmática da Mina do Seival, Formação Hilário (Bacia do Camaquã – Neoproterozoico), Rio Grande do Sul, Brasil. *Pesquisas em Geociências*, 41:51–64.

Lopes R.W., Mexias A.S., Philipp R.P., Bongiolo E.M., Renac C. , Bicca M.M., Fontana E. 2018. Au–Cu–Ag mineralization controlled by brittle structures in Lavras do Sul Mining District and Seival Mine deposits, Camaquã Basin, southern Brazil. *Journal of South American Earth Sciences*, 88C:197–215.

Martin E.E., Macdougall J.D., Herbert T.D., Paytan A., Kastner M. 1995. Strontium and neodymium isotopic analysis of marine barite separates. *Geochimica et Cosmochimica Acta*, 7:1353–1361.

McDonough W.F., Sun S.S. 1995. The composition of the earth. *Chemical Geology*, 120:223–253.

Mehnert K.R., Büsch W. 1981. The Ba content of K feldspar megacrysts in granites, a criterion for their formation. *Neues Jahrbuch Mineralogie Abhandlungen*, 140:21–252.

Michard G., Alberede F., Michard A., Minster J.F., Charlou J.L., Tan N. 1984. Chemistry of solutions from 13°N East Pacific Rise hydrothermal site. *Earth and Planetary Science Letters*, 67:297–307.

Michard A. 1989. Rare earth element systematics in hydrothermal fluids. *Geochimica et Cosmochimica Acta*, 53:745–750.

Morgan J.W., Wandless G.A. 1980. Rare earth element distribution in some hydrothermal minerals: evidence for crystallographic control. *Geochimica et Cosmochimica Acta*, 44:973–980.

Nardi L.V.S. 1984. *Geochemistry and petrology of the Lavras Granite Complex, RS, Brazil.* PhD Thesis, University of London, 268 p.

Paim P.S.G., Chemale F., Lopes R.C. 2000. *A Bacia do Camaquã*. In: Holz, M.; De Ros, L. F. (Ed.). Geologia do Rio Grande do Sul. Porto Alegre: Ed. Universidade/UFRGS, p. 231–374.

Piper D.Z., 1974. Rare–Earth Elements in the Sedi Cycle: A Summary. *Chemical Geology*, 14:285–304.

Philipp R.P., Pimentel M.M., Chemale Jr. F. 2016. Tectonic evolution of the Dom Feliciano Belt in Southern Brazil: Geological relationships and U–Pb geochronology. *Brazilian Journal of Geology*, 46:83–104.

Reischl J.L. 1978. *Mineralizações cupriferas associadas a vulcânicas na Mina do Seival*. In: XXX CONGRESSO BRASILEIRO DE GEOLOGIA. Recife, p. 1568–1582.

Remus M.V.D., McNaughton N.J., Hartmann L.A., Koppe J.C., Fletcher I.R., Groves D.I., Pinto V.M. 1999. Gold in the Neoproterozoic juvenile Bossoroca volcanic arc of southernmost Brazil, isotopic constraintson timing and sources. *Journal of South American Earth Sciences*, 12:349–366.

Remus M.V.D., Hartmann L.A., McNaughton N.J., Groves D.I., Reischl J.L. 2000. Distal Magmatic–Hydrothermal Origin for the Camaquã Cu (Au–Ag) and Santa Maria Pb, Zn (Cu–Ag) Deposits, Southern Brazil. *Gondwana Research*, 3:155–174.

Renac C., Mexias A.S., Gomes M.E.B., Ronchi L.H., Nardi L.V.S., Laux J.H. 2014. Isotopic fluid changes in a Neoproterozoic porphyry epithermal system: the Uruguay mine, southern Brazil. *Ore Geology Reviews*, 60:146–160.

Ronchi L.H., Lindenmayer Z.G., Bastos Neto A., Murta C.R. 2000. *O stockwork e a zona do minério sulfetado no arenito inferior da Mina Uruguai, RS*. In: Ronchi L.H., Lobato, A.O.C. (Orgs) Minas do Camaquã, um estudo multidisciplinar. UNISINOS/FAPERGS (Universidade do Vale do Rio dos Sinos/Fundação de Amparo à Pesquisa do Estado do Rio Grande do Sul). São Leopoldo, p. 165–190.

Saalmann K., Hartmann L.A., Remus M.V.D., Koester E., Conceição R.V. 2005. Sm–Nd isotope geochemistry of metamorphic volcano–sedimentary successions in the São Gabriel Block, southernmost Brazil: evidence for the existence of juvenile Neoproterozoic oceanic crust to the east of the Rio de la Plata craton. *Gondwana Research*, 8:143–161.

Schleicher A.M., van der Pluijm B.A., Warr L.N. 2012. Chlorite–smectite clay minerals and fault behavior: New evidence from the San Andreas Fault Observatory at Depth (SAFOD) core. *Lithosphere*, 4, 209–220.

Shabani M.B., Akagi T., Masuda A. 1992. Preconcentration of trace Rare Earth Elements in sea water by complexation with bis (2–ethylhexyl) hydrogen phosphate and 2–ethylhexyl dihydrogen phosphate adsorbed on a C18 cartridge and determination by inductively coupled plasma mass spectrometry. *Analytical Chemistry*, 64:737–743.

Sorrell C.A. 1962. Solid state formation of barium, strontium and lead feldspars in clay–sulfate mixtures. *The American Mineralogist*, 47:291–309.

Sverjensky, D.A. 1984. Europium redox equilibria in aqueous solution. *Earth and Planetary Science Letters*, 67:70–78.

Toniolo J.A., Remus M.V.D., Macambira M.J.B., Moura C.A.V. 2004. Metalogênese do Depósito de Cobre Cerro dos Martins, RS, Revisão e Geoquímica Isotópica de Sr, S, O e C. *Pesquisas em Geociências*, 31:41–67.

Toniolo J.A., Gil C.A.A., Sander A. 2007. Projeto BANEO–Metalogenia das Bacias Neoproterozóico–Eopaleozóicas do Sul do Brasil – Bacia do Camaquã. CPRM – Serviço Geológico do Brasil, CD Rom.

Vaughan D.J., Craig J.R. 1997. *Sulfide ore mineral stabilities, morphlogies, and intergrowth textures*. In: H. L. Barnes (ed.) Geochemistry of hydrothermal ore deposits, third edition. New York, John Willey & Sons, Inc., 367–434.

Vaughan D.J., Corkhill C.L. 2017. Mineralogy of sulfides. *Elements*, 13:81–87.

Wildner W., Lima E.F., Nardi L.V.S., Sommer C.A. 2002. Volcanic cycles and setting in the Neoproterozoic III to Ordovician Camaquã Basin succession in southern Brazil: characteristics of post–collisional magmatism. *Journal of Volcanology and Geothermal Research,* 118:261–283.

Wolgemuth K., Broecker W.S. 1970. Barium in sea water. *Earth and Planetary Science Letters*, 8:372–378.

Worrall F., Pearson, D.G. 2001. Water–rock interaction in an acidic mine discharge as indicated by rare earth element patterns. *Geochimica Cosmochimica Acta*, 65, 3027–3040.

Zarasvandi A., Zaheri N., Pourkaseb H., Chrachi A., Bagheri H. 2014. Geochemistry and fluid–inclusion microthermometry of the Farsesh barite deposit, Iran. *Geologos*, 20:201–214.

5. SÍNTESE INTEGRADORA

A tese foi desenvolvida na forma de manuscritos científicos submetidos a periódicos, conforme exigência do Programa de Pós-Graduação em Geociências da Universidade Federal do Rio Grande do Sul, estando um deles já publicado.

As medidas de geologia estrutural na Mina do Seival e no Distrito Mineiro de Lavras do Sul são apresentadas no **manuscrito I** (parte 4.1). Em ambas as áreas ocorre um intenso fraturamento e falhas em regime rúptil. As mineralizações são associadas com falhas transcorrentes e fraturas extensionais de direções NE-SE e NW-SE. A determinação dos principais campos de tensões possibilitou a interpretação do controle estrutural das mineralizações e dos diques. Os principais estresses obtidos foram: compressão NW-SE; compressão NE-SW; distenção ENE-WSW. A reconstrução do paleostresse indicou o controle da circulação de fluidos e, consequentemente, da deposição de minério. A compressão NW-SE foi considerada anterior em relação à compressão NE-SW. Este paleostresse de direção NW-SE também foi associado ao controle das estruturas mineralizadas. A fragilidade das rochas vulcanogênicas da Mina do Seival evidencia outros paleostresses como a compressão NE-SW e a distensão ENE-WSW, sendo esta última relacionada aos movimentos tectônicos finais na área. As mineralizações possuem direção NW-SE para o Distrito Mineiro de Lavras do Sul, enquanto que as mineralizações na Mina do Seival possuem direção NE-SW. A mesma orientação é encontrada nos diques de monzonito, andesito e traquiandesito para ambas as áreas. As falhas e fraturas com direções NW-SE são associadas à falha de Palma-Jacques e à Zona de Cisalhamento de Ibaré. As falhas e fraturas com direção NE-SW são associadas à falha principal Cabritos-Perau e à Zona de Cisalhamento de Caçapava do Sul. Com isso, foi possível relacionar a compressão NW-SE com a evolução tectônica durante o estágio de transtensão (600-580 Ma) associados com as zonas de cisalhamento e a aglutinação dos blocos no Escudo Sul-rio-grandense, e consequentemente a circulação de fluidos e mineralizações.

A química mineral de estágios magmáticos e hidrotermais tardi-magmáticos na área da Mina do Seival é apresentada no **manuscrito II** (parte 4.2). Este estudo

caracterizou a assinatura química de minerais magmáticos preservados, os efeitos da albitização e os produtos de alteração hidrotermal como clorita, esmectita e interestratificados relacionados à precipitação de sulfetos de cobre. A mineralogia sugere magmas ricos em voláteis cristalizando biotita e minerais de alteração tardi-magmática como a titanita e processo de albitização do plagioclásio magmático em temperaturas entre 650 a 250°C. A albitização (<350°C) foi associada com precipitação de pirita e calcopirita. Esta alteração de alta temperatura está relacionada com fluidos magmáticos tardios, como indicado pela geoquímica de Elementos Terras Raras de plagioclásios primários e secundários. A cloritização (312 a 120°C) e formação de clorita, interestratificados de clorita/esmectita e esmectita foram associadas com a formação de bornita-calcocita e barita. A química de minerais de alteração hidrotermal, como esmectita, interestratificado clorita/esmectita, Fe-clinocloro e Mg-chamosita refletem a metaestabilidade dos minerais magmáticos com entrada de água meteórica e diminuição de temperatura.

Por fim, os dados de composição e de Elementos Terras Raras em baritas são apresentados no **manuscrito III** (parte 4.3). A composição química de barita e plagioclásios foram utilizados para uma melhor compreensão do processo hidrotermal de baixa temperatura na área. Os concentrados de barita mostraram enriquecimento em Elementos Terras Raras em comparação às análises de calcita e rocha total. As baritas possuem a fonte de bário provavelmente magmática provenientes da albitização do plagioclásio. A análise de rocha total evidenciou que a albitização do plagioclásio está relacionada com a elevação dos teores de Elementos Terras Raras em baritas e indicou um fluido oxidante meteórico rico em SO_4^{-2} como fonte de sulfato, uma vez que a fonte de calor e fluidos quentes pode estar relacionada com intrusões andesíticas. Dessa maneira, foi possível interpretar a alteração hidrotermal que precipitou barita, calcita e hematita como sendo de baixa temperatura (<157°C).

Portanto, as estruturas de direção NW-SE e NE-SW controlam o fluxo hidrotermal, os diques e as mineralizações. A associação petrográfica de albita e clorita com pirita e calcopirita sugerem um guia prospectivo para as mineralizações

de cobre, e os interestratificados de clorita/esmectita podem ser relacionados com o processo de enriquecimento em cobre. A cristalização de barita, calcita e hematita sugerem uma condição mais oxidante e de mais baixa temperatura (<150°C) do que albita, clorita-esmectita e sulfetos ricos em cobre.

6. REFERÊNCIAS BIBLIOGRÁFICAS

Almeida, F.F.M., Hasuy, Y., 1984. O Pré-Cambriano do Brasil. São Paulo: Edgard Blücher, 378 p.

Almeida, D.P.M., Zerfass, H., Basei, M.A., Petry, K., Gomes, C.H., 2002. The Acampamento Velho Formation, a Lower Cambrian bimodal volcanic package: geochemical and stratigraphics studies from the Cerro do Bugio, Perau and Serra de Santa Bárbara (Caçapava do Sul, Rio Grande do Sul, RS-Brazil). Gondwana Research, 5, 721-733.

Almeida, D.P.M., Chemale Jr., F., Machado, A., 2012. Late to Post–Orogenic Brasiliano–Pan–African Volcano–Sedimentary Basins in the Dom Feliciano Belt, Southernmost Brazil, in: Al–Juboury, A.I. (Ed.), Petrology – New Perspectives and Applications, pp. 73-135.

Angelier, J., 1994. Fault slip analysis and paleostress reconstruction. in: P.L. Hancock (ed.) Continental Deformation, Pergamon, Oxford, pp. 101-120.

Barbosa, A.F., Constantino, W., 1961. A Mineralização de Cobre de Volta Grande e Sua Relação com o granito de Lavras, Estado do Rio Grande do Sul, Boletim da Sociedade Brasileira de Geologia, São Paulo, 10p.

Basei, M.A.S., Drukas, C.O., Nutman, A.P., Wemmer, K., Dunyi, L., Santos, P.R., Passarelli, C.R., Campos Neto, M.C., Siga Jr., O., Osako, L., 2011. The Itajaí foreland basin: a tectono–sedimentary record of the Ediacaran period, Southern Brazil. International Journal of Earth Sciences, 100, 543-569.

Beaufort, D., Meunier, A., 1994. Saponite, corrensite and chlorite/saponite mixed–layered minerals and saponite in the Sancerre–Couy deep drill hole (France).Clay Minerals, 29, 47-61.

Bicca, M.M., Chemale Jr., F., Jelinek, A.R., Oliveira, C.H.E., Guadagnin, F., Armstrong, R., 2013. Tectonic evolution and provenance of the Santa Bárbara Group, Camaquã Mines region, Rio Grande do Sul, Brazil. Journal of South American Earth Sciences, 48, 173-192.

Bongiolo, E.M., 2002. Mineralização de Ouro da Região de Lavras do Sul/RS e Alteração Hidrotermal Associada. Porto Alegre. Dissertação de Mestrado, Programa de Pós-graduação em Geociências, Universidade Federal do Rio Grande do Sul.

Bongiolo, E.M., Renac, C., Mexias, A.S., Gomes, M.E.B., Ronchid, L.H., Patrier-Mase, P., 2011. Evidence of Ediacaran glaciation in southernmost Brazil through magmatic to meteoric fluid circulation in the porphyry–epithermal Au–Cu deposits of Lavras do Sul. Precambrian Research, 189, 404-419.

Borba, A.W., Mizusaki, A.M.P., Silva, D.R.A., Koester, E., Noronha, F.L., Casagrande, J., 2006, Provenance of the Neoproterozoic Maricá Formation

(Sul–riograndense Shield, Southern Brazil): Petrographic and Sm–Nd isotopic constraints. Gondwana Research, 9, 464-474.

Borba, A.W., Mizusaki, A.M.P., Santos, J.O.S., McNaughton, N.J., Ono, A.T., Hartmann, L.A., 2008. U–Pb zircon and $^{40}Ar/^{39}Ar$ K–feldspar dating of syn–sedimentary volcanism of the Neoproterozoic Maricá Formation: constraining the age of foreland basin inception and inversion in the Camaquã Basin of southern Brazil. Basin Research, 20, 359-375.

Chemale Jr., F., 2000. Evolução Geológica do Escudo Sul-rio-grandense. In: Holz, M., De Ros, L. F., Geologia do Rio Grande do Sul. Porto Alegre: Ed. Universidade/UFRGS, pp. 13-52.

Cordani, U.G., Halpern, M., Berenhoc, M., 1974. Comentários sobre as determinações geocronológicas da Folha de Porto Alegre. Carta Geológica do Brasil ao Milionésimo-Folha Porto Alegre (SH-22) e Lagoa Mirim (SI-22), pp. 70-80.

Davis, G.H., Reynolds, S.J., 1996. Structural Geology of Rock and Regions. John Wiley and Sons Inc., New York, 287 p.

Delvaux, D., Sperner, B., 2003. New aspects of tectonic stress inversion with reference to the TENSOR program. In: Nieuwland D. (ed.) New insights into structural interpretation and modelling. London, Geological Society of London, Special Publication, 212, pp. 75-100.

Font, E., Ponte Neto, C.F., Ernesto, M., 2011. Paleomagnetism and rock magnetism of the Neoproterozoic Itajaí Basin of the Rio de la Plata craton (Brazil): Cambrian to Cretaceous widespread remagnetizations of South America. Gondwana Research, 20, 782-797.

Fontana, E., 2017. Hidrotermalismo e mineralizações das rochas vulcânicas da Mina do Seival: Evolução geoquímica e isotópica ($\delta^{34}S$, $\delta^{18}O$ e $\delta^{13}C$) dos fluidos e sua correlação com outros depósitos de minérios epitermais da Bacia do Camaquã - Rio Grande do Sul - Brasil. Porto Alegre, Tese de doutorado, Geoquímica. Instituto de Geociências, Universidade Federal do Rio Grande do Sul.

Fontana, E., Mexias, A.S., Renac, C., Nardi, L.V.S., Lopes, R.W., Gomes, M.E.B., Barats, A., 2017. Hydrothermal alteration of volcanic rocks in Seival Mine Cu–mineralization – Camaquã Basin – Brazil (Part I): Chloritization process and geochemical dispersion in alteration halos. Journal of Geochemical Exploration, 177, 45-60.

Gastal, M.C.P., Lafon, J.M., 2001. Novas Idades $^{207}Pb/^{206}Pb$ e Geoquímica Isotópica Nd–Sr para Granitóides Shoshoníticos e Alcalinos das Regiões de Lavras do Sul e Taquerembó, RS. In: SBGq, Congresso Brasileiro de Geoquímica, 1° Simpósio de Geoquímica dos Países do Mercosul, 8, Anais, CD-ROOM.

Gastal, M.C., Lafon, J.M., Ferreira, F.J.F., Magro, F.U.S., Remus, M.V.D., Sommer C.A., 2006. Reinterpretação do Complexo Intrusivo Lavras do Sul - RS, de

acordo com os sistemas vulcano-plutônicos de subsidência. Parte I: Geologia, geofísica e geocronologia ($^{207}Pb/^{206}Pb$ e $^{206}Pb/^{238}U$). Brazilian Journal of Geology, 36, 109-124.

Gastal, M.C., Ferreira. F.J.F., Cunha, J.U., Esmeris, C., Koester, E., Raposo, M.I.B., Rossetti, M.M.M., 2015. Lavras granite emplacement and gold mineralization during the development of the post-collisional volcanoplutonic center, west of the Sul-riograndense Shield: Geophysical and structural data. Brazilian Journal of Geology, 45, 217-241.

Gõni, J.C., 1961. O Rapakivi Lavras: jazidas metaliferas associadas, Lavras do Sul, Rio Grande do Sul, Brasil. Estudos preliminares. Gráfica UFRGS, 75 p.

Guadagnin, F., Chemale Jr., F., Dussin, I.A., Jelinek, A.R., Santos, M.N., Borba, M., Justino, D., Bertotti, A.L., Alessandretti, L., 2010. Depositional age and provenance of the Itajaí Basin, Santa Catarina State, Brazil: Implications for SW Gondwana correlation. Precambrian Research, 180, 156-182.

Hartmann, L.A., Chemale Jr., F., Philipp, R.P., 2007. Evolução Geotectônica do Rio Grande do Sul no Pré-Cambriano. In: Iannuzzi, R.; Frantz, J. C. (Eds). 50 anos de Geologia: Instituto de Geociências. Contribuições. Porto Alegre: Comunicação e Identidade, pp. 99-123.

Hatcher, R.D., 1995. Structural geology (2nd edition): Englewood Cliffs, New Jersey, Prentice–Hall, 525 p.

Janousek, V., Farrow, C.M., Erban, V., 2003. GCDKit: New PC software for interpretation of whole–rock geochemical data from igneous rocks, Geochimical Cosmochimica Acta, 67, A186.

Janikian, L., Almeida, R.P., Fragoso-Cesar, A.R.S., Corrêa, C.R.A., Pelosi, A.P.M.R., 2003. Redefinição do Grupo Bom Jardim (Neoproterozóico III) em sua áreatipo: litoestratigrafia, evolução paleoambiental e contexto tectônico. Brazilian Journal of Geology, 33, 349-362.

Janikian, L., Almeida, R.P., Trindade, R.I.F., Fragoso-Cesar, A.R.S., D´Agrella-Filho, M.S., Dantas, E.L., Tohver, E., 2008. The continental record of Ediacaran volcano–sedimentary successions in southern Brazil and their global implications. Terra Nova, 20, 259-266.

Janikian, L., Almeida, R.P., Fragoso-Cesar, A.R.S., Martins, V.T.S., Dantas, E.L., Tohver, E., McReath, I., D'Agrella-Filho, M.S., 2012. Ages (U–Pb SHRIMP and LA ICPMS) and stratigraphic evolution of the Neoproterozoic volcano–sedimentary successions from the extensional Camaquã Basin, Southern Brazil. Gondwana Research, 21, 466-482

Kaul, P.F.T., Zir Filho, J.A., 1974. Mineralizações Auríferas de Lavras do Sul: tipos, controle tectônico, aspectos genéticos e guias para a localização de novos corpos mineralizados. In.: CONGRESSO BRASILEIRO DE GEOLOGIA, 27, Porto Alegre, SBG.

Laux, J.H., Lindenmayer, Z.G., Teixeira, J.B.G., Neto, A.B., 2005. Ore genesis at the Camaquã copper mine, a neoproterozoic sediment–hosted deposit in Southern Brazil. Ore Geology Review, 26, 71-89.

Leite, J.A.D., 1995. Datação SHRIMP U/Pb em zircões e o exemplo de dois corpos graníticos contrastantes no Escudo Sul-Riograndense. In: SBG, IV Simpósio Sul-Brasileiro de Geologia/I Encontro de Geologia do Cone Sul, Porto Alegre, Boletim de Resumos, pp. 5-12.

Lima, E.F., 1995. Petrologia das Rochas Vulcânicas e Hipabissais da Associação Shoshonítica de Lavras do Sul - ASLS, RS. Porto Alegre, Tese de Doutorado. Instituto de Geociências, Universidade Federal do Rio Grande do Sul.

Lima, E.F., Nardi, L.V.S., 1998. The Lavras do Sul shoshonitic association: implications for origin and evolution of eoproterozoic shoshonitic magmatism in southermost Brazil. Journal of South American Earth Science, 11, 67-77.

Lima, E.F.L., Sommer, C.A., Nardi, L.V.S., 2007. O vulcanismo Neoproterozóico-Ordoviciano no escudo sul-riograndense: os ciclos vulcânicos da Bacia do Camaquâ. In: Iannuzzi, R.; Frantz, J. C. (Eds). 50 anos de Geologia: Instituto de Geociências. Contribuições. Porto Alegre: Comunicação e Identidade, pp. 79-97.

Liz, J.D., Lima, E.F., Nardi, L.V.S., 2009a. Avaliação de fontes magmáticas de séries shoshoníticas pós-colisionais com base na normalização pela Associação Shoshonítica de Lavras do Sul - aplicação de Sliding Normalization. Brazilian Journal of Geology, 39, 55-66.

Liz, J.D., Lima E.F., Nardi L.V.S., Sommer C.A., Saldanha D.L., Pierosan R., 2009b. Petrologia e sucessão estratigráfica das rochas monzoníticas da associação shoshonítica de Lavras do Sul (RS). Brazilian Journal of Geology, 39, 244-255.

Lopes, R.W., 2011. Alteração hidrotermal e mineralização de cobre na Mina do Seival, Bacia do Camaquã, RS. Porto Alegre, Monografia de Conclusão de Curso, Curso de Geologia. Instituto de Geociências, Universidade Federal do Rio Grande do Sul.

Lopes, R.W., 2013. Caracterização petrográfica e geoquímica da Mina do Seival, Bacia do Camaquã, RS. Porto Alegre, Dissertação de Mestrado, Geoquímica. Instituto de Geociências, Universidade Federal do Rio Grande do Sul.

Lopes, R.W., Fontana, E., Mexias, A.S., Gomes, M.E.B., Nardi, L.V.S., Renac, C., 2014. Caracterização petrográfica e geoquímica da sequência magmática da Mina do Seival, Formação Hilário (Bacia do Camaquã - Neoproterozoico), Rio Grande do Sul, Brasil. Pesquisas em Geociências, 41, 51-64.

Matté, V., Sommer, C.A., Lima, E.F., Philipp, R.P., Basei, M.A.S., 2016. Post–collisional Ediacaran volcanism in oriental Ramada Plateau, southern Brazil. Journal of South American Earth Sciences, 71, 201-22.

Meert, J.G., Eide, E.A., Torsvik, T.H., 1997. The Nama Group, Namibia revisited. Geophysical Journal International, 129, 637-650.

Mexias, A.S., Formoso, M.L., Meunier, A., Beaufort, D., 1990a. O Sistema Hidrotermal Fóssil de Volta Grande - Lavras do Sul/RS. Parte I - Petrografia do Hidrotermalismo. Geochimica Brasiliensis, 4, 139-157.

Mexias, A.S., Formoso, M.L., Gomes, M.E.B., Meunier, A., Beaufort, D., Mattos, I., 1990b. O Sistema Hidrotermal Fóssil de Volta Grande - Lavras do Sul/RS. Parte II - Geoquímica das Cloritas. Geochimica Brasiliensis, 4, 159-174.

Mexias, A.S., Formoso, M.L.L., Meunier, A., Beaufort, D., 1990c. Composition and crystallization of corrensite in volcanic and pyroclastic rocks of Hilário Formation (RS). Brazilian Science Geology, 88, 135-143.

Mexias, A.S., Berger, G., Gomes, M.E.B., Formoso, M.L.L., Dani, N., Frantz, J.C., Bongiolo, E.M., 2005. Geochemical modelling of gold precipitation conditions in Bloco do Butiá Mine, Lavras do Sul/Brazil. Anais da Academia Brasileira de Ciências, 77, 1-12.

Mexias, A.S., Bongiolo, E.M., Gomes, M.E.B., Formoso, M.L.L., Frantz, J.C., 2007. Alterações hidrotermais e mineralizações nas rochas da Associação Plutono–Vulcano–Sedimentar da região de Lavras do Sul–RS. In: Iannuzzi, R.; Frantz, J. C. (Eds). 50 anos de Geologia: Instituto de Geociências. Contribuições. Porto Alegre: Comunicação e Identidade, pp. 143-159.

Müller, I.F., Nardi, L.V.S., Lima, E.F., Mexias, A.S., 2012. Os diques latíticos portadores de ouro e sulfetos da Associação Shoshonítica de Lavras do Sul - RS: Petrogênese e Geoquímica. Pesquisas em Geociências, 39, 173-191.

Nardi, L.V.S., 1984. Geochemistry and petrology of the Lavras Granite Complex, RS, Brazil. Londres, PhD Thesis, London University.

Nardi, V.S.N., Lima, E.F., 1985. A Associação Shoshonítica de Lavras do Sul, RS. Brazilian Journal of Geology, 15, 139-146.

Nardi, L.V.S., Bitencourt, M.F., 1989. Geologia, petrologia e geoquímica do Complexo Granítico de Caçapava do Sul. Brazilian Journal of Geology, 19, 153-169.

Oliveira, C.H.E., Chemale Jr., F., Jelinek, A.R., Bicca, M.M., Philipp, R.P., 2014. U–Pb and Lu–Hf isotopes applied to the evolution of the late to post–orogenic transtensional basins of the Dom Feliciano belt, Brazil. Precambrian Research, 246, 240-255.

Paim, P.S.G., Chemale Jr., F., Lopes, R.C., 2000. A Bacia do Camaquã. In: Holz, M., De Ros, L. F., Geologia do Rio Grande do Sul. Porto Alegre: Ed. Universidade/UFRGS, pp. 231-374.

Raposo, M.I.B., Gastal, M.C.P., 2009. Emplacement mechanism of the main granite pluton of the Lavras do Sul Intrusive complex, South Brazil, determined by magnetic anisotropies. Tectonophysics, 466, 18-31.

Reischl, J.L., 1978. Mineralizações cupriferas associadas a vulcânicas na Mina do Seival. In: XXX CONGRESSO BRASILEIRO DE GEOLOGIA, 30. 1978, Recife. Anais, SBG, 4, pp. 1568-1582.

Renac, C., Mexias, A.S., Gomes, M.E.B., Ronchi, L.H., Nardi, L.V.S., Laux, J.H., 2014. Isotopic fluid changes in a Neoproterozoic porphyry–epithermal system: the Uruguay mine, southern Brazil. Ore Geology Review, 60, 146-160.

Remus, M.V.D., McNaughton, N.J., Hartmann, L.A., Koppe, J.C., Fletcher, I.R., Groves, D.I., Pinto, V.M., 1999. Gold in the Neoproterozoic juvenile Bossoroca Volcanic Arc of southernmost Brazil: isotopic constraints on timing and sources. Journal of South American Earth Sciences, 12, 349-366.

Remus, M.V.D., McNaughton, N.J., Hartmann, L.A., Fletcher, I.R., 1997. Zircon SHRIMP dating and Nd isotope data of granitoids of the São Gabriel Block, southern Brazil: evidence of an Archaean/Paleoproterozoic basement. In: INTERNATIONAL SYMPOSIUM ON GRANITES AND ASSOCIATED MINERALIZATION 2, Salvador, Extended Abstracts 1, pp. 217-272.

Remus, M.V.D., Hartmann, L.A., McNaughton, N.J., Groves, D.I., Reischl, J.L., 2000. A distal magmatic–hydrothermal origin for the Camaquã Cu (Au–Ag) and Santa Maria Pb, Zn (Cu–Ag) deposits, southern Brazil. Gondwana Research, 3, 155-174.

Reynolds, R.C., 1985. NEWMOD, a Computer Program for the Calculation of One-dimensional Diffraction Patterns of Mixed-layered Clays. 8 Brook Rd., Hanover, NH, USA.

Ribeiro, M., Bocchi P.R., Figueiredo Filho P.M., Tessari R.I., 1966. Geologia da Quadrícula de Caçapava do Sul, Rio Grande do Sul. Boletim 127, DNPM/DFPM, Rio de Janeiro, 232 p.

Ribeiro, M., Teixeira, C.A.S., 1970. Datações de rochas do Rio Grande do Sul e sua influência nos conceitos estratigráficos e geotectônicos locais. Inheríngia, Série Geológica, 3, 109-120.

Riedel, W., 1929. Zur Mechanik Geologischer Brucherscheinungen. Zentral–blatt fur Mineralogie. Geologie und Paleontologie, B, 354-368.

Ronchi, L.H., Lindenmayer, Z.G., Bastos Neto, A., Murta, C.R., 2000. O stockwork e a zona do minério sulfetado no arenito inferior da Mina Uruguai, RS. In: Ronchi L.H., Lobato, A.O.C. (Orgs) Minas do Camaquã, um estudo multidisciplinar. UNISINOS/FAPERGS (Universidade do Vale do Rio dos Sinos/Fundação de Amparo à Pesquisa do Estado do Rio Grande do Sul). São Leopoldo, 165-190.

Saalmann, K., Hartmann, L.A., Remus, M.V.D., Koester, E., Conceição, R.V., 2005. Sm–Nd isotope geochemistry of metamorphic volcano–sedimentary successions in the São Gabriel Block, southernmost Brazil: evidence for the existence of juvenile Neoproterozoic oceanic crust to the east of the Rio de la Plata craton. Gondwana Research, 8, 143-161.

Sánchez-Bettucci, L., Koukharsky, M., Pazos, P.J., Stareczek, S., 2009. Neoproterozoic subaqueous extrusive–intrusive rocks in the Playa Hermosa Formation in Uruguay: regional and stratigraphic significance. Gondwana Research, 16, 134-144.

Sommer, C.A., Lima, E.F., Nardi, L.V.S., Figueiredo, A.M.G., Pierosan, R., 2005. Potassic and Low– and High–Ti Mildly Alkaline Volcanism in the Neoproterozoic Ramada Plateau, Southernmost Brazil. Journal of South American Earth Sciences, 18, 237-254.

Sommer, C.A., Lima, E.F., Nardi, L.V.S., Liz, J.D., Waichel, B.L., 2006. The evolution of Neoproterozoic magmatism in Southernmost Brazil: shoshonitic, high–K tholeiitic and silica–saturated, sodic alkaline volcanism in post–collisional basins. Anais Academia Brasileira Ciências, 78, 573-89.

Sommer, C.A., Lima, E.F., Pierosan, R., Machado, A., 2011. Reoignimbritos e ignimbritos de alto grau do vulcanismo Acampamento Velho, RS: origem e temperatura de formação. Brazilian Journal of Geology, 41, 420-435.

Tchalenko, J.S., Ambrayses, N.N., 1970. Structural analysis of the Dasht–e Bayaz (Iran) earthquake fractures. Geological Society of America Bulletin, 81, 41-60.

Toniolo, J.A., Remus, M.V.D., Macambira, M.J.B., Moura, C.A.V., 2004. Metalogênese do Depósito de Cobre Cerro dos Martins, RS, Revisão e Geoquímica Isotópica de Sr, S, O e C. Pesquisas em Geociências, 31, 41-67.

Toniolo, J.A., Gil, C.A.A., Sander, A., 2007. Projeto BANEO–Metalogenia das Bacias Neoproterozóico–Eopaleozóicas do Sul do Brasil – Bacia do Camaquã. CPRM – Serviço Geológico do Brasil, CD Rom.

Twiss, R.J., Moores, E.M, 1992. Structural Geology. University of California, 532 p.

Wildner, W., Lima, E.F., Nardi, L.V.S., Sommer, C.A., 2002. Volcanic cycles and setting in the Neoproterozoic III to Ordovician Camaquã Basin succession in southern Brazil: characteristics of post–collisional magmatism. Journal of Volcanology and Geothermal Research, 118, 261-283.

Winchester, J.A., Floyd, P.A., 1977. Geochemical discrimination of different magma series and theiur differentiation products using immobile elements. Chemical Geology, 20, 325-343.

ANEXOS

A) ARTIGOS EM CO-AUTORIA

Manuscrito Fontana et al. 2017

Este manuscrito foi submetido ao *Journal of Geochemical Exploration* e publicado online em 02/03/2017 por Eduardo Fontana como parte principal de sua tese de doutorado.

Journal of Geochemical Exploration 177 (2017) 45–60

Contents lists available at ScienceDirect

Journal of Geochemical Exploration

journal homepage: www.elsevier.com/locate/gexplo

Hydrothermal alteration of volcanic rocks in Seival Mine Cu–mineralization – Camaquã Basin – Brazil (part I): Chloritization process and geochemical dispersion in alteration halos

Eduardo Fontana [a,b,*], André S. Mexias [a], Christophe Renac [b], Lauro V.S. Nardi [a], Rodrigo W. Lopes [a,b], Aurélie Barats [b], Marcia E.B. Gomes [a]

[a] UFRGS – Universidade Federal do Rio Grande do Sul, Av. Bento Gonçalves 9500 – Agronomia, Porto Alegre, RS, Brazil
[b] Université Côte d'Azur, CNRS, OCA, IRD, Géoazur, 250 rue Albert Einstein, Sophia Antipolis 06560, Valbonne, France

ARTICLE INFO

Article history:
Received 26 June 2016
Revised 25 November 2016
Accepted 26 February 2017
Available online 02 March 2017

Keywords:
Geochemistry
Hydrothermal alteration
Chloritization process
C/S mixed-layers
Cu-sulfides

ABSTRACT

The Seival Mines are situated in the NE portion of the Lavras do Sul mining district, southernmost Brazil. They are hosted by volcanic and sub-volcanic rocks of Neoproterozoic age, which are part of the post-collisonal Camaquã Basin volcano-sedimentary sequence. The mineralization occurs in shoshonitic volcanic and sub-volcanic rocks of the Lavras do Sul Shoshonitic Association. They are of intermediate composition and exhibit widespread hydrothermal alteration. The mineralization occurs primarily in the form of bornite, chalcocite, covellite, pyrite, and in supergene phases as malachite. Mineral occurrence is always controlled by fractures. Ore is associated with chloritization processes, which produced smectite, chlorite/smectite and corrensite clay minerals and gangue of carbonate, mostly calcite, and barite. In this study field mapping and drill core sampling, petrography with optical microscopy and electron microscopy, X-ray diffraction for clay size fraction characterization and whole-rock geochemistry are used to understand the spatial distribution and relative chronology of hydrothermal alteration products of different lithology in the mineralized zones. The post-magmatic fluid activity and hydrothermal lower-temperature alteration that produced smectite → chlorite/smectite → chlorite and corrensite → carbonate have changed the major, minor, trace and rare earth element (REE) contents. Lavas and sub-volcanic rocks contain Cu-Fe sulfides. In alteration halos, Cu-sulfides with supergene influence is related to circulation of late hydrothermal fluids. The pH variations and sulfide materials are related to dispersion metals around vertical structures.

B) RESUMOS EM CONGRESSOS

I. XVI Congresso Brasileiro de Geoquímica (Expandido)

Lopes, R.W.; Fontana, E.; Mexias, A.S.; Gomes, M.E.B.; Nardi, L.V.S.; Renac, C.; Lindenberg, M.T.; Miranda, B.P., 2013. Caracterização geoquímica da Sequência Magmática Mina do Seival, Neoproterozoico, Bacia Do Camaquã, RS. 2013. XVI Congresso Brasileiro de Geoquímica. Diamantina, MG.

Caracterização geoquimica da Sequência Magmática Mina do Seival, Neoproterozóico, Bacia Do Camaquã, RS.

Rodrigo W. LOPES[1], Eduardo FONTANA[1-2], André S. MEXIAS[1], Márcia E.B. GOMES[1], Lauro V.S. NARDI[1], Christophe RENAC[2], Marcelo T. LINDENBERG[1] & Bruno P. de MIRANDA[1].

[1] - UFRGS - Universidade Federal do Rio Grande do Sul, Av. Bento Gonçalves 9500 - Agronomia, Porto Alegre, RS - CEP 91501-970 - Caixa-Postal: 15001- Brasil. E-mail*: rodrigowinck@yahoo.com.br; E-mail: fontanageo@gmail.com; E-mail: andre.mexias@ufrgs.br; E-mail: marcia.boscato@ufrgs.br; E-mail: lauro.nardi@ufrgs.br.

[2] - UNICE – Géoazur, Université de Nice Sophia-Antipolis, CNRS, IRD, Observatoire de la Côte d'Azur, 250 rue A. Einstein, F-06560, Sophia Antipolis, FR. E-mail: christophe.renac@unice.fr.

Resumo

A Mina do Seival é constituida por rochas piroclásticos cortados por diques de andesitos e possuem intensa alteração hidrotermal e mineralização de cobre, principalmente ao longo de fraturas e falhas de direção N-NE e NW. Este trabalho discute a caracterização geoquímica dessas sequências magmáticas através de análises de elementos maiores e traço.

Palavra chaves: Mina do Seival, Alteração hidrotermal, Petrografia, magmatismo shoshonitico, depósitos de cobre, Geoquímica, Bacia do Camaquã.

Abstract

Seival Mine is constituted by pyroclastic rocks cutted by andesitic dykes and have an intense hydrothermal alteration and copper mineralization, mainly in N-NE and W-NW faults. This survey will discuss a geochemical characterization of this magmatic sequences through major and trace elements.

Key words: Seival Mine, Hydrothermal alteration, Petrography, Shoshonitic magmatism, Copper deposit, Geochemistry, Camaquã Basin.

Continuação dos RESUMOS EM CONGRESSOS

II. XVI Congresso Brasileiro de Geoquímica (Expandido)

Fontana, E.; Renac, C.; Lopes, R.W.; Mexias, A.S.; Nardi, L.V.S.; Gerbe, M.C., 2013. Mobilidade de elementos maiores e menores na evolução dos fluidos hidrotermais da Mina do Seival – Neoproterozoico – Sul do Brasil. 2013. XVI Congresso Brasileiro de Geoquímica. Diamantina, MG.

Mobilidade de elementos maiores e menores na evolução dos fluidos hidrotermais da Mina do Seival – Neoproterozóico - RS

Eduardo FONTANA[1-2], Christophe RENAC[2], Rodrigo W. LOPES[1], André S. MEXIAS[1], Lauro V.S. NARDI[1], Marie Christine GERBE[3]

1-UFRGS - Universidade Federal do Rio Grande do Sul, Av. Bento Gonçalves 9500 - Agronomia, Porto Alegre, RS. E-mail: eduardo.fontana@ufrgs.br, andre.mexias@ufrgs.br, rodrigowinck@yahoo.com, lauro.nardi@ufrgs.br.

2-UNICE – Géoazur, Université de Nice Sophia-Antipolis, CNRS,IRD, OCA, 250 10, Rue A. Einstein, F-06560, Sophia Antipolis, FR. E-mail: christophe.renac@unice.fr.

3-UJM - Université Jean Monnet - 10, Rue Tréfilerie, Saint-Etienne, FR. E-mail: gerbe@univ-st-etienne.fr

Resumo

A região da Mina do Seival é constituída por depósitos piroclásticos e diques de composição andesítica. Este sistema apresenta intensa alteração e circulação de fluídos decorrentes da evolução do ciclo vulcânico, gerando depósitos metálicos com importância econômica. Este trabalho apresenta a mobilidade de elementos químicos e a evolução dos fluídos hidrotermais associados ao sistema magmático através de balanço de massa e isótopos estáveis (C, O).

Palavra chaves: mobilidade química, hidrotermalismo, isótopos estáveis

Abstract

The host rocks of Seival Mine are mainly pyroclastic deposits and andesitic dikes . This system shows intense hydrothermal alteration and movement of fluids arising from the volcanic avtivity, generating metallic deposits with economic importance. This paper presents the mobility of chemical elements and evolution of hydrothermal fluids associated with magmatic system through mass balance and stable isotopes (C, O).

Keywords: chemical mobility, hydrothermalism, stable isotopes

Continuação dos RESUMOS EM CONGRESSOS

III. XV Congresso Brasileiro de Geoquímica (Expandido)

Lopes, R.W.; Fonatana, E.; Mexias, A.S.; Renac, C., Gomes; M.E.B., 2015. Geoquímica dos Diques de Andesito e Química Mineral dos Plagioclásios da Mina do Seival (Bacia do Camaquã, Neoproterozoico). XV Congresso Brasileiro de Geoquímica. Brasília, DF.

Geoquímica dos Diques de Andesito e Química Mineral dos Plagioclásios da Mina do Seival (Bacia do Camaquã, Neoproterozóico)

Rodrigo W. LOPES[1-2], Eduardo FONTANA[1-2], André S. MEXIAS[1], Christophe RENAC[2], Márcia E. B. GOMES[1]

1-UFRGS - Universidade Federal do Rio Grande do Sul, Av. Bento Gonçalves 9500 - Agronomia, Porto Alegre, RS. E-mail: rodrigo.winck@ufrgs.br, eduardo.fontana@ufrgs.br, andre.mexias@ufrgs.br, marcia.boscato@ufrgs.br

2-UNICE – Géoazur, Université de Nice Sophia-Antipolis, CNRS,IRD, Observatoire de la Côte d'Azur, 250 rue A. Einstein, 06560, Sophia Antipolis, França. E-mail: christophe.renac@unice.fr.

Resumo

As rochas vulcânicas na região da Mina do Seival são cortadas por diques de composição traqui-andesítica. Estes diques possuem fenocristais de plagioclásio albitizados com corrosão interna e preenchimento por uma mistura de argilominerais com teor homogêneo de potássio de ~1%. Este trabalho discute os processos hidrotermais atuantes no plagioclásio e sua alteração para mineralogia secundária.

Palavra chaves: Albitização, hidrotermalismo, Bacia do Camaquã

Abstract

Volcanic rocks in the region of Seival mine are cut by dikes of trachyandesite composition. These dikes have phenocrysts of albite-plagioclase with internal corrosion and fill of a mixture of clay with homogeneous potassium content of ~1%. This work discusses the hydrothermal processes operating in plagioclase and his secondary mineralogy.

Word keys: Albitisation, hydrothermal alteration, Camaquã basin

Continuação dos RESUMOS EM CONGRESSOS

IV. III Simpósio Brasileiro de Metalogenia

Lopes, R.W.; Fontana, E.; Mexias, A.S.; Gomes, M.E.B.; Nardi, L.V.S.; Renac, C.; Lindenberg, M.T.; Miranda, B.P., 2013. Geologia e Química Mineral das mineralizações de cobre na Mina do Seival, Neoproterozoico – Bacia do Camaquã – RS – Brasil. Simpósio Brasileiro de Metalogenia. Gramado, RS.

III Simpósio Brasileiro de Metalogenia
Os Novos Depósitos Minerais Brasileiros
02 a 05 de junho 2013
Hotel Serra Azul Gramado - RS

GEOLOGIA E QUÍMICA MINERAL DAS MINERALIZAÇÕES DE COBRE NA MINA DO SEIVAL, NEOPROTEROZÓICO - BACIA DO CAMAQUÃ - RS - BRASIL

1. **Lopes, W.R., rodrigowinck@yahoo.com.br, UFRGS** Av. Bento Gonçalves 9500 - Porto Alegre, RS -Brasil;
2. **Fontana, E.; UFRGS** Av. Bento Gonçalves 9500 - Porto Alegre, RS -Brasil
3. **Mexias, A.S.; UFRGS** Av. Bento Gonçalves 9500 - Porto Alegre, RS -Brasil
4. **Gomes, M.E.B.; UFRGS** Av. Bento Gonçalves 9500 - Porto Alegre, RS -Brasil
5. **Nardi, L.V.S., UFRGS** Av. Bento Gonçalves 9500 - Porto Alegre, RS -Brasil
6. **Renac, C.; UNICE – GEOAZUR - CNRS, IRD, OCA, 250, Rua A. Einstein, França**
7. **Lindenberg, M.T.; UFRGS** Av. Bento Gonçalves 9500 - Porto Alegre, RS -Brasil
8. **Miranda, B. P.; UFRGS** Av. Bento Gonçalves 9500 - Porto Alegre, RS -Brasil

INTRODUÇÃO

As rochas da Mina do Seival(MS)possuem intensa alteração hidrotermal e mineralizações de Cu e sua geologia relacionada ao estágio pós-colisional do ciclo Brasiliano-Pan-Africano, no alogrupo Bom Jardim, pertencendo à Formação Hilário na Bacia do Camaquã, com idade Neoproterozóica. A região já foi responsável por grande parte da produção desse minério no Brasil, sendo uma das mais importantes no Rio Grande do Sul e explorada principalmente na primeira metade do século XX.Estas mineralizações foram descritas por Reischl (1978) e atualmente por Lopes (2013) e Fontana (2013). Este trabalho apresenta a geologia e química mineral desta mineralizaçãoembasadoem trabalho de campo, petrografia e microscopia eletrônica. A compreensão do hidrotermalismo presente nas sequências vulcânicas da MS colabora com o entendimento da evolução geológica e metalogenética da Bacia do Camaquã.

RESULTADOS E DISCUSSÃO

As rochas da MS tem composição andesítica e traqui-andesítica, e foram divididas em duas sequências. A sequência I contem rochas piroclásticas e efusivas,compostas por cristaloclastos de plagioclásio, quartzo e matriz vítrea microcristalina. Os argilominerais predominantes são clorita, esmectita e corrensita, toda a sequencia é cortada por veios de carbonato associados às intrusões;sequência II composta por diques de andesito com textura traquítica, fenocristais abundantes de plagioclásio, piroxênio, geralmente substituídos por clorita, e calcita. A matriz é fanerítica fina a afanítica composta por plagioclásio, vidro e piroxênio.Os sulfetos são calcosina, pirita, calcopirita e bornita. Estão associados à malaquita, localizados em zona de fratura ou falha, onde se concentram as mineralizações e também ocorrem de maneira disseminada a partir das fraturas ou em pequenos grãos disseminados na rocha. A barita representa uma das fases de baixa temperatura do sistema e ocorre preenchendo fraturas de espessuras centimétricas e sob a forma de cristais tabulares geminados, localmente alterados. A malaquita, azurita, hematita estão presentes como resultado do intenso intemperismo e ocorrem preferencialmente nas amostras de superfície (Fig. 1).A tectônica do estagio pós-colisional controla o posicionamento e geração da mineralização através de estruturas rúpteis com direção NE e distensão regional.

A primeira fase da alteração hidrotermal é representada pela esmectita, que possivelmente está relacionada à processos residuais magmáticos na forma fibrosa e cristalina.A segunda fase é caracterizada pela assembléia mineralógica clorita + epidoto (pistacita) + carbonato (calcita) + sulfeto (pirita e calcosina) + barita + quartzo + hematita como apresentado em Lopes (2013). A terceira fase ocorre nos diques e é caracterizada como propilitização (clorita + epidoto + sulfeto).

Os teores verificados de Cu, Zn e Ni em relação ao protólito menos afetado pelo processo hidrotermal, nos diques e brechas, sugerem que as principais ocorrências de mineralização de cobre têm origem magmática. Processos envolvendo diferentes temperaturas atuaram sobre estas rochas originando produtos de alteração pervasiva, os processos de carbonatação, cloritização e hematitização, estão associados às amostras mais superficiais, acima dos 30 metros de profundidade, e ocorrem em maiores quantidade próximos aos depósitos, ocorrências e diques de andesito.

A presença de um provável dique de lamprófiro na Mina do Seival sugere que os magmas lamprofíricos podem ter papel relevante na formação das mineralizações associadas ao magmatismo shoshonítico(Lima, 1998), conforme sugerido por Müller (2012). Este estudo contribui para a geração de um modelo evolutivo dos processos de alteração hidrotermal possibilitando o entendimento da geologia regional e das mineralizações da Bacia do Camaquã.

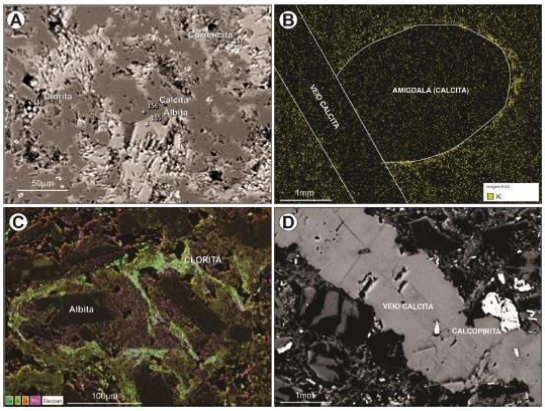

Figura 1:A) Andesito; B) Imagem EDS - Andesito amigdaloide; C) Clorita; D) Calcopirita associada aos veios de calcita.

Continuação dos RESUMOS EM CONGRESSOS

V. 1ª SAPIGEO

Lopes, R.W.; Mexias, A.S.; Renac, C., 2015. Metalogênese e Geocronologia de Rochas Vulcânicas Associadas a Eventos Hidrotermais Pós–Magmáticos e Mineralizações de Cobre, Neoproterozoico, Brasil. 1ª Semana Acadêmica dos Pós–Graduandos do Instituto de Geociências da UFRGS. Porto Alegre, RS.

1ª Semana Acadêmica dos Pós-Graduandos do Instituto de Geociências da UFRGS - Integrando as Geociências - 17 a 20 de agosto de 2015 - Porto Alegre/RS

Metalogênese e Geocronologia de Rochas Vulcânicas Associadas a Eventos Hidrotermais Pós-Magmáticos e Mineralizações de Cobre, Neoproterozóico, Brasil

Rodrigo Winck Lopes[1-2]; André Sampaio Mexias[1]; Christophe Renac[2]
[1]UFRGS - Universidade Federal do Rio Grande do Sul, Av. Bento Gonçalves 9500 - Agronomia, Porto Alegre, RS - CEP 91501-970 - Caixa-Postal: 15001- Brasil. E-mail: rodrigo.winck@ufrgs.br; andre.mexias@ufrgs; [2]UNICE – Géoazur, Université de Nice Sophia-Antipolis, CNRS, IRD, Observatoire de la Côte d'Azur, 250 rue A. Einstein, F-06560, Sophia Antipolis, FR. E-mail: christophe.renac@unice.fr

A Mina do Seival tem sido investigada pelo presente autor desde o projeto temático, intitulado Alteração Hidrotermal e Mineralizações de Cobre na Mina do Seival, Bacia do Camaquã, RS que caracterizou a alteração hidrotermal na área, bem como forneceu um mapa geológico de detalhe para continuidade dos estudos. Dessa forma, o projeto de mestrado teve como meta fornecer informações sobre a petrografia e geoquímica das rochas da região da Mina do Seival, bem como caracterizar as minas e as ocorrências de cobre.

A tese foi iniciada em 2013 e tem como objetivo avançar no conhecimento sobre a geocronologia das rochas vulcânicas e dos eventos hidrotermais mineralizantes. É necessário o conhecimento da idade das rochas da região para enquadra-las em um modelo metalogenético, tentando compreender o tipo de deposito mineral e associa-la aos outras ocorrências de cobre na Bacia do Camaquã. Para tanto, é utilizada determinações isotópicas e geocronológicas de minerais específicos em cada litotipo que ocorre na área e adjacente.

Conforme referido, o objetivo principal da tese é a realização de análises em diversas fases minerais pelo método de datação $^{40}Ar/^{39}Ar$ a fim de obter dados geocronológicos das rochas que ocorrem na área de estudo, e para uma melhor compreensão do hidrotermalismo ocorrente na área. É também pretendido obter dados de U-Pb SHRIMP em zircões de um dique de andesito da área, para complementar os dados geocronológicos.

A metodologia utilizada pode ser descrita nos seguintes passos: separação mineral através de separador magnético, líquidos densos e purificação por catação manual; petrografia; analises por difratometria de raios X pelo método do pó e argilas orientadas; imagiamento e Microscopia Eletrônica de Varredura em lâminas e minerais separados; ICP-MS de rocha total para elementos maiores, metálicos e traços; ICP-MS em concentrados de plagioclásios para elementos maiores e terras raras; Datação pelo método $^{40}Ar/^{39}Ar$ e U-Pb; Microssonda Eletrônica nos minerais de alteração.

A integração das idades pelo método $^{40}Ar/^{39}Ar$ e pelo método U-Pb obtidas com as informações petrológicas e geoquímicas permitirá importantes considerações temporais a respeito da evolução da mineralização na Mina do Seival, além de possibilitar um avanço considerável no conhecimento metalogenético do Escudo Sul-rio-grandense.

Palavras-chave: Alteração Hidrotermal, Bacia do Camaquã, Geocronologia.

Continuação dos RESUMOS EM CONGRESSOS

VI. 48° Congresso Brasileiro de Geologia

Lopes, R.W.; Renac, C.; Mexias, A.S.; Bicca, M.; Fontana, E., 2016. Copper mineralizations controlled by brittles structures from Seival Mine, Neoproterozoic–Cambrian Camaquã Basin, southern Brazil. 48° Congresso Brasileiro de Geologia, 2016, Porto Alegre, RS.

COPPER MINERALIZATIONS CONTROLLED BY BRITTLE STRUCTURES FROM SEIVAL MINE, NEOPROTEROZOIC-CAMBRIAN CAMAQUÃ BASIN, SOUTHERN BRAZIL

Lopes, R.W.[1-2]; Martini, A.[1]; Bicca, M.[1]; Mexias, A.S.[1]; Renac, C.[2]; Fontana, E.[1-2], Petracco, B.M.[1]

[1]Universidade Federal do Rio Grande do Sul; [2]Université de Nice Sophia Antipolis

This study was developed in the Seival Mine, located in Lavras do Sul region, which is composed by volcanoclastic rocks and andesitic dikes associations, belonging to the Hilário Formation. This formation is positioned in the stratigraphic base of the Bom Jardim Group which compounds the depositional sequence of the greater Camaquã Basin, of Neoproterozoic depositional age (Ediacaran-Cambrian). These associations were deposited following evolved tectonic stages of South Rio-grandense shield, controlled by N45°W (Ibaré Lineament) and N40°E (Caçapava do Sul anomalous zone) oriented shear zones. The mineralization is identified in 6 inactive mines with an average of 0.6-2.5% of copper and 15-70 ppm of silver. In the Camaquã Basin, the copper and copper-gold mineralization occurs mainly in the Bom Jardim and Santa Bárbara Groups. For the region of Lavras do Sul, the rocks from Seival Mine does not show any influence from the metamorphic contact with the Lavras do Sul granite unlike the other copper deposits near the area. Until now, a few studies have being developed to understand the mineralization process and its main control in the region. Whit this premise, we performed structural analysis dividing the description into macro (remote sensing data) and meso (fieldwork structural measurements) scales. We have also used an optical microscope and x-ray diffractometry to determine the mineralogy and alteration assembly. The faults and fractures hosting mineralization show intense hydrothermal alteration in areas of highest brittle deformation, locating most of the influence of a hydrothermal mineralization halo in rocks near fault boundaries. The mineralization occurs at the intersection of main NE and NW (> 100 meters) oriented fault plans and near to pyroclastic deposits and lava flow pile lithological contacts. The andesitic and trachy-andesitic dikes occur along NE oriented structures and belongs to the lavas of the Hilário volcanism and may have contributed to the re-circulation of fluids in the volcanic rocks favoring the remobilization and precipitation of the ore minerals in the fault plans. The intense fracturing generates stockwork structures filled by clay (chlorite, mix chlorite-smectite and corrensite), calcite and barite. Structural measurements enable to determine an N-NE major trend for the mineralization and, consequently, for hydrothermal alteration halos. Reactivation of brittle structures, that hosts the copper mineralization, is well preserved in the fault plans and represented by horizontal and vertical fault slickenlines, featuring dominantly transcurrent and normal movements. In this context, we conclude that the mineralization was controlled by brittle structures without any influence of contact metamorphism generated by igneous adjacent rocks, which also hosts hydrothermal clays and copper deposits. These sulfides are remobilized by strain-relief areas characterized by intense fracturing caused by the intersection of faults and fractures.

PALAVRAS-CHAVE: BRITLE STRUCUTURAL GEOLOGY, COOPER MINERALIZATION, HYDROTHERMAL ALTERATION.

Continuação dos RESUMOS EM CONGRESSOS

VII. 16th ICC

Lopes, R.W.; Mexias*, A.S.; Renac, C.; Fontana, E.; Gomes, M.E.B., 2017. Mineral chemistry of magmatic and hydrothermal alteration phases and clay minerals from Seival Mine copper deposits, Camaquã Basin, Neoproterozoic of southern Brazil. 16th ICC, International Clay Conference, Granada, Espanha.

MINERAL CHEMISTRY OF MAGMATIC AND HYDROTHERMAL ALTERATION PHASES AND CLAY MINERALS FROM SEIVAL MINE COPPER DEPOSITS, CAMAQUÃ BASIN, NEOPROTEROZOIC OF SOUTHERN BRAZIL

RODRIGO W. LOPES (1–2), ANDRÉ S. MEXIAS (1)*, CHRISTOPHE RENAC (2), , EDUARDO FONTANA (1–2), MÁRCIA E.B. GOMES (1)

(1) Universidade Federal do Rio Grande do Sul, 91501–970, Porto Alegre, Brazil,
(2) Université Cotê D´Azur, 06560, Valbonne, France

Seival Mine copper deposits [4] are hosted by a Neoproterozoic sequence of volcanic rocks included in the Lavras do Sul Shoshonitic Association, Hilário Formation, in the post–collisional Camaquã Basin. Field and drill–core samples consist of pyroclastic, vesicular lava, porphyritic lavas and andesitic dikes with apparent preserved magmatic minerals and altered ones described as post–magmatic albitization and meteoric–hydrothermal alteration [2]. Whit this premise, the chemical compositions of minerals were determined in thin sections by electron microprobe. Clay minerals with light green colours consist of flake particles (10 to 100 μm) surrounded of andesine–labradorite, albite and augite. Theses clay minerals are dominantly trioctahedral smectite and interlayered chlorite/smectite, chlorite–rich chlorite/smectite, chlorite and corrensite, associated with calcite, titanite, quartz and hematite. Chlorites compositions is Mg–chamosite in pyroxene alteration, hydrothermal vein and matrix of andesite dike. The hydrothermal system started in outgassing, partially segregated into vesicles, which have deposited mainly pyrite and chalcopyrite. The albitization started at temperatures from 600 to 350 °C, and subsequent cooling at ca. <251 °C led to crystallization of titanite and Mg-chamosite. Chloritization continued at ca. 183 °C [3] Mg–saponite and saponite/chlorite mixed layers formed at lower–temperature (150 to 80 °C) [3].

The Mg–chamosite of lavas and pyroclastic rocks may be indicative sulfide bearing hydrothermal vein in Seival Mine area. Saponite, chlorite/smectite and different types of Mg–chamosite may represent mixture of magmatic and meteoric waters [1] or phase reflecting chemical metastability with decreasing temperatures and the intensity of hydrothermal alteration. Clay mineralogy and chemistry do not derive from local equilibrium, but rather from composition of volcanic rocks, water activity, temperature and Al, Si, Fe and Mg chemical changes. Moreover, mass balance calculations [2] have pointed out that hydrothermal alteration occurred in closed chemical systems with respect to Si, Al, Fe and Mg with additional hydrous carbonic fluids. Mg–chamosite formation was probably related with Cu–sulfide and Fe oxide formation.

Continuação dos RESUMOS EM CONGRESSOS

VIII. SIMBRAMME (Expandido)

Lopes, R.W., 2017. Mineralizações e argilominerais da Mina do Seival (Cu–Ag), Bacia do Camaquã. 1° SISBRAMME. Porto Alegre, Brasil.

MINERALIZAÇÕES E ARGILOMINERAIS DA MINA DO SEIVAL (Cu-Ag), BACIA DO CAMAQUÃ

Rodrigo Winck Lopes[1-2]

1 –Universidade Federal do Rio Grande do Sul – Porto Alegre – RS

2 – Université Côte d'Azur – UCA, Géoazur, Valbonne, France

RESUMO: Os depósitos da Mina do Seival (Cu-Ag) são mineralizações associados com argilominerais ferro-magnesianos e sulfetos de cobre. Os argilominerais foram caracterizados por difratometria de raios X sendo eles esmectita, interestratificados de clorita e esmectita, corrensita e clorita. As mineralizações estão relacionadas com a alteração hidrotermal encaixada nas falhas e fraturas com orientação predominante de NNE-SSW.

Palavras-chave: Mina do Seival, mineralizações de cobre, Bacia do Camaquã.

Continuação dos RESUMOS EM CONGRESSOS

IX. XVI Congresso Brasileiro de Geoquímica (Expandido)

Rodrigo W. Lopes, André S. Mexias, Christophe Renac, Eduardo Fontana, Aurélie Barats, Gabriel B. Drago, 2017. Geoquímica de Elementos Terras Raras em veios hidrotermais de barita, Mina do Seival, Bacia do Camaquã, Neoproterozoico. XVI Congresso Brasileiro de Geoquímica. Búzios, RJ.

GEOQUÍMICA DE ELEMENTOS TERRAS RARAS EM VEIOS HIDROTERMAIS DE BARITA, MINA DO SEIVAL, BACIA DO CAMAQUÃ, NEOPROTEROZÓICO

Rodrigo W. Lopes[1] (D), André S. Mexias[1], Christophe Renac[2], Eduardo Fontana[1], Aurélie Barats[2], Gabriel B. Drago[1]

1 - Universidade Federal do Rio Grande do Sul – UFRGS, Instituto de Geociências, Porto Alegre – RS, rodrigo.winck@ufrgs.br, andre.mexias@ufrgs.br, eduardo.fontana@ufrgs.br

2 - Université Côte d'Azur – UCA, Géoazur, Valbonne, France, christophe.renac@unice.fr, aurelie.barats@unice.fr

Resumo: Mineralizações de barita ocorrem como ganga nos depósitos de cobre da Mina do Seival. As baritas dos veios hidrotermais foram analisadas por *ICP-MS* para os elementos terras raras. O elevado teor de elementos terras raras é associado aos estágios finais da alteração hidrotermal caracterizada pelos processos de albitização, cloritização e deposição do sulfeto de cobre.

Palavras-chave: *Geoquímica de elementos terras raras; Veios hidrotermais de Barita; Bacia do Camaquã.*

Rare earth elements geochemistry in hydrothermal veins of barite, Seival Mine, Camaquã Basin, Neoproterozoic

Abstract: Barite mineralization occurs as gangue in the Seival Mine Cu-Ag deposit of hydrothermal. These hydrothermal veins of barites was analyzed by ICP-MS for the rare earth elements. The enrichment of the rare earth elements is associated to albitization, chloritization process and copper-sulfide deposition.

Keywords: *Rare earth elements geochemistry; Hydrothermal barite-veins; Camaquã Basin.*

C) MAPA DE PONTOS

Mapa de pontos marcados na Mina do Seival, exceto pontos RFM 68 e DD 78 localizados fora da área de estudo.

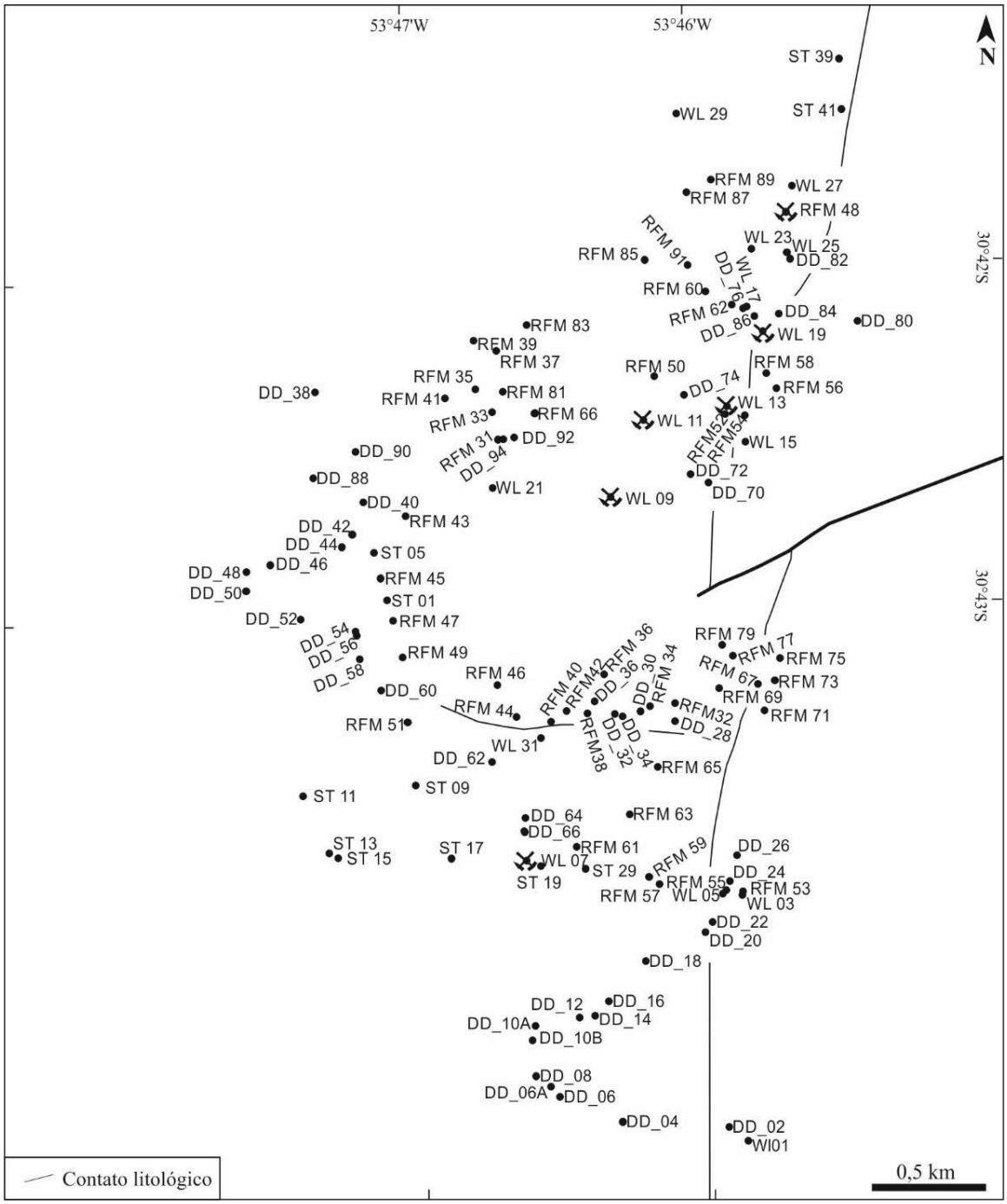

D) TABELA DE PONTOS

2011 - RFM - Trabalho de Campo I (Rodrigo Lopes, E. Fontana e M. Lindenberg)				
PONTO	E	N	UNIDADE	LITOLOGIA
RFM 32	234096	6597972	Hilário	Lava andesítica amigdalóide
RFM 34	233955	6597954	Hilário	Lapili tufo
RFM 36	233703	6598130	Hilário	Lapili tufo
RFM 38	233608	6597916	Hilário	Lapili tufo
RFM 40	233493	6597929	Hilário	Sondagem: SV 78 - 30
RFM 42	233408	6597870	Hilário	Sondagem: SV 78 - 06
RFM 44	233217	6597895	Hilário	Dique de traquiandesito
RFM 46	233112	6598069	Hilário	Sondagem: SV 78 - 02
RFM 48	234707	6600669	Hilário	Lapili tufo
RFM 50	233977	6599766	Hilário	Lapili tufo
RFM 52	234370	6599560	Hilário	Lapili tufo
RFM 54	234479	6599552	Santa Bárbara	Conglomerado polimítico
RFM 56	234656	6599702	Santa Bárbara	Vulcânica vesiculada
RFM 58	234598	6599784	Santa Bárbara	Conglomerado polimítico
RFM 60	234407	6600160	Hilário	Dique de andesito
RFM 62	234262	6600233	Hilário	Lapili tufo
RFM 64	233317	6599563	Hilário	Lapili tufo
RFM 66	233314	6599561	Hilário	Dique de andesito
RFM 31	233114	6599418	Hilário	Lapili tufo
RFM 33	233081	6599567	Hilário	Lapili tufo
RFM 35	232987	6599693	Hilário	Lapili tufo
RFM 37	233104	6599905	Hilário	Lapili tufo
RFM 39	232977	6599960	Hilário	Lapili tufo
RFM 41	232820	6599643	Hilário	Lapili tufo
RFM 43	232604	6598997	Hilário	Lapili tufo
RFM 45	232464	6598655	Hilário	Lapili tufo
RFM 47	232535	6598423	Hilário	Lapili tufo
RFM 49	232588	6598220	Hilário	Lapili tufo
RFM 51	232615	6597866	Hilário	Dique de traquiandesito
RFM 53	234471	6596940	Santa Bárbara	Conglomerado polimítico
RFM 55	234380	6596947	Hilário	Lava andesítica amigdalóide
RFM 57	234010	6596978	Hilário	Lapili tufo
RFM 59	233952	6597019	Hilário	Lapili tufo
RFM 61	233550	6597183	Hilário	Lapili tufo
RFM 63	233843	6597362	Hilário	Lapili tufo
RFM 65	233999	6597622	Hilário	Lapili tufo
RFM 67	234339	6598054	Hilário	Lapili tufo
RFM 69	234554	6598077	Hilário	Lapili tufo
RFM 71	234589	6597931	Santa Bárbara	Conglomerado polimítico
RFM 73	234647	6598098	Santa Bárbara	Conglomerado polimítico
RFM 75	234676	6598220	Santa Bárbara	Conglomerado polimítico
RFM 77	234416	6598232	Hilário	Lapili tufo
RFM 79	234354	6598291	Hilário	Sondagem sem identificação
RFM 81	233141	6599680	Hilário	Lapili tufo

Continuação da TABELA DE PONTOS

RFM 83	233271	6600045	Hilário	Lapili tufo
RFM 85	233924	6600405	Hilário	Lapili tufo
RFM 87	234155	6600777	Hilário	Lapili tufo
RFM 89	234292	6600847	Hilário	Lapili tufo
RFM 91	234161	6600376	Hilário	Lapili tufo
2012 - Minas (Rodrigo Lopes, B. Petracco, L. Petry e A. Martini)				
PONTO	E	N	UNIDADE	LITOLOGIA
WL 01	234503	6595570	Santa Bárbara	Conglomerado polimítico
WL 03	234467	6596919	Santa Bárbara	Conglomerado polimítico
WL 05	234359	6596925	Hilário	Lapili tufo
WL 07	233272	6597108	Hilário	Lapili tufo
WL 09	233737	6599102	Hilário	Lava andesítica porfirítica
WL 11	233920	6599526	Hilário	Lapili tufo
WL 13	234381	6599601	Hilário	Lava andesítica porfirítica
WL 15	234482	6599406	Santa Bárbara	Conglomerado Polimítico
WL 17	234491	6600150	Hilário	Dique de traquiandesito
WL 19	234580	6600015	Hilário	Lava andesítica porfirítica
WL 23	234516	6600465	Hilário	Lapili tufo
WL 25	234712	6600447	Hilário	Dique de traquiandesito
WL 27	234739	6600813	Hilário	Lapili tufo
WL 29	234100	6601209	Hilário	Lapili tufo
WL 31	233351	6597780	Hilário	Sondagem sem identificação
2013 - Diques (Rodrigo Lopes, M. Lindenberg e B. Petracco)				
PONTO	E	N	UNIDADE	LITOLOGIA
DD_02	234395	6595647	Santa Bárbara	Vulcânica vesiculada
DD_04	233807	6595673	Hilário	Aglomerado vulcânico
DD_06	233459	6595811	Hilário	Aglomerado vulcânico
DD_06_A	233410	6595866	Hilário	Lava andesítica amigdalóide
DD_08	233326	6595924	Hilário	Aglomerado vulcânico
DD_10_A	233306	6596120	Hilário	Aglomerado vulcânico
DD_10_B	233324	6596201	Hilário	Aglomerado vulcânico
DD_12	233568	6596246	Hilário	Aglomerado vulcânico
DD_14	233654	6596256	Hilário	Aglomerado vulcânico
DD_16	233729	6596336	Hilário	Aglomerado vulcânico
DD_18	233932	6596556	Hilário	Aglomerado vulcânico
DD_20	234265	6596713	Hilário	Lapili tufo
DD_22	234303	6596770	Hilário	Lapili tufo
DD_24	234400	6596994	Hilário	Lapili tufo
DD_26	234438	6597138	Hilário	Lapili tufo
DD_28	234093	6597871	Hilário	Dique de andesito
DD_30	233902	6597927	Hilário	Sondagem sem identificação
DD_32	233805	6597899	Hilário	Lapili tufo
DD_34	233761	6597913	Hilário	Lapili tufo
DD_36	233648	6597982	Hilário	Dique de traquiandesito
DD_38	232100	6599678	Hilário	Lapili tufo
DD_40	232369	6599072	Hilário	Dique de traquiandesito
DD_42	232307	6598896	Hilário	Lapili tufo

Continuação da TABELA DE PONTOS

DD_44	232249	6598827	Hilário	Lapili tufo
DD_46	231855	6598728	Hilário	Lapili tufo
DD_48	231723	6598691	Hilário	Lapili tufo
DD_50	231720	6598584	Hilário	Lapili tufo
DD_52	232023	6598428	Hilário	Lapili tufo
DD_54	232333	6598339	Hilário	Lapili tufo
DD_56	232325	6598362	Hilário	Lapili tufo
DD_58	232349	6598211	Hilário	Lapili tufo
DD_60	232468	6598040	Hilário	Lapili tufo
DD_62	233082	6597649	Hilário	Dique de andesito
DD_64	233261	6597269	Hilário	Lapili tufo
DD_66	233262	6597263	Hilário	Lapili tufo
DD_70	234278	6599184	Hilário	Dique de andesito
DD_72	234180	6599228	Hilário	Lapili tufo
DD_74	234142	6599664	Hilário	Lapili tufo
DD_76	234469	6600140	Hilário	Lapili tufo
WL_11	233930	6599542	Hilário	Lapili tufo
DD_78	237255	6606138	Santa Bárbara	Conglomerado polimítico
DD_80	235102	6600070	Santa Bárbara	Conglomerado polimítico
DD_82	234730	6600412	Hilário	Dique de andesito
DD_84	234667	6600109	Acampamento Velho	Dique de riolito
DD_86	234533	6600097	Santa Bárbara	Conglomerado polimítico
DD_88	232090	6599205	Hilário	Lapili tufo
DD_90	232325	6599351	Hilário	Dique de traquiandesito
DD_92	233203	6599428	Hilário	Lapili tufo
DD_94	233144	6599419	Hilário	Dique de andesito
2016 - Diques (Rodrigo Lopes, M. M. Bicca e B. Petracco)				
PONTO	E	N	UNIDADE	LITOLOGIA
ST 01	232519	6598417	Hilário	Lapili tufo
ST 05	232448	6598646	Hilário	Lapili tufo
ST 09	232666	6597473	Hilário	Lava andesítica porfirítica
ST 11	232158	6597431	Hilário	Lava andesítica porfirítica
ST 13	232273	6597167	Hilário	Lava andesítica porfirítica
ST 15	232273	6597167	Hilário	Lava andesítica porfirítica
ST 17	232841	6597150	Hilário	Lapili tufo
ST 19	233223	6597116	Hilário	Lapili tufo
ST 21	233255	6597112	Hilário	Lapili tufo
ST 29	233461	6597089	Hilário	Lapili tufo
ST 39	234733	6600848	Hilário	Lapili tufo
ST 41	234777	6600571	Hilário	Lapili tufo
SV 78-11 (30°43'21" S e 53°46'56" O)				
AMOSTRA	PROF. (m)	LINHA 800	UNIDADE	LITOLOGIA
FM 01	4,3		Hilário	Lava andesítica amigdalóide
FM 02	4,7		Hilário	Lava andesítica amigdalóide
FM 03	9,6		Hilário	Lava andesítica amigdalóide
FM 04	10,7		Hilário	Lava andesítica amigdalóide
FM 05	12,3		Hilário	Lava andesítica amigdalóide

Continuação da TABELA DE PONTOS

FM 06	13,1		Hilário	Lava andesítica amigdalóide
FM 07	13,7		Hilário	Lava andesítica amigdalóide
SV 13,3	13,3		Hilário	Lava andesítica amigdalóide
SV 14,3	14,3		Hilário	Lapili tufo
SV 16,3	16,3		Hilário	Lapili tufo
FM 08	15,5		Hilário	Lava andesítica amigdalóide
FM 09	16,8		Hilário	Lapili tufo
FM 10	20,5		Hilário	Lapili tufo
SV 23,4	23,4		Hilário	Lapili tufo
SV 30,4	30,4		Hilário	Lapili tufo
FM 11	33		Hilário	Lapili tufo
FM 12	33,4		Hilário	Dique de andesito
FM 13	38,5		Hilário	Dique de andesito
FM 14	41,5		Hilário	Dique de andesito
SV 40,7	40,7		Hilário	Dique de andesito
FM 15	43		Hilário	Dique de andesito
FM 16	50,5		Hilário	Lapili tufo
FM 17	54		Hilário	Lapili tufo
SV 55	55		Hilário	Lapili tufo
FM 18	59		Hilário	Lapili tufo
FM 19	63,5		Hilário	Lapili tufo
SV 64,8	64,8		Hilário	Lapili tufo
FM 20	70		Hilário	Lapili tufo
FM 21	72,5		Hilário	Lapili tufo
FM 22	72,5		Hilário	Lapili tufo
SV 77	77		Hilário	Lapili tufo
SV 78-01 (30°43'22" S e 53°47'0" O)				
AMOSTRA	PROF. (m)	LINHA 800	UNIDADE	LITOLOGIA
FM 23	4,5		Hilário	Lapili tufo
FM 24	6,3		Hilário	Lapili tufo
FM 25	16		Hilário	Lapili tufo
FM 26	16,9		Hilário	Lapili tufo
FM 27	19		Hilário	Lapili tufo
FM 28	20,6		Hilário	Lapili tufo
FM 29	28		Hilário	Lava andesítica amigdalóide
FM 30	36,8		Hilário	Lava andesítica amigdalóide
FM 31	37,7		Hilário	Lapili tufo
FM 32	38,5		Hilário	Dique de andesito
FM 33	39,5		Hilário	Dique de andesito
FM 34	39,8		Hilário	Dique de andesito
FM 35	70,5		Hilário	Lapili tufo
FM 36	73,3		Hilário	Lapili tufo
FM 37	83,6		Hilário	Lapili tufo
FM 38	86,8		Hilário	Lapili tufo
FM 39	94,8		Hilário	Lapili tufo
FM 40	95,5		Hilário	Lapili tufo
FM 41	108		Hilário	Lapili tufo

Continuação da TABELA DE PONTOS

FM 42	110		Hilário	Lapili tufo
FM 43	112		Hilário	Lapili tufo
FM 44	116		Hilário	Lapili tufo
FM 45	116,9		Hilário	Lapili tufo
FM 46	119,5		Hilário	Lapili tufo
FM 47	120,6		Hilário	Lapili tufo
FM 48	128,5		Hilário	Lapili tufo
FM 49	129		Hilário	Lapili tufo
FM 50	129,6		Hilário	Lapili tufo
SV 78-15 (30°43'14" S e 53°47'18" O)				
AMOSTRA	PROF. (m)	LINHA 700	UNIDADE	LITOLOGIA
FM 51	4,5		Hilário	Lapili tufo
FM 51A	11,8		Hilário	Lapili tufo
FM 52	15		Hilário	Lapili tufo
FM 53	16,8		Hilário	Lapili tufo
FM 54	23		Hilário	Lapili tufo
FM 55	23,5		Hilário	Lapili tufo
FM 56	27,8		Hilário	Lapili tufo
FM 57	30,9		Hilário	Lava andesítica porfirítica
FM 58	31,6		Hilário	Lava andesítica porfirítica
FM 59	36		Hilário	Lapili tufo
FM 60	38		Hilário	Lapili tufo
FM 61	38,7		Hilário	Lapili tufo
FM 62	50,1		Hilário	Lapili tufo
SV 78-16 (30°43'12" S e 53°47'20" O)				
AMOSTRA	PROF. (m)	LINHA 700	UNIDADE	LITOLOGIA
FM 63	5,9		Hilário	Lapili tufo
FM 64	9,1		Hilário	Lapili tufo
FM 65	22		Hilário	Lapili tufo
FM 66	22,5		Hilário	Lapili tufo
FM 67	25,4		Hilário	Lapili tufo
FM 68	40,3		Hilário	Lapili tufo
FM 69	44,3		Hilário	Lapili tufo
FM 70	48,3		Hilário	Lapili tufo
FM 71	51,5		Hilário	Lava andesítica porfirítica
FM 72	62		Hilário	Lapili tufo
SV 78-18 (30°42'26" S e 53°46'41" O)				
AMOSTRA	PROF. (m)	MINA DO MEIO	UNIDADE	LITOLOGIA
FM 73	7,6		Hilário	Lapili tufo
FM 74	8		Hilário	Lapili tufo
FM 75	15,3		Hilário	Lapili tufo
FM 76	18		Hilário	Lava andesítica amigdalóide
FM 77	18,7		Hilário	Lava andesítica amigdalóide
FM 78	24		Hilário	Lapili tufo
FM 79	30,5		Hilário	Lapili tufo
FM 80	43		Hilário	Lapili tufo

Continuação da TABELA DE PONTOS

SV 78-09 (30°42'27" S e 53°46'44" S)				
AMOSTRA	PROF. (m)	MINA DO MEIO	UNIDADE	LITOLOGIA
FM 81	8		Hilário	Lapili tufo
FM 82	27,5		Hilário	Lapili tufo
FM 83	49,8		Hilário	Lapili tufo
FM 84	63,9		Hilário	Lapili tufo
FM 85	74		Hilário	Lapili tufo
FM 86	75		Hilário	Lapili tufo
FM 87	76,9		Hilário	Lava andesítica amigdalóide
FM 88	77		Hilário	Lava andesítica amigdalóide
FM 89	78		Hilário	Lapili tufo
FM 90	93		Hilário	Lapili tufo
FM 91	80		Hilário	Lapili tufo
SV 001 (30°43'45" S e 53°47'08" O)				
AMOSTRA	PROF. (m)	MINA ALCIDES	UNIDADE	LITOLOGIA
NF01	13		Hilário	Lapili tufo
NF02	31		Hilário	Lapili tufo
NF03	113		Hilário	Lava andesítica amigdalóide
NF04	122		Hilário	Lava andesítica amigdalóide
NF05	122		Hilário	Lava andesítica amigdalóide
NF06	124		Hilário	Lava andesítica amigdalóide
NF07	126		Hilário	Lava andesítica amigdalóide
NF08	149	Topo do derrame	Hilário	Lapili tufo e lava amigdalóide
NF 09	162		Hilário	Lapili tufo
NF 10	183		Hilário	Lapili tufo

E) TABELA SUPLEMENTAR DO MANUSCRITO I: Lavras do Sul

Lavras do Sul Granite											
N°	Slickenside	Slickenline	Kin	Slickenline*	Kin*	N°	Slickenside	Slickenline	Kin	Slickenline*	Kin*
1	350/88	070/06	D	070/06	D	3	042/82	120/24	D	120/24	D
1	202/40	298/08	D	298/08	D	3	020/84	085/08	D	109/11	D
1	214/55	290/10	S	290/10	S	3	020/84	085/24	D	107/28	D
1	212/57	295/02	D	295/02	D	3	025/88	320/06	S	295/08	S
1	248/23	300/14	D	300/14	D	4	002/82	094/08	D	094/08	D
1	200/42	092/07	S	283/06	D	4	012/78	086/10	D	099/13	D
1	185/59	062/99	N	183/59	N	4	064/86	168/12	D	153/11	D
1	187/70	097/06	S	097/06	S	4	026/88	114/22	D	114/22	D
1	202/76	108/16	S	108/16	S	4	016/87	102/18	D	102/18	D
2	028/88	124/20	D	124/20	D	4	348/86	264/10	S	264/10	S
2	030/86	300/21	S	300/21	S	4	358/84	110/18	S	086/17	D
2	025/88	110/45	D	110/45	D	4	016/80	106/18	D	106/18	D
2	034/80	116/12	D	116/12	D	4	240/76	140/26	S	156/23	S
2	035/84	118/34	D	118/34	D	4	354/82	080/12	D	080/12	D
2	052/80	118/08	D	140/13	D	5	190/82	100/18	S	100/18	S
2	062/68	140/06	D	140/06	D	5	026/64	092/15	D	105/22	D
2	045/80	315/09	S	315/09	S	5	326/70	240/18	S	240/18	S
2	132/72	218/06	D	218/06	D	5	326/70	238/16	S	238/16	S
2	140/60	230/15	D	230/15	D	5	326/70	230/14	S	240/11	S
2	302/74	300/54	N	297/74	N	5	332/52	048/26	D	048/26	D
3	040/65	310/25	S	121/19	D	5	352/56	048/12	D	064/25	D
3	318/82	148/35	S	252/71	S	5	335/76	060/09	D	060/09	D
3	310/35	050/08	D	223/02	S	5	340/60	072/12	D	072/12	D
3	310/36	050/08	D	223/02	S	5	340/72	084/28	D	062/23	D
3	208/55	118/02	S	118/02	S	5	352/78	072/30	D	072/30	D
3	045/86	132/09	D	132/09	D	5	132/72	070/18	S	051/26	S
3	050/82	142/04	D	142/04	D	5	128/88	230/18	D	217/18	D
3	330/75	050/05	D	050/05	D	5	240/34	304/22	D	304/22	D
3	055/80	145/36	D	145/36	D	5	100/82	010/11	S	010/11	S
3	045/82	120/09	D	133/11	D	5	232/88	142/30	S	142/30	S
3	060/86	148/35	D	148/35	D	5	008/70	104/18	D	093/14	N
3	068/80	148/35	D	148/35	D	5	040/64	122/34	D	122/34	D
3	308/86	224/06	S	224/06	S	5	054/72	114/40	D	114/40	D
3	050/82	142/04	D	142/04	D	5	038/70	110/38	D	110/38	D
3	042/80	112/25	D	127/28	D	5	030/74	086/32	D	106/40	D
3	040/65	112/25	D	115/29	D	5	034/74	110/14	D	110/14	D
3	054/65	112/25	D	126/33	D						

Tabela suplementar do manuscrito I. Medidas estruturais dos pontos de Lavras do Sul. Chaves: N° = numero do ponto; Kin = cinemática; Linha* = linha calculada; Kin* = cinemática calculada; S = sinistral; D = dextral; N = normal. A localização dos pontos pode ser encontrada na Figura 14 da tese e na Figura 10 do manuscrito I (parte 4.2).

Continuação: TABELA SUPLEMENTAR DO MANUSCRITO I: Formação Hilário

Hilário Formation											
N°	Slickenside	Slickenline	Kin	Slickenline*	Kin*	N°	Slickenside	Slickenline	Kin	Slickenline*	Kin*
6	174/88	086/40	S	086/40	S	6	176/83	060/24	N	089/23	S
6	148/86	064/24	S	064/24	S	6	160/86	064/20	S	064/20	S
6	182/84	086/18	S	086/18	S	6	346/82	074/20	D	074/20	D
6	174/88	080/22	S	080/22	S	6	182/86	090/22	S	090/22	S
6	008/88	090/22	D	090/22	D	6	214/88	286/40	D	302/42	D
6	190/88	104/18	S	104/18	S	6	292/80	020/36	D	020/36	D
6	342/78	070/18	D	070/18	D	6	172/88	070/16	S	083/16	S
6	184/87	050/52	N	099/60	S	6	278/74	358/40	D	358/40	D

Tabela suplementar do manuscrito I. Medidas estruturais dos pontos da Formação Hilário. Chaves: N° = numero do ponto; Kin = cinemática; Linha* = linha calculada; Kin* = cinemática calculada; S = sinistral; D = dextral; N = normal. A localização dos pontos pode ser encontrada na Figura 14 da tese e na Figura 10 do manuscrito I (parte 4.2).

Continuação: TABELA SUPLEMENTAR DO MANUSCRITO I: Mina do Seival

Seival Mine											
N°	Slickenside	Slickenline	Kin	Slickenline*	Kin*	N°	Slickenside	Slickenline	Kin	Slickenline*	Kin*
7	214/78	314/10	D	302/08	D	9	090/70	013/32	S	013/32	S
7	085/76*	002/40	S	007/39	S	9	351/87	074/80	N	074/80	N
7	085/76*	001/82	N	054/74	N	9	347/78	259/30	S	259/30	S
7	082/89	004/73	N	355/73	N	9	308/50	010/34	N	010/34	N
7	081/90	350/22	S	350/22	S	9	355/24	047/12	D	047/12	D
7	093/52	010/13	X	012/11	X	9	338/40	002/38	D	002/38	D
7	001/90	075/26	D	091/27	D	9	074/62	353/22	S	353/22	S
7	095/74	015/43	D	020/42	D	10	054/83	180/02	D	180/02	D
7	273/86	001/51	S	358/51	S	10	269/75	350/00	D	350/01	D
7	238/70	330/05	S	327/04	S	10	245/60	071/08	D	270/54	D
7	100/78	011/60	S	029/57	S	10	077/84	295/42	D	014/77	D
8	060/62	060/62	N	060/62	N	10	236/64*	315/10	D	315/10	D
8	005/90	280/00	D	280/01	D	10	236/64*	310/30	D	310/30	D
8	355/75	270/00	D	270/01	D	10	102/75	180/18	D	180/18	D
8	057/13	115/08	D	115/08	D	10	260/60	005/03	D	172/04	D
8	295/84	025/05	S	025/05	S	10	098/83	185/18	D	185/18	D
8	252/60	315/40	D	315/40	D	10	091/72	176/45	N	176/45	N
8	245/60	323/10	D	323/10	D	10	272/63	110/61	N	251/61	N
8	160/90	075/27	D	075/27	D	11	303/76	224/50	S	224/50	S
8	254/78	327/14	S	327/14	S	11	100/66*	175/30	D	175/30	D
8	328/68	233/00	D	233/01	D	11	100/66*	010/76	N	010/76	N
8	255/76	345/08	S	345/08	S	11	122/90	215/12	S	215/12	S
9	316/66*	255/56	S	255/56	S	12	193/68	260/39	D	263/40	D
9	316/66*	316/66	N	316/66	N	12	176/70	150/40	D	127/61	D
9	113/68	036/26	S	036/26	S	12	193/68	260/35	D	265/37	D
9	108/70	191/30	S	191/30	S	12	099/60	054/64	S	065/55	S
9	155/73	251/00	D	251/01	D	12	182/58	260/52	D	239/41	D
9	090/70	172/10	D	172/10	D	12	276/26	276/26	N	276/26	N
9	123/54	200/14	S	200/14	S	12	290/42	290/42	N	290/42	N
9	183/58	234/08	S	256/25	S	12	350/86	350/86	N	350/86	N
9	083/84	000/20	D	001/20	D	12	130/44	130/44	N	130/44	N
9	138/76	047/08	D	047/08	D	12	350/85	350/85	N	350/85	N
9	165/76	061/20	S	061/20	S	12	285/60	285/60	N	285/60	N
9	158/88	060/18	D	060/18	D	12	251/40	288/36	N	287/34	N
9	053/65	325/10	D	325/10	D	12	233/52	290/42	N	286/38	N
9	328/70	328/70	N	328/70	N	12	108/78	030/40	S	028/40	S
9	331/84	063/70	N	063/70	N	12	108/60	035/32	S	038/30	S

Tabela suplementar do manuscrito I. Medidas estruturais dos pontos da mina do Seival. Chaves: N° = numero do ponto; Kin = cinemática; Linha* = linha calculada; Kin* = cinemática calculada; S = sinistral; D = dextral; N = normal; X = indefinida. A localização dos pontos pode ser encontrada na Figura 14 da tese e na Figura 10 do manuscrito I (parte 4.2).

F) TABELA SUPLEMENTAR DO MANUSCRITO II: A) Piroxênio

Sample	DD 62	DD 62	DD 62	DD 62	DD 62	DD 62	DD 62	DD 62	DD 62	DD 62	DD 62	DD 62	DD 62	FM 25	FM 25	FM 25	FM 25	FM 25	FM 25
Point	1px_c	2px_c	3px_h	4px_b	5px_b	1px2_b	1px3_b	2px3_b	3px3_b	4px3_b	5px3_c	6px3_c	7px3_c	49_px1	50_px1	51_px1	52_px1	53_px1	54_px1
SiO_2 (wt.%)	53.24	51.81	51.34	53.36	50.34	51.32	53.92	54.01	54.15	52.07	53.25	53.25	54.00	53.01	51.55	52.21	51.76	51.77	51.28
TiO_2	0.34	0.85	0.77	0.24	0.85	0.81	0.31	0.26	0.25	0.46	0.25	0.30	0.29	0.33	0.57	0.53	0.58	0.52	0.77
Al_2O_3	2.11	2.42	2.41	1.61	3.03	2.47	1.52	1.46	1.39	2.93	1.94	1.65	1.52	1.96	3.41	2.26	3.74	3.50	4.46
FeO	6.54	11.15	11.39	5.67	12.36	9.16	5.68	5.77	5.36	6.21	5.56	5.98	5.53	6.88	6.74	8.64	7.08	6.55	7.04
MnO	0.21	0.26	0.31	0.19	0.36	0.22	0.15	0.19	0.18	0.16	0.16	0.14	0.15	0.16	0.15	0.17	0.12	0.16	0.20
MgO	16.93	14.64	14.49	17.28	14.12	14.73	17.44	17.52	17.57	16.37	17.31	17.22	17.71	16.46	15.97	15.49	15.94	16.23	15.74
CaO	19.80	18.88	18.38	20.08	17.54	20.4	20.43	20.11	19.97	20.20	20.55	19.95	20.19	19.93	19.85	19.45	19.74	20.13	19.72
Na_2O	0.32	0.41	0.42	0.31	0.54	0.37	0.28	0.27	0.28	0.34	0.32	0.29	0.28	0.43	0.45	0.50	0.46	0.42	0.45
K_2O	-0.01	0	0	0	-0.01	-0.01	-0.01	0	-0.01	0	0	0	0	0	-0.01	-0.01	-0.02	0	0
Total	99.49	100.41	99.53	98.74	99.14	99.46	99.71	99.58	99.14	98.73	99.33	98.78	99.67	99.2	98.92	99.02	99.78	99.18	99.66
Number of ions on the basis 12																			
Si	1.96	1.92	1.93	1.97	1.90	1.91	1.97	1.98	1.99	1.93	1.95	1.97	1.98	1.96	1.91	1.94	1.91	1.91	1.89
Ti	0.01	0.02	0.02	0.01	0.02	0.02	0.01	0.01	0.01	0.01	0.01	0.01	0.01	0.01	0.02	0.01	0.02	0.01	0.02
Al	0.09	0.11	0.11	0.07	0.13	0.11	0.07	0.06	0.06	0.13	0.08	0.07	0.07	0.09	0.15	0.10	0.16	0.15	0.19
Fe^{3+}	0	0.03	0.03	0	0.06	0.04	0	0	0	0.01	0.01	0	0	0.01	0.02	0.02	0.02	0.03	0.02
Fe^{2+}	0.20	0.32	0.33	0.18	0.33	0.24	0.17	0.18	0.16	0.18	0.16	0.19	0.17	0.21	0.19	0.25	0.20	0.17	0.20
Mn	0.01	0.01	0.01	0.01	0.01	0.01	0	0.01	0.01	0.01	0	0	0	0.01	0	0.01	0	0.01	0.01
Mg	0.93	0.81	0.81	0.95	0.79	0.82	0.95	0.96	0.96	0.90	0.95	0.95	0.97	0.91	0.88	0.86	0.88	0.89	0.86
Ca	0.78	0.75	0.74	0.80	0.71	0.82	0.80	0.79	0.79	0.80	0.81	0.79	0.79	0.79	0.79	0.78	0.78	0.80	0.78
Na	0.02	0.03	0.03	0.02	0.04	0.03	0.02	0.02	0.02	0.02	0.02	0.02	0.02	0.03	0.03	0.04	0.03	0.03	0.03
K	0	0	0	0	0	0	0	0	0	0	0	0	0	0	0	0	0	0	0
Total	4	4	4	4	4	4	4	4	4	4	4	4	4	4	4	4	4	4	4
Wo	0.46	0.42	0.42	0.47	0.40	0.46	0.47	0.46	0.47	0.47	0.47	0.46	0.46	0.46	0.47	0.45	0.46	0.47	0.46
En	0.39	0.33	0.33	0.40	0.32	0.33	0.40	0.40	0.41	0.38	0.40	0.40	0.41	0.38	0.38	0.36	0.37	0.38	0.37
Fs	0.15	0.25	0.26	0.13	0.28	0.21	0.13	0.13	0.12	0.15	0.13	0.14	0.13	0.16	0.16	0.20	0.17	0.15	0.17
$Na_2O/(CaO+Na_2O)$	0.02	0.02	0.02	0.02	0.03	0.02	0.01	0.01	0.01	0.02	0.02	0.01	0.01	0.02	0.02	0.03	0.02	0.02	0.02
$MgO/(MgO+FeO_t)$	0.72	0.57	0.56	0.75	0.53	0.62	0.75	0.75	0.77	0.73	0.76	0.74	0.76	0.71	0.70	0.64	0.69	0.71	0.69
Charge	0.01	-0.08	-0.09	0.01	-0.18	-0.13	0.01	0.02	0.04	-0.03	-0.04	0.01	0.01	-0.02	-0.06	-0.07	-0.05	-0.09	-0.06

Tabela suplementar do manuscrito II. Tabela A: Análises por microssonda eletrônica de piroxênio.

Continuação da TABELA SUPLEMENTAR DO MANUSCRITO II: B) Biotita

More pristine biotite compositions				Less pristine biotite compositions		
Sample	DD 36	DD 36	DD 36	DD 36	DD 36	DD 36
Point	1 / 1 .	3 / 1 .	7 / 1 .	2 / 1 .	4 / 1 .	5 / 1 .
SiO_2 (wt.%)	31.99	33.57	34.05	33.3	32.59	35.06
TiO_2	3.69	5.27	6.42	4.86	5.94	5.50
Al_2O_3	16.49	14.56	14.00	14.02	13.17	13.95
FeO	17.55	16.37	14.49	14.43	13.52	13.41
MnO	0.25	0.18	0.08	0.11	0.08	0.09
MgO	16.29	13.25	12.5	10.91	11.58	11.59
CaO	0.15	0.15	0.06	0.11	0.04	0.11
Na_2O	0.31	0.65	0.82	0.63	0.74	0.69
K_2O	3.02	5.94	6.99	5.72	6.95	6.44
F	0.08	0.22	0.50	0.28	0.50	0.31
*Li_2O	0	0.08	0.22	0.01	0	0.51
*H_2O	3.79	3.69	3.55	3.45	3.34	3.60
Sum	93.58	93.84	93.46	87.72	88.22	91.13
Number of ions on the basis 22						
Si	5.02	5.31	5.39	5.57	5.46	5.61
Al^{iv}	2.98	2.69	2.61	2.43	2.54	2.39
Al^{vi}	0.07	0.02	0	0.33	0.07	0.24
Ti	0.44	0.63	0.76	0.61	0.75	0.66
Fe^{2+}	2.30	2.16	1.92	2.02	1.90	1.79
Mn	0.03	0.02	0.01	0.02	0.01	0.01
Mg	3.81	3.12	2.95	2.72	2.89	2.76
*Li	0	0.05	0.14	0	0	0.33
Ca	0.03	0.02	0.01	0.02	0.01	0.02
Na	0.09	0.20	0.25	0.20	0.24	0.21
K	0.61	1.20	1.41	1.22	1.49	1.31
OH	3.96	3.89	3.75	3.85	3.73	3.84
F	0.04	0.11	0.25	0.15	0.27	0.16
Sum	19.37	19.43	19.45	19.15	19.35	19.34
Fe/Fe+Mg	0	0.41	0.39	0.43	0.40	0.39
Mg/Mg+Fe	0.62	0.59	0.61	0.57	0.60	0.61
$Al^{vi}/Al^{vi}+Al^{iv}$	0.02	0.01	0	0.12	0.03	0.09
Charge	1.87	1.54	1.15	1.41	1.15	1.13

Tabela suplementar do manuscrito II. Tabela B: Análises por microssonda eletrônica de biotita.

Continuação da TABELA SUPLEMENTAR DO MANUSCRITO II: C) Titanita

Sample	DD 62	DD 62	DD 62	DD 62	DD 62	DD 62	DD 62	DD 62	DD 62	DD 62	DD 62	FM 13	FM 13	FM 13	FM 13
Point	1ep1dir	3ep1esq	4ep2	5ep3	6ep4	8epclay2	10epclay2	16clay3epi	17clay3epi	4pln_3	5pln_3	6ep1d	7ep1d	8ep2d	9ep3d
SiO_2 (wt.%)	31.22	31	31.02	31.19	31.27	30.49	31	30.60	30.96	31.06	31.32	30.46	30.13	30.05	29.65
TiO_2	32.88	32.96	32.95	33.07	32.9	32.38	32.93	32.75	32.78	32.81	30.64	32.61	33.00	34.55	34.49
Al_2O_3	2.43	2.47	2.62	2.49	2.3	2.63	2.66	2.65	2.83	2.45	2.77	4.05	3.72	2.47	2.46
FeO	1.67	1.64	1.64	1.85	2.2	2.68	1.63	1.94	1.62	1.59	3.38	1.02	1.17	1.94	1.71
MnO	0.04	0.04	0.01	0.04	0.03	0.02	-0.02	0.03	0.04	-0.01	0.02	-0.02	-0.01	0.02	0.01
MgO	0.15	0.10	0.11	0.21	0.17	0.60	0.08	0.22	0.14	0.10	0.26	-0.02	0.01	-0.01	0
CaO	26.87	27	26.99	27.09	26.9	25.68	26.82	26.2	26.68	26.92	26.57	28.04	28.16	27.88	27.85
Na_2O	0.06	0	0.02	0.04	0.04	0.03	0.03	0.01	0.01	0.02	0.05	0.02	-0.02	0	-0.01
K_2O	0.08	0.07	0.04	0.04	0.05	0.04	0.13	0.04	0.04	0.08	0.17	0	-0.02	-0.02	0.01
Sum	95.39	95.29	95.4	96.02	95.85	94.72	95.37	94.59	96.14	95.02	95.17	96.59	96.31	97.42	96.81
Number of ions on the basis 5															
Si	1.06	1.05	1.05	1.05	1.06	1.05	1.05	1.05	1.05	1.06	1.07	1.03	1.02	1.01	1.01
Ti	0.84	0.84	0.84	0.84	0.84	0.84	0.84	0.84	0.84	0.84	0.79	0.83	0.84	0.88	0.88
Al	0.10	0.10	0.11	0.10	0.09	0.11	0.11	0.11	0.11	0.10	0.11	0.16	0.15	0.10	0.10
Fe^{3+}	0.04	0.04	0.04	0.05	0.06	0.07	0.04	0.05	0.04	0.04	0.09	0.03	0.03	0.05	0.04
Fe^{2+}	0	0	0	0	0	0	0	0	0	0	0	0	0	0	0
Mn	0	0	0	0	0	0	0	0	0	0	0	0	0	0	0
Mg	0.01	0	0.01	0.01	0.01	0.03	0	0.01	0.01	0	0.01	0	0	0	0
Ca	0.98	0.98	0.98	0.98	0.98	0.94	0.98	0.96	0.97	0.98	0.97	1.01	1.02	1.01	1.01
Na	0	0	0	0	0	0	0	0	0	0	0	0	0	0	0
K	0	0	0	0	0	0	0.01	0	0	0	0.01	0	0	0	0
H	0	0	0	0	0	0	0	0	0	0	0	0	0	0	0

Tabela suplementar do manuscrito II. Tabela C: Análises por microssonda eletrônica de titanita.

Continuação da TABELA SUPLEMENTAR DO MANUSCRITO II: D) Feldspatos - Albita

Sample	Ponto 1	Ponto 2	Ponto 3	Ponto 6	Ponto 7	Ponto 8	Ponto 1	Ponto 3	Ponto 5	Ponto 7	Ponto 12	Ponto 13	Ponto 16	Ponto 1	Ponto 2	Ponto 3	Ponto 5	Ponto 14
Point	FM 12	FM 12	FM 12	FM 12	FM 12	FM 12	DD 36	DD 36	DD 36	DD 36	DD 36	DD 36	DD 36	DD 40	DD 40	DD 40	DD 40	DD 40
SiO_2 (wt.%)	66.12	65.60	67.45	66.54	66.07	67.07	67.04	67.87	68.35	67.71	67.4	64.78	66.93	66.06	65.66	67.52	65.19	66.67
TiO_2	0.07	0.11	0.03	0.02	0.03	0.01	0.01	0.03	0.01	0.03	0.02	0.02	0.03	0.06	0.02	0.02	0.01	0.02
Al_2O_3	19.61	20.20	20.08	20.3	20.98	20.13	20.01	19.88	19.75	19.9	20.00	19.63	20.23	21.25	21.56	20.56	20.12	20.51
FeO	0.65	0.56	0.07	0.04	0.05	0.03	0.08	0.01	0.02	0.02	0.76	1.91	0.75	0.28	0.23	0.21	0.12	0.32
MnO	-0.01	0.03	0.01	0.05	0.01	0.02	0.01	0.04	0.03	0.01	0.01	0.05	0.01	0.06	0.02	0.02	0.01	0.03
MgO	0.28	0.42	0.01	0.01	0.01	-0.01	0	0.02	0.01	0	0.26	0.73	0.38	0.06	0.10	0.08	0.02	0.06
CaO	0.72	0.99	0.25	0.19	0.38	0.14	0.13	0.10	0.04	0.11	0.14	0.18	0.10	0.28	0.18	0.13	0.10	0.17
Na_2O	10.25	9.84	11.10	11.25	10.82	11.13	10.23	11.10	11.11	11.05	10.47	9.30	10.79	10.05	10.17	10.88	11.21	10.36
K_2O	0.74	0.48	0.09	0.10	0.56	0.07	0.86	0.03	0.03	0.09	0.45	1.63	0.52	0.81	1.19	0.44	0.14	0.88
Sum	98.42	98.24	99.1	98.47	98.88	98.59	98.31	99.03	99.32	98.90	99.52	98.23	99.71	100	100	100	100	99.03
Number of ions on the basis 32																		
Si	11.81	11.72	12.05	11.89	11.80	11.98	11.91	12.06	12.14	12.03	11.98	11.51	11.89	11.7	11.63	11.82	11.77	11.8
Ti	0.01	0.02	0	0	0	0	0.01	0	0	0	0	0	0	0.01	0	0	0	0
Al	4.13	4.25	4.23	4.27	4.42	4.24	4.19	4.16	4.14	4.17	4.19	4.11	4.24	4.44	4.50	4.25	4.28	4.28
Fe^{2+}	0.10	0.08	0.01	0.01	0.01	0.01	0.01	0	0	0	0.11	0.28	0.11	0.04	0.03	0.03	0.02	0.05
Mn	0.01	0.01	0	0.01	0.01	0	0.01	0.01	0	0	0	0.01	0	0.01	0	0	0	0.01
Mg	0.08	0.11	0	0.01	0	0	0	0	0.01	0	0.07	0.19	0.10	0.01	0.03	0.02	0.01	0.02
Ca	0.14	0.19	0.05	0.04	0.07	0.03	0.02	0.02	0.01	0.02	0.03	0.04	0.02	0.05	0.03	0.02	0.02	0.03
Na	3.55	3.41	3.84	3.90	3.75	3.85	3.52	3.82	3.83	3.81	3.61	3.20	3.72	3.45	3.49	3.70	3.93	3.56
K	0.17	0.11	0.02	0.02	0.13	0.02	0.19	0.01	0.01	0.02	0.10	0.37	0.12	0.18	0.27	0.10	0.03	0.20
Sum	19.97	19.89	20.21	20.13	20.18	20.12	19.85	20.08	20.13	20.05	20.09	19.72	20.20	19.89	20	19.95	20.06	19.94
An	0.04	0.05	0.01	0.01	0.02	0.01	0.01	0	0	0.01	0.01	0.01	0	0.01	0.01	0.01	0	0.01
Al	0.92	0.92	0.98	0.99	0.95	0.99	0.94	0.99	1	0.99	0.97	0.89	0.96	0.94	0.92	0.97	0.99	0.94
Or	0.04	0.03	0.01	0.01	0.03	0	0.05	0	0	0.01	0.03	0.10	0.03	0.05	0.07	0.03	0.01	0.05
Charge	0.02	-0.01	0.89	0.41	0.54	0.58	0.08	0.62	0.88	0.52	0.62	-1	0.59	0	0	0	0	0

Tabela suplementar do manuscrito II. Tabela D: Análises por microssonda eletrônica de albita.

Continuação da TABELA SUPLEMENTAR DO MANUSCRITO II: D) Feldspatos - Albita

Sample	Ponto 15	Ponto 14	Ponto 15	Ponto 16	Ponto 17	Ponto 30	Ponto 31	Ponto 32	3pln_1b	4pln_1b	6pln_1	8pln_1	11pln_1	12pln_1	15pln_1	16pln_1	1pln_2	7pln_2	2pln_3	6pln_3
Point	DD 40	WL 13	WL 13	WL 13	WL 13	WL 13	WL 13	WL 13	DD 62	DD 62	DD 62	DD 62	DD 62	DD 62	DD 62	DD 62	DD 62	DD 62	DD 62	DD 62
SiO_2 (wt.%)	65.43	67.65	67.58	68.01	68.27	67.46	66.33	67.41	65.8	67.22	67.92	67.73	68.49	67.33	66.88	66.81	66.45	66.81	65.45	67.5
TiO_2	0	0.03	0.02	0.01	0	0.07	0.03	0.03	-0.01	0.01	0.05	0	0.02	0	0.01	0.04	0.05	0	0.02	0
Al_2O_3	21.06	19.83	20.1	19.67	19.92	20.06	20.26	20.25	22.61	21.06	20.02	20.74	20.39	21.98	21.09	22.00	21.54	21.98	22.19	20.80
FeO	0.78	0	0.10	0.07	0.06	0.11	0.28	0.24	0.26	0.04	0.06	0.22	0.04	0.07	0.05	0.15	0.08	0.12	0.16	0.09
MnO	0.02	0.09	0.02	0.01	0.01	0.01	0.02	0	0.01	0.02	-0.01	0.05	0.04	0.03	-0.03	0.04	0.05	-0.01	0.01	0.01
MgO	0.15	0.02	0.01	0.02	0.02	0.02	0.09	0.07	0.04	0.01	0.02	0.05	0	0.01	0.01	0.03	0.01	0.01	0.02	0
CaO	0.24	0.05	0.11	0.04	0.04	0.11	0.13	0.07	0.30	0.52	0.28	0.57	0.27	0.42	0.78	0.52	0.61	0.54	1.13	0.49
Na_2O	9.92	11.26	11.4	11.16	11.18	10.73	10.39	10.85	10.23	11.18	10.95	10.71	11.65	11.23	11.21	10.89	10.87	11.22	10.50	11.41
K_2O	1.05	0.03	0.03	0.05	0.04	0.31	0.67	0.26	1.01	0.13	0.04	0.85	0.05	0.36	0.11	0.31	0.77	0.30	0.50	0.17
Sum	98.65	98.96	99.35	98.98	99.52	98.85	98.20	99.18	100.25	100.21	99.33	100.91	100.94	101.43	100.10	100.8	100.43	100.98	99.98	100.47
Number of ions on the basis 32																				
Si	11.66	11.93	11.91	11.99	12.04	11.89	11.69	11.88	12.47	12.74	12.87	12.83	12.98	12.76	12.67	12.66	12.59	12.66	12.40	12.79
Ti	0	0	0	0	0	0.01	0	0	0	0	0.01	0	0	0	0	0.01	0.01	0	0	0
Al	4.42	4.12	4.18	4.09	4.14	4.17	4.21	4.21	5.05	4.70	4.47	4.63	4.55	4.91	4.71	4.91	4.81	4.91	4.96	4.65
Fe^{2+}	0.12	0	0.01	0.01	0.01	0.02	0.04	0.03	0.04	0.01	0.01	0.03	0.01	0.01	0.01	0.02	0.01	0.02	0.03	0.01
Mn	0	0.01	0	-0.01	0	0	0	0	0	0	0	0.01	0.01	0.01	0	0.01	0.01	0	0	0
Mg	0.04	0.01	0	0	0.01	0	0.02	0.02	0.01	0	0.01	0.01	0	0	0	0.01	0	0	0	0
Ca	0.04	0.01	0.02	0.01	0.01	0.02	0.02	0.01	0.06	0.10	0.06	0.12	0.05	0.08	0.16	0.11	0.12	0.11	0.23	0.10
Na	3.43	3.85	3.9	3.81	3.82	3.67	3.55	3.71	3.76	4.11	4.02	3.93	4.28	4.12	4.12	4.00	3.99	4.12	3.86	4.19
K	0.24	0.01	0.01	0.01	0.01	0.07	0.15	0.06	0.24	0.03	0.01	0.21	0.01	0.09	0.03	0.07	0.19	0.07	0.12	0.04
Sum	19.96	19.94	20.03	19.92	20.03	19.85	19.70	19.93	21.63	21.7	21.45	21.77	21.89	21.98	21.69	21.8	21.73	21.89	21.6	21.78
An	0.01	0	0.01	0	0	0.01	0.01	0	0.01	0.02	0.01	0.03	0.01	0.02	0.04	0.03	0.03	0.03	0.05	0.02
Al	0.92	1	0.99	0.99	1	0.98	0.95	0.98	0.92	0.97	0.98	0.92	0.98	0.96	0.96	0.96	0.93	0.96	0.92	0.97
Or	0.06	0	0	0	0	0.02	0.04	0.02	0.06	0.01	0	0.05	0	0.02	0.01	0.02	0.04	0.02	0.03	0.01
Charge	0	0	0.17	0.09	0.43	-0.07	-0.69	0.08	5.24	5.44	5.09	5.71	6.00	6.18	5.29	5.76	5.29	5.81	4.99	5.55

Tabela suplementar do manuscrito II. Continuação da Tabela D: Análises por microssonda eletrônica de albita.

Continuação da TABELA SUPLEMENTAR DO MANUSCRITO II: D) Feldspatos - Albita

Sample	7pln_3	8pln_3	10pln_3	12pln_3	17pln_3	1pln_4	3pln_4	8pln_4	9pln_4	11pln_4	12pln_4	16pln_4	3pln_1	6pln_1	8pln_1	9pln_1	12pln_1	13pln_1	16pln_1	18pln_1
Point	DD 62	DD 62	DD 62	DD 62	DD 62	DD 62	DD 62	DD 62	DD 62	DD 62	DD 62	DD 62	FM 13	FM 13	FM 13	FM 13	FM 13	FM 13	FM 13	FM 13
SiO_2 (wt.%)	67.44	66.51	66.66	67.67	68.07	67.19	68.28	67.61	68.06	68.02	64.66	67.34	68.46	67.16	68.91	68.64	68.21	68.19	68.79	67.33
TiO_2	0	0.01	0.04	0.04	-0.02	0.01	0.02	0.01	0.04	0.01	0.06	0.02	0	0.02	0	0.01	0	0	0.01	0
Al_2O_3	21.01	21.52	21.94	20.67	20.96	20.97	20.12	20.95	21.11	20.35	23.34	21.54	20.28	21.16	19.98	20.63	20.07	19.63	19.83	20.88
FeO	0.19	0.08	0.25	0.03	0.02	0.36	0.02	-0.04	0.04	-0.01	0.17	0.08	0.05	0.08	-0.01	0.03	0	0.01	0.01	0.03
MnO	-0.03	0	0.01	0.01	0.01	0.02	-0.01	0	-0.01	0.02	0	-0.02	0.02	0	-0.01	-0.02	-0.01	-0.02	-0.02	0
MgO	0.08	0.01	0.01	0.01	-0.03	0.15	0	-0.01	-0.01	0.01	0.05	0	-0.01	0.05	-0.01	0.01	-0.01	0.01	0	0.01
CaO	0.35	1.07	0.81	0.61	0.39	0.36	0.18	0.33	0.60	0.31	1.13	0.61	0.17	1.21	0.19	0.15	0.27	0.3	0.19	0.9
Na_2O	10.67	10.92	11.040	11.50	11.67	11.37	11.88	11.28	11.15	11.71	10.03	11.34	11.82	10.96	11.71	11.74	11.63	11.61	11.74	11.2
K_2O	0.21	0.17	0.52	0.04	0.06	0.14	0.03	0.03	0.48	0.01	1.01	0.14	0.05	0.12	0.07	0.08	0.03	0.07	0.06	0.09
Sum	99.91	100.30	101.29	100.58	101.11	100.57	100.53	100.17	101.47	100.45	100.45	101.05	100.85	100.75	100.82	101.27	100.21	99.81	100.6	100.43
Number of ions on the basis 32																				
Si	12.78	12.60	12.63	12.82	12.90	12.73	12.94	12.81	12.89	12.89	12.25	12.76	11.87	11.69	11.94	11.85	11.90	11.94	11.95	11.74
Ti	0	0	0.01	0.01	0	0	0	0	0.01	0	0.01	0	0	0	0	0	0	0	0	0
Al	4.69	4.81	4.90	4.62	4.68	4.68	4.49	4.68	4.72	4.55	5.21	4.81	4.15	4.34	4.08	4.2	4.13	4.05	4.06	4.29
Fe^{2+}	0.03	0.01	0.04	0	0	0.06	0	-0.01	0.01	0	0.03	0.01	0.01	0.01	0	0	0	0	0	0
Mn	-0.01	0	0	0	0	0	0	0	0	0	0	0	0	0	0	0	0	0	0	0
Mg	0.02	0	0	0	-0.01	0.04	0	0	0	0	0.01	0	0	0.01	0	0	0	0	0	0
Ca	0.07	0.22	0.16	0.12	0.08	0.07	0.04	0.07	0.12	0.06	0.23	0.12	0.03	0.23	0.03	0.03	0.05	0.06	0.04	0.17
Na	3.92	4.01	4.06	4.22	4.29	4.18	4.36	4.14	4.09	4.30	3.68	4.16	3.98	3.7	3.93	3.93	3.93	3.94	3.95	3.79
K	0.05	0.04	0.12	0.01	0.01	0.03	0.01	0.01	0.11	0	0.24	0.03	0.01	0.03	0.01	0.02	0.01	0.02	0.01	0.02
Sum	21.56	21.7	21.93	21.81	21.95	21.80	21.84	21.70	21.95	21.81	21.67	21.90	20.05	20.00	20.00	20.02	20.01	20.01	20.01	20.02
An	0.02	0.05	0.04	0.03	0.02	0.02	0.01	0.02	0.03	0.01	0.06	0.03	0.01	0.06	0.01	0.01	0.01	0.01	0.01	0.04
Al	0.97	0.94	0.93	0.97	0.98	0.98	0.99	0.98	0.95	0.99	0.89	0.96	0.99	0.94	0.99	0.99	0.99	0.98	0.99	0.95
Or	0.01	0.01	0.03	0	0	0.01	0	0	0.03	0	0.06	0.01	0	0.01	0	0	0	0	0	0.01
Charge	5.39	5.35	5.84	5.65	6.06	5.54	5.69	5.55	6.21	5.64	5.14	5.94	0	0	0	0	0	0	0	0

Tabela suplementar do manuscrito II. Continuação da Tabela D: Análises por microssonda eletrônica de albita.

Continuação da TABELA SUPLEMENTAR DO MANUSCRITO II: D) Feldspatos - Albita

Sample	19pln_1	23pln_1	24pln_1	28pln_1	29pln_1	30pln_1	31pln_1	32pln_2	33pln_2	34pln_2	35pln_2	36pln_2	37pln_2	38pln_2	39pln_2	40pln_2	42pln_2	43pln_2
Point	FM 13	FM 13	FM 13	FM 13	FM 13	FM 13	FM 13	FM 13	FM 13	FM 13	FM 13	FM 13	FM 13	FM 13	FM 13	FM 13	FM 13	FM 13
SiO_2 (wt.%)	68.17	67.5	68.58	68.41	68.66	68.60	68.00	68.81	68.11	67.99	68.69	67.99	68.43	67.51	69.22	68.35	67.59	68.49
TiO_2	0.02	0.01	0.01	0.01	0.01	0.02	0.01	0	0.01	0.02	0.01	0.02	-0.01	0.03	0.04	0.01	0.01	-0.01
Al_2O_3	19.94	20.08	20.09	19.76	19.85	19.99	19.96	19.56	20.21	20.18	19.74	20.37	20.01	20.03	19.45	20.26	20.27	19.88
FeO	0.05	0.01	0.09	0.11	0	0.01	0.04	0.02	0.01	-0.04	-0.04	0.06	0.01	0.05	0.05	0.03	0	-0.01
MnO	0.01	-0.03	0.01	-0.01	0.01	-0.01	-0.01	0	0.02	0	0	0	0.02	-0.01	-0.04	0	-0.01	0
MgO	-0.01	-0.01	-0.01	0	0	-0.01	-0.01	-0.02	0	0.01	0	0	-0.02	0	0	0.01	0	-0.01
CaO	0.17	0.69	0.13	0.21	0.07	0.06	0.26	0.19	0.32	0.18	0.06	0.15	0.34	0.26	0.03	0.15	0.22	0.05
Na_2O	11.76	11.37	11.6	11.78	11.63	11.90	11.67	11.82	11.72	11.36	11.84	11.66	11.4	11.66	11.98	11.71	11.67	11.84
K_2O	0.05	0.07	0.05	0.04	0.03	0.04	0.07	0.05	0.12	0.04	0.05	0.09	0.03	0.05	0.04	0.04	0.13	0.05
Sum	100.17	99.69	100.53	100.31	100.27	100.60	100.00	100.42	100.52	99.75	100.35	100.32	100.21	99.58	100.77	100.56	99.89	100.30
Number of ions on the basis 32																		
Si	11.9	11.85	11.92	11.93	11.95	11.92	11.89	11.97	11.86	11.89	11.96	11.85	11.92	11.86	12.00	11.88	11.84	11.93
Ti	0	0	0	0	0	0	0	0	0	0	0	0	0	0	0	0	0	0
Al	4.1	4.15	4.11	4.06	4.07	4.09	4.12	4.01	4.15	4.16	4.05	4.19	4.11	4.15	3.97	4.15	4.19	4.08
Fe^{2+}	0.01	0	0.01	0.02	0	0	0.01	0	0	-0.01	-0.01	0.01	0	0.01	0.01	0	0	0
Mn	0	0	0	0	0	0	0	0	0	0	0	0	0	0	-0.01	0	0	0
Mg	0	0	0	0	0	0	0	0	0	0	0	0	0	0	0	0	0	0
Ca	0.03	0.13	0.02	0.04	0.01	0.01	0.05	0.04	0.06	0.03	0.01	0.03	0.06	0.05	0.01	0.03	0.04	0.01
Na	3.98	3.87	3.91	3.98	3.93	4.01	3.96	3.99	3.96	3.85	4.00	3.94	3.85	3.97	4.03	3.95	3.96	4.00
K	0.01	0.02	0.01	0.01	0.01	0.01	0.02	0.01	0.03	0.01	0.01	0.02	0.01	0.01	0.01	0.01	0.03	0.01
Sum	20.04	20.01	19.98	20.04	19.98	20.04	20.04	20.02	20.06	19.95	20.02	20.03	19.95	20.05	20.02	20.02	20.06	20.03
An	0.01	0.03	0.01	0.01	0	0	0.01	0.01	0.01	0.01	0	0.01	0.02	0.01	0	0.01	0.01	0
Al	0.99	0.96	0.99	0.99	1	1	0.98	0.99	0.98	0.99	0.99	0.99	0.98	0.99	1	0.99	0.98	0.99
Or	0	0	0	0	0	0	0	0	0.01	0	0	0	0	0	0	0	0.01	0
Charge	0	0	0	0	0	0	0	0	0	0	0	0	0	0	0	0	0	0

Tabela suplementar do manuscrito II. Continuação da Tabela D: Análises por microssonda eletrônica de albita.

Continuação da TABELA SUPLEMENTAR DO MANUSCRITO II: D) Feldspatos - Albita

Sample	44pln_2	45pln_2	46pln_2	47pln_2	50pln_2	51pln_3	52pln_3	53pln_3	54pln_3	56pln_3	57pln_3	58pln_3	59pln_3	55pln_3	61pln_3	62pln_3	63pln_3	4clay1f
Point	FM 13	FM 13	FM 13	FM 13	FM 13	FM 13	FM 13	FM 13	FM 13	FM 13	FM 13	FM 13	FM 13	FM 13	FM 13	FM 13	FM 13	FM 13
SiO_2 (wt.%)	68.39	68.80	66.90	68.28	67.86	68.35	68.26	69.31	68.65	68.17	68.4	68.94	68.55	68.92	68.02	68.57	68.24	69.44
TiO_2	0.04	0	0.03	0.01	0.02	-0.02	0.02	-0.02	0.02	-0.01	0.01	0	0	-0.01	0.03	0.01	0.03	0.01
Al_2O_3	20.25	19.9	21.3	20.72	20.38	20.14	20.73	19.81	20	20.53	19.95	20.12	20.4	20.18	19.82	19.84	20.14	20.92
FeO	-0.01	0.04	0.09	0.03	0.02	0.05	0	0.03	0	0.01	0.05	0.02	0.03	0.01	0	0.03	0.02	0.40
MnO	-0.01	0.01	0.01	-0.04	0.02	-0.03	0.03	0.03	0.03	0.02	0.04	-0.02	0	-0.02	-0.01	-0.01	0	0.01
MgO	-0.02	-0.01	0.05	0	0	-0.02	0.01	0	0.01	0	0.01	0	0	0	0	0.01	-0.01	0.02
CaO	0.18	0.03	0.38	0.12	0.18	0.09	0.26	0.08	0.18	0.45	0.1	0.12	0.09	0.03	0.42	0.07	0.22	0.51
Na_2O	11.67	11.74	10.84	11.72	11.65	11.70	11.82	11.85	11.78	11.52	11.86	11.85	11.67	11.75	11.58	11.87	11.7	10.42
K_2O	0.05	0.03	0.59	0.16	0.04	0.09	0.06	0.05	0.04	0.09	0.05	0.04	0.04	0.06	0.04	0.03	0.05	0.49
Sum	100.54	100.52	100.19	101.00	100.17	100.36	101.18	101.13	100.72	100.79	100.48	101.08	100.77	100.91	99.90	100.41	100.40	102.48
Number of ions on the basis 32																		
Si	11.88	11.95	11.70	11.82	11.84	11.9	11.81	11.97	11.91	11.83	11.91	11.92	11.88	11.92	11.91	11.93	11.88	11.87
Ti	0.01	0	0	0	0	0	0	0	0	0	0	0	0	0	0	0	0	0
Al	4.15	4.07	4.39	4.23	4.19	4.13	4.23	4.03	4.09	4.20	4.09	4.10	4.17	4.12	4.09	4.07	4.13	4.21
Fe^{2+}	0	0.01	0.01	0	0	0.01	0	0	0	0	0.01	0	0	0	0	0	0	0.06
Mn	0	0	0	-0.01	0	0	0	0	0	0	0.01	0	0	0	0	0	0	0
Mg	-0.01	0	0.01	0	0	-0.01	0	0	0	0	0	0	0	0	0	0	0	0.01
Ca	0.03	0.01	0.07	0.02	0.03	0.02	0.05	0.01	0.03	0.08	0.02	0.02	0.02	0	0.08	0.01	0.04	0.09
Na	3.93	3.95	3.68	3.94	3.94	3.95	3.96	3.97	3.97	3.88	4.00	3.97	3.92	3.94	3.93	4.01	3.95	3.45
K	0.01	0.01	0.13	0.04	0.01	0.02	0.01	0.01	0.01	0.02	0.01	0.01	0.01	0.01	0.01	0.01	0.01	0.11
Sum	20.01	19.99	20.00	20.05	20.03	20.02	20.07	20.00	20.02	20.02	20.05	20.02	20.00	20.00	20.02	20.04	20.03	19.8
An	0.01	0	0.02	0.01	0.01	0	0.01	0	0.01	0.02	0	0.01	0	0	0.02	0	0.01	0.03
Al	0.99	1	0.95	0.99	0.99	0.99	0.98	0.99	0.99	0.97	0.99	0.99	0.99	1	0.98	1	0.99	0.95
Or	0	0	0.03	0.01	0	0.01	0	0	0	0	0	0	0	0	0	0	0	0.03
Charge	0	0	0	0	0	0	0	0	0	0	0	0	0	0	0	0	0	0

Tabela suplementar do manuscrito II. Continuação da Tabela D: Análises por microssonda eletrônica de albita.

Continuação da TABELA SUPLEMENTAR DO MANUSCRITO II: D) Feldspatos - Albita

Sample	60pln_3	5clay1	1pl1	2pl1	3pl1	4pl1c	5pl1	6pl1	7pl1	8pl1	9pl1	10pl1c	11pl1c	12pl2b	13pl2b	14pl2b	15pl2b	16pl2b	17pl2b	18pl2b	19pl2c	20pl2c	21pl2c	22pl2c
Point	FM 13	FM 13	WL 19	WL 19	WL 19	WL 19	WL 19	WL 19	WL 19	WL 19	WL 19	WL 19	WL 19	WL 19	WL 19	WL 19	WL 19	WL 19	WL 19	WL 19	WL 19	WL 19	WL 19	WL 19
SiO_2 (wt.%)	71.70	69.08	69.83	67.93	70.40	70.43	69.20	70.60	69.99	70.50	70.27	70.64	70.91	70.41	69.74	69.66	69.42	69.85	69.14	69.49	68.89	69.31	70.08	70.45
TiO_2	0	0.04	0.02	0.02	0.02	0.03	0.13	0.05	0.02	0	0.01	0.03	0.02	0.01	0.01	0.01	0	0.01	0	-0.01	0.02	0.01	0.02	0.02
Al_2O_3	20.83	20.22	20.48	20.10	20.26	20.47	21.79	20.58	20.26	20.64	20.27	20.40	20.38	20.29	20.19	20.56	20.04	20.40	20.07	20.31	20.23	20.45	20.40	20.62
FeO	0.06	0.39	0.07	0	0.07	0.05	0.5	0.25	0.19	0.05	0.15	0.05	0.02	0.05	0.07	0.02	-0.01	0.02	-0.02	0	0.05	0.02	0.01	0.04
MnO	-0.03	0.01	0.01	0.06	0.03	0.04	0.03	-0.05	0.02	0.04	0.10	0.06	0.02	-0.02	0.01	-0.02	-0.01	0.01	0.01	-0.02	0	0	0	-0.03
MgO	-0.01	0.01	-0.01	-0.01	-0.01	0.02	0.12	0.02	0	-0.01	0.01	0	0.01	0.02	0	0.01	0	-0.01	0	0.01	-0.02	-0.01	-0.01	-0.01
CaO	0.08	0.75	0.04	0.09	0.06	0.09	0.67	0.18	0.06	0.08	0.06	0.07	0.04	0.03	0.04	0.06	0.03	0.02	0.04	0.04	0.03	0.08	0.05	0.10
Na_2O	5.67	10.24	11.94	12.04	11.74	11.77	10.71	11.62	11.90	11.83	11.90	11.58	11.85	11.77	11.80	11.62	11.79	12.01	11.70	11.65	11.92	11.83	11.74	11.83
K_2O	0.04	1.12	0.04	0.02	0.03	0.03	0.62	0.25	0.03	0.05	0.03	0.04	0.04	0.03	0.02	0.07	0.01	0.02	0.06	0.03	0.05	0.04	0.05	0.03
Sum	98.35	101.80	102.39	100.07	102.59	103.04	103.72	103.64	102.25	102.95	102.79	103.06	103.32	102.35	101.89	101.85	101.16	102.46	100.79	101.61	101.33	101.80	102.24	103.17
Number of ions on the basis 32																								
Si	12.34	11.90	11.91	11.86	11.97	11.94	11.70	11.92	11.94	11.93	11.95	11.97	11.98	11.97	11.95	11.92	11.96	11.92	11.95	11.94	11.90	11.90	11.95	11.93
Ti	0	0	0	0	0	0	0.02	0.01	0	0	0	0	0	0	0	0	0	0	0	0	0	0	0	0
Al	4.23	4.11	4.12	4.14	4.06	4.09	4.34	4.10	4.07	4.12	4.06	4.07	4.06	4.07	4.08	4.15	4.07	4.11	4.09	4.11	4.12	4.14	4.10	4.12
Fe^{2+}	0.01	0.06	0.01	0	0.01	0.01	0.07	0.04	0.03	0.01	0.02	0.01	0	0.01	0.01	0	0	0	0	0	0.01	0	0	0.01
Mn	0	0	0	0.01	0	0.01	0	-0.01	0	0.01	0.01	0.01	0	0	0	0	0	0	0	0	0	0	0	0
Mg	0	0	0	0	0	0	0.03	0.01	0	0	0	0	0	0	0	0	0	0	0	0	0	0	0	0
Ca	0.02	0.14	0.01	0.02	0.01	0.02	0.12	0.03	0.01	0.01	0.01	0.01	0.01	0.01	0.01	0.01	0	0	0.01	0.01	0.01	0.01	0.01	0.02
Na	1.89	3.42	3.95	4.08	3.87	3.87	3.51	3.81	3.93	3.88	3.92	3.81	3.88	3.88	3.92	3.85	3.94	3.97	3.92	3.88	3.99	3.94	3.88	3.88
K	0.01	0.25	0.01	0	0.01	0.01	0.13	0.05	0.01	0.01	0.01	0.01	0.01	0.01	0	0.01	0	0	0.01	0.01	0.01	0.01	0.01	0.01
Sum	18.49	19.87	20.01	20.11	19.94	19.95	19.93	19.95	19.99	19.96	19.99	19.89	19.94	19.94	19.97	19.94	19.98	20.01	19.97	19.95	20.04	20.00	19.95	19.95
An	0.01	0.04	0	0	0	0	0.03	0.01	0	0	0	0	0	0	0	0	0	0	0	0	0	0	0	0
Al	0.99	0.90	1	0.99	1	0.99	0.93	0.98	1	0.99	1	0.99	1	1	1	0.99	1	1	0.99	1	1	0.99	0.99	0.99
Or	0	0.06	0	0	0	0	0.04	0.01	0	0	0	0	0	0	0	0	0	0	0	0	0	0	0	0
Charge	0	0	0	0	0	0	0	0	0	0	0	0	0	0	0	0	0	0	0	0	0	0	0	0

Tabela suplementar do manuscrito II. Continuação da Tabela D: Análises por microssonda eletrônica de albita.

Continuação da TABELA SUPLEMENTAR DO MANUSCRITO II: D) Feldspatos - Albita

Sample	32_px	33_px	34_px	35_px	27_ve	28_ve	29_ve	30_ve	31_ve	5clat	1_chl	12clat	20cla
Point	WL 19	WL 19	WL 19	WL 19	RFM 48	RFM 48	RFM 48	RFM 48	RFM 48	RFM 48		RFM 48	RFM 48
SiO_2 (wt.%)	68.42	70.18	70.76	70.27	69.23	69.17	66.09	68.39	71.22	72.02		71.34	70.87
TiO_2	0	0	0.02	-0.01	0.01	0.02	0.03	0	0	0.01		0	0.02
Al_2O_3	20.04	20.32	20.26	20.16	20.48	20.45	20.25	20.08	21.01	20.51		20.32	20.41
FeO	0.11	0.03	0.05	0.05	0.26	0.43	2.94	0.24	0.5	0.59		0.42	0.19
MnO	0.02	0.03	0.02	0.02	0	-0.04	0.01	-0.01	-0.01	-0.01		0.01	0.04
MgO	-0.01	0.01	-0.01	-0.01	0	0.01	1.42	0.02	0.04	0		0	0.01
CaO	0.03	0.03	0.04	0.06	0.07	0.11	0.04	0.05	0.07	0.06		0.07	0.04
Na_2O	11.91	11.89	11.86	11.83	11.89	11.91	10.60	12.05	11.58	11.94		12.11	12.10
K_2O	0.04	0.04	0.06	0.02	0.05	0.10	0.16	0.02	0.31	0.09		0.09	0.04
Sum	100.50	102.31	102.95	102.43	102.09	102.19	101.31	100.82	104.63	105.01		104.35	103.59
Number of ions on the basis 32													
Si	11.90	11.95	11.98	11.97	11.88	11.86	11.55	11.88	11.90	11.97		11.96	11.95
Ti	0	0	0	0	0	0	0	0	0	0		0	0
Al	4.11	4.08	4.04	4.05	4.14	4.13	4.17	4.11	4.14	4.02		4.02	4.06
Fe^{2+}	0.02	0	0.01	0.01	0.04	0.06	0.43	0.03	0.07	0.08		0.06	0.03
Mn	0	0	0	0	0	-0.01	0	0	0	0		0	0.01
Mg	0	0	0	0	0	0	0.37	0	0.01	0		0	0
Ca	0	0	0.01	0.01	0.01	0.02	0.01	0.01	0.01	0.01		0.01	0.01
Na	4.02	3.93	3.89	3.91	3.96	3.96	3.59	4.06	3.75	3.85		3.94	3.95
K	0.01	0.01	0.01	0	0.01	0.02	0.04	0	0.07	0.02		0.02	0.01
Sum	20.06	19.98	19.95	19.96	20.03	20.06	20.17	20.10	19.94	19.95		20.01	20.01
An	0	0	0	0	0	0.01	0	0	0	0		0	0
Al	1	1	1	1	0.99	0.99	0.99	1	0.98	0.99		0.99	1
Or	0	0	0	0	0	0.01	0.01	0	0.02	0		0	0
Charge	0	0	0	0	0	0	0	0	0	0		0	0

Tabela suplementar do manuscrito II. Continuação da Tabela D: Análises por microssonda eletrônica de albita.

Continuação da TABELA SUPLEMENTAR DO MANUSCRITO II: D) Feldspatos - K-feldspato e andesina-labradorita.

Sample	13pln_1	21pln_1	3pln_2	5pln_2	16pln_3	Sample	10pln_1	11pln_1	14pln_1	21pln_1	41pln_2	8pln_2	10pln_2	12pln_2	18pln_1	20pln1	10pln4	55pl1	56pl1	57pl1	58pl1
Point	DD 62	DD 62	DD 62	DD 62	DD 62	Point	FM 13	FM 13	FM 13	FM 13	FM 13	DD 62	DD 62	DD 62	DD 62	DD 62	DD 62	FM 25	FM 25	FM 25	FM 25
SiO_2 (wt.%)	63.38	53.79	55.24	62.48	63.33	SiO_2	56.70	55.14	54.86	54.52	55.46	55.74	54.73	55.45	53.71	54.08	55.48	56.67	56.77	56.52	56.75
TiO_2	0.09	0.16	0.17	0.05	0.01	TiO_2	0.08	0.05	0.10	0.09	0.09	0.05	0.07	0.09	0.07	0.06	0.09	0.09	0.10	0.10	0.11
Al_2O_3	18.42	19.44	19.46	18.77	18.26	Al_2O_3	25.81	27.01	27.33	27.57	27.00	27.02	27.77	27.16	28.07	27.86	27.11	27.28	26.91	26.97	26.85
FeO	0.19	0	0	0.1	0	FeO	0.53	0.54	0.52	0.55	0.47	0.59	0.60	0.59	0.58	0.55	0.52	0.68	0.56	0.54	0.61
MnO	0.07	-0.06	0.01	-0.01	-0.02	MnO	-0.01	0.01	0.02	-0.04	0.03	0.01	0.01	-0.02	0.01	0	0	0	0.03	-0.05	0
MgO	0	-0.02	0.01	-0.01	0.01	MgO	0.06	0.07	0.08	0.07	0.06	0.08	0.08	0.08	0.07	0.09	0.06	0.11	0.11	0.10	0.11
CaO	0.10	0	-0.02	-0.02	-0.03	CaO	8.74	9.99	10.49	10.80	9.47	9.71	10.59	9.89	10.69	10.76	9.85	9.71	9.46	9.65	9.50
Na_2O	0.50	0.23	0.16	0.32	0.05	Na_2O	6.10	5.21	4.83	4.88	5.38	5.35	5.10	5.33	4.93	4.78	5.32	5.41	5.50	5.47	5.60
K_2O	15.76	12	12.96	15.99	16.33	K_2O	0.64	0.76	0.68	0.63	0.89	0.81	0.67	0.80	0.70	0.66	0.80	0.58	0.60	0.57	0.58
Sum	98.51	85.54	87.99	97.67	97.94	Sum	98.64	98.79	98.91	99.07	98.85	99.36	99.62	99.38	98.82	98.84	99.24	100.54	100.04	99.86	100.10
Number of ions on the basis 32						Number of ions on the basis 32															
Si	12.01	10.19	10.47	11.84	12	Si	10.35	10.09	10.02	9.96	10.13	10.56	10.37	10.51	10.18	10.25	10.51	10.16	10.22	10.19	10.21
Ti	0.01	0.02	0.02	0.01	0	Ti	0.01	0.01	0.01	0.01	0.01	0.01	0.01	0.01	0.01	0.01	0.01	0.01	0.01	0.01	0.01
Al	4.11	4.34	4.35	4.19	4.08	Al	5.55	5.83	5.89	5.94	5.81	6.03	6.20	6.07	6.27	6.22	6.05	5.77	5.71	5.73	5.70
Fe^{2+}	0.03	0	0	0.02	0	Fe^{2+}	0.08	0.08	0.08	0.08	0.07	0.09	0.09	0.09	0.09	0.09	0.08	0.1	0.08	0.08	0.09
Mn	0.01	-0.01	0	0	0	Mn	0	0	0	-0.01	0.01	0	0	0	0	0	0	0	0	-0.01	0
Mg	0	-0.01	0	0	0	Mg	0.02	0.02	0.02	0.02	0.02	0.02	0.02	0.02	0.02	0.03	0.02	0.03	0.03	0.03	0.03
Ca	0.02	0	0	0	-0.01	Ca	1.71	1.96	2.05	2.11	1.85	1.97	2.15	2.01	2.17	2.18	2.00	1.87	1.82	1.86	1.83
Na	0.18	0.09	0.06	0.12	0.02	Na	2.16	1.85	1.71	1.73	1.91	1.97	1.88	1.96	1.81	1.76	1.95	1.88	1.92	1.91	1.96
K	3.81	2.9	3.13	3.86	3.95	K	0.15	0.18	0.16	0.15	0.21	0.20	0.16	0.19	0.17	0.16	0.19	0.13	0.14	0.13	0.13
Sum	20.19	17.53	18.03	20.03	20.04	Sum	20.02	20.01	19.95	20.00	20.01	20.85	20.89	20.86	20.72	20.69	20.83	19.95	19.94	19.95	19.97
An	0.01	0	0	0	0	An	0.43	0.49	0.52	0.53	0.47	0.48	0.51	0.48	0.52	0.53	0.48	0.48	0.47	0.48	0.47
Al	0.05	0.03	0.02	0.03	0	Al	0.54	0.46	0.44	0.43	0.48	0.48	0.45	0.47	0.44	0.43	0.47	0.48	0.49	0.49	0.50
Or	0.95	0.97	0.98	0.97	1	Or	0.04	0.04	0.04	0.04	0.05	0.05	0.04	0.05	0.04	0.04	0.05	0.03	0.04	0.03	0.03
Charge	0.54	-7.16	-5.81	-0.05	0.18	Charge	0	0	0	0	0	2.71	2.69	2.67	2.09	2.19	2.61	0	0	0	0

Tabela suplementar do manuscrito II. Continuação da Tabela D: Análises por microssonda eletrônica de K-feldspato e andesina-labradorita.

Continuação da TABELA SUPLEMENTAR DO MANUSCRITO II: E) Clorita

Chlorite of filled pores (sulfide bearing rocks)									Chlorite as alteration of residual augite (sulfide bearing rocks)									
Sample	RFM 48	RFM 48	RFM 48	RFM 48	RFM 48	RFM 48	RFM 48	RFM 48	WL13	WL13	WL13	WL13	WL13	WL13	WL13	WL13	WL13	WL13
Point	11cl	23_ve	13clat	14clat	15clat	17clat	19clat	21clat	1 / 1 .	Ponto 11	Ponto 12	13 / 1 .	Ponto 22	Ponto 23	24 / 1 .	25 / 1 .	26 / 1 .	27 / 1 .
SiO_2	27.54	26.45	27.88	28.02	28.41	28.08	27.65	27.59	27.83	27.05	27.44	27.85	28.6	26.15	27.50	28.24	27.14	26.72
TiO_2	0.02	0	0.02	0.01	0.03	0.02	0.04	0.02	0.03	0.05	0.05	0.04	0.02	0.01	0.01	0.06	0.06	0.09
Al_2O_3	19.76	21.19	19.47	19.06	18.73	19.51	21.73	21.53	18.70	19.34	18.56	18.03	18.92	17.70	17.79	16.95	17.71	18.66
FeO	29.53	30.71	29.89	30.46	30.11	29.94	27.84	28.33	29.58	26.11	28.50	30.01	23.39	29.41	24.98	28.62	29.72	28.77
MnO	0.09	0.08	0.05	0.06	0.03	0.07	0.03	0.05	0.09	0.19	0.13	0.06	0.21	0.10	0.09	0.11	0.12	0.11
MgO	11.10	10.01	11.10	10.85	10.62	11.15	11.28	10.46	10.20	10.14	10.08	9.52	12.44	9.090	10.80	9.74	9.25	9.29
CaO	0.05	0.02	0.08	0.09	0.13	0.08	0.08	0.05	0.19	0.23	0.20	0.22	0.22	0.22	0.25	0.22	0.23	0.19
Na_2O	0	0.01	0.04	0.05	0.03	0.03	0.02	0.02	0.03	0.03	0.04	0.03	0	0.04	0.01	0.01	0.03	0.03
K_2O	0	0.01	0.05	0.03	0.21	0.05	0.02	0.18	0.04	0.11	0.10	0.09	0.20	0.03	0.10	0.14	0.07	0.08
Sum	88.09	88.49	88.59	88.64	88.30	88.92	88.69	88.23	86.70	83.26	85.09	85.85	84.01	82.76	81.52	84.09	84.33	83.94
Number of ions on the basis 28																		
Si	5.83	5.62	5.88	5.92	6.01	5.89	5.73	5.76	5.99	5.96	6.00	6.07	6.12	5.95	6.15	6.24	6.04	5.94
Al^{iv}	2.17	2.38	2.12	2.08	1.99	2.11	2.27	2.24	2.01	2.04	2.00	1.93	1.88	2.05	1.85	1.76	1.96	2.06
Sum^{iv}	8	8	8	8	8	8	8	8	8	8	8	8	8	8	8	8	8	8
Al^{vi}	2.79	2.95	2.75	2.70	2.72	2.75	3.08	3.11	2.77	3.03	2.82	2.75	2.95	2.73	2.89	2.7	2.73	2.87
Ti	0	0	0	0	0	0	0.01	0	0	0.01	0.01	0.01	0	0	0	0.01	0.01	0.01
Fe^{3+}	0.35	0.31	0.33	0.33	0.38	0.35	0.45	0.46	0.42	0.54	0.44	0.45	0.57	0.37	0.57	0.52	0.42	0.45
Fe^{2+}	4.88	5.14	4.94	5.05	4.95	4.90	4.38	4.48	4.91	4.27	4.77	5.02	3.61	5.23	4.11	4.77	5.11	4.90
Mn	0.02	0.02	0.01	0.01	0.01	0.01	0.01	0.01	0.02	0.04	0.02	0.01	0.04	0.02	0.02	0.02	0.02	0.02
Mg	3.50	3.17	3.49	3.42	3.35	3.49	3.49	3.26	3.27	3.33	3.28	3.09	3.97	3.09	3.60	3.21	3.07	3.08
Ca	0.01	0	0.02	0.02	0.03	0.02	0.02	0.01	0.04	0.06	0.05	0.05	0.05	0.05	0.06	0.05	0.06	0.04
Na	0	0.01	0.04	0.04	0.03	0.02	0.02	0.02	0.03	0.02	0.03	0.02	0	0.04	0.01	0.01	0.02	0.03
K	0	0	0.03	0.02	0.11	0.02	0.01	0.09	0.02	0.06	0.06	0.05	0.11	0.02	0.05	0.08	0.04	0.05
OH	16	16	16	16	16	16	16	16	16	16	16	16	16	16	16	16	16	16
R^{2+}	8.40	8.33	8.43	8.48	8.30	8.40	7.87	7.75	8.20	7.64	8.07	8.13	7.62	8.33	7.72	8.00	8.20	8.00
R^{3+}	3.14	3.27	3.08	3.04	3.09	3.10	3.53	3.58	3.19	3.57	3.26	3.20	3.52	3.11	3.46	3.22	3.15	3.32
4Si	1.46	1.40	1.47	1.48	1.50	1.47	1.43	1.44	1.50	1.49	1.50	1.52	1.53	1.49	1.54	1.56	1.51	1.49
$3R^{2+}$	2.80	2.78	2.81	2.83	2.77	2.80	2.62	2.58	2.73	2.55	2.69	2.71	2.54	2.78	2.57	2.67	2.73	2.67
Fe/Fe+Mg	0.58	0.62	0.59	0.60	0.60	0.58	0.56	0.58	0.60	0.56	0.59	0.62	0.48	0.63	0.53	0.60	0.62	0.61
M^+	0.02	0.02	0.10	0.10	0.20	0.08	0.06	0.13	0.14	0.19	0.18	0.18	0.21	0.16	0.18	0.19	0.17	0.16
Charge	0.09	0.09	0.07	0.08	0	0.07	0.12	0.06	0.09	0.10	0.07	0.07	0.05	0.08	0.10	0.05	0.08	0.08

Tabela suplementar do manuscrito II. Tabela E: Análises por microssonda eletrônica de clorita.

Continuação da TABELA SUPLEMENTAR DO MANUSCRITO II: E) Clorita

Representative chlorite compositions of matrix of andesite dike								
Sample	DD 62	DD 62	DD 62	DD 62	DD 62	DD 62	DD 62	DD 62
Point	2clay1	3clay1	5clay1	2clay1	3clay1	4clay2	12clay	14clay
SiO_2	30.94	30.06	29.67	29.64	31.01	29.73	28.82	30.36
TiO_2	0.01	0.02	0.04	0.05	0.04	0.02	0.03	0.03
Al_2O_3	12.40	11.95	11.81	13.90	13.44	12.61	15.01	14.97
FeO	28.91	30.68	29.79	28.52	27.17	29.57	29.41	25.80
MnO	0.19	0.19	0.18	0.28	0.32	0.19	0.44	0.42
MgO	14.73	14.09	13.93	14.01	15.04	14.14	13.73	15.08
CaO	0.19	0.11	0.14	0.24	0.28	0.15	0.17	0.54
Na_2O	-0.01	0	0.02	0.03	0.02	0.03	0.02	0.01
K_2O	0.09	0.04	0.04	0.08	0.09	0.02	0.06	0.09
Sum	87.45	87.14	85.6	86.76	87.41	86.47	87.7	87.28
Number of ions on the basis 28								
Si	6.62	6.55	6.56	6.40	6.56	6.49	6.20	6.39
Al^{iv}	1.38	1.45	1.44	1.60	1.44	1.51	1.80	1.61
Sum^{iv}	8	8	8	8	8	8	8	8
Al^{vi}	1.76	1.63	1.65	1.95	1.93	1.74	2.01	2.13
Ti	0	0	0.01	0.01	0.01	0	0	0
Fe^{3+}	0.20	0.10	0.12	0.19	0.27	0.12	0.11	0.28
Fe^{2+}	4.97	5.49	5.39	4.96	4.54	5.27	5.18	4.26
Mn	0.03	0.04	0.03	0.05	0.06	0.04	0.08	0.07
Mg	4.70	4.58	4.59	4.51	4.74	4.60	4.40	4.73
Ca	0.04	0.03	0.03	0.06	0.06	0.04	0.04	0.12
Na	0	0	0.01	0.02	0.01	0.03	0.01	0
K	0.05	0.02	0.02	0.05	0.05	0.01	0.04	0.05
OH	16	16	16	16	16	16	16	16
R^{2+}	9.70	10.11	10.02	9.52	9.34	9.91	9.66	9.06
R^{3+}	1.96	1.72	1.77	2.13	2.20	1.87	2.12	2.41
4Si	1.65	1.64	1.64	1.60	1.64	1.62	1.55	1.60
$3R^{2+}$	3.23	3.37	3.34	3.17	3.11	3.30	3.22	3.02
Fe/Fe+Mg	0.51	0.55	0.54	0.52	0.49	0.53	0.54	0.47
M^+	0.13	0.08	0.11	0.18	0.19	0.11	0.13	0.30
Charge	-0.01	0	0	0	0	0.01	-0.01	0.01

Tabela suplementar do manuscrito II. Continuação da Tabela E: Análises por microssonda eletrônica de clorita.

Continuação da TABELA SUPLEMENTAR DO MANUSCRITO II: F) Esmectita

Sample	77	77	77	77	77	77	77	77	77	77	77	77	77	77	77	77	77
Point	1cla	2cla	3cla	4cla	5cla	6cla	9cla	10cla	11cla	13cla	14cla	15cla	16cla	17cla	18cla	19cla	23cla
SiO_2	42.12	40.31	40.18	43.54	42.48	42.60	42.74	38.87	40.46	42.32	45.29	38.99	43.80	39.63	41.91	40.71	42.79
TiO_2	0.01	0.01	0.02	0.03	0.01	0	0.05	0.04	0.02	0.02	0.03	0.05	0.02	0.01	0.02	0.04	0.03
Al_2O_3	8.79	8.62	8.77	8.42	8.56	6.41	8.38	8.40	8.11	9.29	7.42	8.71	7.75	8.62	7.64	7.58	6.95
FeO	13.19	12.83	12.73	12.33	12.29	9.82	12.10	12.90	11.90	12.33	12.22	12.20	10.96	11.10	10.40	10.35	10.09
MnO	0.15	0.15	0.13	0.12	0.16	0.12	0.15	0.20	0.11	0.16	0.20	0.18	0.12	0.12	0.13	0.14	0.12
MgO	20.70	19.45	19.97	20.75	20.31	18.44	20.68	18.66	18.70	21.23	20.30	18.50	19.94	18.67	18.93	18.62	18.84
CaO	1.09	1.14	1.17	1.24	1.28	1.62	1.25	1.36	1.80	1.33	1.74	1.49	1.79	1.69	1.49	1.44	1.56
Na_2O	0.07	0.15	0.05	0.07	0.09	0.14	0.06	0.05	0.08	0.08	0.09	0.10	0.08	0.06	0.09	0.10	0.13
K_2O	0.19	0.18	0.25	0.36	0.26	0.15	0.13	0.16	0.14	0.12	0.11	0.15	0.10	0.32	0.12	0.15	0.14
H_2O	3.90	3.74	3.76	3.95	3.88	3.66	3.90	3.63	3.69	3.95	3.99	3.63	3.88	3.65	3.71	3.63	3.72
Sum	90.22	86.58	87.03	90.83	89.33	82.97	89.44	84.26	85.02	90.83	91.39	83.98	88.45	83.86	84.44	82.75	84.35
Number of ions on the basis 22																	
Si	6.47	6.46	6.41	6.61	6.56	6.98	6.58	6.43	6.58	6.43	6.81	6.44	6.77	6.52	6.77	6.73	6.90
Al^{iv}	1.53	1.54	1.59	1.39	1.44	1.02	1.42	1.57	1.42	1.57	1.19	1.56	1.23	1.48	1.23	1.27	1.10
Sum^{iv}	8	8	8	8	8	8	8	8	8	8	8	8	8	8	8	8	8
Al^{vi}	0.07	0.09	0.06	0.11	0.12	0.22	0.10	0.07	0.13	0.09	0.12	0.14	0.18	0.19	0.23	0.20	0.22
Ti	0	0	0	0	0	0	0.01	0	0	0	0	0.01	0	0	0	0	0
Fe^{2+}	1.70	1.72	1.70	1.56	1.59	1.35	1.56	1.78	1.62	1.57	1.54	1.69	1.42	1.53	1.41	1.43	1.36
Mn	0.02	0.02	0.02	0.02	0.02	0.02	0.02	0.03	0.02	0.02	0.02	0.02	0.02	0.02	0.02	0.02	0.02
Mg	4.74	4.65	4.75	4.69	4.68	4.5	4.75	4.6	4.53	4.81	4.55	4.56	4.59	4.58	4.56	4.59	4.53
Ca	0.18	0.20	0.20	0.20	0.21	0.28	0.21	0.24	0.31	0.22	0.28	0.26	0.30	0.30	0.26	0.26	0.27
Na	0.02	0.05	0.02	0.02	0.03	0.04	0.02	0.02	0.02	0.02	0.03	0.03	0.02	0.02	0.03	0.03	0.04
K	0.04	0.04	0.05	0.07	0.05	0.03	0.03	0.03	0.03	0.02	0.02	0.03	0.02	0.07	0.02	0.03	0.03
OH	4	4	4	4	4	4	4	4	4	4	4	4	4	4	4	4	4
R^{2+}	6.46	6.39	6.47	6.27	6.29	5.87	6.32	6.41	6.17	6.40	6.11	6.27	6.03	6.12	5.98	6.04	5.91
R^{3+}	0.07	0.09	0.06	0.11	0.12	0.22	0.10	0.07	0.13	0.09	0.12	0.14	0.18	0.19	0.23	0.2	0.22
4Si	1.62	1.62	1.60	1.65	1.64	1.74	1.64	1.61	1.64	1.61	1.70	1.61	1.69	1.63	1.69	1.68	1.73
$3R^{2+}$	2.15	2.13	2.16	2.09	2.10	1.96	2.11	2.14	2.06	2.13	2.04	2.09	2.01	2.04	1.99	2.01	1.97
M^{+}	0.42	0.48	0.47	0.49	0.50	0.64	0.46	0.53	0.68	0.48	0.61	0.59	0.64	0.68	0.57	0.57	0.61
Charge	-0.04	-0.04	-0.05	-0.07	-0.05	-0.03	-0.03	-0.03	-0.03	-0.02	-0.02	-0.03	-0.02	-0.07	-0.02	-0.03	-0.03

Tabela suplementar do manuscrito II. Tabela F: Análises por microssonda eletrônica de esmectita.

Continuação da TABELA SUPLEMENTAR DO MANUSCRITO II: G) Interestratificados clorita/esmectita

Sample	FM 25	FM 25	FM 25	FM 25	FM 25	FM 25	FM 25	FM 25	FM 25	FM 25	FM 25	FM 25	FM 25	FM 25	FM 25
Point	1_cla	3_cla	4_cla	5_cla	6_cla	9_cla	11_cla	12_cla	14_cla	15_cla	16_cla	17_cla	19_cla	20_cla	22_cla
SiO_2	34.70	33.78	32.22	33.17	33.68	33.33	30.25	33.49	35.06	34.55	30.14	31.72	31.85	32.53	33.58
TiO_2	0	0.02	0.02	0.02	-0.01	0	0.03	0	0.05	0.02	0.05	0.03	0.01	0.01	0.02
Al_2O_3	12.17	11.96	12.59	11.95	12.56	13.14	8.32	12.56	11.98	12.76	12.82	13.20	12.76	13.16	11.38
FeO	20.17	21.07	21.38	19.91	21.16	22.40	16.01	20.94	20.33	21.22	21.85	21.88	21.76	21.55	17.91
MnO	0.15	0.21	0.25	0.24	0.17	0.20	0.13	0.28	0.18	0.19	0.18	0.15	0.21	0.20	0.14
MgO	20.22	20.05	19.31	18.43	19.55	19.47	17.86	19.60	20.93	20.77	17.99	18.28	18.40	19.24	20.45
CaO	0.49	0.39	0.35	0.44	0.42	0.38	0.63	0.45	0.73	0.60	0.43	0.38	0.40	0.40	0.56
Na_2O	0.07	0.05	0.05	0.05	0.07	0.05	0.04	0.08	0.12	0.07	0.06	0.07	0	0.05	0.06
K_2O	0.05	0.02	0.01	0.05	0.05	0.01	0.03	0.03	0.03	0.08	0.03	0.04	0.01	0.05	0.02
Sum	88.01	87.55	86.19	84.25	87.65	88.98	73.30	87.42	89.40	90.27	83.55	85.75	85.41	87.18	84.12
Number of ions on the basis 28															
Si	6.95	6.86	6.69	6.95	6.83	6.71	7.23	6.81	6.93	6.80	6.53	6.64	6.69	6.67	6.98
Al^{iv}	1.05	1.14	1.31	1.05	1.17	1.29	0.77	1.19	1.07	1.20	1.47	1.36	1.31	1.33	1.02
Sum^{iv}	8	8	8	8	8	8	8	8	8	8	8	8	8	8	8
Al^{vi}	1.84	1.75	1.79	1.93	1.85	1.84	1.59	1.84	1.74	1.78	1.81	1.91	1.87	1.87	1.79
Ti	0	0	0	0	0	0	0	0	0.01	0	0.01	0	0	0	0
Fe^{3+}	0.43	0.34	0.27	0.49	0.37	0.30	0.46	0.35	0.36	0.31	0.18	0.30	0.32	0.29	0.43
Fe^{2+}	2.95	3.24	3.45	3.00	3.22	3.47	2.74	3.21	3.00	3.18	3.77	3.53	3.51	3.40	2.68
Mn	0.03	0.04	0.04	0.04	0.03	0.03	0.03	0.05	0.03	0.03	0.03	0.03	0.04	0.03	0.03
Mg	6.04	6.07	5.98	5.76	5.91	5.84	6.37	5.94	6.17	6.10	5.81	5.70	5.76	5.88	6.34
Ca	0.10	0.08	0.08	0.10	0.09	0.08	0.16	0.10	0.16	0.13	0.1	0.09	0.09	0.09	0.12
Na	0.05	0.04	0.04	0.04	0.05	0.04	0.04	0.06	0.09	0.06	0.05	0.06	0	0.04	0.05
K	0.02	0.01	0.01	0.03	0.03	0.01	0.02	0.01	0.02	0.04	0.02	0.02	0.01	0.03	0.01
R^{2+}	9.01	9.35	9.47	8.81	9.16	9.35	9.13	9.20	9.19	9.31	9.61	9.26	9.31	9.32	9.05
R^{3+}	2.27	2.09	2.06	2.42	2.22	2.15	2.06	2.20	2.10	2.09	2	2.21	2.19	2.17	2.22
4Si	1.74	1.72	1.67	1.74	1.71	1.68	1.81	1.70	1.73	1.70	1.63	1.66	1.67	1.67	1.75
$3R^{2+}$	3.00	3.12	3.16	2.94	3.05	3.12	3.04	3.07	3.06	3.10	3.20	3.09	3.1	3.11	3.02
M^+	0.29	0.22	0.21	0.27	0.27	0.21	0.38	0.27	0.42	0.35	0.27	0.25	0.18	0.24	0.31
Charge	0.05	0.05	0.04	0.06	0.04	0.05	0.04	0.05	0.05	0.02	0.02	0.04	0.05	0.03	0.06

Tabela suplementar do manuscrito II. Tabela G: Análises por microssonda eletrônica de interestratificados clorita/esmectita.

Continuação da TABELA SUPLEMENTAR DO MANUSCRITO II: G) Interestratificados clorita/esmectita

Sample	FM 25	FM 25	FM 25	FM 25	FM 25	FM 25	FM 25	FM 25	WL 19	WL 19	WL 19	WL 19	WL 19	WL 19
Point	23_cla	24_cla	25_cla	26_cla	27_cla	28_cla	30_cla	31_cla	24_cla	25_cla	28_cla	29_cla	30_cla	31_cla
SiO_2	34.01	32.40	32.97	32.92	35.29	32.25	32.35	32.15	31.29	32.41	31.50	31.29	31.43	31.88
TiO_2	0	0.01	0.01	0.01	0.02	0.02	-0.01	0.01	0.03	0.02	0.08	0.14	0.06	0.03
Al_2O_3	12.69	12.80	13.08	13.37	12.18	12.59	12.59	12.56	15.59	14.60	15.58	15.89	14.35	15.85
FeO	21.18	21.77	21.77	21.62	20.9	21.02	21.17	21.87	17.49	16.10	17.4	17.01	18.18	16.93
MnO	0.21	0.20	0.19	0.23	0.23	0.21	0.21	0.21	0.35	0.37	0.36	0.34	0.32	0.41
MgO	19.94	19.17	19.43	19.16	20.88	19.23	19.06	18.83	17.90	18.89	18.43	18.30	18.47	18.66
CaO	0.48	0.39	0.38	0.47	0.49	0.41	0.21	0.25	0.29	0.23	0.25	0.28	0.32	0.29
Na_2O	0.08	0.04	0.06	0.08	0.06	0.06	0.06	0.05	0.07	0.08	0.08	0.03	0.06	0.08
K_2O	0.01	0.03	0.04	0.04	0.03	0.03	0.09	0.08	0.03	0.03	0.05	0.05	0.03	0.03
Sum	88.60	86.81	87.92	87.89	90.09	85.82	85.74	86.00	83.04	82.73	83.75	83.33	83.23	84.16
Number of ions on the basis 28														
Si	6.82	6.69	6.70	6.69	6.93	6.71	6.74	6.71	6.56	6.75	6.55	6.52	6.62	6.56
Al^{iv}	1.18	1.31	1.30	1.31	1.07	1.29	1.26	1.29	1.44	1.25	1.45	1.48	1.38	1.44
Sum^{iv}	8	8	8	8	8	8	8	8	8	8	8	8	8	8
Al^{vi}	1.84	1.82	1.86	1.91	1.77	1.82	1.85	1.82	2.45	2.37	2.40	2.46	2.21	2.45
Ti	0	0	0	0	0	0	0	0	0	0	0.01	0.02	0.01	0
Fe^{3+}	0.36	0.28	0.30	0.32	0.38	0.29	0.31	0.28	0.55	0.61	0.52	0.56	0.46	0.56
Fe^{2+}	3.20	3.48	3.40	3.35	3.05	3.37	3.38	3.54	2.51	2.19	2.50	2.40	2.74	2.36
Mn	0.04	0.03	0.03	0.04	0.04	0.04	0.04	0.04	0.06	0.07	0.06	0.06	0.06	0.07
Mg	5.96	5.90	5.89	5.80	6.11	5.97	5.92	5.86	5.59	5.86	5.71	5.68	5.80	5.73
Ca	0.10	0.09	0.08	0.10	0.10	0.09	0.05	0.06	0.06	0.05	0.06	0.06	0.07	0.06
Na	0.06	0.03	0.05	0.06	0.05	0.05	0.05	0.04	0.06	0.06	0.06	0.02	0.05	0.06
K	0.01	0.02	0.02	0.02	0.02	0.02	0.05	0.04	0.01	0.02	0.03	0.03	0.01	0.02
R^{2+}	9.19	9.41	9.32	9.19	9.20	9.37	9.33	9.43	8.16	8.12	8.27	8.15	8.60	8.16
R^{3+}	2.20	2.10	2.16	2.23	2.15	2.11	2.16	2.10	3.00	2.98	2.92	3.02	2.68	3.01
4Si	1.70	1.67	1.68	1.67	1.73	1.68	1.68	1.68	1.64	1.69	1.64	1.63	1.65	1.64
$3R^{2+}$	3.06	3.14	3.11	3.06	3.07	3.12	3.11	3.14	2.72	2.71	2.76	2.72	2.87	2.72
M^+	0.27	0.22	0.23	0.28	0.27	0.24	0.19	0.19	0.20	0.18	0.21	0.17	0.21	0.21
Charge	0.06	0.04	0.04	0.04	0.05	0.04	0.01	0.01	0.11	0.11	0.09	0.10	0.08	0.11

Tabela suplementar do manuscrito II. Continuação da Tabela G: Análises por microssonda eletrônica de interestratificados clorita/esmectita.

G) DIFRATOGRAMAS DE RAIOS X

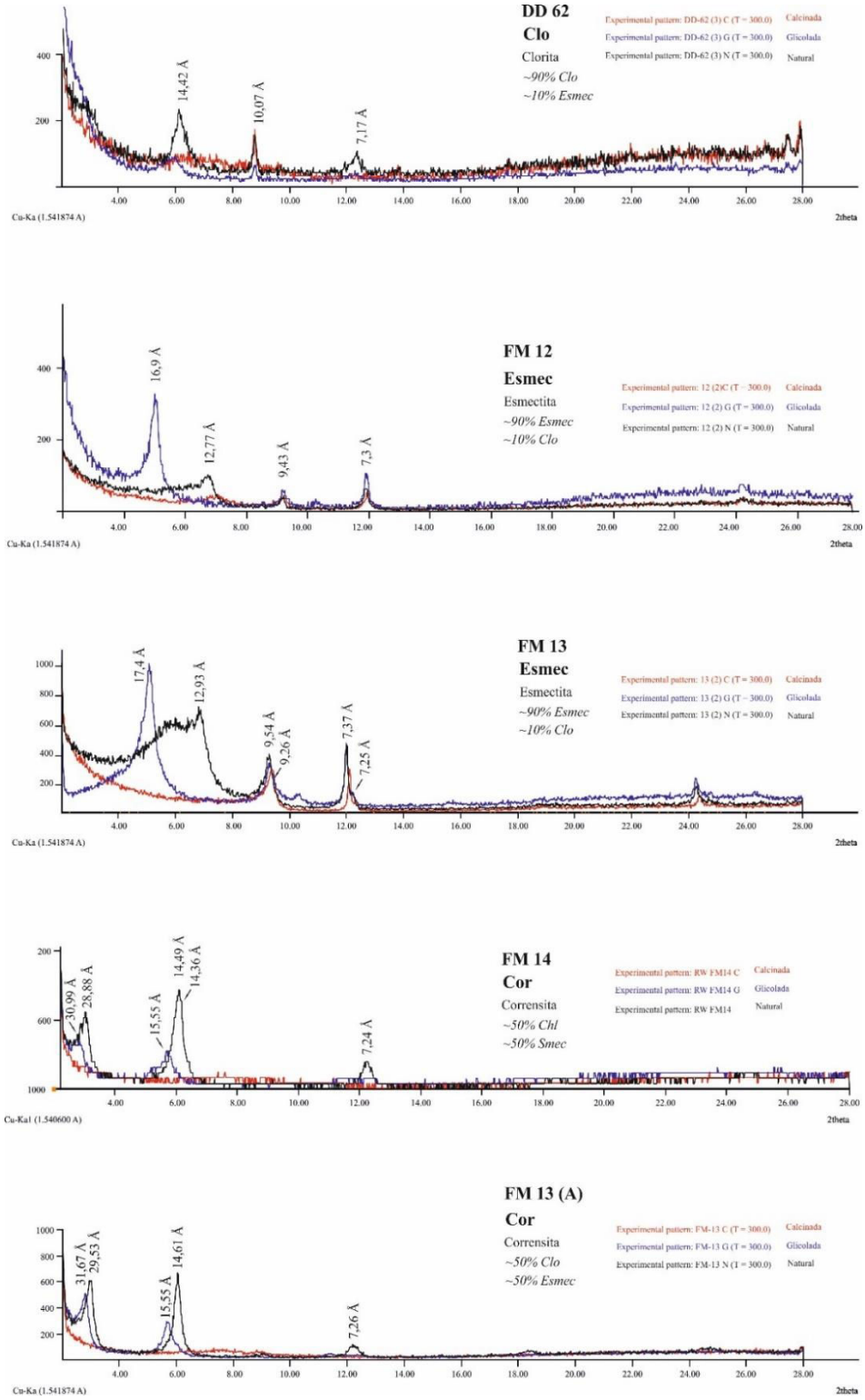

Difratogramas de raios X pelo método das amostras orientadas. A localização e descrição das amostras podem ser encontradas na Tabela de Pontos no ANEXO D.

Continuação: DIFRATOGRAMAS DE RAIOS X

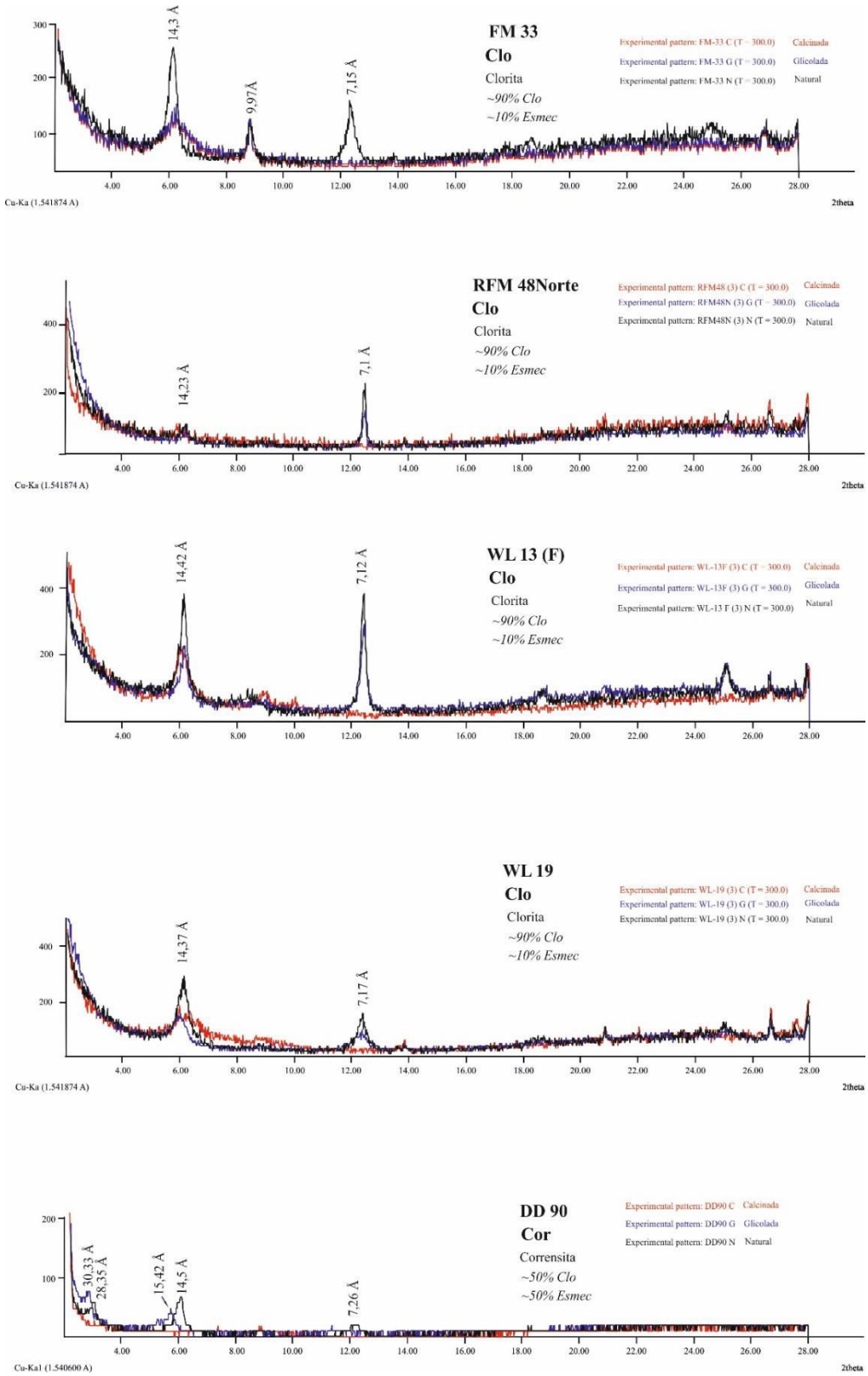

Difratogramas de raios X pelo método das amostras orientadas. A localização e descrição das amostras podem ser encontradas na Tabela de Pontos no ANEXO D.

Continuação: DIFRATOGRAMAS DE RAIOS X

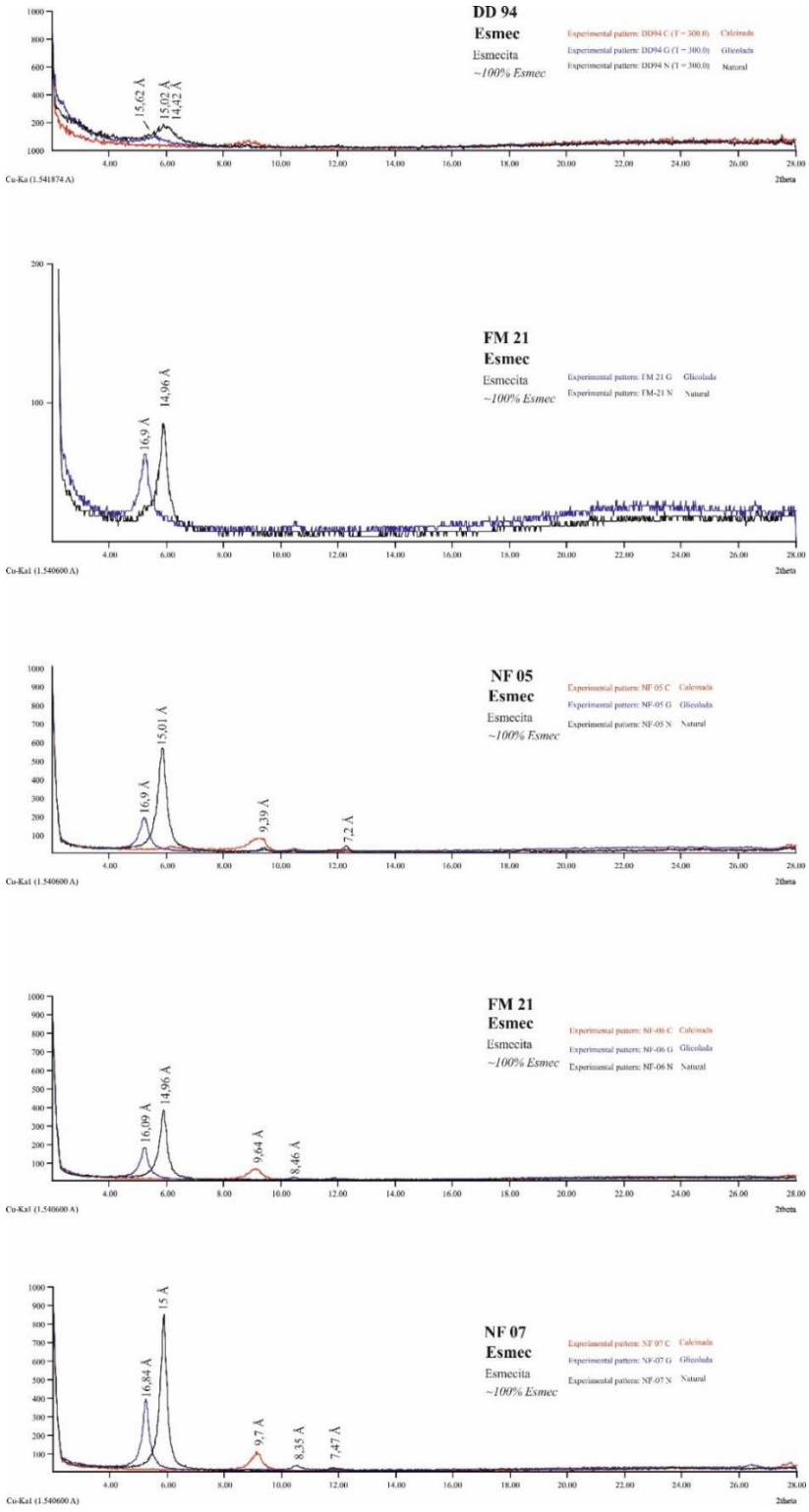

Difratogramas de raios X pelo método das amostras orientadas. A localização e descrição das amostras podem ser encontradas na Tabela de Pontos no ANEXO D.

Continuação: DIFRATOGRAMAS DE RAIOS X

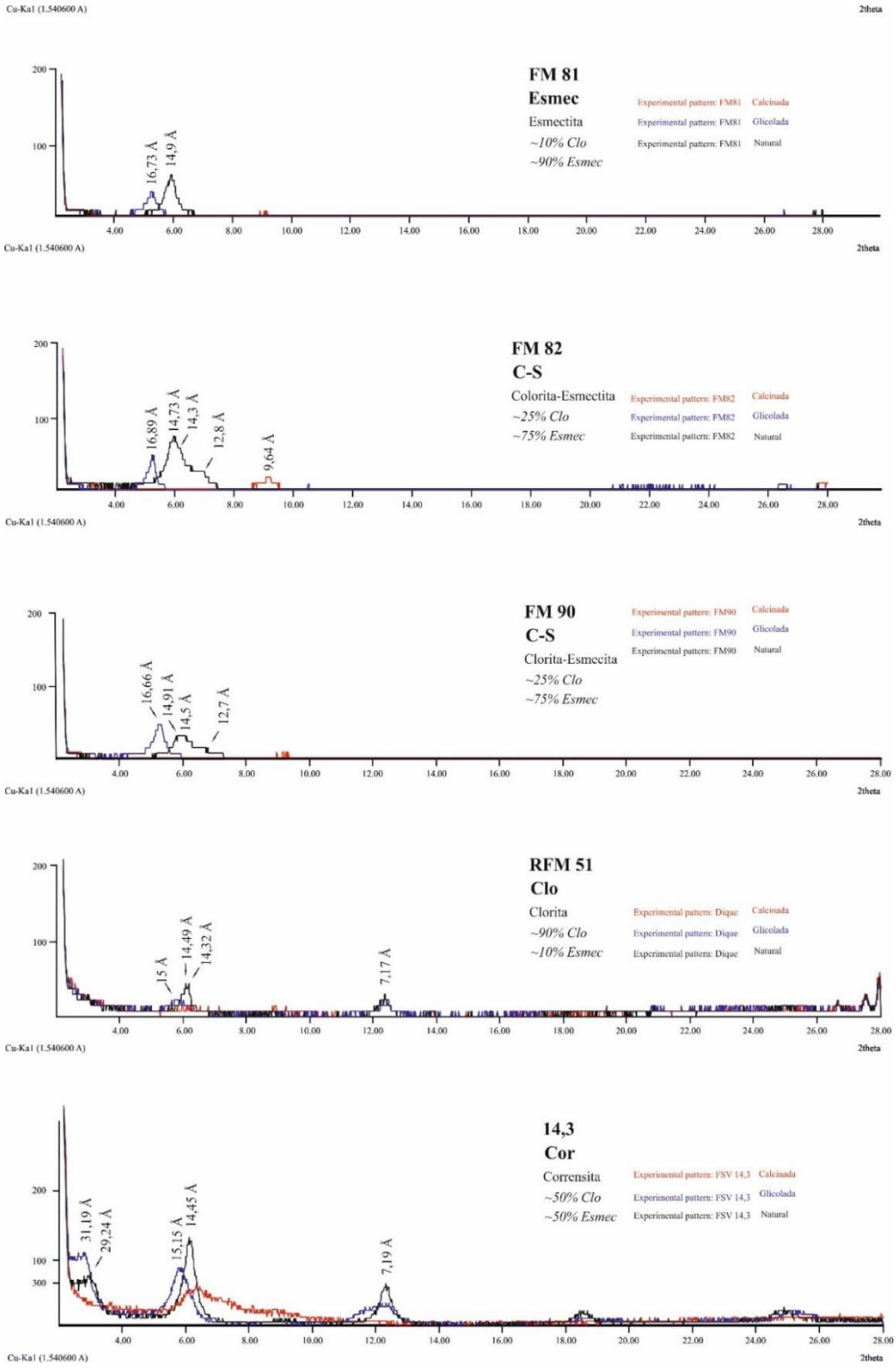

Difratogramas de raios X pelo método das amostras orientadas. A localização e descrição das amostras podem ser encontradas na Tabela de Pontos no ANEXO D.

Continuação: DIFRATOGRAMAS DE RAIOS X

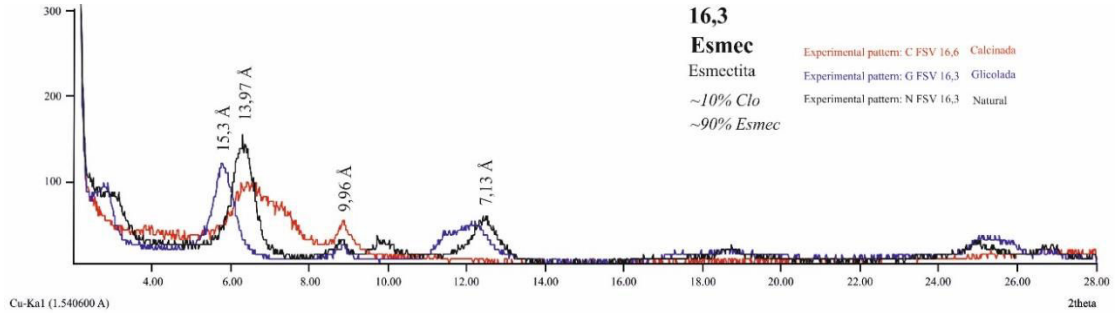

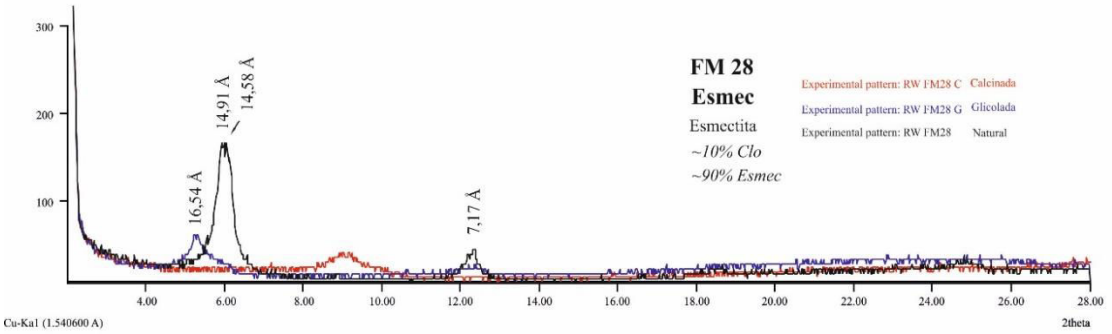

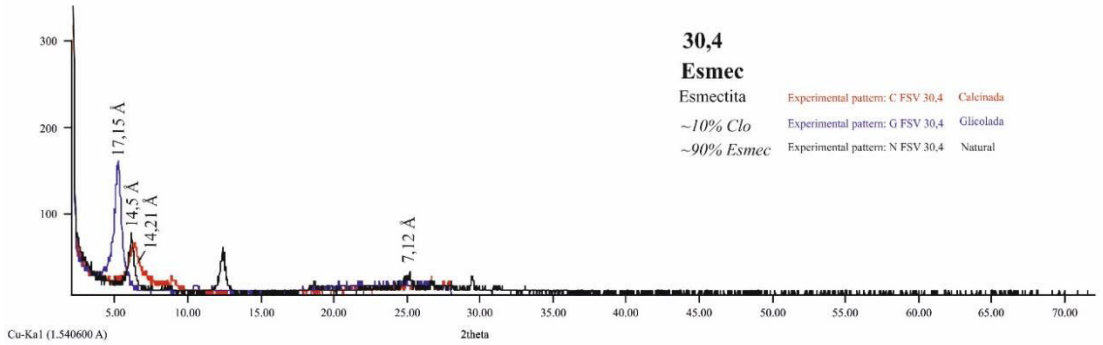

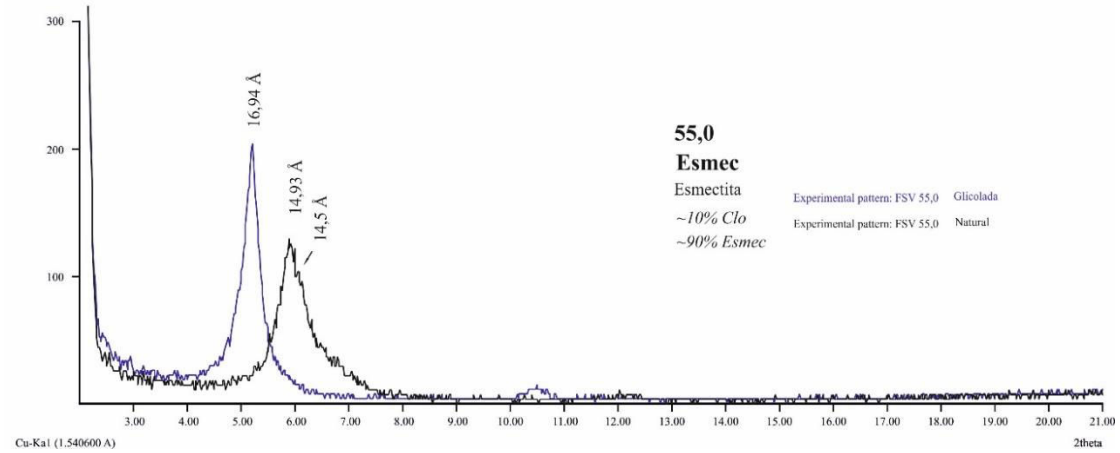

Difratogramas de raios X pelo método das amostras orientadas. A localização e descrição das amostras podem ser encontradas na Tabela de Pontos no ANEXO D.